Star formation histories of brightest group galaxies in CLoGS

OC Havenga



orcid.org 0000-0003-0995-0785

Dissertation accepted in partial fulfilment of the requirements for the degree *Master of Science in Astrophysical Sciences* at the North-West University

Supervisor: Prof SI Loubser

Graduation July 2020

24909629

Acknowledgements

Firstly I want to thank NASSP (the National Astrophysics and Space Science Programme) and NRF (National Research Foundation) for the funding during my master's studies. I also want to thank Tannie Petro Sieberhagen and Lendl Fransman for the financial administration as well as Elanie van Rooyen and Lee-Ann van Wyk for all the other administration.

I want to thank Prof Ilani Loubser for being a great supervisor and pulling me back in line all the time. I also want to thank Dr Ando Ratzimbazafy for the initial stages of the data analyses, and Dr Konstantinos Kolokythas for the interpretation help at the end. Thank you Me C. van Zyl for the language editing.

Thanks to the whole CSR (Centre for Space Research) for the support, including Prof SES Ferreira as the research director and Prof RA Burger as the NWU NASSP node manager.

I want to thank my parents and brothers, as well as my grandparents (Okkie and Retha Britz as well as Joey Havenga) for their emotional support and prayers. A great big thanks to all my friends who supported me through this time emotionally and physically.

Abstract

An important component of galaxy formation and evolution studies, is to accurately constrain the star formation histories (SFHs) of galaxies. While the SFHs of most massive early-type galaxies can be described using a single passively-evolving stellar component (Single Stellar Population [SSP]), there is a fraction of massive early-type galaxies in the centres of galaxy groups and galaxy clusters where recent star formation is observed and their SFHs are better described by two or more stellar components (Composite Stellar Population [CSP]). In this project we identify and constrain possible recent star formation episodes in a sample of 23 BGGs (Brightest Group Galaxies) in the centres of X-ray rich groups that are closer than 80 Mpc, and a sub-sample of the Complete Local-Volume Groups Sample (CLoGS). We use archival spatially-resolved long-slit spectroscopy from the Hobby-Eberly Telescope (HET) at the McDonald Observatory, and determine whether the BGGs are better described by a SSP or a CSP using Université de Lyon Spectroscopic analysis Software (ULySS). Although the stellar population models fit the spectra of the galaxies, we find that we are not able to detect young stellar components with confidence, due to the lack of blue age-sensitive absorption features in spectra of the wavelength range of 4600 Å - 6200 Å. One feature, however, that does not fit well, is the sodium doublet NaD. This is due to an overabundance that is not predicted in the stellar population models. A detailed analysis is done to investigate the effects of different model ingredients (e.g. initial mass function [IMF], α-enhancement, etc.) on the predicted spectra, in an effort to identify a possible origin for this mismatch with observations. The stellar population results of these BGGs are also compared to those from a comparable analysis of a sample of 32 Brightest Cluster Galaxies (BCGs) in rich galaxy clusters at redshifts $0.05 < z < 0.3$. In this comparison we found that the sodium overabundance in the galaxies must be a physical phenomenon, rather than an artefact of the stellar population modelling, and might show a weak correlation to mass. The analysis of the stellar population models can be improved by using [Na/Fe]-enhanced models, whereas using α-enhanced models will worsen the mismatch between the data and models. A full suite of [Na/Fe]-enhanced models, however, still need to be developed for packages such as ULySS.

Keywords: galaxies: elliptical and lenticular, cD - galaxies: abundances - galaxies: kinematics and dynamics - galaxies: stellar content - techniques: spectroscopic

Contents

1 Introduction and background information **17**

1.1 The theory of hierarchical galaxy formation . . . 17

1.2 Galaxy clusters, galaxy groups and galaxy evolution . . . 17

1.3 Stellar evolution and stellar populations . . . 19

1.3.1 Basic stellar evolution . . . 19

1.3.2 Stellar spectra . . . 20

1.3.3 Libraries of synthetic stellar spectra . . . 21

1.4 Spectra of galaxies (integrated light) . . . 21

1.4.1 Stellar populations . . . 21

1.4.2 IMF . . . 23

1.5 The important spectral features . . . 27

1.5.1 Breaking the degeneracy between metallicity and age . . . 27

1.6 Illustration of stellar population models by varying age and metallicity . . . 28

1.6.1 Varying age . . . 28

1.6.2 Varying metallicity . . . 30

1.7 Motivation for this study . . . 32

2 Sample of BGGs and data **34**

2.1 Description of the CLoGS sample . . . 34

2.2 Description of the sub-sample of 23 BGGs . . . 35
2.3 Observations from HET . . . 35
2.3.1 HET . . . 37
2.3.2 Marcario Low-Resolution Spectrograph . . . 37
2.4 Optical spectral analysis . . . 37
2.4.1 Reduction . . . 37
2.4.2 Determining the amount of pixels in each FITS-file for each bin . . . 37
2.4.3 Creating the spectra for inner and outer apertures . . . 38
2.4.4 ULySS . . . 39
2.4.5 Other galaxy and group properties . . . 41

3 SSP and CSP results **47**
3.1 Construction of the stellar populations . . . 47
3.2 Classification results . . . 48
3.3 Different models . . . 56
3.4 Checking the reliability of the solutions . . . 62
3.5 Mock spectra analysis . . . 64
3.6 Brightest cluster galaxies . . . 66

4 Analysis of SSP models **68**
4.1 Analysis of model with the use of α-enhancements . . . 69
4.1.1 What is α-enhancement? . . . 69
4.1.2 Analysis of the model . . . 70
4.1.3 Varying α-enhancement . . . 70
4.1.4 Varying α-enhancement and varying age . . . 72
4.1.5 Varying α-enhancement and varying metallicity . . . 74
4.2 Analysis of model with the use of [Na/Fe]-enhancements . . . 78
4.2.1 What is [Na/Fe]-enhancement? . . . 78
4.2.2 Varying [Na/Fe]-enhancement . . . 79
4.2.3 Varying [Na/Fe]-enhancement and varying age . . . 80
4.2.4 Varying [Na/Fe]-enhancement and varying metallicity . . . 83

4.3 Varying IMF . . . 84
4.3.1 Varying unimodal IMF slope . . . 84
4.3.2 Varying IMF type . . . 85
4.3.3 Varying α-enhancement and varying IMF type . . . 87
4.3.4 Varying [Na/Fe]-enhancement and varying IMF . . . 91
4.4 Conclusion of SSP model analysis . . . 96

5 NaD mismatches and analysis **97**
5.1 Measuring the Na overabundances . . . 97
5.2 NaD Overabundance measurements . . . 98
5.3 Correlation with observed properties . . . 101
5.3.1 Observations in other wavelengths (X-ray, radio, sub-mm) . . . 101
5.3.2 Correlation between Na overabundance and other galaxy and group properties . . . 101

6 Summary, conclusions and future work **105**

Appendices **108**

A Observations in other wavelengths **109**
A.1 Observations in other wavelengths (X-ray, radio, sub-mm) . . . 109
A.2 High-richness galaxy groups . . . 109
A.2.1 NGC0410 in LGG18 . . . 109
A.2.2 NGC0584 in LGG27 . . . 109
A.2.3 NGC0777 in LGG42 . . . 109
A.2.4 NGC0924 in LGG61 . . . 110
A.2.5 NGC1060 in LGG72 . . . 110
A.2.6 NGC1453 in LGG103 . . . 110
A.2.7 NGC1587 in LGG117 . . . 110
A.2.8 NGC2563 in LG158 . . . 110
A.2.9 NGC4261 in LG278 . . . 111
A.2.10 NGC5353 in LGG363 . . . 111
A.2.11 NGC5846 in LGG393 . . . 111

A.2.12 NGC5982 in LGG402 . . . 111
A.2.13 NGC6658 in LGG421 . . . 112
A.2.14 NGC7619 in LGG473 . . . 112
A.3 Low-richness galaxy groups . . . 112
A.3.1 NGC0315 in LGG14 . . . 112
A.3.2 NGC0524 in LGG23 . . . 112
A.3.3 NGC1779 in LGG126 . . . 112
A.3.4 NGC2768 in LGG167 . . . 112
A.3.5 NGC3613 in LGG232 . . . 113
A.3.6 NGC3665 in LGG236 . . . 113
A.3.7 NGC5127 in LGG350 . . . 113
A.3.8 NGC5490 in LGG376 . . . 113
A.3.9 NGC5629 in LGG383 . . . 113

B Other documents **114**

C SAIP Proceedings **115**

Abbreviations and Acronyms

ΛCDM	Lambda Cold Dark Matter
ACIS	Advanced CCD Imaging Spectrometer
AGN	Active Galactic Nuclei
BaSTI	Bag of Stellar Tracks and Isochrones
BCG	Brightest Cluster Galaxy
BGE	Brightest Group Elliptical
BGG	Brightest Group Galaxy
CCD	Charged Coupled Device
CLoGS	Complete Local-Volume Groups Sample
CSP	Composite Stellar Population
DEC	DEClination
FJR	Faber-Jackson Relation
FWHM	Full-Width Half-Maximum
GMRT	Giant Metrewave Radio Telescope
HET	Hobby-Eberly Telescope
HR-diagram	Hertzsprung-Russel diagram
IDL	Interactive Data Language
IGM	Intra-Group Medium
IMF	Initial Mass Function
INT	Isaac Newton Telescope
IRAF	Image Reduction and Analysis Facility
LGG	Lyon Galaxy Group
MILES	Medium-resolution INT Library of Empirical Spectra
M/L	Mass to Light ratio
NED	NASA Extragalactic Database
NGC	New General Catalogue
NRAO	National Radio Astronomy Observatory
NVSS	NRAO VLA Sky Survey
RA	Right Ascension

RASS	ROSAT All-Sky Survey
ROSAT	Röntgensatellit
SED	Spectral Energy Distribution
SF	Star Formation
SFH	Star Formation History
SPS	Stellar Population Synthesis
SSP	Simple Stellar Population
ULySS	Universite de Lyon Spectroscopic Analysis Software
UV	Ultra-Violet
VLA	Very Large Array
XMM	X-ray Multi-Mirror Mission

List of Figures

1.1 The two models for galaxy formation: monolithic or classical formation and hierarchical merging (Ellis et al., 2000) . . . 18

1.2 The HR-diagram can be used to show the evolution of different types of stars by using their absolute magnitude and effective surface temperature. The figure is obtained from https://www.researchgate.net/figure/The-Hertzsprung-Russell-diagram-HR-diagram-shows-the-relationship-between-luminosity_fig1_277879903. . . . 20

1.3 This figure, by Conroy (2013), explains the composition of an SSP and a CSP. The IMF, isochrones and stellar spectra are needed to build the single stellar populations. These, together with the star formation (SF), chemical evolution, and the dust, are used to build up the CSPs. . . . 23

1.4 Five of the different types of IMF slopes. The dark blue line indicates the Salpeter unimodal IMF (Salpeter, 1955), the green line indicates a bimodal IMF (Scalo, 1986), the red line indicates the Kroupa IMF (Kroupa, 2000), the light blue line shows the Chabrier IMF for individual stars, and the purple line shows the Chabrier IMF for stellar systems (Chabrier, 2003). This image is by Johannes Buchner from https://commons.wikimedia.org/w/index.php?curid=44779435. . . . 26

1.5 The MILES-model for an SSP of varying age, with metallicity at $[Fe/H] = 0.15$ and no α-enhancements. The y-axis (flux) is normalised with respect to the maximum value of the SSP with age 0.03 Gyr. This was done to study the influence of the age and metallicity on the spectra. From a young SSP (0.03 Gyr) in the bottom right corner to an old SSP (14 Gyr) in the upper left corner, in increments of 0.01 Gyr for the first 0.1 Gyr, increments of 0.05 Gyr up to 1 Gyr, 0.25 Gyr up to 4 Gyr and 0.5 Gyr increments to 14 Gyr. The variable increments are necessary to see the notable differences at the younger ages. . . . 29

1.6 The MILES-model for an SSP of varying metallicity, with age at 14 Gyr and no α-enhancements. The y-values are normalised with respect to the maximum value of the SSP with $[Fe/H] = -2.27$ with the metallicity increasing from -2.27 to 0.40. . . . 30

1.7 The MILES-model for an SSP of varying metallicity, with age fixed at 14 Gyr. The y-axis is normalised with respect to the maximum value of the galaxy with $[Fe/H] = -2.27$ with the metallicity increasing from -2.27 to 0.40. 31

2.1 The Hobby-Eberly Telescope (on the left) at the McDonald Observatory in Texas, US, from https://mcdonaldobservatory.org/news/gallery/het-dome-dusk. The Marcario Low Resolution Spectrograph can be seen on the right (from https://www.noao.edu/gateway/het/pfip_lrs_lift_tn.jpg). 35

2.2 The spectrum of NGC0524 for the full observed wavelength-range. The black line indicates the observed spectrum, the blue line is the stellar population model of the best fit and the red is deviations that are masked during the fitting process. The light blue line shows the multiplicative polynomial that is used to normalise the continuum. The residuals are shown in the lower panel, where the green lines indicate the residuals as allowed by the error spectra (i.e. residuals larger than the green lines indicate deviations from the model as opposed to fluctuations caused by the noise in the spectrum). 41

2.3 The same spectrum of NGC0524 as shown in Figure 2.2, but now truncated at 4600-6200 Å. Therefore, the atmospheric features are excluded without losing important indices. 41

3.1 The SSP (a and c) and CSP (b and d) fit for the inner aperture (a and b) and outer aperture (c and d) for NGC1779. The different lines and colours have the same meaning as described in Figure 2.2. . . 49

3.2 Plots of the χ^2 values of the SSP fits for NGC0410 inner bin for different metallicities and ages. The solution of the SSP fit is an age of 16468 Myr and [Fe/H] = 0.10 with χ^2=0.104. 63

3.3 Plots of the χ^2 values of the SSP fits for NGC1779 inner bin for different metallicities and ages. The solution of the SSP fit is an age of 5876 Myr and [Fe/H] = 0.20 with χ^2=0.052. 63

3.4 Plots of the χ^2 values of the SSP fits for NGC5846 inner bin for different metallicities and ages. The solution of the SSP fit is an age of 17780 Myr and [Fe/H] = -0.23 with χ^2=0.032. 63

3.5 Figure obtained from Loubser et al. (2016), their figure 10. The SSP ages of the inner apertures of 19 of the 32 BCGs that were analysed are plotted against the minimum cooling time (t_c) vs free-fall time (t_{ff}) ratio. The BCGs in blue have prominent young stellar components and are shown at Log (SSP age) = 0 for reference. 66

3.6 The BGGs are plotted in blue, while the BCGs are plotted in green and red. Note the two different Faber-Jackson relations (FJRs) for the two classes. Figure from Loubser et al. (2018). 67

4.1 This is the spectrum of NGC0410 (inner aperture). The NaD feature can be seen at 5900 $\mathring{A}$ (between the red dashed lines). The colours have the same meaning as in Figure 2.2. Just note that the observed spectrum and the model are almost indistinguishable, except for the NaD feature and other small variations. 69

4.2 The MILES-model for an SSP of 14.0 Gyr and [Fe/H]=0.15 with variable α-enhancement. The y-values are normalised with respect to the maximum value of the Base model spectrum. 71

4.3 The MILES-model for an SSP of 14.0 Gyr and [Fe/H]=0.15 with variable α-enhancement. The y-axis is normalised with respect to the maximum value of the Base α spectrum and the wavelength range is from 5200 $\mathring{A}$ to 5400 $\mathring{A}$. 71

4.4 The MILES-model for an SSP of 14.0 Gyr and [Fe/H]=0.15 with variable α-enhancement. The y-axis is normalised with respect to the maximum value of the Base α spectrum and the wavelength range is from 5916 $\AA$ to 6120 $\AA$. 72

4.5 The MILES-model for an SSP of [Fe/H]=0.15 with variable α-enhancement as well as variable age (increasing from 0.03 Gyr to 14.0 Gyr). The y-axis is normalised with respect to the maximum value of the Base α spectrum of the 0.03 Gyr model. 73

4.6 The MILES-model for an SSP of [Fe/H]=0.15 with variable α-enhancement as well as variable age (increasing from 0.03 Gyr to 14.0 Gyr). The y-axis is normalised with respect to the maximum value of the Base α spectrum of the 0.03 Gyr model and the wavelength range is from 5916 $\AA$ to 6120 $\AA$. The NaD absorption lines can be seen at the shifted wavelength of 6007.45 $\AA$ and 6013.84 $\AA$ (z = 0.02, rest wavelengths are 5889.95 $\AA$ and 5895.92 $\AA$). 74

4.7 The MILES-model for an SSP of 14.0 Gyr with variable α-enhancement as well as variable metallicity (increasing from $[Fe/H] = -2.27$ to $[Fe/H] = 0.40$). The y-axis is normalised with respect to the maximum value of the Base-α spectrum of the $[Fe/H] = -2.27$ model. 75

4.8 The MILES-model for an SSP of 14.0 Gyr with variable α-enhancement as well as variable metallicity (increasing from $[Fe/H] = -2.27$ to $[Fe/H] = 0.40$). The y-axis is normalised with respect to the maximum value of the Base-α spectrum of the $[Fe/H] = -2.27$ model and the wavelength range is from 5916 $\AA$ to 6120 $\AA$. The NaD absorption doublet can be seen at the shifted wavelength of 6007.45 $\AA$ and 6013.84 $\AA$ (rest wavelengths are 5889.95 $\AA$ and 5895.92 $\AA$). 76

4.9 The MILES-model for an SSP of 14.0 Gyr with variable α-enhancement as well as variable metallicity (increasing from $[Fe/H] = -2.27$ to $[Fe/H] = 0.40$). The y-axis is normalised with respect to the maximum value of the Base-α spectrum of the $[Fe/H] = -2.27$ model and the wavelength range is from 5200 $\AA$ to 5400 $\AA$. The Mg absorption line can be seen at the shifted wavelength of 5280.2 $\AA$ (rest wavelength is 5176.7 $\AA$). 77

4.10 The same plots as in Figure 4.9, but only at $[Fe/H] = -2.27$ (left) and $[Fe/H] = 0.40$ (right). 78

4.11 The E-MILES-model for an SSP of 14.0 Gyr and [Fe/H]=0.15 with variable [Na/Fe]-enhancement ($[Na/Fe] = +0.3, 0.6, 0.9, 1.2$). The y-axis is normalised with respect to the maximum value of the $[Na/Fe] = +0.3$ enhanced spectrum. 79

4.12 The E-MILES-model for an SSP of 14.1 Gyr and [Fe/H]=0.22 with variable [Na/Fe]-enhancement. The y-axis is normalised with respect to the maximum value of the $[Na/Fe] = +0.3$ enhanced spectrum and the wavelength range is from 5800 $\AA$ to 6000 $\AA$. The well-known NaD double absorption lines can be seen at 5889.95 $\AA$ and 5895.92 $\AA$. 79

4.13 The E-MILES-model for an SSP of [Fe/H]=0.22 with variable [Na/Fe]-enhancement as well as variable age (increasing from 1 Gyr to 17.78 Gyr). The y-axis is normalised with respect to the maximum value of the spectrum with [Na/Fe] = 0.3 and age of 1 Gyr. 81

4.14 The E-MILES-model for an SSP of [Fe/H]=0.22 with variable [Na/Fe]-enhancement as well as variable age (increasing from 1 Gyr to 17.78 Gyr). The y-axis is normalised with respect to the maximum value of the spectrum with [Na/Fe] = 0.3 and age of 1 Gyr and the wavelength range is from 5800 $\AA$ to 6000 $\AA$. The well-known NaD double absorption lines can be seen at 5889.95 $\AA$ and 5895.92 $\AA$. 82

4.15 The E-MILES-model for an SSP of age 14.1 Gyr with variable [Na/Fe]-enhancement as well as variable metallicities (from $[Fe/H] = -0.40$ increasing to $[Fe/H] = 0.22$). The y-axis is normalised with respect to the maximum value of the spectrum with [Na/Fe] = 0.3 and metallicity of $[Fe/H] = 0.22$. 83

4.16 The E-MILES-model for an SSP of age 14.1 Gyr with variable [Na/Fe]-enhancement as well as variable metallicities (from $[Fe/H] = -0.40$ increasing to $[Fe/H] = 0.22$). The y-axis is normalised with respect to the maximum value of the spectrum with [Na/Fe] = 0.3 and metallicity of $[Fe/H] = 0.22$ and the wavelength range is from 5800 $\AA$ to 6000 $\AA$. The well-known NaD double absorption lines can be seen at 5889.95 $\AA$ and 5895.92 $\AA$. 83

4.17 The MILES-model for an SSP of varying unimodal IMF slopes (from a slope of 0.3 to 3.5), age at 14 Gyr, metallicity at $[Fe/H] = 0.15$ and no α-enhancements. The y-axis is normalised with respect to the maximum value of the galaxy with IMF slope = 0.03. This figure shows how the IMF slope influences the form of the whole observed spectrum. For a clearer view of the smaller changes in spectra, please refer to Figure 4.18. 84

4.18 The MILES-model for an SSP of varying IMF (from a slope of 0.3 to 3.5), a constant age at 14 Gyr and metallicity at $[Fe/H] = 0.15$ and no α-enhancements. The y-axis is normalised with respect to the maximum value of the galaxy with IMF slope = 0.3 85

4.19 The MILES-model for an SSP of varying IMF type with an IMF slope of 1.3, age at 14 Gyr, metallicity at $[Fe/H] = 0.15$ and no α-enhancements. The y-axis is normalised with respect to the maximum value of the galaxy with unimodal IMF type. 86

4.20 The MILES-model for an SSP of varying IMF type with an IMF slope of 1.3, age at 14 Gyr, metallicity at $[Fe/H] = 0.15$ and no α-enhancements. This graph shows the NaD feature. All the plots are normalised so that the influence on the depth of the NaD feature can be investigated. 86

4.21 The MILES-model for an SSP of 14.0 Gyr and $[Fe/H] = 0.15$ with variable α-enhancement as well as variable IMF slope (from a slope of 0.3 to 3.5). The bimodal and unimodal IMFs are plotted next to each other. The y-axis is normalised with respect to the maximum value of the Base α spectrum of the unimodal IMF with a slope of 0.30. 88

4.22 The MILES-model for an SSP of 14.0 Gyr and $[Fe/H] = 0.15$ with variable α-enhancement as well as variable IMF slope (from a slope of 0.3 to 3.5). The bimodal and unimodal IMFs are plotted next to each other. The y-axis is normalised with respect to the maximum value of the Base α spectrum of the unimodal IMF with a slope of 0.30 and the wavelength range is from 5200 Å to 5400 Å. The Na absorption line can be seen at the shifted wavelength of 5280.2 $\AA$ (rest wavelength is 5176.7 $\AA$). 89

4.23 The MILES-model for an SSP of 14.0 Gyr and $[Fe/H] = 0.15$ with variable α-enhancement as well as variable IMF type. The y-axis is normalised with respect to the maximum value of the Base α spectrum of the unimodal IMF. The different IMF types are unimodal (un1.30), bimodal (bi1.30), Chabrier IMF (ch1.30), Kroupa binary corrected (kb1.30) and the Kroupa Universal IMF (ku1.30). . . 90

4.24 The MILES-model for an SSP of 14.0 Gyr and $[Fe/H] = 0.15$ with variable α-enhancement as well as variable IMF type. The y-axis is normalised with respect to the maximum value of the Base Alpha spectrum of the unimodal IMF and the wavelength range is from 5200 $\AA$ to 5400 $\AA$. The Na absorption line can be seen at the shifted wavelength of 5280.2 $\AA$ (rest wavelength is 5176.7 $\AA$). 91

4.25 The E-MILES-model for an SSP of age 14.1 Gyr and $[Fe/H] = 0.22$ with variable [Na/Fe]-enhancement as well as variable IMF (from a slope of 0.3 to 3.3). The y-axis is normalised with respect to the maximum value of the spectrum with [Na/Fe] = 0.3 and IMF slope of 0.3. 92

4.26 The E-MILES-model for an SSP of age 14.1 Gyr and $[Fe/H] = 0.22$ with variable [Na/Fe]-enhancement as well as variable IMF (from a slope of 0.3 to 3.3). The y-axis is normalised with respect to the maximum value of the spectrum with [Na/Fe] = 0.3 and IMF slope of 0.3 and the wavelength range is from 5800 $\AA$ to 6000 $\AA$. The well-known NaD double absorption lines can be seen at 5889.95 $\AA$ and 5895.92 $\AA$. 93

4.27 The E-MILES-model for an SSP of age 14.1 Gyr and $[Fe/H] = 0.22$ with variable [Na/Fe]-enhancement as well as variable IMF type (unimodal and bimodal) and slope. The y-axis is normalised with respect to the maximum value of the spectrum with [Na/Fe] = 0.3 and unimodal IMF slope of 0.3. 95

4.28 The E-MILES-model for an SSP of age 14.1 Gyr and $[Fe/H] = 0.22$ with variable [Na/Fe]-enhancement as well as variable IMF type (unimodal and bimodal) and slope. The y-axis is normalised with respect to the maximum value of the spectrum with [Na/Fe] = 0.3 and unimodal IMF slope of 0.3 and the wavelength range is from 5800 $\AA$ to 6000 $\AA$. The well-known NaD double absorption lines can be seen at 5889.95 $\AA$ and 5895.92 $\AA$. 96

5.1 The spectrum of NGC4261 inner SSP fit. The variables for the different measurements are: $A \rightarrow B = b$ and $B \rightarrow C = a$. 98

5.2 The fraction of NaD overabundance in the SSP (left) and CSP (right) fits of the galaxies, vs the velocity dispersion from Table 2.4. Note that the red points indicate galaxies that have both inner and outer bin overabundances. 102

5.3 The fraction of NaD overabundance in the SSP (left) and CSP (right) fits of the galaxies, vs the velocity dispersion slope from Table 2.4. Note that the red points indicate galaxies that have both inner and outer bin overabundances. 102

5.4 The fraction of NaD overabundance in the SSP (left) and CSP (right) fits of the galaxies, vs the radio output at 235 MHz from Table 2.6. 103

5.5 The fraction of NaD overabundance in the SSP (left) and CSP (right) fits of the galaxies, vs the radio output at 610 MHz from Table 2.6. 103

5.6 The fraction of NaD overabundance in the SSP (left) and CSP (right) fits of the galaxies, vs the radio spectral index from Table 2.6. 104

List of Tables

1.1 From Tayler (1994). The effective temperature for the spectral classes of main sequence stars. 21

1.2 From Salaris & Cassisi (2005). As can be seen in the **Units** column, most of the spectral indices are expressed in units of Angstrom, but broader molecular indices are expressed in units of magnitude. The chemical elements listed in column 6 are those that contribute to that specific spectral index. Those that are in brackets increase the index line strength when their abundance decreases. 27

1.3 From Worthey (1994). The metallicity sensitivity of different absorption indices. 28

2.1 The information regarding the 23 galaxies was extracted from NED (NASA Extragalactic Database). This includes the galaxy name, the redshift, right-ascension (RA), declination (DEC) and recession velocity. Loubser et al. (2018) provided the ellipticity (ϵ) and the absolute K-band luminosity (M_K). The spiral fraction F_{sp} (which is the ratio of number of late-type galaxies plus unknown galaxies to the total number of galaxies) is provided by Kolokythas et al. (2018) in their table 8. The spiral fraction of the low-richness BGGs is provided by Kolokythas et al. (2019). A spiral fraction lower than 0.75 indicates a more evolved galaxy group with the gas concentrated to the centre. R_{500} is where the density is 500 times the critical density, and M_{500} is the total mass within that radius as derived from system temperature by O'Sullivan et al. (2017), who also provided the local galaxy group name (LGG) to which the galaxies belong. 36

2.2 Binning and slit information 38

2.3 The galaxy kinematics have been derived by Loubser et al. (2018): the central velocity dispersion σ_0, the rotation V_{max}/σ_0 (which was measured in the same inner bin as the stellar populations in our analysis) and the velocity dispersion slope $\eta \pm \Delta\eta$. This table is from Loubser et al., (2018, their table 4). 42

2.4 O'Sullivan et al. (2017) provide the central isochoric cooling time (CCT), the entropy at 10 kpc (K_{10}) and the minimum isochoric cooling time / free fall time ratio ($(t_c/t_{ff})_{min}$). The cool-core status, derived by O'Sullivan et al. (2017) using temperature profiles (T profile) is indicated as CC (cool-core) and non-cool-core (NCC) and those based on the scheme of Hudson et al. (2010) are indicated as strong cool-core (SCC), weak cool-core (WCC) or non-cool-core (NCC). This table also provides the current radio and X-ray morphology as well as notes on the galaxy group kinematics. The radio morphology for the low-richness BGGs was obtained from Kolokythas et al. (2019). Unfortunately, the X-ray properties were not available for the low-richness galaxy groups. 43

2.5 The following information regarding the BGGs is obtained from O'Sullivan et al. (2018), their table 1 and table B.1. The H I masses are from NED, while the stellar and H II masses are derived by O'Sullivan et al. (2018). The 1.4 GHz fluxes are drawn from NVSS (Condon et al., 1998, 2002). The dust masses are from O'Sullivan et al. (2018) and O'Sullivan et al. (2015a). The CO luminosities are from O'Sullivan et al. (2015a) and O'Sullivan et al. (2018) and are in units of [K km s^{-1} pc^2]. 44

2.6 The radio spectral index and radio power output of the BGGs, from Kolokythas et al. (2019) and Kolokythas et al. (2018). 45

2.7 The star formation rate (SFR), the depletion timescales (τ) and the specific star formation rate (sSFR) are determined by O'Sullivan et al. (2018), their table 4. The SFR values indicated by * are obtained from Kolokythas et al. (2019) and these are the SFR as obtained from far ultra-violet (FUV). 46

3.1 The results of the CSP fits of the 23 galaxy spectra. 52

3.2 The SSP fit results and a comparison of the SSP and CSP fit χ^2 values. 53

3.3 A table depicting the best fit of each specific galaxy spectrum. 55

3.4 The first part of the CSP fit results using the four different models in ULySS. In this table, **A** stands for aperture, **C** for component, **I** for inner aperture and **O** for outer aperture. 57

3.5 The second part of the CSP fit results using the four different models in ULySS. 58

3.6 The SSP fit results as well as the comparison between the SSP and CSP χ^2 values for the four different models. 59

3.7 A table depicting the best fit of each specific galaxy spectrum for the 4 different models. The apertures in bold indicate those for which the 4 models have the same outcome. 61

3.8 The discrepancies in the possible star formation from the stellar population fits. For this table, the results from the four models were compared. In the star formation columns, a '✓' was made if three or four of the models showed a CSP best fit. If two of the models showed SSP and two showed CSP, then it was marked with a '?'. If three or four of the models showed an SSP best fit, an 'x' can be seen. 62

3.9 A summary of the SSP and CSP fit results of the mock spectra as described above. The results in bold are where we recover the SFHs used as input to construct the mock spectra. 64

3.10 A summary of the SSP and CSP fit results of the mock spectra in Loubser et al. (2016) for the wavelength range of 3500 Å – 4900 Å. The results in bold indicate the fit (SSP or CSP) that best fit the mock spectrum. 65

5.1 The readings of the NaD absorption line mismatches are recorded in this table. Refer to the discussion about how the measurements were done. The columns $a + b$ and b were measured in arbitrary flux units and then the columns a and FO (fraction overabundance) were calculated. Note that the errors were also calculated using the error propagation rule for subtraction and the error propagation rule for division. Where the FO was measured as zero, the model showed no significant mismatch. In the case of the outer bin for NGC5846, the signal-to-noise ratio was too little to make a measurement. . . . 99

5.2 The readings of the NaD absorption line mismatches (in arbitrary flux units) are recorded in this table. It is important to note that the model that was used here, is the Kroupa Binary Corrected stellar population model. 99

5.3 The difference between the fraction overabundance between the unimodal IMF model and the Kroupa Binary corrected model. The difference is $FO_{Kroupa} - FO_{Unimodal}$. The **Better fit** column shows which model provides the best description of this specific feature in the galaxy spectrum (thus, the model that shows the smallest fraction overabundance). 100

CHAPTER 1

Introduction and background information

The task to constrain the star formation histories (SFHs) of galaxies is one that has, in the past, been oversimplified by some and overcomplicated by others. Many studies have been done on brightest cluster galaxies (BCGs), but their lower-mass counterparts in groups, called brightest group galaxies (BGGs) have been neglected. To effectively interpret the SFHs of BGGs, we first need to understand BCGs and BGGs, as well as the link between galaxy groups and galaxy clusters.

1.1 The theory of hierarchical galaxy formation

Cole et al. (2000) describes the formation of galaxies: Initial galaxies formed from primordial Gaussian density fluctuations generated during inflation. Gravitational instability acting on cold dark matter (which is the dominant mass component of the Universe) amplified these fluctuations. As gas is initially mixed with the dark matter, the visible components of galaxies also accumulate when the dark matter halos collapse. The visible components accumulate as stars condense out of gas that has cooled onto a disk. It is important to remember that galaxies form inside the dark matter halos. The merger of the galaxies are therefore governed by the merger of these dark matter halos (Baugh, 2006).

1.2 Galaxy clusters, galaxy groups and galaxy evolution

Longair (1998) describe two possible mechanisms for the formation of galaxy clusters: the formation of isolated, spherical galaxies as well as three-dimensional hierarchical clustering. These two mechanisms describe how fluctuations in the matter density lead to galaxy formation and how gravity then formed the large-scale structure of the universe as we see it today.

Galaxy clusters are a collection of galaxies bound by their gravitational attraction. There is a gravitational potential well in which the galaxies of the cluster are trapped, usually with a bright galaxy at the centre of the potential

well, called the BCG. As these BCGs are at the centres of the galaxy clusters, understanding them leads to a better understanding of the galaxy cluster as a whole.

Most galaxies are not in galaxy clusters, but in a smaller gravitationally bound system, called a galaxy group (Geller & Huchra, 1983; Fukugita et al., 1998; Eke et al., 2005). Galaxy groups consist of anything between three and ten galaxies and even more. Galaxy groups are some of the best environments to study the impact of galaxies on the surrounding intergalactic medium, e.g. Ponman et al. (2003). Because galaxy groups have a smaller gravitational potential well than galaxy clusters, the effects of the intragroup medium and the intergalactic medium on the galaxies might be somewhat different than those in galaxy clusters.

As in galaxy clusters, there are also a brightest member galaxy within the group, called the BGG. These BGGs can also be studied to learn more about the galaxy group as a whole.

There are two main theories of how galaxies form. The two theories have been introduced by Eggen et al. (1962) and White & Rees (1978) as hierarchical merging and monolithic formation, respectively, and are illustrated in Figure 1.1.

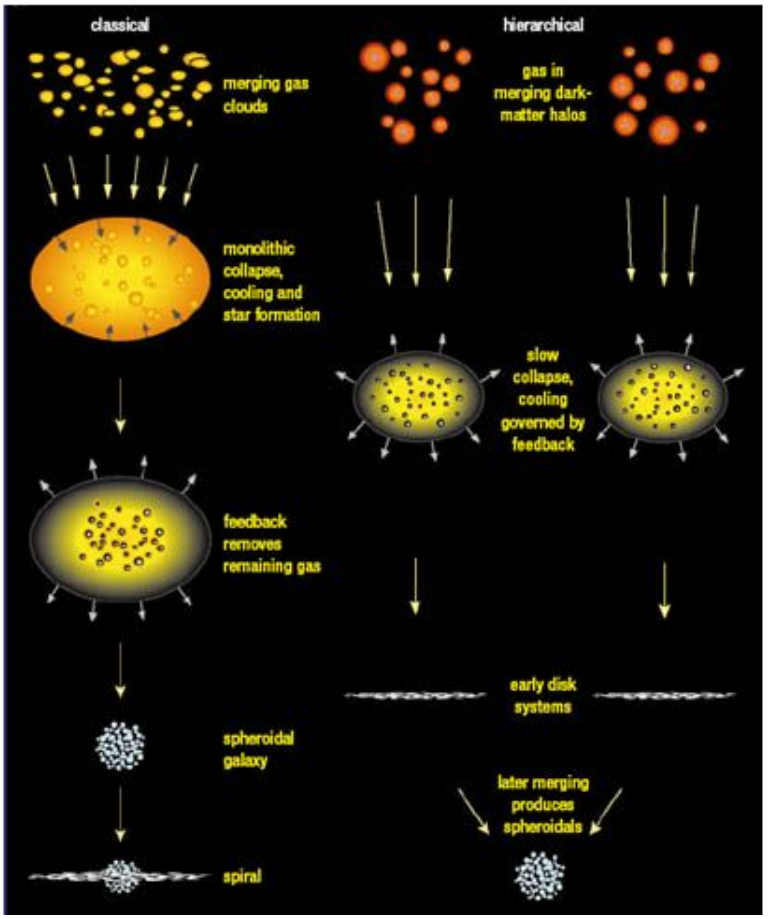


Figure 1.1: *The two models for galaxy formation: monolithic or classical formation and hierarchical merging (Ellis et al., 2000)*

The bottom-up model (hierarchical merging in which massive galaxies are built up through mergers) is the model that is most supported by observations (Le Fèvere et al., 2000; Patton et al., 2000, 2002; Bell et al., 2006; Kartaltepe et al., 2007; Trager et al., 2008; Niederste-Ostholt et al., 2010).

1.3 Stellar evolution and stellar populations

Understanding the formation and evolution of stars is very important in order to understand the formation and evolution of galaxies, as stars make up a very important component of the integrated light from galaxies.

1.3.1 Basic stellar evolution

The Universe consists of baryonic matter (e.g. stars and gas), dark matter and dark energy. Much of the interstellar medium is made up of gas. The interstellar gas consists of mostly hydrogen and helium, but can also consist of heavier elements. When localised density inhomogeneities occur, this gas can start to contract due to gravitational force. As the gravitational force increases, but the gas pressure is still present, the contracting gas heats up. As the gas contracts, the core of the instability heats up more and more, until the core's temperature is sufficiently high to start fusing hydrogen. Before nucleosynthesis starts, the contracting gas is called a protostar.

When nucleosynthesis takes place, the contraction stops, as the gravitational force is now equalised by the opposing radiation pressure. When almost all of the hydrogen is exhausted, the star then contracts again until the core temperature is high enough to start fusing helium atoms.

This process continues until the star's core mainly consists of iron. The energy needed to fuse iron atoms is more than the energy output, making it uneconomic to fuse iron. The star then collapses and its envelope is expelled in a supernova to form a neutron star or a black hole (Salaris & Cassisi, 2005). To distinguish between different types of stars, we must first discuss the Hertzsprung-Russel diagram (HR-diagram) as is shown in Figure 1.2.

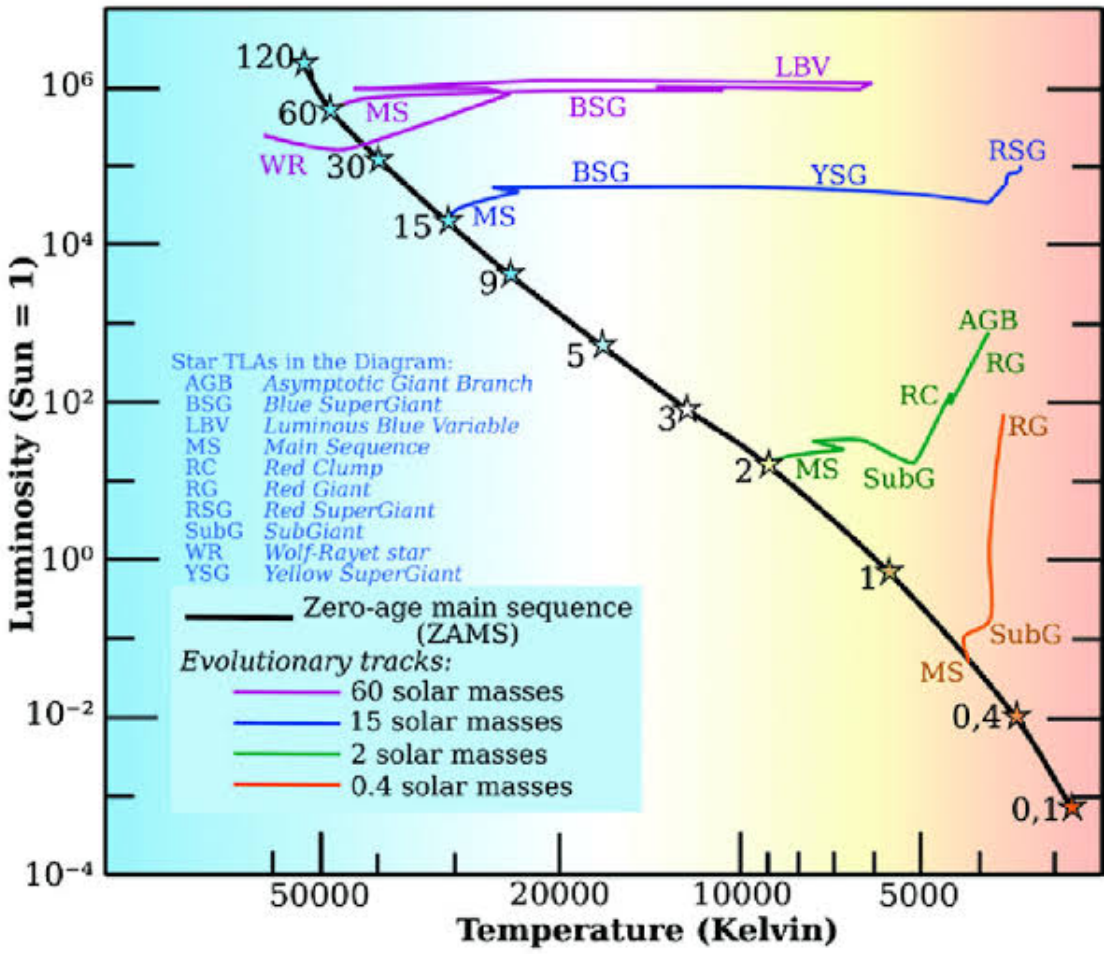


Figure 1.2: *The HR-diagram can be used to show the evolution of different types of stars by using their absolute magnitude and effective surface temperature. The figure is obtained from* https://www.researchgate.net/figure/The-Hertzsprung-Russell-diagram-HR-diagram-shows-the-relationship-between-luminosity_fig1_277879903.

The HR-diagram shows the absolute magnitude of stars versus their colour index (which is also proportional to their surface temperature). This surface temperature also divides the stars into different classes: O, B, A, F, G, K, M, R, N and S. Each spectral type has its own properties (e.g. the O type, which is rich in ionised helium and metals, but has weak hydrogen lines, Tayler, 1994).

1.3.2 Stellar spectra

As mentioned in Section 1.3.1, the fusion of helium (which includes the formation of lithium) is the second step in nucleosynthesis. According to Kaler (1997), the amount of lithium in a star decreases as it gets older, so that the strength of the lithium absorption line also gets weaker as the star moves down the HR-diagram (from F-type to early K-type stars). This lithium doublet is observed at a wavelength of 6708 Å. Kaler (1997) also states that lithium is an important clue to star formation. Just as the lithium absorption lines give information of the star formation, so do many other elements, as is seen in Section 1.5.

All elements have different but well-defined characteristic spectra (Tayler, 1994). If these elements are in the line-of-sight between an observer and a light source, the elements will absorb some frequencies and emit in other, creating the well-defined absorption and emission lines in stellar spectra. When observing stars, these absorption lines indicate the presence of certain elements in the outer layers of stars.

The spectral classes, which were already mentioned, were created because of the abundance of certain elements in certain stars. The reason why surface temperatures of these classes are directly correlated to a certain element abundance, is the fact that electrons in the atoms of elements need to be at a certain level of energy to absorb or emit photons. Table 1.1 gives the effective temperatures of spectral classes for main sequence stars.

Spectral type	**O**	**B0**	**A0**	**F0**	**G0**	**K0**	**M0**	**M5**	**R,N,S**
T_e/K	50 000	25 000	11 000	7 600	6 000	5 100	3 600	3 000	3 000

Table 1.1: *From Tayler (1994). The effective temperature for the spectral classes of main sequence stars.*

1.3.3 Libraries of synthetic stellar spectra

Through the years, different stellar libraries have been compiled of the observed stars (i.e. empirical libraries) in the solar neighbourhood. One example of such an empirical library is the MILES (Medium-resolution INT [Isaac Newton Telescope] Library of Empirical Spectra) library (Sánchez-Blázquez et al., 2007). Researchers then also developed synthetic stellar spectra and also combined these into libraries. An example of such a synthetic stellar library is the Elodie library (Prugniel & Soubiran, 2001) that consists of observed spectra and a grid of interpolated spectra. The Elodie library, for instance, first consisted of observed spectra by an Echelle Spectrograph (Prugniel & Soubiran, 2001), and then adapted to also include synthetic interpolated spectra to complete the library (Prugniel & Soubiran, 2004).

1.4 Spectra of galaxies (integrated light)

The light from galaxies is the light from the stars, interstellar gas and interstellar dust. It is therefore integrated light along the line-of-sight. Usually, the galaxy spectra are dominated by the spectra of stars. According to Appenzeller (2013), the contribution of the stars to the spectra of the galaxy depends on the age of the stellar populations. Most massive elliptical galaxies, with only an old stellar component, contain mainly cool stars with red and near-infrared continua. These galaxies also contain minimal or no cool or warm ($\sim 10^4 K$) interstellar matter, with only hot interstellar matter ($> 10^6 K$) and highly ionised plasma, which radiates in the X-ray regime. Galaxies with younger stellar populations (such as spiral galaxies) also contain hot blue stars that dominate the ultra-violet (UV) and optical region of the galaxy spectra. These galaxies also usually contain cool interstellar matter. This cooler interstellar medium has rich absorption and emission spectra from the molecules, atoms and ions (Appenzeller, 2013).

1.4.1 Stellar populations

Baade (1944) invented the concept of stellar populations. Stellar population synthesis (SPS) originated in 1972 (see Faber, 1972) and the technique that is still in use today, is also referred to as the 'evolutionary population synthesis' (e.g. Maraston, 1998). According to Worthey (1994), the aim of stellar population analysis is to define the distribution of metallicities and ages in a given population (i.e. whether this is a composite or single population) and then to connect that information to certain formation and evolution scenarios.

In any stellar population model, the simple stellar population (SSP) is the starting point, as this describes the evolution of the spectral energy distribution (SED) of a single stellar population at a single metallicity and abundance pattern (Conroy, 2013).

The stars within a collection of stars may have more or less the same age, or may have ages differing by billions of years, which may have been caused by several star formation episodes. The simplest form of stellar populations is the simple stellar population (SSP), which, according to Salaris & Cassisi (2005), consists of stars that have formed at the same time in a burst of star formation. Several natural counterparts exist for SSPs, such as globular and open clusters, some dwarf galaxies as well as some elliptical galaxies.

But even elliptical galaxies sometimes have different star formation epochs, due to cooling flows of the host cluster, mergers, etc. This may lead to a stellar system better described by a composite stellar population (CSP), consisting of at least two different formation epochs.

We firstly focus on how an SSP is built. As can be seen in Figure 1.3, an SSP is dependent on three ingredients: isochrones (which are influenced by the stellar evolution theory), the IMF and spectral libraries. The following equation shows how an SSP is described mathematically:

$$f_{\mathrm{SSP}}(t, Z) = \int_{m_{\mathrm{lower}}}^{m_{\mathrm{upper}}(t)} f_{\mathrm{star}}[T_{\mathrm{eff}}(M), \log\, g(M)|t, Z]\Phi(M)dM \tag{1.1}$$

In equation 1.1, M is the initial stellar mass, the IMF is given by $\Phi(M)$, the stellar spectrum by f_{star}, and f_{SSP} is the time and metallicity-dependent single stellar population spectrum. The lower limit of integration is typically the hydrogen burning limit, while the upper limit depends on the stellar evolution (Conroy, 2013). In this expression, the isochrones determine the relation between the effective temperature, surface gravity and mass for a given time and metallicity.

SSPs

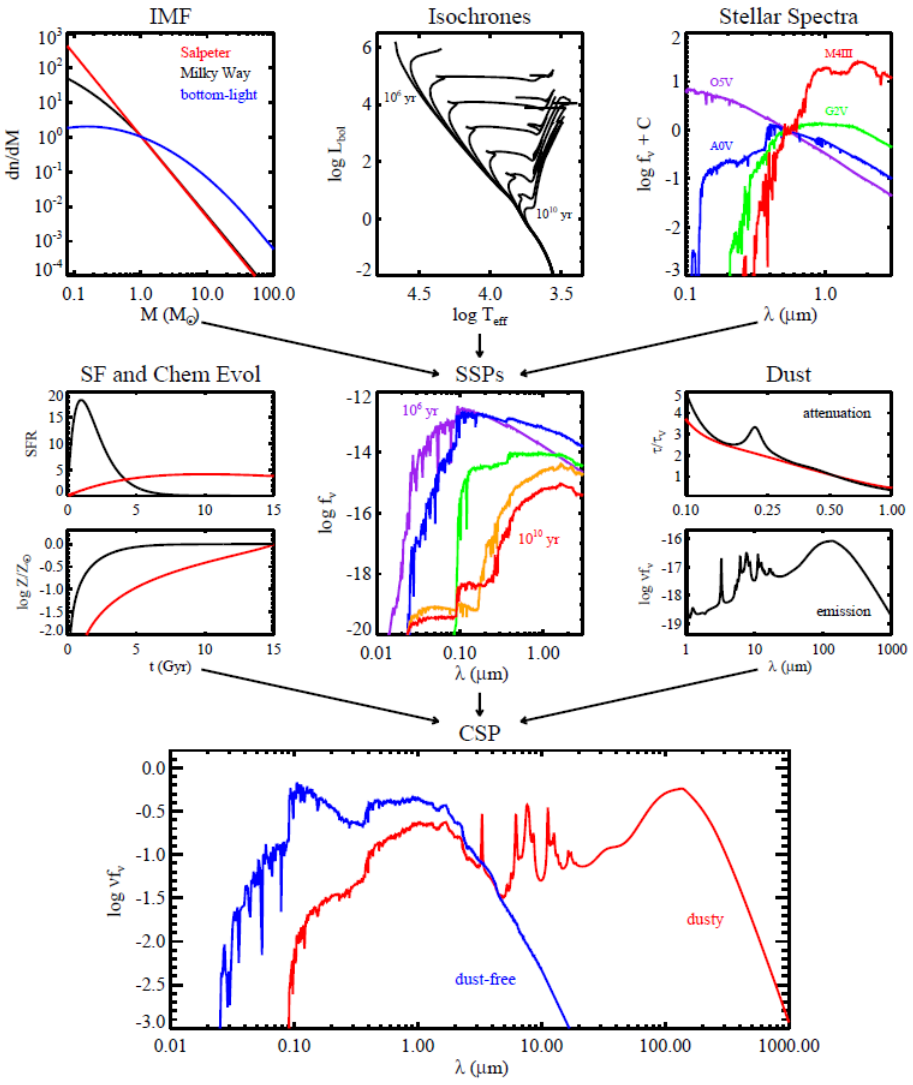


Figure 1.3: *This figure, by Conroy (2013), explains the composition of an SSP and a CSP. The IMF, isochrones and stellar spectra are needed to build the single stellar populations. These, together with the star formation (SF), chemical evolution, and the dust, are used to build up the CSPs.*

1.4.2 IMF

The IMF of stellar systems, also known as the initial distribution of stellar masses along the main sequence, is a topic that has been researched for more than 60 years (e.g. Salpeter, 1955), but is still a topic of controversy among astrophysicists (Bastian et al., 2010; Mo et al., 2010; Conroy, 2013). Many researchers investigate the universality of the IMF for different types of galaxies, e.g. Zakharova (1989), Bastian et al. (2010), Dib (2014), Ferreras et al. (2016) and Drinkwater (2017). They found that most observations agree with the "universal IMF", however, several authors also note that there are indications of a "non-standard IMF" in some local and extragalactic environments, which need to be studied further.

Whatever the case may be, it is important to include the study of the IMF whenever research about stellar populations is conducted, as this is one of the building blocks of SPSs.

Salpeter (1955) introduced the power law IMF of the mathematical form:

$$\Phi(\log(m)) = dN/d\log(m) \propto m^{-\Gamma} \tag{1.2}$$

Here, Φ is the IMF, m the mass, N the number of stars with masses in the range $m + dm$ and Γ the slope of the IMF.

Bastian et al. (2010) also discuss the IMF within the context of a mass spectrum, with the distribution function in linear mass units, with the equation:

$$\chi(m) = dN/dm \propto m^{-\alpha} \tag{1.3}$$

Here, χ is the IMF and α the IMF slope.

An important note is that α and Γ cannot be used interchangeably, as they are connected by Equation 1.4. Some studies use the logarithmic function (with Γ), while others use the linear mass equation (with α).

$$\alpha = \Gamma + 1 \tag{1.4}$$

Conroy (2013) summarises the properties of the IMF with regard to SPS: The overall normalisation of the mass-to-light ratio (M/L) is determined by the IMF. For a passively evolving stellar population, the IMF also determines the rate of luminosity evolution. Now, for single stellar populations, the IMF has a small effect on the shape of the SED, but only for IMFs that are close to the Salpeter IMF. In single stellar populations, the integrated light is mostly dominated by stars of the same mass, called the turnoff mass. For composite stellar populations, the IMF does affect the SED because of the range of turnoff masses contributing to the integrated light.

According to Larson (2006), the main features of the stellar IMF are the peak at a mass of a few tenths of solar masses and a power-law tail toward higher masses (this power-law tail is similar to the original Salpeter function).

Since Salpeter (1955), several different IMF functions and slopes have been proposed. Some of them can be seen in Figure 1.4. Some of these different IMF slopes will be discussed.

Vazdekis et al. (1996) describe the unimodal IMF and bimodal IMF, which will also be used in the analysis of the SSP models with regard to IMF slopes.

Unimodal IMF

The unimodal IMF has the shape as described by equation 1.3. This is the type of IMF that Salpeter (1955) introduced.

Bimodal IMF

The bimodal IMF is described by the following set of equations, and is based on observational results of Scalo (1986) and Kroupa et al. (1993):

$$\begin{aligned} \Phi(m) &= \beta 0.4^{-\alpha}, && m \leq 0.2M_{\odot}, \\ \Phi(m) &= \beta p(m), && 0.2M_{\odot} < m < 0.6M_{\odot}, \\ \Phi(m) &= \beta m^{-\alpha}, && m \geq 0.6M_{\odot} \end{aligned} \tag{1.5}$$

In this equation, β is a constant and $p(m)$ is a spline that is solved by using the following boundary conditions:

$$\begin{aligned} p(0.2) &= 0.4^{-\alpha}, \\ p'(0.2) &= 0, \\ p(0.6) &= 0.6^{-\alpha}, \\ p'(0.6) &= -\alpha 0.6^{-\alpha-1} \end{aligned} \tag{1.6}$$

Kroupa uses a multi-part power-law IMF for both of its versions, and so does Chabrier with his take on the IMF.

Kroupa universal

Kroupa (2001) also uses

$$\chi(m) \propto m^{-\alpha_i} \tag{1.7}$$

$$\begin{aligned} \alpha_0 &= +0.3 \pm 0.7, && 0.01 \leq m/M_{\odot} < 0.08, \\ \alpha_1 &= +1.3 \pm 0.5, && 0.08 \leq m/M_{\odot} < 0.50, \\ \alpha_2 &= +2.3 \pm 0.3, && 0.50 \leq m/M_{\odot} < 1.00, \\ \alpha_3 &= +2.3 \pm 0.7, && 1.00 \leq m/M_{\odot} \end{aligned} \tag{1.8}$$

Kroupa revised

Kroupa (2001), however, revised his version of the IMF, also taking into account the systematic bias towards unresolved binaries.

$$\begin{aligned} \alpha_0 &= +0.3 \pm 0.7, && 0.01 \leq m/M_{\odot} < 0.08, \\ \alpha_1 &= +1.8 \pm 0.5, && 0.08 \leq m/M_{\odot} < 0.50, \\ \alpha_2 &= +2.7 \pm 0.3, && 0.50 \leq m/M_{\odot} < 1.00, \\ \alpha_3 &= +2.3 \pm 0.7, && 1.00 \leq m/M_{\odot} \end{aligned} \tag{1.9}$$

Chabrier

Chabrier (2003) uses a multi-part power-law IMF, and did so for different stellar combinations. The two that we are naming here, are the IMF for single objects below 1 $M_\odot$ and the IMF for stellar systems (for instance binaries)

The Chabrier IMF for single objects below 1 $M_\odot$ is given mathematically as:

$$\xi(\log(m))_{m\leq 1} = 0.158^{+0.051}_{-0.046}\, e^{g(m)} (\log M_\odot)^{-1} \mathrm{pc}^{-3},$$
$$\text{with} \qquad g(m) = -\frac{[\log(m) - \log(0.079^{-0.016}_{+0.021})]^2}{2 \times (0.69^{-0.01}_{+0.05})^2} \tag{1.10}$$

The Chabrier IMF for stellar systems is given mathematically as:

$$\xi(\log(m))_{m\leq 1} = 0.086\, e^{h(m)} (\log M_\odot)^{-1} \mathrm{pc}^{-3},$$
$$\text{with} \qquad h(m) = -\frac{[\log(m) - \log(0.22)]^2}{2 \times 0.57^2} \tag{1.11}$$

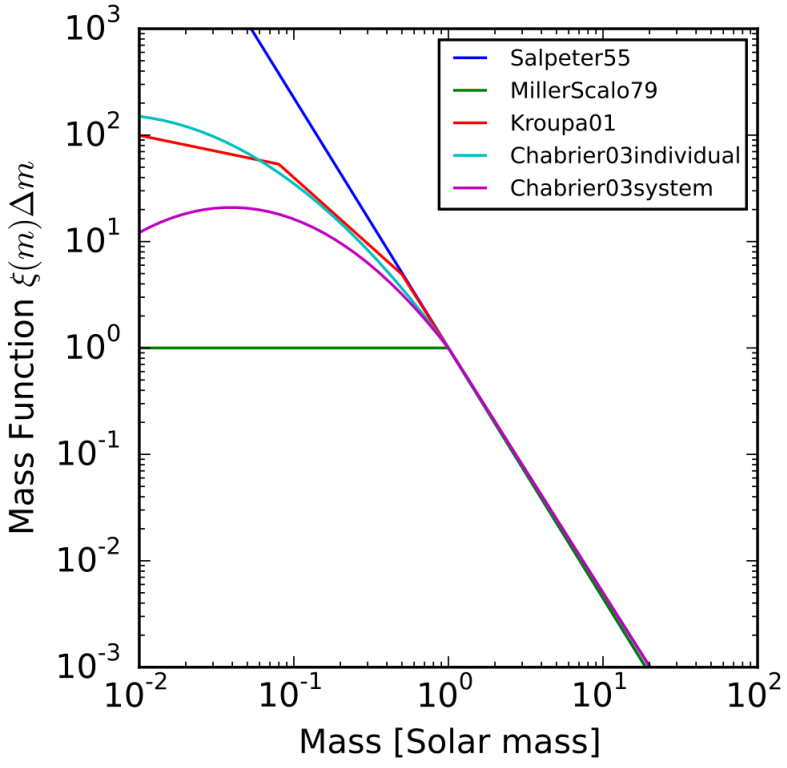


Figure 1.4: *Five of the different types of IMF slopes. The dark blue line indicates the Salpeter unimodal IMF (Salpeter, 1955), the green line indicates a bimodal IMF (Scalo, 1986), the red line indicates the Kroupa IMF (Kroupa, 2000), the light blue line shows the Chabrier IMF for individual stars, and the purple line shows the Chabrier IMF for stellar systems (Chabrier, 2003). This image is by Johannes Buchner from* https://commons.wikimedia.org/w/index.php?curid=44779435.

1.5 The important spectral features

Some of the important spectral absorption line features that are used to measure the age and metallicity of a galaxy, and that fall within this study's spectral wavelength range are given in Table 1.2 (see Salaris & Cassisi, 2005). It is important to note that each absorption feature has two sidebands, which provide a reference level, which is called the pseudo-continuum.

Some of the indices in Table 1.2 are more age sensitive and others are more metallicity sensitive, for example the three indices marked with * are most sensitive to metallicity.

Spectral index	Index band	Blue continuum	Red continuum	Units	Measures
$C_2$4668	4634.00-4720.25	4611.50-4630.25	4742.75-4756.50	Å	C, (O), (Si)
H_β	4847.88-4876.63	4827.88-4847.88	4876.63-4891.63	Å	
*Fe5015	4977.75-5054.00	4946.50-4977.75	5054.00-5065.25	Å	(Mg), Ti, Fe
Mg_1	5069.13-5134.13	4895.13-4957.63	5301.13-5366.13	mag	C, Mg, (O), (Fe)
Mg_2	5154.13-5196.63	4895.13-4957.63	5301.13-5366.13	mag	Mg, C, (Fe), (O)
Mg_b	5160.13-5192.63	5142.63-5161.38	5191.38-5206.38	Å	Mg, (C), (Cr)
Fe5270	5245.65-5285.65	5233.15-5248.15	5285.65-5318.15	Å	Fe, C, (Mg)
Fe5335	5312.13-5352.13	5304.63-5315.88	5353.38-5363.38	Å	Fe, (C), (Mg), Cr
Fe5406	5387.50-5415.00	5376.25-5387.50	5415.00-5425.00	Å	Fe
*Fe5709	5696.63-5720.38	5672.88-5696.63	5722.88-5736.63	Å	(C), Fe
*Fe5782	5776.63-5796.63	5765.38-5775.38	5797.88-5811.63	Å	Cr
Na_D	5876.88-5909.38	5860.63-5875.63	5797.88-5811.623	Å	Na, C, (Mg)
TiO_1	5936.63-5994.13	5816.63-5849.13	6038.63-6103.63	mag	C
TiO_2	6189.63-6272.13	6066.63-6141.63	6372.63-6415.13	mag	C, V, Sc

Table 1.2: *From Salaris & Cassisi (2005). As can be seen in the* ***Units*** *column, most of the spectral indices are expressed in units of Angstrom, but broader molecular indices are expressed in units of magnitude. The chemical elements listed in column 6 are those that contribute to that specific spectral index. Those that are in brackets increase the index line strength when their abundance decreases.*

1.5.1 Breaking the degeneracy between metallicity and age

The metallicity of a galaxy is defined by the formula:

$$[Fe/H] = log_{10}(\frac{N_{Fe}}{N_H})_{galaxy} - log_{10}(\frac{N_{Fe}}{N_H})_{sun} \tag{1.12}$$

In Equation 1.12, N_{Fe} and N_H are the numbers of iron and hydrogen atoms per unit volume respectively (Matteucci, 2012).

In the papers by O'Connell (1986), Worthey (1992) and O'Connell (1994), it was already evident that some metallicity effects in stellar population models mask certain age effects. This was especially the case with broadband colours studies. Worthey (1994) investigated the absorption features in spectra that are either sensitive to age or metallicity and with which this degeneracy can be broken. A metallicity sensitivity parameter was introduced in Worthey (1994). If the intensity of a certain index changes with ΔI, either a metallicity variation (ΔZ) or an age variation (Δage) can be deduced from this change. The sensitivity parameter is then calculated by taking the ratio of the percentage

change in age to the percentage change in metallicity. If an index therefore has a large sensitivity parameter, the index will be more metallicity sensitive, as illustrated in Table 1.3. Worthey (1994) found, for instance, that the absorption lines Fe4668, Fe5015, Fe5709 and Fe5782 are very good metallicity indicators (these can also be seen in Table 1.3 as the features with the highest sensitivity parameters). In Table 1.3, the sensitivity of different indices are listed with the metallicity sensitivity parameter.

Index	CN_1	CN_2	**Ca4227**	**G4300**	**Fe4383**	**Ca4455**	**Fe4531**	**Fe4668**	**Hβ**	**Fe5015**	Mg_1
$(\frac{\Delta age/age}{\Delta Z/Z})_I$	1.9	2.1	1.5	1.0	1.9	2.0	1.9	4.9	0.6	4.0	1.8
Index	Mg_2	**Mg b**	**Fe5270**	**Fe5335**	**Fe5406**	**Fe5709**	**Fe5782**	**Na D**	TiO_1	TiO_2	**D(4000)**
$(\frac{\Delta age/age}{\Delta Z/Z})_I$	1.8	1.7	2.3	2.8	2.5	6.5	5.1	2.1	1.5	2.5	1.3

Table 1.3: *From Worthey (1994). The metallicity sensitivity of different absorption indices.*

1.6 Illustration of stellar population models by varying age and metallicity

To illustrate the difference between spectra of different ages and metallicities, a model illustration was done by downloading model spectra from the MILES website[1]. For this illustration, the MILES spectral library was used, with the BaSTI (a Bag of Stellar Tracks and Isochrones, Cassisi et al., 2006) Isochrone. A unimodal Salpeter IMF with a slope of $\alpha = 1.3$ was chosen. The wavelength step was chosen as 0.1 Å per pixel, the sampling is linear, the resolution as 4.8 Å full-width half-maximum (FWHM). All of the spectra are also redshifted to $z = 0.02$, as this is the upper limit for the redshift of the galaxies that will be analysed later.

1.6.1 Varying age

Figure 1.5 was obtained by keeping the metallicity constant at $[Fe/H] = 0.15$ as well as the IMF slope at the Salpeter IMF ($\alpha = 1.3$).

In Figure 1.5, the difference between the young stellar populations and the older stellar populations is quite distinct when considering the extremes (age < 1 Gyr and age > 10 Gyr). The absorption lines to the blue end of the spectrum in the younger populations are much stronger than in the older populations. Therefore, these lines can be used to differentiate between the different ages in the younger stellar populations more effectively than in the older stellar populations where the spectrum looks the same for different ages.

Some of the age and metallicity indices, as described in Table 1.2, can be seen in these plots[2]. The blue-end of the wavelength-range is therefore very important to determine younger stellar populations, as very distinct absorption lines occur here.

[1] http://www.iac.es/proyecto/miles/pages/webtools/tune-ssp-models.php

[2] A separate set of plots were created only using the wavelength range that is used in our SSP and CSP fits, namely 4600 Å – 6200 Å. These plots can be seen at https://drive.google.com/file/d/1fYM86LJDOVYFatcHAvurBHF7m1zaABgC/view?usp=sharing.

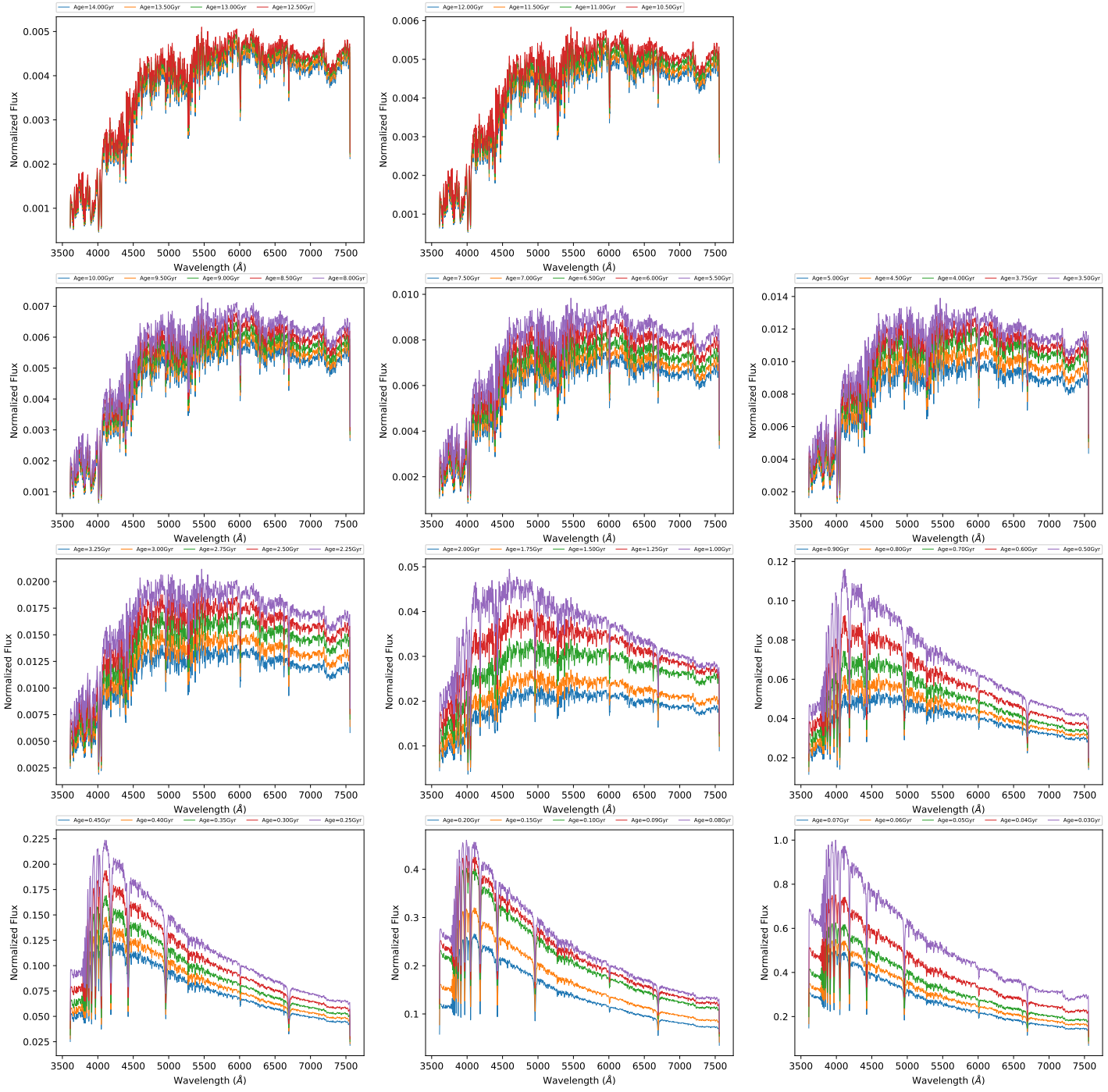


Figure 1.5: *The MILES-model for an SSP of varying age, with metallicity at* $[Fe/H] = 0.15$ *and no* α*-enhancements. The y-axis (flux) is normalised with respect to the maximum value of the SSP with age 0.03 Gyr. This was done to study the influence of the age and metallicity on the spectra. From a young SSP (0.03 Gyr) in the bottom right corner to an old SSP (14 Gyr) in the upper left corner, in increments of 0.01 Gyr for the first 0.1 Gyr, increments of 0.05 Gyr up to 1 Gyr, 0.25 Gyr up to 4 Gyr and 0.5 Gyr increments to 14 Gyr. The variable increments are necessary to see the notable differences at the younger ages.*

There are also still distinct changes in the spectra between $\sim$ 0.03 Gyr and $\sim$ 7.50 Gyr (when looking at the relative flux as well as the shape of the continuum from 0.45 Gyr – 1.00 Gyr and then from 2.00 Gyr – 4.00 Gyr) while the higher ages ($\sim$ 8.00 Gyr – 14.00 Gyr) show very similar spectra with very small differences. It is therefore safer to estimate composite stellar populations by using two different age components: a younger component ($<\sim$ 2 Gyr) and

an older component ($>\sim$ 2 Gyr). It is very difficult to distinguish for instance between a 12 Gyr SSP and a 14 Gyr SSP based on their spectra.

1.6.2 Varying metallicity

Figures 1.6 and 1.7 were obtained by keeping the age constant at 14.0 Gyr as well as the IMF slope at the Salpeter IMF ($\alpha = 1.3$).

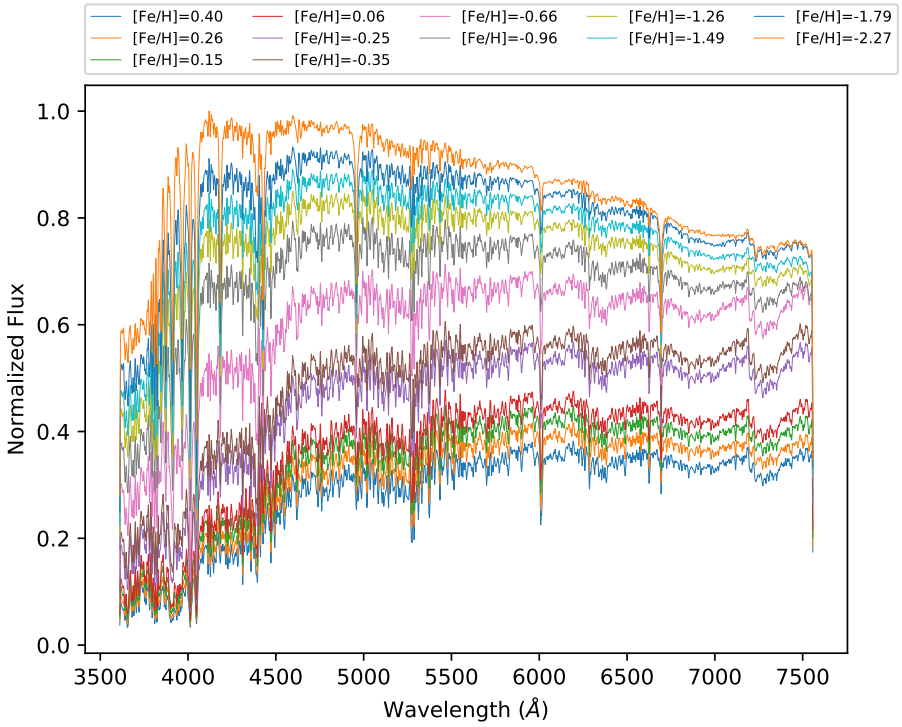


Figure 1.6: *The MILES-model for an SSP of varying metallicity, with age at 14 Gyr and no α-enhancements. The y-values are normalised with respect to the maximum value of the SSP with $[Fe/H] = -2.27$ with the metallicity increasing from -2.27 to 0.40.*

As can be seen in Figure 1.6, the relative fluxes of the spectra decrease as the metallicity increases. However, the relative flux is also higher in the red-end of the spectrum in the higher metallicities than at the blue-end. The opposite is true for the lower metallicities.

Figure 1.7 was plotted to examine the differences between the different metallicities in more detail. The shape of the continuum also changes as the metallicity changes, as can be seen in Figure 1.7. There are small changes between $[Fe/H] = -2.27$ and $[Fe/H] = -0.66$ and between $[Fe/H] = 0.06$ and $[Fe/H] = 0.40$, but the changes are quite notable between $[Fe/H] = -0.66$ and $[Fe/H] = 0.06$. Also, the absorption lines in the red-end of the spectrum are much more distinct in the metal-rich spectrum than in the metal-poor spectrum. The absorption lines in the blue-end of the metal-poor spectrum are again more distinct than the spectrum of the metal-rich SSP.

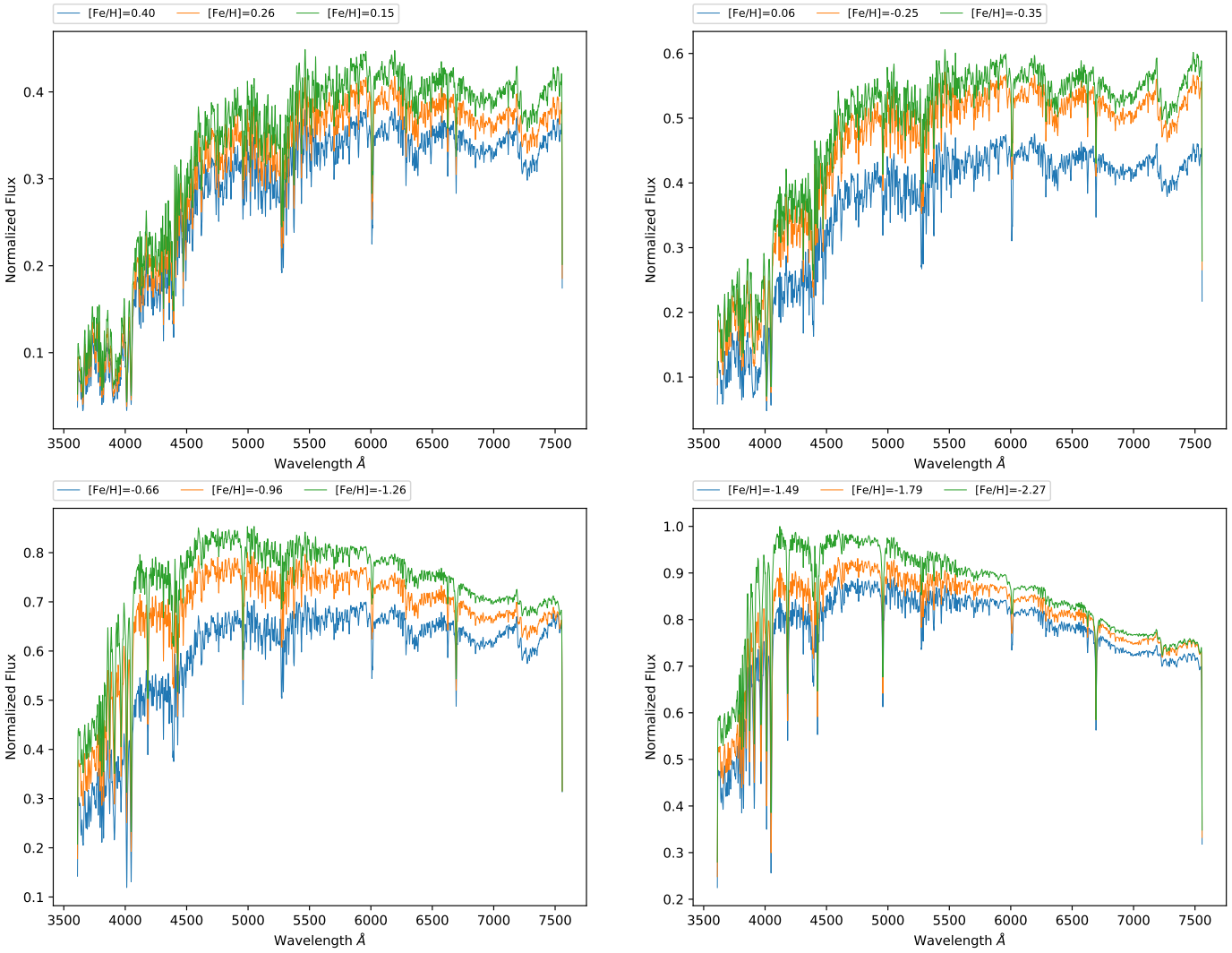


Figure 1.7: *The MILES-model for an SSP of varying metallicity, with age fixed at 14 Gyr. The y-axis is normalised with respect to the maximum value of the galaxy with* $[Fe/H] = -2.27$ *with the metallicity increasing from -2.27 to 0.40.*

1.7 Motivation for this study

According to Fukugita et al. (1998), the majority of matter in the universe, including more than half of the galaxies (Eke et al., 2006), resides in galaxy groups. According to Tully (1987), approximately 70% of all galaxies are found in groups. Still, much more is known about galaxy clusters, e.g. Hu et al. (1985); Burns (1990); McCarthy et al. (2004); Rafferty et al. (2006); Best et al. (2007); McCarthy et al. (2008); Cavagnolo et al. (2008b,a); Donahue et al. (2008); Bildfell et al. (2008); Loubser et al. (2009); Hudson et al. (2010); Hoekstra et al. (2011); Gaspari et al. (2012); Loubser & Sánchez-Blázquez (2012); Loubser & Soechting (2013); Loubser & Sánchez-Blázquez (2015); Loubser et al. (2016, 2018), than galaxy groups, e.g. Fukugita et al. (1998); Eke et al. (2005, 2006); McIntosh et al. (2008); O'Sullivan et al. (2011); Alonso et al. (2012); O'Sullivan et al. (2015b, 2017); Kolokythas et al. (2018); O'Sullivan et al. (2018). The aim of the CLoGS survey is to learn more about these galaxy groups, within 80 Mpc[3].

The aim of this research project is to study the stellar populations of 23 BGGs (Brightest Group Galaxies), a sub-sample of CLoGS, and then compare their stellar populations with X-ray, radio and sub-mm data as well as other host galaxy group properties to, amongst others, study the influences of the environment on the galaxies' SFHs. The aim is also to study various properties of BGGs that serve as signatures of their evolutionary paths and also interpret the influence of the environment. The central galaxies (or BGGs) are in the centres of the groups' massive dark matter haloes and are therefore ideal probes of galaxy evolution. According to McIntosh et al. (2008) and Alonso et al. (2012), the low velocity dispersions of galaxy groups are important for galaxy mergers and tidal interactions. These are key in galaxy evolution. The study of galaxy formation and evolution is important in galaxy groups, as these are environments where the influence of the local environment on the properties and evolution of the galaxies are significant (Forbes et al., 2006; Sun, 2012; Kolokythas et al., 2019). Some studies (Ponman et al., 1999; Lloyd-Davies et al., 2000) also looked at the excess in the entropy in the inner regions of poor clusters and groups, and outside the central dense regions where cooling might radiate away entropy. According to Toomre & Toomre (1972), galaxies in groups are ideal to study the merging process in the morphological transformation of galaxies. Van den Bosch et al. (2014) and Haines et al. (2018) suggest that galaxies are pre-processed in galaxy groups before forming part of galaxy clusters. The link between rich cluster environments and group environments is also important (Bekki et al., 1999; Moss & Whittle, 2000) as the early evolution of galaxy clusters is linked to the evolution of galaxies in groups.

Loubser et al. (2016) did a complimentary study on brightest **cluster** galaxies (B**C**Gs), generally more massive and in denser environments than BGGs, where they identified BCGs with young stellar populations, and therefore recent star formation from the integrated spectra.

The convention is that most giant elliptical galaxies are passively evolving (see Loubser et al., 2016). There is a non-negligible fraction of star-forming BCGs, and whether this is also true for BGGs, can be revealed by the SFHs of the galaxies.

Loubser et al. (2016) found that the star forming BCGs conform to two thresholds, the central entropy and the ratio of cooling-time (t_{cool}) to free-fall time (t_{ff}). According to Loubser et al. (2016) this ratio, when dropping below a threshold value of ~ 10, indicates that the diffuse X-ray emitting gas in the cluster's centre becomes highly susceptible to local thermal instabilities. We are interested in whether we can detect BGGs with recent star formation, and whether there is any correlation with the X-ray, radio and sub-mm properties of the host groups.

The aim in this research is to study stellar populations of BGGs. Identifying star forming BGGs can be done by classifying the galaxies as more accurately described by a single stellar population (SSP) or a composite stellar population (CSP).

[3]The official website for CLoGS can be found at http://www.sr.bham.ac.uk/~ejos/CLoGS.html.

This dissertation is structured as follows. In Chapter 2, a description of the CLoGS sample as well as our data sub-sample is given. The data reduction method that is used in this dissertation is also described. A description of the software package, ULySS, is also given as well as the galactic and group properties of our data sample. In Chapter 3, the construction of the stellar population is described, and the stellar population-fitting results are given. Four different models have been used in this analysis, which are also described here. The reliability of the solutions is also discussed and a mock spectra analysis is done. Chapter 4 is the analysis of the SSP models, due to the findings in the previous chapter, using the MILES online spectral libraries. In this chapter, α-enhancements and [Na/Fe]-enhancements are also discussed and their influence on SSP spectra is analysed. The influence of the IMF is also discussed. In Chapter 5, the amount of sodium overabundance is measured using the sodium doublet feature, NaD, which occured in the analysis. The properties of the galaxies and the galaxy groups are also compared to these overabundances to look for any possible correlations. Chapter 6 contains the summary and conclusions, as well as future work. Throughout this dissertation, a ΛCDM cosmology (lambda cold dark matter) is adopted, with the cosmological parameters $\Omega_m = 0.27$ (matter density parameter), $\Omega_\Lambda = 0.73$ (dark energy density parameter) and $H_0 = 70$ km s^{-1}Mpc^{-1} (Hubble constant).

CHAPTER 2

Sample of BGGs and data

Some parts of this analysis were published in Havenga, Loubser, O'Sullivan, Babul & Ratsimbazafy (2019) in Proceedings of SAIP 2018, the 63rd Annual Conference of the South African Institute of Physics (University of the Free State, Bloemfontein, 2018), p. 178–183, ISBN: 978–0–620–85406–1. See Appendix C.

2.1 Description of the CLoGS sample

The CLoGS sample is an optically-selected sample of 53 galaxy groups within 80 Mpc. The sample was selected from the Lyon Galaxy Group (LGG) catalogue. There were four selection criteria. The group had to have:

(i) four or more galaxy members (to exclude small galaxy associations that may not have group-scale halos);

(ii) more than one elliptical galaxy;

(iii) an optical luminosity of more than $3 \times 10^{10} L_{\odot}$ for the BGG (to exclude groups that mainly consist of spiral galaxies);

(iv) a declination of more than $-30°$ (to be properly observed by VLA [Very Large Array] and GMRT [Giant Metrewave Radio Telescope]).

The sample selection is described in detail in O'Sullivan et al. (2017). X-ray, radio and sub-mm data have been collected for the entire sample and are listed in Section 2.4.5. In addition, Loubser et al. (2018) have analysed galaxy kinematics from spatially-resolved long-slit spectroscopy from the 10m Hobby-Eberly Telescope (HET at the McDonald Observatory observed in September 2010 Van den Bosch et al., 2015) for a sub-sample of 23 BGGs. Here, we use the same sub-sample and study the stellar populations of the 23 BGGs.

2.2 Description of the sub-sample of 23 BGGs

Table 2.1 gives information about the galaxies in this sub-sample. The sample was divided into two categories: a high-richness category and a low-richness category. O'Sullivan et al. (2017) defined a richness parameter (R) as the number of galaxies within that group (within 1 Mpc from the centre and 3σ in velocity of the BGG) with the luminosity constraint: $\log L_B \geq 10.2$. Groups with $4 \leq R \leq 8$ were classified as high-richness groups and groups with $R =$ 2-3 were classified as low-richness groups.

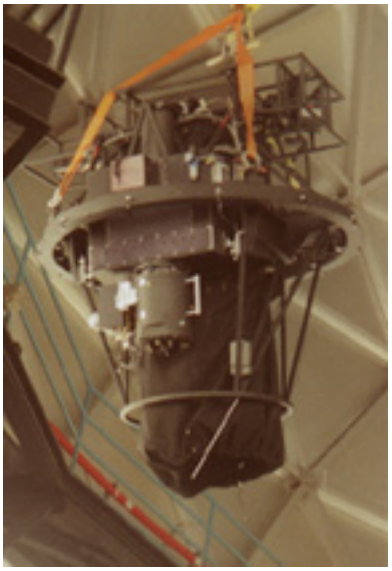
The information in Table 2.1, regarding the 23 galaxies, was extracted from NED (NASA Extragalactic Database)[1].

2.3 Observations from HET

The data that are used in this research, of which the observations were done from September 2010, were initially obtained by Van den Bosch et al. (2015). The galaxies were observed using the Marcario Low Resolution Spectrograph (an optical long-slit spectrograph as can be seen in Figure 2.1b), which has a slit length of $4'$ and the Charged Coupled Device (CCD) has 3000×1000 pixels. The wavelength range 4200-7400 Å was observed. There were two different slits used for the observations. The width of the slit, the resolution and the dispersion, can be seen in Table 2.2. The Marcario Low-Resolution Spectrograph is on the HET at the McDonald Observatory in Texas, shown in Figure 2.1a.



(a)



(b)

Figure 2.1: *The Hobby-Eberly Telescope (on the left) at the McDonald Observatory in Texas, US, from https://mcdonaldobservatory.org/news/gallery/het-dome-dusk. The Marcario Low Resolution Spectrograph can be seen on the right (from https://www.noao.edu/gateway/het/pfip_lrs_lift_tn.jpg).*

[1] https://ned.ipac.caltech.edu

Galaxy and group information										
LGG	**Galaxy**	**Redshift**	**RA**	**DEC**	**Velocity (km/s)**	ϵ	F_{sp}	M_K	M_{500} (10^3 $M_\odot$)	R_{500} **(kpc)**
High-richness										
18	NGC0410	0.018	01h10m58.9s	+33d09m07s	5294	0.26	0.52	–25.76 ± 0.02	$2.78^{+0.10}_{-0.09}$	458^{+5}_{-5}
27	NGC0584	0.006	01h31m20.7s	–06d52m05s	1802	0.38	0.64	–24.22 ± 0.03	–	–
42	NGC0777	0.017	02h00m14.9s	+31d25m46s	5015	0.16	0.56	–25.61 ± 0.02	$2.37^{+0.09}_{-0.09}$	434^{+5}_{-5}
61	NGC0924	0.015	02h26m46.8s	+20d29m51s	4461	0.40	0.71	–24.37 ± 0.03	–	–
72	NGC1060	0.017	02h43m15.0s	+32d25m30s	5190	0.16	0.80	–25.97 ± 0.02	$2.97^{+0.15}_{-0.14}$	468^{+8}_{-8}
103	NGC1453	0.013	03h46m27.2s	–03d58m08s	3886	0.22	0.76	–25.48 ± 0.02	$1.74^{+0.12}_{-0.12}$	392^{+9}_{-9}
117	NGC1587	0.012	04h30m39.9s	+00d39m42s	3694	0.22	0.62	–25.00 ± 0.03	$0.55^{+0.21}_{-0.14}$	267^{+31}_{-25}
158	NGC2563	0.015	08h20m35.7s	+21d04m04s	4480	0.22	0.72	–25.02 ± 0.02	$4.18^{+0.06}_{-0.06}$	525^{+2}_{-2}
278	NGC4261	0.007	12h19m23.2s	+05d49m31s	2212	0.14	0.71	–25.47 ± 0.03	$4.83^{+0.18}_{-0.12}$	552^{+7}_{-5}
363	NGC5353	0.008	13h53m26.7s	+40d16m59s	2325	0.52	0.91	–25.06 ± 0.02	$1.67^{+0.04}_{-0.04}$	387^{+3}_{-3}
393	NGC5846	0.006	15h06m29.3s	+01d36m20s	1712	0.05	0.48	–25.11 ± 0.02	$2.65^{+0.05}_{-0.05}$	452^{+3}_{-3}
402	NGC5982	0.010	15h38m39.8s	+59d21m21s	3017	0.30	0.86	–24.92 ± 0.02	$1.20^{+0.03}_{-0.03}$	346^{+3}_{-3}
421	NGC6658	0.014	18h33m55.6s	+22d53m18s	4270	0.76	0.60	–24.25 ± 0.03	$0.36^{+0.18}_{-0.12}$	233^{+34}_{-28}
473	NGC7619	0.013	23h20m14.5s	+08d12m22s	3762	0.20	0.62	–25.28 ± 0.02	$2.88^{+0.05}_{-0.05}$	464^{+3}_{-3}
Low-richness										
14	NGC0315	0.016	00h57m48.9s	+30d21m09s	4942	0.22	0.70	–26.02 ± 0.02	–	–
23	NGC0524	0.008	01h24m47.7s	+09d32m20s	2403	0.10	0.64	–25.09 ± 0.01	–	–
126	NGC1779	0.011	05h05m18.1s	–09d08m50s	3313	0.42	0.92	–24.55 ± 0.02	–	–
167	NGC2768	0.005	09h11m37.5s	+60d02m14s	1353	0.54	0.89	–24.54 ± 0.03	–	–
232	NGC3613	0.007	11h18m36.1s	+58d00m00s	2051	0.52	0.90	–24.35 ± 0.02	–	–
236	NGC3665	0.007	11h24m43.7s	+38d45m46s	2069	0.24	0.86	–24.84 ± 0.02	–	–
350	NGC5127	0.016	13h23m45.0s	+31d33m57s	4862	0.26	0.95	–24.81 ± 0.03	–	–
376	NGC5490	0.016	14h09m57.3s	+17d32m44s	4855	0.22	0.50	–25.20 ± 0.02	–	–
383	NGC5629	0.015	14h28m16.4s	+25d50m56s	4498	0.10	0.95	–24.79 ± 0.02	–	–

Table 2.1: *The information regarding the 23 galaxies was extracted from NED (NASA Extragalactic Database). This includes the galaxy name, the redshift, right-ascension (RA), declination (DEC) and recession velocity. Loubser et al. (2018) provided the ellipticity (ϵ) and the absolute K-band luminosity (M_K). The spiral fraction F_{sp} (which is the ratio of number of late-type galaxies plus unknown galaxies to the total number of galaxies) is provided by Kolokythas et al. (2018) in their table 8. The spiral fraction of the low-richness BGGs is provided by Kolokythas et al. (2019). A spiral fraction lower than 0.75 indicates a more evolved galaxy group with the gas concentrated to the centre. R_{500} is where the density is 500 times the critical density, and M_{500} is the total mass within that radius as derived from system temperature by O'Sullivan et al. (2017), who also provided the local galaxy group name (LGG) to which the galaxies belong.*

2.3.1 HET

The Hobby-Eberly Telescope is one of the largest optical telescopes in the world. It has an 11 m mirror, consisting of 91 hexagonal mirror segments. The construction was finished in 1997, and since then, the telescope was mainly used for spectroscopy. Similar to the Southern-African Large Telescope (SALT), the HET mirror also has a fixed position of 55° above the horizon. The tracker allows the telescope to move in six directions, allowing it to cover 70 % of the night sky [2].

2.3.2 Marcario Low-Resolution Spectrograph

The Marcario LRS is a long-slit imaging spectrograph. It has a plate scale of 0.235″ per pixel and a 4′×4′ field of view. We used the default 2×2 binning. The LRS has five different slits, but only the 1″ and the 2″ wide slits were used in these observations. The default blocking filter, GG385, was used, with the g2 grism, which gives the 1300 resolving power at 1″ and 650 resolving power at 2″ [3].

2.4 Optical spectral analysis

2.4.1 Reduction

Since the data provided by Van den Bosch et al. (2015) were not sky-subtracted, the first step was to do sky-subtraction. The data were spatially binned into two bins – an inner bin (from 0 – 1 kpc from the centre of the galaxy on both sides of the galaxy centre) and an outer bin (from 1 – 2 kpc). The inner bin was binned into one bin from the start, while the outer bin from both sides of the centre had to be added to form one 1D spectrum. This is done for each of the individual galaxies observed. This binning refers to binning along the spatial direction of the 2D spectra. This was done to ensure a high enough signal-to-noise ratio to have acceptable errors on the derived ages and metallicities.

2.4.2 Determining the amount of pixels in each FITS-file for each bin

First we needed to determine, for each galaxy, how many arcseconds (or pixels) correspond to one kiloparsec (the projected distance at the distance of the BGG). For this, we used the platescale of 0.235″ per pixel, as well as the number of arcseconds per kiloparsec at the distance of the BGG. This is given in the Table 2.2.

[2] This information was obtained from the McDonald Observatory website: https://mcdonaldobservatory.org/research/telescopes/HET

[3] This information was obtained from the HET instruments website: https://www.noao.edu/gateway/het/HET_inst.html.

Table 2.2: *Binning and slit information*

Binning and slit information						
	Binning information			Slit information		
Galaxy	**arcsec /kpc**	**# pixels /kpc**	**Min S/N**	**SW (″)**	**Instrumental resolution (Å)**	**Dispersion (kms^{-1})**
High-richness						
NGC0410	3.07	13	40	2.0	7.5	180
NGC0584	10.00	43	21	2.0	7.5	180
NGC0777	3.23	14	35	2.0	7.5	180
NGC0924	2.64	11	46	2.0	7.5	180
NGC1060	3.09	13	35	2.0	7.5	180
NGC1453	4.07	17	23	2.0	7.5	180
NGC1587	4.22	18	27	2.0	7.5	180
NGC2563	3.26	14	35	2.0	7.5	180
NGC4261	5.95	25	20	1.0	4.8	108
NGC5353	6.06	26	44	2.0	7.5	180
NGC5846	8.00	34	5	1.0	4.8	108
NGC5982	5.00	21	36	2.0	7.5	180
NGC6658	3.70	16	54	2.0	7.5	180
NGC7619	4.50	19	23	2.0	7.5	180
Low-richness						
NGC0315	3.31	14	43	2.0	7.5	180
NGC0524	7.23	31	20	1.0	4.8	108
NGC1779	4.60	20	30	2.0	7.5	180
NGC2768	10.31	44	27	1.0	4.8	108
NGC3613	6.90	29	37	1.0	4.8	108
NGC3665	6.54	28	33	1.0	4.8	108
NGC5127	3.01	13	20	1.0	4.8	108
NGC5490	3.02	13	32	2.0	7.5	180
NGC5629	3.27	14	33	2.0	7.5	180

The information on how the galaxies were spatially binned. The slit width information is from Van den Bosch et al. (2015, their table 1). ***SW*** *is the slit width. The instrumental resolution and instrumental dispersion are determined at a night sky line of wavelength 5577 Å. The exposure times for all the observations here, were 900 seconds for each galaxy.*

2.4.3 Creating the spectra for inner and outer apertures

We then apply *wavedit.py*[4] (written in Python) to the FITS image to resample and to change the data to a normal logarithmic wavelength dispersion. Then, the program *hdredit.pro* (written in interactive data language or IDL[5]) is applied to change the FITS-file extension setting within the header to *False*. This file is then changed to a format that the routine *snratio*, within the REDUCEME software package, can use (thus changed from a *.fits*-file to a *.u*-file), with the associated error file. REDUCEME (Cardiel et al., 2015) is an astronomical data reduction package[6].

[4]All codes are available at https://drive.google.com/file/d/1cd1r1P1B-h7Oq2zDdyKsHkEG5FMDpt7M/view?usp=sharing.
[5]The IDL language's official website is https://idlsgroup.com/.
[6]The software's official website can be found at https://REDUCEME.readthedocs.io/en/latest/.

The signal-to-noise ratio (S/N) is then measured by using the package *snratio*. We can then check whether the extracted spectrum, within the first two kpc from the centre, has high enough signal-to-noise ratios for our analysis.

After this, the program *get_wave_infos.pro* (in IDL) was used to take the raw FITS image and sky-subtracted image file and produce the clean data file with its associated error, both of which the wavelength dispersion was now in normal logarithmic steps. The code *hdredit.py* was used again to change the clean FITS image's extension setting in the header to *False*. These two files were then changed to REDUCEME format by using the *leefits-new* package, but this time not for checking the S/N ratio, but to do the actual binning. The package *adnsc* in REDUCEME was used to do the binning. The data were binned into three bins: one centre bin and one outer at each side. These files were written into FITS files using *writefits*. The code, *separate_spec.pro*, in IDL, was used to separate the three spectra of each galaxy with their error spectra. The package *sarith* in IRAF was used to combine the two outer spectra into one. This resulted in the inner spectrum with its error spectrum and the outer spectrum with its error spectrum.

2.4.4 ULySS

The basis of ULySS

For the analysis, the stellar population code ULySS (Université de Lyon Spectroscopic analysis Software) was used. ULySS is written in IDL and developed by M Koleva, P Prugniel, A.Bouchard and Y Wu. The publication Koleva et al. (2009) introduced this software with a description of the method used to build the software [7].

ULySS does full-spectral fitting by directly comparing the whole observed spectrum to a set of models or an empirical library on a pixel-by-pixel basis, thereby not only looking at certain spectral features. This has some advantages and disadvantages. One of the greatest advantages is that this method makes use of the entire signal optimally, but this is also the greatest disadvantage. All features are fitted simultaneously and not individually. Therefore, some information that could be extracted from an individual feature may be lost. Consequently one loses the ability, to some extent, to interpret the stellar population per index.

This software package uses this spectral fitting for the determination of stellar atmospheric parameters as well as the age and metallicity of galaxies.

The models used

The models that are used in the analysis, are made by a linear combination of non-linear components and convolved with the line-of-sight velocity distribution and multiplied by a polynomial.

The following four models were used in this analysis, with the first one being the prime focus in our analysis:

1. Grid of Vazdekis models computed with the MILES library (Sánchez-Blázquez et al., 2006) and Salpeter IMF (Salpeter, 1955). This model's version 9, which is described in Vazdekis et al. (2010), uses scaled-solar isochrones with the MILES (Medium resolution INT Library of Empirical Spectra) stellar spectral library.
2. Grid of Vazdekis models computed with the Miles library, but the IMF is Kroupa 2001, corrected for binaries.
3. Grid of Pegase HR SSPs computed with the Elodie 3.1 Library (Prugniel et al., 2007) and Salpeter IMF. This model is described in full in Le Borgne et al. (2004).
4. Grid of Pegase HR SSPs computed with the Elodie 3.2 Library and Salpeter IMF and resolved in [α/Fe].

[7] More information about the software can be found at http://ulyss.univ-lyon1.fr/.

The analysis of the 23 BGGs

The main routine in ULySS was used to compare the spectrum of a galaxy to the Vazdekis-MILES models (Vazdekis et al., 2010), which is based on the stellar library consisting of 985 stars.

A multiplicative polynomial is used to subtract the continuum and dust as well as to account for any possible flux calibration differences between the galaxy and stellar template spectra. This replaces the normalisation to the pseudo-continuum that other models use (Koleva et al., 2009). The next step was to test the degree of the multiplicative polynomial. For this, an SSP-fit was run for all 23 BGGs and for all MDs (multiplicative polynomial degrees) between 1 and 30. After this, the resulting metallicity and age were plotted against the different MDs. The optimal choice, where the curves of age and metallicity vs MD tend to flatten, was an MD of 16. In Appendix B.5, the different plots were made to decide which multiplicative polynomial degree to use.

Although the majority of stars inside the BCGs are believed to be old, we want to identify recent star formation episodes in the BGGs, by running both an SSP and a CSP fit for all 23 galaxies. This method is described in full in Loubser et al. (2016). Therefore, to accurately determine whether there is recent star formation in a galaxy, a CSP with two very different age components was chosen: a young component and an old component, even though no age or metallicity restrictions were placed on the two components, inside the boundaries of the Vazdekis model ([Fe/H] = [-2.3;0.2] and age = [63;17780] Myr).

The best way to do stellar population fitting is with a wide range of wavelengths, to break the age-metallicity degeneracy (Worthey, 1999), as some features are more age-sensitive and some more sensitive to the metallicity (refer to Section 1.5). Due to some atmospheric features at the red-end of the spectrum (as can be seen in Figure 2.2 and Figure 2.3), the spectrum was truncated at 6200 Å, yielding a wavelength range of 4600-6200 Å. The loss of this red-part of the wavelength has no significant influence on the results. Vazdekis et al. (2010), which describes the SP model that is used in this analysis, indicated that the range of wavelengths for this model is 3525-7500 Å, but that the redder part of this spectrum shows a larger deviation between the model and actual observations.

In Figure 2.2, the SSP fit of the spectrum of NGC0524 is shown. The black line indicates the observed spectrum, the blue line is the stellar population model of the best fit and the red lines are deviations that are masked during the fitting process. The light blue line shows the multiplicative polynomial that is used to normalise the continuum. The residuals are shown in the lower panel, where the green lines indicate the residuals as allowed by the error spectra (i.e. residuals larger than the green lines indicate deviations from the model, whereas certain fluctuations caused by the noise in the spectrum are allowed as can be seen in the black lines in the residuals). Therefore, the red lines in the spectrum corresponds to red lines in the residuals where the residuals are greater than allowed by the error spectra.

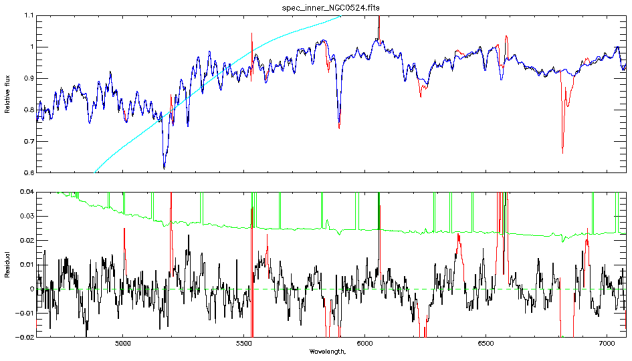


Figure 2.2: *The spectrum of NGC0524 for the full observed wavelength-range. The black line indicates the observed spectrum, the blue line is the stellar population model of the best fit and the red is deviations that are masked during the fitting process. The light blue line shows the multiplicative polynomial that is used to normalise the continuum. The residuals are shown in the lower panel, where the green lines indicate the residuals as allowed by the error spectra (i.e. residuals larger than the green lines indicate deviations from the model as opposed to fluctuations caused by the noise in the spectrum).*

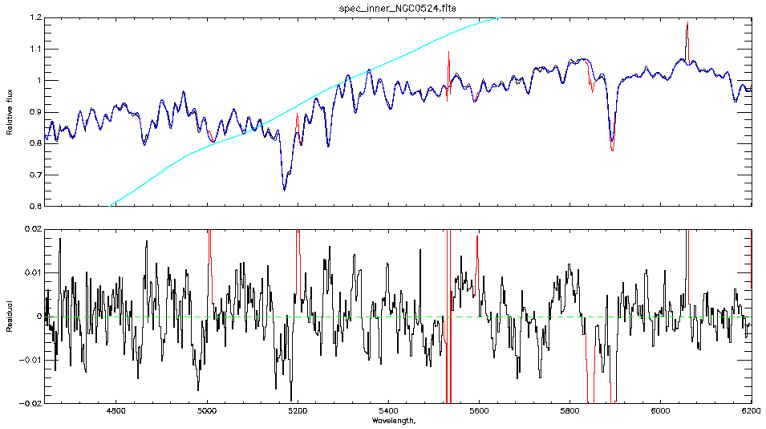


Figure 2.3: *The same spectrum of NGC0524 as shown in Figure 2.2, but now truncated at 4600-6200 Å. Therefore, the atmospheric features are excluded without losing important indices.*

2.4.5 Other galaxy and group properties

In this subsection, several BGG and host group properties are listed from several studies, including Condon et al. (1998), Condon et al. (2002), Hudson et al. (2010), O'Sullivan et al. (2015a), O'Sullivan et al. (2017), O'Sullivan et al. (2018), Kolokythas et al. (2018), Loubser et al. (2018) and Kolokythas et al. (2019), with the aim to later compare these properties to the stellar population results.

Galaxy kinematics			
Galaxy	$\sigma_0(kms^{-1})$	V_{max}/σ_0	$\eta \pm \Delta\eta$
High-richness			
NGC0410	311 ± 6	0.09 ± 0.03	–0.068 ± 0.009
NGC0584	220 ± 6	0.85 ± 0.05	–0.120 ± 0.010
NGC0777	321 ± 9	0.13 ± 0.02	–0.078 ± 0.010
NGC0924	201 ± 8	1.02 ± 0.04	–0.173 ± 0.021
MGC1060	326 ± 6	0.06 ± 0.04	–0.067 ± 0.010
NGC1453	312 ± 6	0.37 ± 0.02	–0.068 ± 0.011
NGC1587	239 ± 6	0.63 ± 0.03	–0.054 ± 0.011
NGC2563	287 ± 6	0.44 ± 0.02	–0.091 ± 0.017
NGC4261	314 ± 4	0.11 ± 0.05	–0.057 ± 0.007
NGC5353	300 ± 4	0.85 ± 0.02	–0.173 ± 0.011
NGC5846	195 ± 4	0.38 ± 0.05	–0.095 ± 0.023
NGC5982	260 ± 7	0.22 ± 0.05	–0.100 ± 0.019
NGC6658	210 ± 9	0.62 ± 0.10	–0.076 ± 0.030
NGC7619	331 ± 5	0.06 ± 0.06	–0.078 ± 0.011
Low-richness			
NGC0315	339 ± 8	0.22 ± 0.04	–0.028 ± 0.011
NGC0524	245 ± 5	0.51 ± 0.03	–0.078 ± 0.014
NGC1779	164 ± 10	1.16 ± 0.05	–0.093 ± 0.022
NGC2768	172 ± 3	0.61 ± 0.07	0.062 ± 0.012
NGC3613	214 ± 4	0.65 ± 0.05	–0.026 ± 0.010
NGC3665	224 ± 5	0.67 ± 0.02	–0.028 ± 0.007
NGC5127	194 ± 5	0.05 ± 0.05	–0.051 ± 0.015
NGC5490	353 ± 6	0.25 ± 0.02	–0.119 ± 0.018
NGC5629	257 ± 8	0.31 ± 0.04	–0.055 ± 0.026

Table 2.3: *The galaxy kinematics have been derived by Loubser et al. (2018): the central velocity dispersion σ_0, the rotation V_{max}/σ_0 (which was measured in the same inner bin as the stellar populations in our analysis) and the velocity dispersion slope $\eta \pm \Delta\eta$. This table is from Loubser et al., (2018, their table 4).*

Galaxy Group kinematics									
LGG	**BGG**	**CCT** (Gyr)	K_{10} ($keV\ cm^{-2}$)	$(t_c/t_{ff})_{min}$	**Core type** T profile	Hudson	**Radio Morph.**	**X-ray Morph.**	**Notes**
				High-richness					
18	NGC0410	$0.102^{+0.007}_{-0.007}$	34.5 ± 1.9	18.2 ± 1.3	CC	SCC	Point	Group	–
27	NGC0584	–	> 272.7	–	–	–	Point	–	–
42	NGC0777	$0.314^{+0.044}_{-0.039}$	34.8 ± 3.9	39.2 ± 5.2	NCC	SCC	Point	Group	–
61	NGC0924	–	> 406.1	–	–	–	Point	–	–
72	NGC1060	$0.132^{+0.018}_{-0.022}$	41.8 ± 2.7	10.4 ± 1.7	CC	SCC	SSJ	Group	Merger
103	NGC1453	$0.390^{+0.036}_{-0.036}$	40.4 ± 20.1	64.4 ± 6.7	NCC	SCC	Point	Group	–
117	NGC1587	$0.101^{+0.064}_{-0.038}$	$15.3^{+4.2}_{-6.7}$	$31.6^{+20.2}_{-12.2}$	NCC	SCC	Diffuse	Group	–
158	NGC2563	$1.954^{+0.389}_{-0.396}$	60.6 ± 3.4	41.0 ± 8.3	CC	WCC	Point	Group	–
278	NGC4261	$0.097^{+0.017}_{-0.010}$	39.1 ± 3.3	15.0 ± 2.1	CC	SCC	LSJ	Group	–
363	NGC5353	$0.288^{+0.037}_{-0.024}$	35.2 ± 4.7	32.4 ± 3.5	NCC	SCC	Point	Group	Compact Group
393	NGC5846	$0.138^{+0.002}_{-0.003}$	25.6 ± 0.6	14.7 ± 0.4	CC	SCC	SSJ	Group	Sloshing
402	NGC5982	$0.254^{+0.069}_{-0.428}$	22.6 ± 7.0	25.6 ± 11.5	NCC	SCC	Point	Group	–
421	NGC6658	–	> 591.3	–	–	–	–	Point	–
473	NGC7619	$0.135^{+0.011}_{-0.008}$	36.4 ± 4.9	24.5 ± 1.8	CC	SCC	Point	Group	Merger
				Low-richness					
14	NGC0315						LSJ		
23	NGC0524						Point		
126	NGC1779						Point		
167	NGC2768						Point		
232	NGC3613						Point		
236	NGC3665						SSJ		
350	NGC5127						LSJ		
376	NGC5490						LSJ		
383	NGC5629						–		

Table 2.4: *O'Sullivan et al. (2017) provide the central isochoric cooling time (CCT), the entropy at 10 kpc (K_{10}) and the minimum isochoric cooling time / free fall time ratio ($(t_c/t_{ff})_{min}$). The cool-core status, derived by O'Sullivan et al. (2017) using temperature profiles (T profile) is indicated as CC (cool-core) and non-cool-core (NCC) and those based on the scheme of Hudson et al. (2010) are indicated as strong cool-core (SCC), weak cool-core (WCC) or non-cool-core (NCC). This table also provides the current radio and X-ray morphology as well as notes on the galaxy group kinematics. The radio morphology for the low-richness BGGs was obtained from Kolokythas et al. (2019). Unfortunately, the X-ray properties were not available for the low-richness galaxy groups.*

BGG Gas Information							
BGG	**log M(HI)** ($M_\odot$)	**log** M ($M_\odot$)	**log M(HII)** ($10^8 M_\odot$)	$F_{\mathbf{1.4\ GHz}}$	**log** M_{dust} ($L_\odot$)	$L'_{CO}/10^8$ CO(1-0)	$L'_{CO}/10^8$ CO(2-1)
High-richness							
NGC0410	–	11.37	< 1.17	5.8	–	< 0.25	< 0.08
NGC0584	8.08	10.62	<0.11	0.6	6.06	< 0.02	< 0.005
NGC0777	–	–	< 2.08	7	3.60	0.45	0.13
NGC0924	9.96	10.76	0.52 ±0.10	0.9	7.30	< 0.24	0.11 ± 0.02
NGC1060	–	–	< 0.76	9	6.49	0.16	0.21
NGC1453	9.01	11.16	<0.78	28	7.15	< 0.17	< 0.09
NGC1587	9.40	–	2.3 ± 0.48	131	–	0.49	0.1
NGC2563	< 8.73	11.02	<0.93	0.7	–	< 0.20	< 0.06
NGC4261	< 8.69	11.05	< 0.37	19700	5.04	< 0.08	< 0.01
NGC5353	9.72	11.05	1.90 ± 0.25	40	3.91	0.41 ± 0.06	0.29 ± 0.02
NGC5846	8.48	10.83	0.14 ± 0.06	21	3.99	0.03 ± 0.01	0.008 ± 0.002
NGC5982	7.49	–	< 0.25	< 0.5	5.48	0.06	0.03
NGC6658	–	10.76	< 0.71	–	–	< 0.15	< 0.05
NGC7619	7.41	11.21	< 0.29	20	6.98	0.07	0.04
Low-richness							
NGC0315	7.86	–	0.74 ± 0.17	6630	5.87		
NGC0524	6.76	–	1.9 ± 0.23	3	6.06		
NGC1779	9.26	10.75	4.57 ± 0.60	5.4	6.53		0.99 ± 0.13
NGC2768	7.81	–	0.18 ± 0.01	15	4.36	0.04	0.03
NGC3613	< 7.32	–	< 0.46	< 0.3	–		
NGC3665	< 7.34	–	6.00 ± 0.32	133	6.68		
NGC5127	9.68	–	0.77 ± 0.05	1980	–		
NGC5490	–	11.15	< 0.64	1300	–		
NGC5629	–	10.95	< 0.91	4.6	–		

Table 2.5: *The following information regarding the BGGs is obtained from O'Sullivan et al. (2018), their table 1 and table B.1. The H I masses are from NED, while the stellar and H II masses are derived by O'Sullivan et al. (2018). The* 1.4 *GHz fluxes are drawn from NVSS (Condon et al., 1998, 2002). The dust masses are from O'Sullivan et al. (2018) and O'Sullivan et al. (2015a). The CO luminosities are from O'Sullivan et al. (2015a) and O'Sullivan et al. (2018) and are in units of [K km* s^{-1} pc^2*].*

BGG Radio Power			
BGG	α_{235MHz}^{610MHz}	$P_{235MHz}(10^{23}WHz^{-1})$	$P_{610MHz}(10^{23}WHz^{-1})$
		High-richness	
NGC0410	0.78	0.201	0.096
NGC0584	–	–	–
NGC0777	0.75	0.133	0.065
NGC0924	–	–	0.008
NGC1060	0.87	0.197	0.086
NGC1453	0.16	0.221	0.190
NGC1587	$>$ 1.13	2.042	0.692
NGC2563	–	–	0.007
NGC4261	0.52	59.193	36.126
NGC5353	0.38	0.096	0.067
NGC5846	0.52	0.047	–
NGC5982	0.90	0.010	0.004
NGC6658	–	–	–
NGC7619	0.58	0.195	0.112
		Low-richness	
NGC0315	$\leq$1.91	99.691	16.172
NGC0524	–	$\leq$0.015	0.003
NGC1779	0.60 $\pm$ 0.04	0.011	0.006
NGC2768	0.14	0.008	0.007
NGC3613	–	$\leq$ 0.002	$\leq$ 0.0002
NGC3665	0.43	0.275	0.182
NGC5127	1.32	35.464	10.159
NGC5490	0.36	6.804	4.864
NGC5629	–	$\leq$0.011	$\leq$0.002

Table 2.6: *The radio spectral index and radio power output of the BGGs, from Kolokythas et al. (2019) and Kolokythas et al. (2018).*

BGG Star formation			
BGG	**SFR** ($M_\odot(yr^{-1})$)	**τ (Gyr)**	**sSFR** (Gyr^{-1})
High-richness			
NGC0410	–	–	–
NGC0584	0.024 ± 0.004	–	5.8×10^{-4}
NGC0777	–	–	–
NGC0924	0.545 ± 0.381	0.10 ± 0.02	9.5×10^{-3}
NGC1060	–	–	–
NGC1453	0.217 ± 0.032	–	1.5×10^{-3}
NGC1587	–	–	–
NGC2563	–	–	–
NGC4261	0.034 ± 0.010	–	3.1×10^{-4}
NGC5353	0.095 ± 0.009	2.01 ± 0.26	8.4×10^{-4}
NGC5846	0.019 ± 0.003	0.72 ± 0.31	2.9×10^{-4}
NGC5982	–	–	–
NGC6658	–	–	–
NGC7619	0.255 ± 0.081	–	1.6×10^{-3}
Low-richness			
NGC0315	–	–	–
NGC0524	*0.027	–	–
NGC1779	0.926 ± 0.187	0.49 ± 0.06	1.6×10^{-2}
NGC2768	*0.026	–	–
NGC3613	*0.014	–	–
NGC3665	–	–	–
NGC5127	–	–	–
NGC5490	–	–	–
NGC5629	–	–	–

Table 2.7: *The star formation rate (SFR), the depletion timescales (τ) and the specific star formation rate (sSFR) are determined by O'Sullivan et al. (2018), their table 4. The SFR values indicated by * are obtained from Kolokythas et al. (2019) and these are the SFR as obtained from far ultra-violet (FUV).*

In Table 2.7, the specific star formation rate (sSFR) is defined by O'Sullivan et al. (2018) as SFR per unit stellar mass of the galaxy.

CHAPTER 3

SSP and CSP results

3.1 Construction of the stellar populations

For this analysis, we wanted to know if we can confidently classify the 23 BGGs into two classes, those better described by a single stellar population (SSP) and those with recent star formation (CSP). For both the SSP and CSP, we used $MD = 16$ (as determined in Section 2.4.4) and the wavelength range of 4600 to 6200 Å. We also used the error spectra of each galaxy to fit stellar population models and not a constant, fixed signal-to-noise ratio. The DG value (initial guess or fixed value for the velocity dispersion in km/s) was taken as 200 and the redshift of each galaxy was also used. For the SSPs, we did not place any constraints on the age or metallicity.

The following code was used in GDL for the SSP fits:

```
ulyss,‘spec_inner_NGC0410.fits’, smp, FILE_OUT=’ULySS_NGC0410_inner_CSP_md16’, /PLOT, /CLEAN,
SG =0.017659, DG=200, ERR_SP=‘spec_inner_err_NGC0410.fits’, mdegree=16
```

In the code, *smp* is the array of the model components for the SSP fit and *SG* is the guess for the galaxy's redshift.

For the CSPs, we used two components: one old component with an initial age guess of 15.00 Gyr and one young component with an initial age guess of 0.20 Gyr.

Therefore, these extra three lines of code were entered to change *smp* in the previous code to a composite stellar population, thus *cmp*, which is the array of the model components for the CSP fit:

```
cmp1 = uly_ssp(model=’/Users/ULySS/ulyss/models/Vaz_Miles.fits’,AG=[200.])
cmp2 = uly_ssp(model=’/Users/ULySS/ulyss/models/Vaz_Miles.fits’,AG=[15000.])
cmp = [cmp1, cmp2]
```

3.2 Classification results

All the SSP and CSP plots from this analysis can be found at https://drive.google.com/file/d/1LP_WBPRHCn4BeTytbrl5-vJwvYEIzr0n/view?usp=sharing. Figure 3.1 is an example of the plots that were obtained. Table 3.1 gives the results of the CSP fits, and Table 3.2 the SSP results of the 23 galaxies using the Vazdekis model.

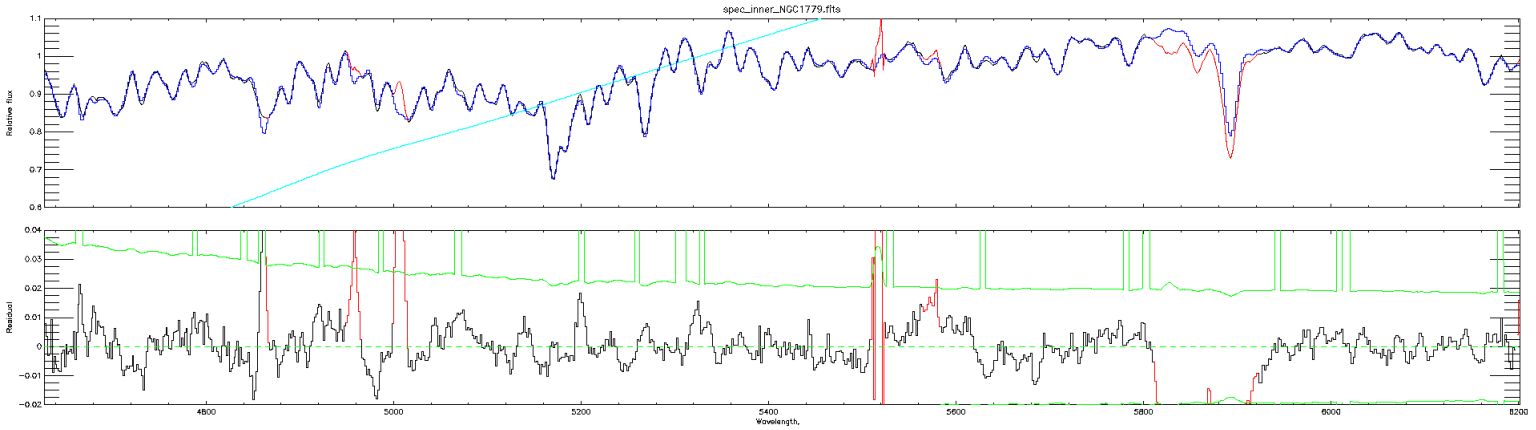
According to Koleva et al. (2008), the χ^2 values (as seen in different tables from Table 3.2) were determined using the following formula:

$$\chi^2 = \frac{1}{\texttt{nfreedom}} \frac{(\texttt{observation - model})^2}{\texttt{errors}^2} \tag{3.1}$$

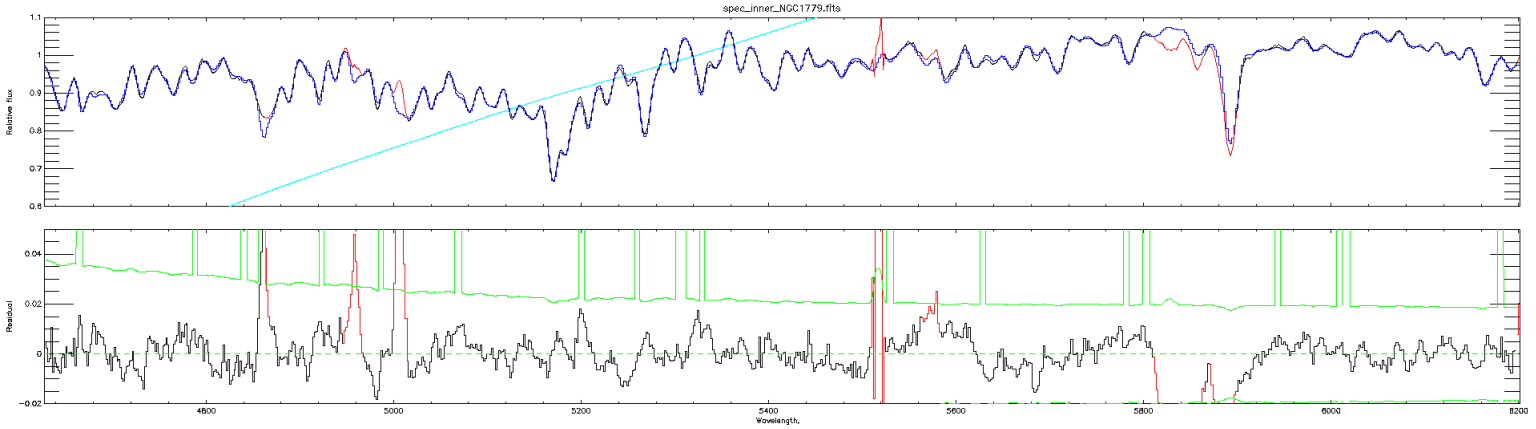
In Equation 3.1, `nfreedom` is the number of pixels in the original data. The errors are determined as follows: $\texttt{errors}^2 = \texttt{errors}^2_{\texttt{models}} + \texttt{errors}^2_{\texttt{obs}}$, where $\texttt{errors}_{\texttt{models}}$ is the errors in the models and $\texttt{errors}_{\texttt{obs}}$ is the errors in the observations.

The errors in the model is defined by Vazdekis et al. (2010), in the model description, as deviation due to asymmetries in the distribution of stars and stellar masses which may effect the age and metallicity guess.

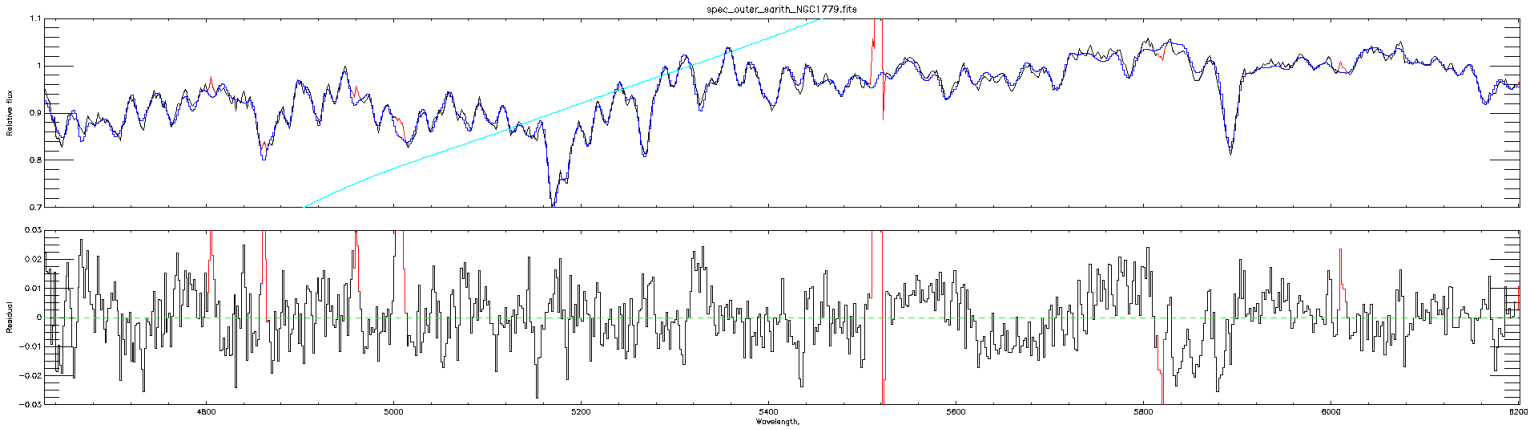
The χ^2 values are one of the first values to look at to determine the effectiveness of the model to fit the galaxy spectrum. However, the χ^2 value should not be used on its own, and should be interpreted with a holistic view of the results, including the correlation between SSP and CSP fit results.



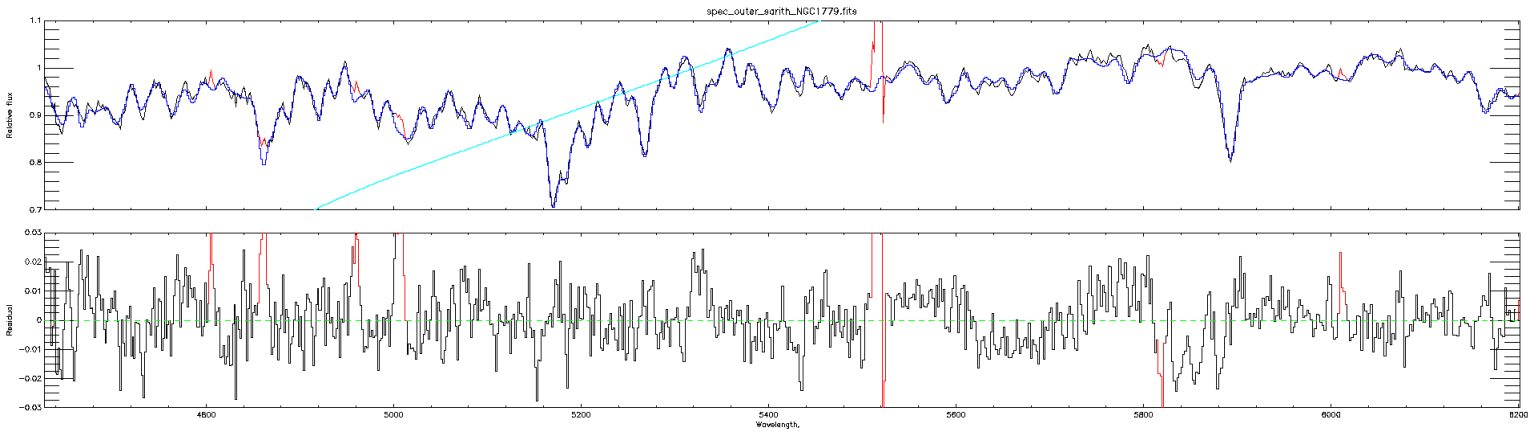
(a)



(b)



(c)



(d)

Figure 3.1: *The SSP (a and c) and CSP (b and d) fit for the inner aperture (a and b) and outer aperture (c and d) for NGC1779. The different lines and colours have the same meaning as described in Figure 2.2.*

Composite Stellar Population fitting					
High-richness					
Galaxy	**Aperture**	**Component**	**Age (Myr)**	**[Fe/H] dex**	**Luminosity fraction**
NGC0410	Inner	1	12530 ± 57700	—2.32 ± 0.00	4.58 ± 0.56
	Inner	2	17360 ± 2700	0.12 ± 0.07	95.42 ± 0.55
	Outer	1	17110 ± 128480	—2.26 ± 5.62	9.54 ± 1.56
	Outer	2	16140 ± 5900	0.20 ± 0.15	90.46 ± 1.52
NGC0584	Inner	1	130 ± 150	–0.50 ± 0.43	11.65 ± 0.29
	Inner	2	15800 ± 1950	0.15 ± 0.03	88.35 ± 0.28
	Outer	1	80 ± 1040	0.11 ± 11.17	5.86 ± 1.87
	Outer	2	14120 ± 15560	–0.18 ± 0.31	94.14 ± 1.79
NGC0777	Inner	1			0.00 ± 0.00
	Inner	2	17500 ± 2100	0.06 ± 0.07	100.00 ± 0.07
	Outer	1			0.00 ± 0.00
	Outer	2	17160 ± 7900	0.20 ± 0.13	100.00 ± 1.18
NGC0924	Inner	1	150 ± 110	–0.76 ± 0.81	6.97 ± 0.37
	Inner	2	16550 ± 2150	0.21 ± 0.03	93.03 ± 0.35
	Outer	1			0.00 ± 0.00
	Outer	2	17780 ± 0	–0.48 ± 0.17	100.00 ± 0.22
NGC1060	Inner	1	3350 ± 3300	–2.32 ± 0.00	0.75 ± 0.58
	Inner	2	17780 ± 0	0.22 ± 0.00	99.25 ± 0.56
	Outer	1	1340 ± 0	–2.32 ± 0.00	0.17 ± 1.78
	Outer	2	17780 ± 0	0.07 ± 0.14	99.83 ± 1.72
NGC1453	Inner	1			0.00 ± 0.00
	Inner	2	17140 ± 2100	0.19 ± 0.04	100.00 ± 0.08
	Outer	1			0.00 ± 0.00
	Outer	2	17660 ± 9490	0.04 ± 0.20	100.00 ± 0.35
NGC1587	Inner	1	100 ± 3110	–0.00 ± 23.86	0.12 ± 0.26
	Inner	2	17780 ± 0	0.13 ± 0.03	99.88 ± 0.25
	Outer	1			0.00 ± 0.00
	Outer	2	17780 ± 0	–0.11 ± 0.15	100.00 ± 0.27
NGC2563	Inner	1	1750 ± 1390	–0.60 ± 0.65	7.96 ± 0.62
	Inner	2	16680 ± 2140	0.20 ± 0.06	92.04 ± 0.61
	Outer	1	430 ± 5890	–1.86 ± 11.02	4.25 ± 1.41
	Outer	2	17780 ± 0	0.19 ± 0.16	95.75 ± 1.37
NGC4261	Inner	1			0.00 ± 0.00
	Inner	2	17780 ± 0	–0.15 ± 0.06	100.00 ± 0.08
	Outer	1	260 ± 6830	0.07 ± 19.88	3.71 ± 1.52
	Outer	2	17780 ± 0	0.15 ± 0.22	96.29 ± 1.45
NGC5353	Inner	1	330 ± 0	0.21 ± 0.00	0.04 ± 0.26
	Inner	2	17780 ± 0	–0.05 ± 0.04	99.96 ± 0.25
	Outer	1	16280 ± 10610	0.22 ± 0.00	31.36 ± 5.21
	Outer	2	17780 ± 0	–0.16 ± 0.37	68.64 ± 5.25
NGC5846	Inner	1			0.00 ± 0.00

	Inner	2	17770 ± 4790	–0.19 ± 0.30	100.00 ± 0.13
	Outer	1	17780 ± 0	0.22 ± 0.00	100.00 ± 11.32
	Outer	2			0.00 ± 0.00
NGC5982	Inner	1	1340 ± 510	–0.66 ± 0.48	17.32 ± 0.69
	Inner	2	17780 ± 0	0.20 ± 0.06	82.68 ± 0.66
	Outer	1			0.00 ± 0.00
	Outer	2	17780 ± 0	–0.39 ± 0.31	100.00 ± 0.32
NGC6658	Inner	1	60 ± 0	–0.48 ± 0.81	10.29 ± 0.45
	Inner	2	17340 ± 3390	0.17 ± 0.06	89.71 ± 0.42
	Outer	1			0.00 ± 0.00
	Outer	2	16510 ± 11460	–0.57 ± 0.30	100.00 ± 0.32
NGC7619	Inner	1	16290 ± 2740	0.22 ± 0.00	48.58 ± 1.92
	Inner	2	17780 ± 0	–0.19 ± 0.17	51.42 ± 1.94
	Outer	1	200 ± 205790	0.07 ± 622.59	0.08 ± 1.56
	Outer	2	17780 ± 0	–0.01 ± 0.17	99.92 ± 1.48
Low-richness					
Galaxy	**Aperture**	**Component**	**Age (Myr)**	**[Fe/H] dex**	**Luminosity fraction**
NGC0315	Inner	1	17660 ± 390290	–2.32 ± 16.88	1.47 ± 0.62
	Inner	2	17030 ± 2050	0.22 ± 0.00	98.53 ± 0.61
	Outer	1	17780 ± 0	–0.23 ± 0.53	33.69 ± 5.23
	Outer	2	16780 ± 5820	0.22 ± 0.00	66.31 ± 5.19
NGC0524	Inner	1	340 ± 0	–2.28 ± 0.00	1.07 ± 0.80
	Inner	2	17780 ± 0	–0.04 ± 0.08	98.93 ± 0.76
	Outer	1	11030 ± 80280	–2.11 ± 4.99	12.90 ± 3.97
	Outer	2	17780 ± 0	–0.02 ± 0.32	87.10 ± 3.84
NGC1779	Inner	1	240 ± 340	0.19 ± 1.12	10.39 ± 0.39
	Inner	2	11020 ± 1860	0.22 ± 0.00	89.61 ± 0.37
	Outer	1	110 ± 380	0.22 ± 3.32	10.05 ± 1.28
	Outer	2	13970 ± 8810	–0.08 ± 0.17	89.95 ± 1.19
NGC2768	Inner	1	5180 ± 4140	–0.68 ± 0.56	32.96 ± 1.58
	Inner	2	17500 ± 5200	0.18 ± 0.18	67.04 ± 1.53
	Outer	1	200 ± 0	–0.47 ± 0.00	0.07 ± 3.47
	Outer	2	15190 ± 15000	–0.51 ± 0.40	99.93 ± 3.25
NGC3613	Inner	1	17780 ± 0	–2.32 ± 0.00	7.08 ± 0.79
	Inner	2	17780 ± 0	–0.04 ± 0.05	92.92 ± 0.76
	Outer	1	10330 ± 50480	0.22 ± 0.00	16.01 ± 6.69
	Outer	2	7800 ± 13150	–0.50 ± 0.64	83.99 ± 6.83
NGC3665	Inner	1	13780 ± 50620	–2.25 ± 2.51	9.94 ± 1.20
	Inner	2	17780 ± 0	–0.08 ± 0.10	90.06 ± 1.17
	Outer	1			0.00 ± 0.00
	Outer	2	7080 ± 14780	–0.44 ± 0.51	100.00 ± 0.533
NGC5127	Inner	1	17330 ± 88190	–2.32 ± 0.00	8.17 ± 1.04
	Inner	2	16660 ± 4140	0.18 ± 0.09	91.83 ± 1.01
	Outer	1	370 ± 43680	–0.73 ± 88.28	1.11 ± 2.46

	Outer	2	16420 ± 14510	–0.09 ± 0.30	98.89 ± 2.36
NGC5490	Inner	1	5010 ± 199750	–2.29 ± 31.04	0.50 ± 0.50
	Inner	2	16530 ± 2100	0.22 ± 0.00	99.50 ± 0.49
	Outer	1	17780 ± 0	–0.32 ± 0.52	37.93 ± 5.68
	Outer	2	16450 ± 7490	0.22 ± 0.00	62.07 ± 5.63
NGC5629	Inner	1	170 ± 750	–0.06 ± 3.58	3.56 ± 0.38
	Inner	2	17780 ± 0	0.05 ± 0.04	96.44 ± 0.35
	Outer	1	14390 ± 306030	–1.35 ± 16.61	1.86 ± 5.57
	Outer	2	17610 ± 13370	–0.14 ± 0.34	98.14 ± 5.42

Table 3.1: *The results of the CSP fits of the 23 galaxy spectra.*

In Table 3.1, the results of the CSP fits are given. Vazdekis et al. (2010) determined the luminosity fraction by using the RMODEL as described by Cardiel et al. (2003). Something that immediately draws the attention is the large error margins in some of the results, as well as the null errors (which indicate the best fit hitting the upper or lower limit of the model). The reason for the uncertainty is discussed in Section 3.5. This can also be seen in Table 3.2, where the results of the SSP fits are given as well as the χ^2 values of the SSP and CSP fits. In Table 3.1 some of the galaxies' two age components are both old or both young, as opposed to the first being the young component and the second the old component. The reason for this may be that the the spectrum of that bin has a definite young component (calculating both components as young components) or a definite old component (calculating both components as old components). It is, however, important to verify this with the SSP fits.

Comparison of SSP and CSP					
High-richness					
Galaxy	**Aperture**	**CSP χ^2**	**SSP χ^2**	**SSP age (Myr)**	**SSP [Fe/H] dex**
NGC0410	Inner	0.095	0.104	16470 ± 2380	0.10 ± 0.05
	Outer	0.036	0.037	17400 ± 5930	0.10 ± 0.10
NGC0584	Inner	0.115	0.093	14010 ± 1540	–0.06 ± 0.03
	Outer	0.008	0.008	11480 ± 7260	–0.21 ± 0.22
NGC0777	Inner	0.175	0.121	17780 ± 0	–0.06 ± 0.04
	Outer	0.035	0.035	17100 ± 7350	0.21 ± 0.12
NGC0924	Inner	0.138	0.152	15600 ± 2130	0.17 ± 0.03
	Outer	0.046	0.042	11760 ± 4410	–0.18 ± 0.14
NGC1060	Inner	0.137	0.136	17610 ± 1460	0.22 ± 0.00
	Outer	0.031	0.030	17780 ± 0	0.07 ± 0.09
NGC1453	Inner	0.138	0.138	16970 ± 2090	0.20 ± 0.04
	Outer	0.022	0.022	17580 ± 11400	0.06 ± 0.18
NGC1587	Inner	0.161	0.113	17780 ± 0	0.00 ± 0.03
	Outer	0.025	0.025	17780 ± 0	–0.08 ± 0.12
NGC2563	Inner	0.124	0.105	17780 ± 0	0.02 ± 0.04
	Outer	0.027	0.027	17780 ± 0	0.15 ± 0.08
NGC4261	Inner	0.063	0.060	17780 ± 0	–0.10 ± 0.05
	Outer	0.024	0.024	17780 ± 0	0.11 ± 0.12
NGC5353	Inner	0.124	0.268	17780 ± 0	0.12 ± 0.03
	Outer	0.022	0.021	17780 ± 0	–0.09 ± 0.09

NGC5846	Inner	0.028	0.032	17780 ± 0	–0.23 ± 0.07
	Outer	0.004	0.004	17780 ± 0	0.22 ± 0.00
NGC5982	Inner	0.079	0.056	17780 ± 0	–0.12 ± 0.05
	Outer	0.020	0.020	17780 ± 0	–0.34 ± 0.24
NGC6658	Inner	0.074	0.082	17780 ± 0	0.08 ± 0.04
	Outer	0.030	0.030	16380 ± 12450	0.57 ± 0.28
NGC7619	Inner	0.147	0.222	17780 ± 0	0.19 ± 0.02
	Outer	0.019	0.019	17780 ± 0	0.00 ± 0.14
Low-richness					
Galaxy	**Aperture**	**CSP χ^2**	**SSP χ^2**	**SSP age (Myr)**	**SSP [Fe/H] dex**
NGC0315	Inner	0.100	0.100	16610 ± 1740	0.22 ± 0.00
	Outer	0.025	0.026	17780 ± 0	0.10 ± 0.07
NGC0524	Inner	0.038	0.040	17780 ± 0	–0.03 ± 0.05
	Outer	0.010	0.011	17780 ± 0	–0.14 ± 0.18
NGC1779	Inner	0.065	0.052	5880 ± 1150	0.20 ± 0.07
	Outer	0.015	0.015	10900 ± 5520	–0.11 ± 0.16
NGC2768	Inner	0.031	0.023	17780 ± 0	–0.19 ± 0.07
	Outer	0.013	0.013	15340 ± 13390	–0.52 ± 0.38
NGC3613	Inner	0.045	0.048	17780 ± 0	–0.10 ± 0.03
	Outer	0.019	0.020	10920 ± 11940	–0.41 ± 0.28
NGC3665	Inner	0.036	0.032	17780 ± 0	–0.19 ± 0.06
	Outer	0.015	0.015	7830 ± 9820	–0.44 ± 0.49
NGC5127	Inner	0.053	0.057	16430 ± 3980	0.12 ± 0.06
	Outer	0.022	0.022	14380 ± 11130	–0.06 ± 0.23
NGC5490	Inner	0.170	0.132	17780 ± 0	0.07 ± 0.04
	Outer	0.028	0.029	17780 ± 0	0.06 ± 0.08
NGC5629	Inner	0.083	0.076	17780 ± 0	–0.06 ± 0.04
	Outer	0.030	0.030	17400 ± 12390	–0.16 ± 0.22

Table 3.2: *The SSP fit results and a comparison of the SSP and CSP fit χ^2 values.*

Although there are large uncertainties in the results, as discussed in Section 3.5, we summarise the results by classifying the galaxies as best described by an SSP or CSP using the abovementioned results as well as the plots of the stellar population fits.

Best described by SSP or CSP		
High-richness		
Galaxy	**Aperture**	**Best described by**
NGC0410	Inner	SSP
	Outer	SSP
NGC0584	Inner	CSP
	Outer	CSP
NGC0777	Inner	SSP
	Outer	SSP
NGC0924	Inner	CSP
	Outer	SSP
NGC1060	Inner	SSP
	Outer	SSP
NGC1453	Inner	SSP
	Outer	SSP
NGC1587	Inner	SSP
	Outer	SSP
NGC2563	Inner	CSP
	Outer	CSP
NGC4261	Inner	SSP
	Outer	CSP
NGC5353	Inner	SSP
	Outer	SSP
NGC5846	Inner	SSP
	Outer	SSP
NGC5982	Inner	CSP
	Outer	SSP
NGC6658	Inner	CSP
	Outer	SSP
NGC7619	Inner	SSP
	Outer	SSP
Low-richness		
Galaxy	**Aperture**	**Best described by**
NGC0315	Inner	SSP
	Outer	SSP
NGC0524	Inner	SSP
	Outer	SSP
NGC1779	Inner	CSP
	Outer	CSP
NGC2768	Inner	CSP
	Outer	SSP
NGC3613	Inner	SSP
	Outer	SSP
NGC3665	Inner	SSP

	Outer	SSP
NGC5127	Inner	SSP
	Outer	SSP
NGC5490	Inner	SSP
	Outer	SSP
NGC5629	Inner	CSP
	Outer	SSP

Table 3.3: *A table depicting the best fit of each specific galaxy spectrum.*

In most cases where the galaxy can be better described by a CSP, the SSP fit will give an age somewhere between the older stellar component and the younger stellar component of the CSP. This can be seen in the results of NGC0584. The inner bin of this galaxy is best described by a CSP with an age of 130 ± 150 Myr for the younger stellar component and an age of 15800 ± 1950 Myr for the older stellar component. The SSP fit for this galaxy gives an age of 14010 ± 1540 Myr. In such a case, the inner bin of galaxy NGC0584 is thought to be better described by a CSP. This is because any young population of stars will bias the SSP-equivalent age to younger ages (see Serra & Trager, 2007).

In Table 3.3, it is evident that some of the galaxies' inner bins are better described by a CSP, while the outer bins are better described using an SSP. This is to be expected as the older stellar components mostly lie on the outskirts of the galaxy and the star formation mostly takes place in the central part of the galaxy (as is the case in NGC0924, NGC5982, NGC6658, NGC0524 and NGC5629). However, as is evident in NGC4261, NGC3613 and NGC5127, the inverse may also be possible (as described by O'Sullivan et al., 2015b and Davis et al., 1995). For these three galaxies, it was found that the inner bin was best fit by a single population, while the outer bin was best fit by a composite population. Naively, one might expect recent star formation to occur in the central parts of the BGGs. However, it is possible that processes such as galaxy mergers or infalling satellites can lead to younger stars in the outer parts. Whether this is indeed the case here, needs to be further investigated by also looking at the X-ray and radio observations. [1]

Some of the troubling results, however, can be seen for instance in the case of NGC2563. According to Table 3.3, it is better described by a CSP for both the inner and the outer bins. This is because of the reasonable percentage light fraction from the young stellar components. However, when looking at the SSP fits, the model seems to hit the upper limit for both bins (Table 3.1). This is quite contradictory. Another contradictory result is in the case where there seems to be only one stellar population component (too small light fraction of young component, no young component, or two components with too small a difference in age) and the SSP age then also hits the upper limit. These two contradictions appear to affect many of the results.

To investigate the contradictory results, we first investigate using different stellar population models that are available to use in ULySS. The same wavelength range, as for the previous analysis, was used: 4600 to 6200 Å.

[1] Some of this work is published in Havenga et al. (2019).

3.3 Different models

The four models that were used to compare the influence of the model on the SSP and CSP results, are[2]:

Model 1: Vazdekis models computed with the MILES library.
Model 2: PEGASE HR models with ELODIE 3.2 library, resolved in [α/Fe].
Model 3: Grid of Pegase HR SSPs computed with the Elodie 3.1 library.
Model 4: Vazdekis v9.0 models computed from the MILES library with Kroupa (2001) binaries corrected IMF.

In Section 1.4.1, it can be seen that the isochrones, IMF and stellar spectral libraries are the main ingredients for a stellar population model. Models 1 and 4 both use the MILES library, but model 4 uses the Kroupa binary corrected IMF, while model 1 uses the Salpeter IMF. Models 2 and 3 use the Elodie library, where model 2 is a more updated version and the spectra are resolved in [α/Fe] (meaning that different models were used in the [α/Fe] = 0 and [α/Fe] = 0.4, cases respectively). See Section 4.1.1 for a detailed discussion on α-enhancements.

For all the plots of the analysis using four different models, please refer to https://drive.google.com/file/d/1-r7bAWSD--NwlFuo06oSSmW6XMIVMwWx/view?usp=sharing.

Looking at Tables 3.4, 3.5, 3.6 and 3.7, the general result (in some of the galaxies) of model 1, which is also used in the first part of this chapter, is also obtained from the other models. Table 3.4 gives the CSP results of all four models on all 23 galaxies. Table 3.5 gives the corresponding SSP results. Table 3.6 gives the comparison between the SSP and CSP fits and Table 3.7 shows which was the better fit between CSP and SSP for each model. NGC0584 is described as a CSP in the inner and outer bins of model 1. This is also obtained with models 2, 3 and 4, with the exception of model 2, where the outer bin is thought to be better described by an SSP.

[2]The four models are described in more detail on the official ULySS website: http://ulyss.univ-lyon1.fr/optional.html.

Composite stellar population fitting														
Galaxy	A	C	Age (Myr)				[Fe/H] dex				Luminosity fraction			
			Model 1	Model 2	Model 3	Model 4	Model 1	Model 2	Model 3	Model 4	Model 1	Model 2	Model 3	Model 4
High-richness														
NGC0410	I	1	12530 ± 57710	9780 ± 23400	1130 ± 0	12460 ± 15650	2.32 ± 0.00	−2.25 ± 1.65	0.69 ± 0.00	−2.32 ± 0.00	4.58 ± 0.56	8.55 ± 0.43	0.29 ± 0.98	2.76 ± 0.56
		2	17360 ± 2700	19700 ± 13180	17650 ± 5460	17760 ± 2360	0.12 ± 0.07	0.09 ± 0.07	0.01 ± 0.03	0.08 ± 0.07	95.42 ± 0.55	91.45 ± 0.42	99.71 ± 0.97	97.24 ± 0.55
	O	1	17110 ± 128480	130 ± 1140	220 ± 46130	17780 ± 0	−2.26 ± 5.62	0.68 ± 5.91	−0.94 ± 162.30	−1.39 ± 0.84	9.54 ± 1.56	2.27 ± 0.84	0.30 ± 0.82	11.55 ± 1.91
		2	16140 ± 5900	19140 ± 13780	19000 ± 10580	16090 ± 6570	0.20 ± 0.15	−0.02 ± 0.18	−0.05 ± 0.19	0.20 ± 0.14	90.46 ± 1.52	97.73 ± 0.80	99.70 ± 0.79	88.45 ± 1.87
NGC0584	I	1	130 ± 150	3420 ± 5720	1430 ± 1240	60 ± 0	−0.51 ± 0.43	0.70 ± 0.00	0.70 ± 0.00	0.20 ± 0.18	11.65 ± 0.29	18.19 ± 2.13	10.50 ± 1.34	9.82 ± 0.25
		2	15800 ± 1950	11650 ± 7350	16340 ± 3040	17780 ± 0	0.15 ± 0.04	−0.16 ± 0.09	−0.09 ± 0.06	0.11 ± 0.03	88.35 ± 0.28	81.81 ± 2.14	89.50 ± 1.33	90.18 ± 0.24
	O	1	80 ± 1040	9570 ± 8750	2500 ± 12040	90 ± 1370	0.11 ± 11.17	−0.17 ± 0.34	0.47 ± 1.40	0.10 ± 11.04	5.86 ± 1.87	100.00 ± 0.38	24.02 ± 23.47	6.11 ± 1.89
		2	14120 ± 15560		16190 ± 35510	14160 ± 10840	−0.18 ± 0.31		−0.40 ± 0.64	−0.19 ± 0.27	94.14 ± 1.79	0.00 ± 0.00	75.98 ± 23.47	93.89 ± 1.80
NGC0777	I	1	17500 ± 2100	18840 ± 13420	20000 ± 0	5400 ± 0	0.06 ± 0.07	−2.09 ± 0.76	−0.06 ± 0.05	−2.30 ± 0.00	100.00 ± 0.07	6.87 ± 0.49	100.00 ± 0.07	1.37 ± 0.61
		2		20000 ± 0		17780 ± 0		−2.09 ± 0.76		−0.05 ± 0.06	0.00 ± 0.00	93.13 ± 0.47	0.00 ± 0.00	98.63 ± 0.59
	O	1		19580 ± 31810	150 ± 0	200 ± 0		0.70 ± 0.00	−0.39 ± 0.00	−0.37 ± 0.00	0.00 ± 1.27	9.66 ± 11.04	0.06 ± 1.14	0.20 ± 1.28
		2	17160 ± 7900	20000 ± 0.00	20000 ± 0	16920 ± 8990	0.20 ± 0.13	0.013 ± 0.25	0.00 ± 0.17	0.12 ± 0.13	100.00 ± 1.18	90.34 ± 11.01	99.94 ± 1.06	99.80 ± 1.19
NGC0924	I	1	150 ± 110	13150 ± 2890	440 ± 0	8130 ± 3080	−0.76 ± 0.81	0.00 ± 0.05	−0.06 ± 0.00	−2.32 ± 0.00	6.97 ± 0.37	100.00 ± 0.07	2.11 ± 0.38	8.67 ± 0.56
		2	16550 ± 2150		16130 ± 4060	16200 ± 1940	0.21 ± 0.03		−0.05 ± 0.05	0.22 ± 0.00	93.03 ± 0.35	0.00 ± 0.00	97.89 ± 0.36	91.33 ± 0.54
	O	1	17780 ± 0	20000 ± 0	0 ± 0	17620 ± 8130	−0.48 ± 0.17	−1.60 ± 28.65	−0.17 ± 0.00	−0.47 ± 0.24	100.00 ± 0.22	11.86 ± 2.44	3.76 ± 1.19	100.00 ± 0.22
		2		12530 ± 13260	13260 ± 12030			−0.28 ± 0.60	−0.34 ± 0.19		0.00 ± 0.00	88.14 ± 2.37	96.24 ± 1.12	0.00 ± 0.00
NGC1060	I	1	3350 ± 3300	19640 ± 14290	180 ± 3100	16790 ± 2010	−2.32 ± 0.00	−2.30 ± 0.00	0.70 ± 0.00	0.22 ± 0.00	0.75 ± 0.58	11.99 ± 0.60	0.54 ± 0.38	100.00 ± 0.00
		2	17780 ± 0	19610 ± 13260	20000 ± 0		0.22 ± 0.00	0.10 ± 0.11	−0.01 ± 0.05		99.25 ± 0.56	88.01 ± 0.58	99.46 ± 0.37	0.00 ± 0.00
	O	1	1340 ± 0	310 ± 6150	60 ± 0	970 ± 16620	−2.32 ± 0.00	0.70 ± 0.00	0.67 ± 0.00	−2.26 ± 13.47	0.17 ± 1.78	1.35 ± 1.19	0.05 ± 0.84	1.16 ± 1.44
		2	17780 ± 0	19740 ± 20250	20000 ± 0	17680 ± 7580	0.07 ± 0.14	0.01 ± 0.18	−0.01 ± 0.15	0.12 ± 0.14	99.83 ± 1.72	98.65 ± 1.14	99.95 ± 0.80	98.44 ± 1.39
NGC1453	I	1	17140 ± 2100	5100 ± 47810	130 ± 2980	440 ± 0	0.19 ± 0.04	−2.16 ± 8.04	−0.34 ± 15.60	0.22 ± 0.00	100.00 ± 0.08	1.61 ± 0.48	1.37 ± 0.30	3.10 ± 0.40
		2		18660 ± 10330	19240 ± 7990	17780 ± 0		0.08 ± 0.08	0.05 ± 0.06	0.14 ± 0.05	0.00 ± 0.00	98.39 ± 0.46	98.63 ± 0.29	96.90 ± 0.38
	O	1	17660 ± 9490	760 ± 179030	18600 ± 21340	17780 ± 0	0.04 ± 0.20	−0.57 ± 180.38	0.00 ± 0.22	0.01 ± 0.19	100.00 ± 0.35	1.14 ± 1.81	100.00 ± 0.36	100.00 ± 0.35
		2		15990 ± 21340				0.03 ± 0.49			0.00 ± 0.00	98.86 ± 1.75	0.00 ± 0.00	0.00 ± 0.00
NGC1587	I	1	100 ± 3110	20000 ± 0	190 ± 0	16740 ± 3410	0.00 ± 23.86	−2.30 ± 0.00	−0.15 ± 0.00	0.22 ± 0.00	0.12 ± 0.26	1.76 ± 0.48	0.03 ± 0.26	44.24 ± 1.91
		2	17780 ± 0	20000 ± 0	20000 ± 0	17780 ± 0	0.13 ± 0.03	−0.01 ± 0.06	−0.04 ± 0.04	−0.20 ± 0.17	99.88 ± 0.25	98.34 ± 0.46	99.97 ± 0.25	55.76 ± 1.93
	O	1	17780 ± 0	16130 ± 16070	18760 ± 13960	17780 ± 0	−0.11 ± 0.15	−0.09 ± 0.18	−0.11 ± 0.19	−0.13 ± 0.16	100.00 ± 0.27	100.00 ± 0.27	100.00 ± 0.27	100.00 ± 0.27
		2									0.00 ± 0.00	0.00 ± 0.00	0.00 ± 0.00	0.00 ± 0.00
NGC2563	I	1	1750 ± 1390	1890 ± 4230	130 ± 420	16020 ± 3600	−0.60 ± 0.65	−0.95 ± 2.22	0.69 ± 2.63	0.22 ± 0.00	7.96 ± 0.62	4.89 ± 0.45	2.02 ± 0.29	51.80 ± 2.30
		2	16680 ± 2140	20000 ± 0	20000 ± 0	17780 ± 0	0.20 ± 0.06	0.07 ± 0.08	0.04 ± 0.04	−0.20 ± 0.26	92.04 ± 0.61	95.11 ± 0.44	97.98 ± 0.28	48.20 ± 2.31
	O	1	430 ± 5890	15520 ± 10070	100 ± 8070	11930 ± 25280	−1.86 ± 11.02	0.00 ± 0.15	0.60 ± 62.50	0.22 ± 0.00	4.25 ± 1.41	100.00 ± 0.24	0.22 ± 0.93	11.26 ± 42.36
		2	17780 ± 0		16200 ± 17830	17780 ± 0	0.19 ± 0.16		−0.01 ± 0.17	0.13 ± 0.08	95.75 ± 1.37	0.00 ± 0.00	99.78 ± 0.90	88.74 ± 42.32
NGC4261	I	1	17780 ± 0	20000 ± 0	20000 ± 0	17760 ± 8650	−0.15 ± 0.06	−2.25 ± 0.56	−0.09 ± 0.05	0.17 ± 4.55	100.00 ± 0.08	9.59 ± 0.57	100.00 ± 0.08	100.00 ± 0.08
		2		19450 ± 11270				0.04 ± 0.08			0.00 ± 0.00	90.41 ± 0.55	0.00 ± 0.00	0.00 ± 0.00
	O	1	260 ± 6830	50 ± 400	50 ± 16960	60 ± 110	0.07 ± 19.88	0.69 ± 6.94	0.70 ± 0.00	0.22 ± 0.00	3.71 ± 1.52	4.24 ± 1.20	0.12 ± 1.24	5.61 ± 1.44
		2	17780 ± 0	20000 ± 0	20000 ± 0	17780 ± 0	0.15 ± 0.22	0.00 ± 0.20	−0.07 ± 0.26	0.15 ± 0.15	96.29 ± 1.45	95.76 ± 1.14	99.88 ±1.19	94.39 ± 1.37
NGC5353	I	1	330 ± 0	310 ± 160	120 ± 870	17780 ± 0	0.21 ± 0.00	0.70 ± 0.00	−1.74 ± 6.24	−0.07 ± 0.04	0.04 ± 0.26	2.35 ± 0.26	1.61 ± 0.21	100.00 ± 0.05
		2	17780 ± 0	20000 ± 0	20000 ± 0		−0.05 ± 0.04	0.05 ± 0.03	0.03 ± 0.03		99.96 ± 0.25	97.65 ± 0.26	98.39 ± 0.20	0.00 ± 0.00
	O	1	16280 ± 10610	1800 ± 2320	20000 ± 0	16110 ± 14790	0.22 ± 0.00	0.68 ± 0.56	−0.10 ± 0.15	0.22 ± 0.00	31.36 ± 5.21	17.83 ± 5.27	100.00 ± 0.15	25.24 ± 5.22
		2	17780 ± 0	19970 ± 8320		17780 ± 0	−0.16 ± 0.37	−0.23 ± 0.25		−0.16 ± 0.40	68.64 ± 5.25	82.17 ± 5.25	0.00 ± 0.00	74.76 ± 5.26
NGC5846	I	1	17770 ± 4790	16190 ± 7320	20000 ± 0.00	16960 ± 7610	−0.19 ± 0.30	−0.21 ± 0.08	−2.30 ± 0.00	0.22 ± 0.00	100.00 ± 0.13	100.00 ± 0.13	8.76 ± 1.23	27.38 ± 3.29
		2			16670 ± 10860	17780 ± 0			−0.23 ± 0.24	−0.30 ± 0.23	0.00 ± 0.00	0.00 ± 0.00	91.24 ± 1.19	72.62 ± 3.34
	O	1	17780 ± 0	290 ± 0	190 ± 256040	17780 ± 0	0.22 ± 0.00	−0.09 ± 0.00	0.70 ± 0.00	0.22 ± 0.00	100.00± 11.32	51.80 ± 64.41	7.85 ± 57.61	100.00± 11.32
		2		3960 ± 114810	7210 ± 257780			0.28 ± 6.16	0.21 ± 7.70		0.00 ± 0.00	48.20 ± 57.42	92.15 ± 52.93	0.00 ± 0.00
NGC5982	I	1	1340 ± 510	250 ± 2050	0 ± 0	1970 ± 900	−0.66 ± 0.48	−2.06 ± 7.43	0.27 ± 0.00	−0.71 ± 0.71	17.32 ± 0.69	4.74 ± 0.35	0.32 ± 0.25	21.61 ± 0.78
		2	17780 ± 0	19220 ± 4550	18530 ± 6150	17740 ± 3120	0.20 ± 0.06	−0.05 ± 0.08	−0.11 ± 0.07	0.22 ± 0.10	82.68 ± 0.66	95.26 ± 0.33	99.68 ± 0.24	78.39 ± 0.75
	O	1	17780 ± 0	40 ± 0	10 ± 0	60 ± 0	−0.39 ± 0.31	−1.06 ± 0.00	−0.26 ± 0.00	0.05 ± 0.00	100.00 ± 0.32	5.28 ± 1.84	5.44 ± 2.12	0.18 ± 2.14
		2		18910 ± 15340	18610 ± 23920	17780 ± 0		−0.33 ± 0.42	−0.40 ± 0.32	−0.37 ± 0.32	0.00 ± 0.00	94.72 ± 1.70	94.56 ± 1.97	99.82 ± 2.00
NGC6658	I	1	60 ± 0	0 ± 0	10470 ± 33980	2500 ± 1910	−0.48 ± 0.81	−1.08 ± 1.37	0.31 ± 1.50	−0.69 ± 0.54	10.29 ± 0.45	12.93 ± 0.38	23.41 ± 2.84	21.32 ± 1.07
		2	17340 ± 3390	18970 ± 11140	16110 ± 11720	16610 ± 3250	0.17 ± 0.06	0.12 ± 0.10	−0.19 ± 1.20	0.22 ± 0.00	89.71 ± 0.42	87.07 ± 0.36	76.59 ± 2.87	78.68 ± 1.04
	O	1	16510 ± 11460	590 ± 0	0 ± 0	16570 ± 11530	−0.57 ± 0.30	0.70 ± 0.00	0.59 ± 0.00	−0.57 ± 0.29	100.00 ± 0.32	0.84 ± 3.30	0.29 ± 1.14	100.00 ± 0.32
		2		13910 ± 14140	18610 ± 11350			−0.52 ± 0.19	−0.50 ± 0.25		0.00 ± 0.00	99.16 ± 3.22	99.71 ± 1.08	0.00 ± 0.00
NGC7619	I	1	16290 ± 2740	19730 ± 6100	2540 ± 4490	130 ± 1770	0.22 ± 0.00	−2.05 ± 0.51	−2.30 ± 0.00	0.22 ± 0.00	48.58 ± 1.92	14.52 ± 0.40	0.75 ± 0.30	0.35 ± 0.23
		2	17780 ± 0	18850 ± 4720	20000 ± 0	17780 ± 0	−0.19 ± 0.17	0.18 ± 0.09	0.03 ± 0.04	0.19 ± 0.04	51.42 ± 1.94	85.48 ± 0.38	99.25 ± 0.29	99.65 ± 0.22
	O	1	200 ± 205790	13800 ± 0	3130 ± 5920	80 ± 0	0.07 ± 622.59	0.70 ± 0.00	0.70 ± 0.00	−0.59 ± 0.00	0.08 ± 1.56	3.45 ± 6.62	2.58 ± 18.18	0.42 ± 1.50
		2	17780 ± 0	16790 ± 22130	18750 ± 18270	17780 ± 0	−0.01 ± 0.17	−0.03 ± 0.24	−0.07 ± 0.28	−0.01 ± 0.18	99.92 ± 1.48	96.55 ± 6.52	97.42 ± 18.20	99.58 ± 1.42

Table 3.4: *The first part of the CSP fit results using the four different models in ULySS. In this table,* ***A*** *stands for aperture,* ***C*** *for component,* ***I*** *for inner aperture and* ***O*** *for outer aperture.*

Composite stellar population fitting													
Galaxy	A	C	Age (Myr)				[Fe/H] dex				Luminosity fraction			
			Model 1	Model 2	Model 3	Model 4	Model 1	Model 2	Model 3	Model 4	Model 1	Model 2	Model 3	Model 4
Low-richness														
NGC0315	I	1	17660 ± 390290	1010 ± 0	19950 ± 5930	1330 ± 0	−2.32 ± 16.88	−1.68 ± 0.00	0.03 ± 0.06	0.20 ± 0.00	1.47 ± 0.62	0.04 ± 0.39	100.00 ± 0.09	0.12 ± 0.78
		2	17030 ± 2050	1010 ± 0		16710 ± 2550	0.22 ± 0.00	0.03 ± 0.05		0.20 ± 0.04	98.53 ± 0.61	99.96 ± 0.37	0.00 ± 0.00	99.88 ± 0.76
	O	1	17780 ± 0	3470 ± 50260	300 ± 0	130 ± 780	−0.23 ± 0.53	−2.30 ± 11.88	0.68 ± 0.00	−0.30 ± 4.69	33.69 ± 5.23	3.15 ± 1.10	0.30 ± 0.97	2.84 ± 0.84
		2	16780 ± 5820	18260 ± 13200	17360 ± 12730	17780 ± 0	0.22 ± 0.00	0.05 ± 0.17	0.02 ± 0.12	0.11 ± 0.11	66.31 ± 5.19	96.85 ± 0.98	99.70 ± 0.93	97.16 ± 0.81
NGC0524	I	1	340 ± 0	16970 ± 7030	19380 ± 0	17780 ± 0	−2.28 ± 0.00	−0.07 ± 0.07	−2.21 ± 0.66	−0.05 ± 0.06	1.07 ± 0.80	100.00 ± 0.11	0.14 ± 0.92	100.00 ± 0.11
		2	17780 ± 0		20000 ± 0		−0.04 ± 0.08		−0.12 ± 0.13		98.93 ± 0.76	0.00 ± 0.00	99.86 ± 0.89	0.00 ± 0.00
	O	1	11030 ± 80280	0 ± 0	80 ± 0	10190 ± 131280	−2.11 ± 4.99	0.60 ± 48.83	0.69 ± 0.00	−2.23 ± 9.36	12.90 ± 3.97	0.42 ± 1.35	1.87 ± 1.81	11.81 ± 3.92
		2	17780 ± 0	11600 ± 16970	12240 ± 16970	14430 ± 16880	−0.02 ± 0.32	−0.12 ± 0.51	−0.18 ± 0.35	0.01 ± 0.38	87.10 ± 3.84	99.58 ± 1.25	98.13 ± 1.69	88.19 ± 3.79
NGC1779	I	1	240 ± 340	0 ± 0	3780 ± 1090	7430 ± 990	0.19 ± 1.12	−0.75 ± 0.00	0.50 ± 0.13	−0.64 ± 1.25	10.39 ± 0.39	0.20 ± 0.35	60.84 ± 2.97	7.29 ± 0.56
		2	11020 ± 1860	5550 ± 1090	16720 ± 20150	7780 ± 1590	0.22 ± 0.00	0.16 ± 0.06	−0.34 ± 0.31	0.22 ± 0.00	89.61 ± 0.37	99.80 ± 0.34	39.16 ± 3.00	92.71 ± 0.54
	O	1	110 ± 380	1520 ± 6630	0 ± 600	90 ± 390	0.22 ± 3.32	−0.67 ± 3.89	0.70 ± 0.00	0.15 ± 3.15	10.05 ± 1.28	15.96 ± 2.80	1.10 ± 1.09	11.77 ± 1.29
		2	13970 ± 8810	9350 ± 13840	6200 ± 5810	14140 ± 9860	−0.08 ± 0.17	−0.01 ± 0.31	−0.06 ± 0.30	−0.08 ± 0.17	89.95 ± 1.19	84.04 ± 2.29	98.90 ± 1.02	88.23 ± 1.20
NGC2768	I	1	5180 ± 4140	1170 ± 3380	220 ± 1900	2020 ± 1890	−0.68 ± 0.56	−1.10 ± 3.74	0.70 ± 0.00	−0.78 ± 0.58	32.96 ± 1.58	6.45 ± 0.80	1.58 ± 0.70	24.77 ± 1.22
		2	17500 ± 5200	15300 ± 6920	16230 ± 11720	17780 ± 0	0.18 ± 0.18	−0.09 ± 0.21	−0.16 ± 0.10	0.12 ± 0.15	67.04 ± 1.53	93.55 ± 0.76	98.42 ± 0.66	75.23 ± 1.17
	O	1	200 ± 0	0 ± 520	1 ± 0	140 ± 0	−0.47 ± 0.00	0.61 ± 319.36	−0.53 ± 95.22	−0.52 ± 0.00	0.07 ± 3.47	0.02 ± 1.82	0.72 ± 1.80	0.01 ± 0.00
		2	15190 ± 15000	12980 ± 30220	14400 ± 30280	15080 ± 14930	−0.51 ± 0.40	−0.42 ± 0.65	−0.52 ± 0.61	−0.52 ± 0.39	99.93 ± 3.25	99.98 ± 1.65	99.28 ± 1.63	99.99 ± 3.37
NGC3613	I	1	17780 ± 0	130 ± 6920	140 ± 420	110 ± 100	−2.32 ± 0.00	0.70 ± 0.00	0.58 ± 1.99	0.22 ± 0.00	7.08 ± 0.79	4.11 ± 0.39	2.87 ± 0.42	5.59 ± 0.41
		2	17780 ± 0	13680 ± 4470	14250 ± 4630	17780 ± 0	−0.04 ± 0.05	−0.08 ± 0.08	−0.10 ± 0.07	−0.06 ± 0.05	92.92 ± 0.76	95.89 ± 0.37	97.13 ± 0.39	94.41 ± 0.38
	O	1	10330 ± 50480	50 ± 630	6700 ± 6900	100 ± 720	0.22 ± 0.00	0.70 ± 0.00	−0.35 ± 0.38	0.22 ± 5.77	16.01 ± 6.69	2.83 ± 1.60	100.00 ± 0.37	5.50 ± 1.99
		2	7800 ± 13150	6540 ± 8800		11090 ± 14510	−0.50 ± 0.64	−0.25 ± 0.34		−0.35 ± 0.31	83.99 ± 6.83	97.17 ± 1.49	0.00 ± 0.00	94.50 ± 1.85
NGC3665	I	1	13780 ± 50620	19870 ± 48360	6490 ± 668320	2330 ± 1450	−2.25 ± 2.51	−2.30 ± 0.00	−2.30 ± 0.00	−0.49 ± 0.58	9.94 ± 1.20	4.54 ± 0.39	1.98 ± 0.97	22.42 ± 1.74
		2	17780 ± 0	11080 ± 5430	11400 ± 7120	17780 ± 0	−0.08 ± 0.10	−0.07 ± 0.20	−0.15 ± 0.20	−0.05 ± 0.14	90.06 ± 1.17	93.89 ± 1.12	98.02 ± 0.95	77.58 ± 1.70
	O	1	7080 ± 14780	0 ± 0	220 ± 0	1510 ± 0	−0.44 ± 0.51	−2.30 ± 0.00	0.69 ± 0.00	−0.14 ± 0.00	100.00 ± 0.53	0.17 ± 3.12	2.34 ± 3.52	1.69 ± 12.66
		2		5750 ± 8900	6010 ± 14730	5730 ± 6730		−0.32 ± 0.91	−0.45 ± 0.75	−0.37 ± 0.43	0.00 ± 0.00	99.83 ± 3.07	97.66 ± 3.46	98.31 ± 12.56
NGC5127	I	1	17320 ± 88190	12290 ± 5490	150 ± 0	60 ± 190	−2.32 ± 0.00	0.02 ± 0.09	0.70 ± 0.00	0.22 ± 0.00	8.17 ± 1.04	100.00 ± 0.14	0.13 ± 0.58	2.48 ± 0.58
		2	16660 ± 4140		16120 ± 6620	11640 ± 3070	0.18 ± 0.09		0.00 ± 0.08	0.20 ± 0.06	91.83 ± 1.01	0.00 ± 0.00	99.87 ± 0.56	97.52
	O	1	370 ± 43680	320 ± 4550	10440 ± 12720	370 ± 57150	−0.73 ± 88.28	0.22 ± 9.83	0.08 ± 0.26	−0.75 ± 116.01	1.11 ± 2.46	1.38 ± 2.34	100.00 ± 0.45	0.84 ± 2.49
		2	16420 ± 14510	16750 ± 14310		15560 ± 16520	−0.09 ± 0.30	−0.05 ± 0.21		−0.09 ± 0.34	98.89 ± 2.36	98.62 ± 2.26	0.00 ± 0.00	99.16 ± 2.39
NGC5490	I	1	5010 ± 199750	2260 ± 17020	0 ± 0	110 ± 280	−2.29 ± 31.04	−1.75 ± 5.97	−1.89 ± 0.48	0.22 ± 0.00	0.50 ± 0.50	4.54 ± 0.39	2.43 ± 0.18	1.11 ± 0.28
		2	16530 ± 2100	20000 ± 0	20000 ± 0	16670 ± 1920	0.22 ± 0.00	0.05 ± 0.05	0.04 ± 0.05	0.22 ± 0.00	99.50 ± 0.49	95.46 ± 0.38	97.57 ± 0.17	98.89 ± 0.27
	O	1	17780 ± 0	0 ± 0	90 ± 31030	970 ± 4490	−0.32 ± 0.52	−2.30 ± 0.00	0.70 ± 0.00	−1.85 ± 4.97	37.93 ± 5.68	0.82 ± 1.05	2.39 ± 0.91	2.51 ± 1.56
		2	16450 ± 7490	16750 ± 14310	17210 ± 19190	17780 ± 0	0.22 ± 0.00	−0.05 ± 0.21	−0.07 ± 0.18	0.08 ± 0.15	62.07 ± 5.63	99.18 ± 1.01	97.62 ± 0.86	97.49 ± 1.51
NGC5629	I	1	170 ± 750	60 ± 130	110 ± 330	17780 ± 0	−0.06 ± 3.58	0.70 ± 0.00	−1.32 ± 3.54	−2.32 ± 0.00	3.56 ± 0.38	3.39 ± 0.30	4.44 ± 0.34	3.54 ± 0.70
		2	17780 ± 0	16380 ± 5310	16370 ± 5760	17780 ± 0	0.05 ± 0.04	−0.01 ± 0.06	−0.05 ± 0.09	0.03 ± 0.05	96.44 ± 0.35	96.61 ± 0.29	95.56 ± 0.31	96.46 ± 0.67
	O	1	14400 ± 306030	16220 ± 19910	14780 ± 21950	60 ± 1840	−1.35 ± 16.61	−0.10 ± 0.26	−0.19 ± 0.37	0.21 ± 23.28	1.86 ± 5.57	100.00 ± 0.40	100.00 ± 0.40	1.23 ± 1.85
		2	17610 ± 13370			17690 ± 13210	−0.14 ± 0.34			−0.12 ± 0.26	98.14 ± 5.42	0.00 ± 0.00	0.00 ± 0.00	98.77 ± 1.70

Table 3.5: *The second part of the CSP fit results using the four different models in ULySS.*

SSP and CSP comparison																	
Galaxy	A	CSP χ^2				SSP χ^2				SSP age (Myr)				SSP [Fe/H] dex			
		Model 1	Model 2	Model 3	Model 4	Model 1	Model 2	Model 3	Model 4	Model 1	Model 2	Model 3	Model 4	Model 1	Model 2	Model 3	Model 4
High-richness																	
NGC0410	I	0.095	0.091	0.100	0.095	0.104	0.109	0.105	0.104	16470 ± 2380	18270 ± 4840	19540 ± 4210	15550 ± 2600	0.10 ± 0.05	0.02 ± 0.04	0.01 ± 0.03	0.10 ± 0.05
	O	0.036	0.036	0.036	0.036	0.037	0.036	0.036	0.037	17400 ± 5930	18200 ± 12930	18070 ± 11600	17780 ± 0	0.10 ± 0.10	−0.04 ± 0.11	−0.05 ± 0.13	0.07 ± 0.07
NGC0584	I	0.115	0.100	0.102	0.112	0.093	0.125	0.124	0.098	14010 ± 1540	9280 ± 1650	11620 ± 1420	13980 ± 1520	−0.06 ± 0.03	0.01 ± 0.04	−0.03 ± 0.05	−0.08 ± 0.03
	O	0.008	0.008	0.008	0.008	0.008	0.007	0.007	0.008	11480 ± 7260	6400 ± 6580	8360 ± 7260	11350 ± 8930	−0.21 ± 0.22	−0.10 ± 0.25	−0.18 ± 0.36	−0.21 ± 0.23
NGC0777	I	0.175	0.143	0.132	0.136	0.121	0.166	0.132	0.121	17780 ± 0	20000 ± 0	20000 ± 0	177800 ± 0	−0.06 ± 0.04	−0.01 ± 0.04	−0.06 ± 0.04	−0.06 ± 0.04
	O	0.035	0.033	0.032	0.036	0.035	0.033	0.032	0.036	17100 ± 7350	20000 ± 0	20000 ± 0	17020 ± 8010	0.21 ± 0.12	0.05 ± 0.12	0.02 ± 0.14	0.20 ± 0.12
NGC0924	I	0.138	0.122	0.129	0.136	0.152	0.121	0.131	0.145	15600 ± 2130	13550 ± 2740	15440 ± 2630	15870 ± 2310	0.17 ± 0.03	0.00 ± 0.05	−0.03 ± 0.05	0.16 ± 0.03
	O	0.046	0.042	0.041	0.045	0.042	0.041	0.040	0.042	11760 ± 4410	12040 ± 8820	11960 ± 7060	11960 ± 4830	−0.18 ± 0.14	−0.29 ± 0.20	−0.29 ± 0.21	−0.19 ± 0.14
NGC1060	I	0.137	0.088	0.095	0.134	0.136	0.114	0.094	0.134	17610 ± 1460	20000 ± 0	20000 ± 0	17180 ± 1600	0.22 ± 0.00	0.05 ± 0.03	−0.02 ± 0.05	0.22 ± 0.00
	O	0.031	0.031	0.032	0.032	0.030	0.031	0.032	0.030	17780 ± 0	19170 ± 12200	20000 ± 0	17780 ± 0	0.07 ± 0.09	0.01 ± 0.10	0.01 ± 0.10	0.06 ± 0.09
NGC1453	I	0.138	0.093	0.113	0.125	0.138	0.129	0.108	0.138	16970 ± 2090	20000 ± 0	19210 ± 8590	16630 ± 2190	0.20 ± 0.04	0.09 ± 0.05	0.08 ± 0.05	0.20 ± 0.04
	O	0.022	0.022	0.022	0.022	0.022	0.022	0.022	0.022	17580 ± 11410	16390 ± 16690	18140 ± 22590	17090 ± 11900	0.06 ± 0.18	0.03 ± 0.22	0.05 ±0.22	0.05 ± 0.19
NGC1587	I	0.161	0.116	0.123	0.107	0.113	0.116	0.126	0.129	17780 ± 0	20000 ± 0	20000 ± 0	17780 ± 0	0.00 ± 0.03	−0.03 ± 0.03	0.01 ± 0.03	0.04 ± 0.03
	O	0.025	0.025	0.026	0.025	0.025	0.025	0.026	0.025	17780 ± 0	16350 ± 13880	18630 ± 13480	17780 ± 0	−0.08 ± 0.12	−0.08 ± 0.18	−0.09 ± 0.17	−0.09 ± 0.12
NGC2563	I	0.124	0.107	0.104	0.099	0.105	0.109	0.107	0.112	17780 ± 0	20000 ± 0	20000 ± 0	17780 ± 0	0.02 ± 0.04	0.03 ± 0.03	0.03 ± 0.03	0.02 ± 0.04
	O	0.027	0.024	0.025	0.028	0.027	0.025	0.025	0.028	17780 ± 0	16870 ± 12820	16040 ± 10970	17780 ± 0	0.15 ± 0.08	0.02 ± 0.14	−0.01 ± 0.17	0.14 ± 0.08
NGC4261	I	0.063	0.086	0.073	0.141	0.060	0.085	0.074	0.174	17780 ± 0	20000 ± 0	20000 ± 0	17780 ± 0	−0.10 ± 0.05	−0.08 ± 0.04	−0.09 ± 0.05	0.18 ± 0.03
	O	0.024	0.023	0.023	0.024	0.024	0.024	0.024	0.024	17780 ± 0	20000 ± 0	20000 ± 0	17780 ± 0	0.11 ± 0.12	−0.03 ± 0.16	−0.06 ± 0.19	0.10 ± 0.12
NGC5353	I	0.124	0.151	0.118	0.125	0.268	0.191	0.118	0.275	17780 ± 0	18440 ± 4540	20000 ± 0	17780 ± 0	0.12 ± 0.03	0.12 ± 0.03	0.00 ± 0.03	0.12 ± 0.03
	O	0.022	0.020	0.025	0.022	0.021	0.027	0.024	0.021	17780 ± 0	16550 ± 9230	20000 ± 0	17780 ± 0	−0.09 ± 0.09	−0.07 ± 0.11	−0.10 ± 0.09	−0.09 ± 0.09
NGC5846	I	0.028	0.041	0.031	0.036	0.032	0.041	0.040	0.035	17780 ± 0	16310 ± 7530	16420 ± 7890	17780 ± 0	−0.23 ± 0.07	−0.21 ± 0.08	−0.22 ± 0.08	−0.20 ± 0.07
	O	0.004	0.004	0.004	0.004	0.004	0.004	0.004	0.004	17780 ± 0	20000 ± 0	7170 ± 156920	17780 ± 0	0.22 ± 0.00	0.31 ± 6.40	0.25 ± 6.01	0.22 ± 0.00
NGC5982	I	0.079	0.071	0.070	0.078	0.056	0.072	0.070	0.057	17780 ± 0	14210 ± 3460	16770 ± 5000	17780 ± 0	−0.12 ± 0.05	−0.08 ± 0.08	−0.12 ± 0.06	−0.13 ± 0.05
	O	0.020	0.021	0.021	0.020	0.020	0.021	0.020	0.020	17780 ± 0	16410 ± 27230	16250 ± 26740	17780 ± 0	−0.34 ± 0.24	−0.34 ± 0.21	−0.38 ± 0.24	−0.35 ± 0.23
NGC6658	I	0.074	0.070	0.075	0.074	0.082	0.070	0.080	0.082	17780 ± 0	11580 ± 2960	15720 ± 4330	17780 ± 0	0.08 ± 0.04	−0.04 ± 0.09	−0.08 ± 0.07	0.06 ± 0.04
	O	0.030	0.031	0.030	0.030	0.030	0.029	0.030	0.030	16380 ± 12450	18530 ± 14370	18350 ± 12430	16380 ± 12000	0.57 ± 0.28	−0.47 ± 0.15	−0.53 ± 0.18	−0.55 ± 0.30
NGC7619	I	0.147	0.137	0.168	0.225	0.222	0.178	0.173	0.224	17780 ± 0	20000 ± 0	20000 ± 0	17780 ± 0	0.19 ± 0.02	0.03 ± 0.02	0.02 ± 0.03	0.19 ± 0.03
	O	0.019	0.019	0.020	0.019	0.019	0.020	0.020	0.019	17780 ± 0	14490 ± 13400	16960 ± 21690	17780 ± 0	0.00 ± 0.14	−0.01 ± 0.28	−0.03 ± 0.23	−0.01 ± 0.14
Low-richness																	
NGC0315	I	0.100	0.075	0.073	0.099	0.010	0.073	0.083	0.099	16610 ± 1740	20000 ± 0	20000 ± 0	16500 ± 2330	0.22 ± 0.00	0.05 ± 0.04	0.07 ± 0.04	0.21 ± 0.04
	O	0.025	0.025	0.026	0.026	0.026	0.026	0.026	0.026	17780 ± 0	16580 ± 11240	17120 ± 11830	17780 ± 0	0.10 ± 0.07	0.02 ± 0.11	0.03 ± 0.11	0.08 ± 0.07
NGC0524	I	0.038	0.047	0.039	0.040	0.040	0.046	0.046	0.040	17780 ± 0	19410 ± 4890	19960 ± 5260	17780 ± 0	−0.03 ± 0.05	−0.07 ± 0.05	−0.06 ± 0.07	−0.04 ± 0.05
	O	0.010	0.010	0.010	0.010	0.011	0.010	0.010	0.010	17780 ± 0	11120 ± 11900	11920 ± 12920	13830 ± 9270	−0.14 ± 0.18	−0.14 ± 0.38	−0.18 ± 0.33	−0.13 ± 0.24
NGC1779	I	0.065	0.072	0.059	0.053	0.052	0.072	0.031	0.053	5880 ± 1150	5530 ± 860	6250 ± 470	5680 ± 820	0.20 ± 0.07	0.16 ± 0.05	0.17 ± 0.05	0.20 ± 0.06
	O	0.015	0.015	0.015	0.015	0.015	0.015	0.014	0.015	10900 ± 5520	5800 ± 4270	6130 ± 4380	8950 ± 4780	−0.11 ± 0.16	−0.05 ± 0.18	−0.06 ± 0.18	−0.06 ± 0.18
NGC2768	I	0.031	0.034	0.032	0.031	0.023	0.034	0.031	0.023	17780 ± 0	12720 ± 4780	15640 ± 6080	17780 ± 0	−0.19 ± 0.07	−0.13 ± 0.10	−0.19 ± 0.08	−0.20 ± 0.07
	O	0.013	0.012	0.014	0.013	0.013	0.013	0.013	0.013	15340 ± 13390	11850 ± 23610	12130 ± 25060	15100 ± 12930	−0.51 ± 0.38	−0.43 ± 0.55	−0.45 ± 0.50	−0.51 ± 0.36
NGC3613	I	0.045	0.061	0.059	0.044	0.048	0.061	0.060	0.048	17780 ± 0	10600 ± 2270	12190 ± 2500	17780 ± 0	−0.10 ± 0.03	−0.07 ± 0.07	−0.11 ± 0.07	−0.11 ± 0.03
	O	0.019	0.019	0.020	0.019	0.020	0.020	0.020	0.019	10920 ± 11940	6990 ± 7800	6690 ± 6800	7920 ± 6180	−0.41 ± 0.28	−0.30 ± 0.32	−0.34 ± 0.34	−0.36 ± 0.29
NGC3665	I	0.036	0.042	0.040	0.033	0.032	0.041	0.040	0.032	17780 ± 0	9610 ± 3540	11040 ± 3500	17780 ± 0	−0.19 ± 0.06	−0.11 ± 0.12	−0.15 ± 0.12	−0.20 ± 0.06
	O	0.015	0.016	0.016	0.016	0.015	0.017	0.017	0.015	7830 ± 9820	8990 ± 13100	9430 ± 15290	7500 ± 8000	−0.44 ± 0.49	−0.42 ± 0.51	−0.50 ± 0.54	−0.44 ± 0.46
NGC5127	I	0.053	0.053	0.047	0.056	0.057	0.053	0.051	0.057	16430 ± 3980	13160 ± 4820	16650 ± 6440	11650 ± 2200	0.12 ± 0.06	0.02 ± 0.08	0.01 ± 0.07	0.18 ± 0.06
	O	0.022	0.023	0.023	0.022	0.022	0.023	0.023	0.022	14380 ± 11130	10180 ± 12050	12440 ± 10810	13810 ± 10470	−0.06 ± 0.23	0.00 ± 0.29	−0.04 ± 0.33	−0.06 ± 0.25
NGC5490	I	0.170	0.127	0.132	0.171	0.132	0.132	0.131	0.170	17780 ± 0	20000 ± 0	20000 ± 0	16440 ± 1540	0.07 ± 0.04	0.02 ± 0.03	0.00 ± 0.04	0.22 ± 0.00
	O	0.028	0.029	0.028	0.029	0.029	0.029	0.029	0.029	17780 ± 0	16390 ± 12250	16650 ± 14620	17780 ± 0	0.06 ± 0.08	−0.05 ± 0.16	−0.04 ± 0.14	0.05 ± 0.08
NGC5629	I	0.083	0.097	0.084	0.085	0.076	0.098	0.098	0.075	17780 ± 0	14070 ± 3080	16280 ± 3900	17780 ± 0	−0.06 ± 0.04	−0.03 ± 0.07	−0.05 ± 0.06	−0.08 ± 0.04
	O	0.030	0.032	0.031	0.030	0.030	0.031	0.031	0.030	17400 ± 12390	16590 ± 19780	15710 ± 17100	17780 ± 0	−0.16 ± 0.22	−0.16 ± 0.25	−0.20 ± 0.27	−0.16 ± 0.18

Table 3.6: *The SSP fit results as well as the comparison between the SSP and CSP χ^2 values for the four different models.*

Best described by SSP or CSP					
High-richness					
Galaxy	**Aperture**	**Model 1**	**Model 2**	**Model 3**	**Model 4**
NGC0410	**Inner**	SSP	SSP	SSP	SSP
	Outer	SSP	CSP	SSP	SSP
NGC0584	**Inner**	CSP	CSP	CSP	CSP
	Outer	CSP	SSP	CSP	CSP
NGC0777	**Inner**	SSP	SSP	SSP	SSP
	Outer	SSP	SSP	SSP	SSP
NGC0924	Inner	CSP	SSP	CSP	SSP
	Outer	SSP	SSP	CSP	SSP
NGC1060	**Inner**	SSP	SSP	SSP	SSP
	Outer	SSP	SSP	SSP	SSP
NGC1453	Inner	SSP	SSP	SSP	CSP
	Outer	SSP	SSP	SSP	SSP
NGC1587	**Inner**	SSP	SSP	SSP	SSP
	Outer	SSP	SSP	SSP	SSP
NGC2563	Inner	CSP	CSP	CSP	SSP
	Outer	CSP	SSP	SSP	SSP
NGC4261	**Inner**	SSP	SSP	SSP	SSP
	Outer	CSP	CSP	SSP	CSP
NGC5353	Inner	SSP	CSP	SSP	SSP
	Outer	SSP	SSP	SSP	SSP
NGC5846	**Inner**	SSP	SSP	SSP	SSP
	Outer	SSP	CSP	CSP	SSP
NGC5982	Inner	CSP	CSP	SSP	CSP
	Outer	SSP	CSP	CSP	SSP
NGC6658	Inner	CSP	CSP	SSP	CSP
	Outer	SSP	SSP	SSP	SSP
NGC7619	**Inner**	SSP	SSP	SSP	SSP
	Outer	SSP	SSP	CSP	SSP
Low-richness					
Galaxy	**Aperture**	**Model 1**	**Model 2**	**Model 3**	**Model 4**
NGC0315	**Inner**	SSP	SSP	SSP	SSP
	Outer	SSP	CSP	SSP	CSP
NGC0524	**Inner**	SSP	SSP	SSP	SSP
	Outer	SSP	SSP	SSP	SSP
NGC1779	Inner	CSP	SSP	CSP	SSP
	Outer	CSP	SSP	SSP	CSP
NGC2768	Inner	CSP	CSP	SSP	CSP
	Outer	SSP	SSP	SSP	SSP
NGC3613	Inner	SSP	CSP	CSP	CSP
	Outer	SSP	CSP	SSP	CSP
NGC3665	Inner	SSP	SSP	CSP	CSP

	Outer	SSP	SSP	SSP	SSP
NGC5127	Inner	SSP	SSP	SSP	CSP
	Outer	SSP	SSP	SSP	SSP
NGC5490	Inner	SSP	CSP	CSP	SSP
	Outer	SSP	SSP	CSP	CSP
NGC5629	Inner	CSP	CSP	CSP	SSP
	Outer	SSP	SSP	SSP	SSP

Table 3.7: *A table depicting the best fit of each specific galaxy spectrum for the 4 different models. The apertures in bold indicate those for which the 4 models have the same outcome.*

Based on the results from the four models, a table of discrepancies can be seen in Table 3.8. For this table, the results from the four models were compared. If all four models agreed on the classification, there seemed to be no overall discrepancy. In the star formation columns, a '✓' was made if three or four of the models showed a CSP best fit. If two of the models showed SSP and two showed CSP, then it was marked with a '?'. If three or four of the models showed an SSP best fit, an 'x' can be seen.

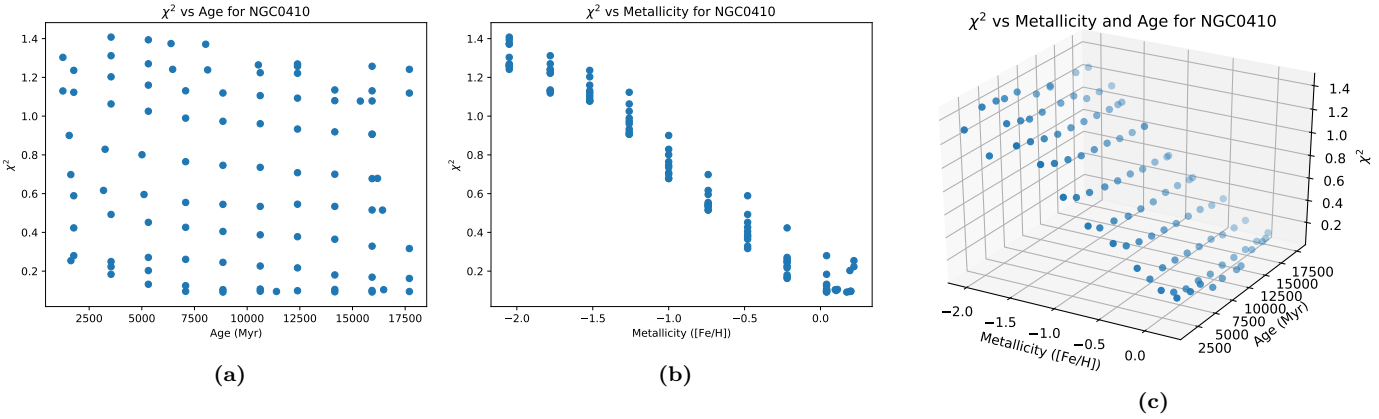
Galaxy	Inner bin result comparison	Star formation inner bin	Outer bin result comparison	Star formation outer bin
High-richness				
NGC0410	✓	x	x	x
NGC0584	✓	✓	x	✓
NGC0777	✓	x	✓	x
NGC0924	x	?	x	x
NGC1060	✓	x	✓	x
NGC1453	x	x	✓	x
NGC1587	✓	x	✓	x
NGC2563	x	✓	x	x
NGC4261	✓	x	x	✓
NGC5353	x	x	✓	x
NGC5846	✓	x	x	?
NGC5982	x	✓	x	?
NGC6658	x	✓	✓	x
NGC7619	✓	x	x	x
Low-richness				
NGC0315	✓	x	x	?
NGC0524	✓	x	✓	x
NGC1779	x	?	x	?
NGC2768	x	✓	✓	x
NGC3613	x	✓	x	?
NGC3665	x	?	✓	x
NGC5127	x	x	✓	x
NGC5490	x	?	x	?
NGC5629	x	✓	✓	x

Table 3.8: *The discrepancies in the possible star formation from the stellar population fits. For this table, the results from the four models were compared. In the star formation columns, a '✓' was made if three or four of the models showed a CSP best fit. If two of the models showed SSP and two showed CSP, then it was marked with a '?'. If three or four of the models showed an SSP best fit, an 'x' can be seen.*

3.4 Checking the reliability of the solutions

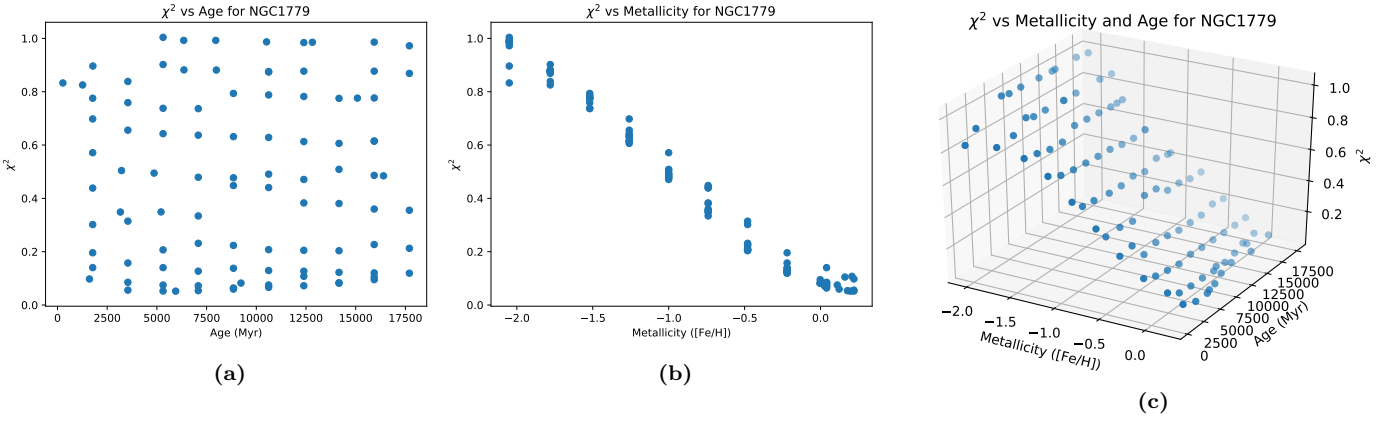
An important value to consider when evaluating the reliability of stellar population fitting, is the χ^2 value. The χ^2 value can best be evaluated by looking at χ^2 plots. Figure 3.2 shows the χ^2 maps of the SSP fit for the inner bin of NGC0410 as an example.

For comparison, a galaxy with a lower SSP age estimate (NGC1779) and a galaxy with a lower metallicity estimate (NGC5846) are also shown as examples. Figure 3.3 shows the χ^2 plots of the SSP fit for the inner bin of NGC1779 and Figure 3.4 shows that of NGC5846.



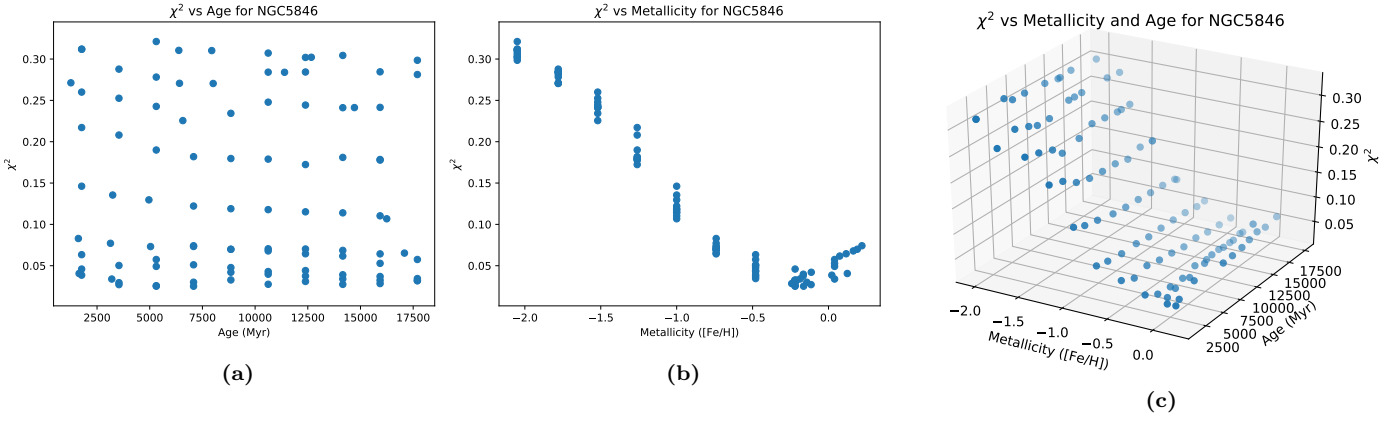
(a) **(b)** **(c)**

Figure 3.2: *Plots of the χ^2 values of the SSP fits for NGC0410 inner bin for different metallicities and ages. The solution of the SSP fit is an age of 16468 Myr and [Fe/H] = 0.10 with χ^2=0.104.*



(a) **(b)** **(c)**

Figure 3.3: *Plots of the χ^2 values of the SSP fits for NGC1779 inner bin for different metallicities and ages. The solution of the SSP fit is an age of 5876 Myr and [Fe/H] = 0.20 with χ^2=0.052.*



(a) **(b)** **(c)**

Figure 3.4: *Plots of the χ^2 values of the SSP fits for NGC5846 inner bin for different metallicities and ages. The solution of the SSP fit is an age of 17780 Myr and [Fe/H] = -0.23 with χ^2=0.032.*

In Figures 3.2, 3.3 and 3.4, it is evident that the age estimates from the stellar population fits do not converge. This, together with the large errorbars and discrepancies seen in the results, indicate a problem for constraining the SFH

of galaxies. The problems are evident in the results of all four models used for fitting (Tables 3.4, 3.5, 3.6, 3.7 and 3.8), therefore indicating a problem with the data or analysis rather than a particular stellar population model. In the following section, a study is done to investigate the wavelength that we used.

3.5 Mock spectra analysis

From the MILES website and the online webtools, several mock spectra were extracted and analysed using ULySS for the same wavelength range as the real data (4600 Å to 6200 Å). The SFHs of the mock spectra were self-defined. There were two components in all the SFHs: an old component (with an age of 16 Gyrs, metallicity of [Fe/H] = –1.2, IMF slope of 1.3 and a variable mass fraction) and a young component (with a variable age between 200 and 2000 Myrs, a fixed metallicity of [Fe/H] = 0.2, IMF slope of 1.3 and a variable mass fraction of between 1% and 5%).

SSP and CSP fits were done for all the mock spectra and presented in Table 3.9 to test whether we can recover the SFH that we used to make the mock spectra within this wavelength range. The initial guess for the two components of the CSP: an old component with an age guess of 15 Gyrs and a young component of 200 Myrs (the same as for the real data). Table 3.9 summarises the findings of the mock spectra SSP and CSP fits.

Age, light and mass fraction contribution of young stellar component					
	1%	**2%**	**3%**	**4%**	**5%**
			200 Myr		
SSP	2496 ± 368	1799 ± 109	1301 ± 27	1233 ± 29	1148 ± 46
CSP	**216 ± 164**	**201 ± 68**	**200 ± 53**	**200 ± 45**	**201 ± 42**
Light %	22 ± 0	34 ± 0	41 ± 0	47 ± 0	52 ± 0
			400 Myr		
SSP	3775 ± 329	2315 ± 151	1884 ± 121	1343 ± 33	1304 ± 25
CSP	1574 ± 312	**287 ± 90**	**296 ± 53**	**341 ± 67**	**347 ± 66**
Light %	37 ± 3	25 ± 0	30 ± 0	37 ± 0	41 ± 0
			800 Myr		
SSP	4911 ± 509	4126 ± 403	3450 ± 327	3195 ± 334	2885 ± 384
CSP	2539 ± 644	1561 ± 358	**321 ± 59**	**449 ± 153**	**462 ± 172**
Light %	18 ± 2	32 ± 3	18 ± 0	22 ± 0	25 ± 0
			1200 Myr		
SSP	5266 ± 615	5050 ± 580	4582 ± 464	4347 ± 462	4254 ± 427
CSP	1653 ± 668	1634 ± 739	1995 ± 422	1986 ± 573	1534 ± 241
Light %	16 ± 2	19 ± 2	30 ± 2	32 ± 2	35 ± 3
			1600 Myr		
SSP	5305 ± 616	5164 ± 558	4894 ± 536	4525 ± 497	4328 ± 461
CSP	2785 ± 885	1624 ± 810	2698 ± 311	220 ± 182	322 ± 79
Light %	32 ± 2	17 ± 2	39 ± 2	12 ± 0	13 ± 0
			2000 Myr		
SSP	5853 ± 632	5292 ± 582	5214 ± 544	5190 ± 521	4899 ± 547
CSP	1633 ± 827	2014 ± 524	1998 ± 519	167 ± 78	170 ± 62
Light %	14 ± 2	24 ± 3	26 ± 3	12 ± 0	12 ± 0

Table 3.9: *A summary of the SSP and CSP fit results of the mock spectra as described above. The results in bold are where we recover the SFHs used as input to construct the mock spectra.*

We indicate the cases where we can confidently recover the young stellar component with this wavelength range used to create the mock spectra in bold. For a young stellar component of 400 Myr, the mass fraction of the young component needs to be $\geq 2\%$ of the mass to be detected confidently. For a young component of 800 Myr, the young component must contribute $\geq 3\%$ to be detected confidently. Also note that the light fraction due to these will be about 18% or higher. For populations older than 1 Gyr, the younger component cannot be isolated with confidence.

The following table shows the results, using mock spectra for a similar test, by Loubser et al. (2016). In this paper, the wavelength range was 3500 to 4900 Å. The mock spectra were also analysed using ULySS, with a Monte Carlo simulation of n = 200, young components as indicated in Table 3.10 with a metallicity of [Fe/H] = 0.20 and an old population of 15 Gyr with a metallicity of [Fe/H] = -0.5.

Age, light and mass fraction contribution of young stellar component					
	1%	**2%**	**3%**	**4%**	**5%**
			200 Myr		
SSP	4550 ± 200	3066 ± 93	1602 ± 47	1324 ± 25	1160 ± 19
CSP	**208 ± 35**	**205 ± 19**	**208 ± 16**	**205 ± 13**	**206 ± 12**
			400 Myr		
SSP	6699 ± 402	3994 ± 300	3078 ± 114	2770 ± 157	1675 ± 90
CSP	**394 ± 154**	**369 ± 54**	**368 ± 40**	**368 ± 32**	**377 ± 30**
			800 Myr		
SSP	12085 ± 937	9618 ± 854	8659 ± 753	7778 ± 534	6273 ± 358
CSP	**1396 ± 760**	**1138 ± 315**	**1005 ± 217**	**919 ± 180**	**819 ± 142**
			1200 Myr		
SSP	**13444 ± 831**	**11863 ± 911**	**10619 ± 918**	9885 ± 893	9383 ± 837
CSP	3094 ± 9893	2495 ± 4840	2378 ± 5336	**1698 ± 574**	**1591 ± 339**
			1600 Myr		
SSP	**13570 ± 851**	**12608 ± 861**	**12321 ± 869**	**11482 ± 882**	10944 ± 905
CSP	3416 ± 3226	3428 ± 2854	2403 ± 1340	2839 ± 1112	**1612 ± 759**
			2000 Myr		
SSP	**14187 ± 874**	**13627 ± 859**	**12924 ± 901**	**12365 ± 861**	**11786 ± 874**
CSP	2409 ± 5894	3520 ± 5312	3463 ± 3123	3029 ± 2068	2606 ± 1844

Table 3.10: *A summary of the SSP and CSP fit results of the mock spectra in Loubser et al. (2016) for the wavelength range of 3500 Å – 4900 Å. The results in bold indicate the fit (SSP or CSP) that best fit the mock spectrum.*

When comparing Tables 3.9 and 3.10, it can be seen that smaller mass fractions of young stellar populations, and older young populations can be recovered if a wavelength range of 3500 Å to 4900 Å (Table 3.10) is used instead of 4600 Å to 6200 Å (Table 3.9); e.g. 1% fraction of 400 Myr can be recovered when using a wavelength range of 3500 Å to 4900 Å, whereas a 1% fraction of 400 Myr cannot be recovered using a wavelength range from 4600 Å to 6200 Å. This is most probably because the wavelength range used in Loubser et al. (2016) is much more efficient for identifying young components since it includes a bigger part of the blue-end of the spectrum where several age sensitive indices reside. Therefore, our analysis and results emphasize that more of the blue-end indices should be included in any analysis where an accurate description of possible star formation beyond 1 Gyr (or small mass fractions) is necessary.

This is the biggest problem with this dataset and also why the errors on the stellar populations cannot be improved effectively.

3.6 Brightest cluster galaxies

The same method (as in subsections 3.1 and 3.2) was used in Loubser et al. (2016) for 32 BCGs to identify recent star formation episodes. Figure 3.5 (obtained from Loubser et al., 2016, their figure 10), shows a comparison of the SSP ages of the inner aperture of 19 of these BCGs, plotted against the minimum ratio of cooling time (t_c) vs free-fall time (t_{ff}). It can be seen that the BCGs with prominent younger stellar components are below the threshold for precipitation of $t_c/t_{ff} \sim 10$. This is the threshold under which the radiatively cooling gas is subject to local thermal instabilities. However, detailed analysis of the BGG data with a different wavelength range showed that the SSP/CSP results obtained from data with a wavelength range that excludes the age-sensitive blue indices can not be reliably interpreted. Therefore we can not (with this data) conclude how SF in BGGs compare with SF in BCGs, and how the environmental thresholds for SF seen in clusters compare to those in groups.

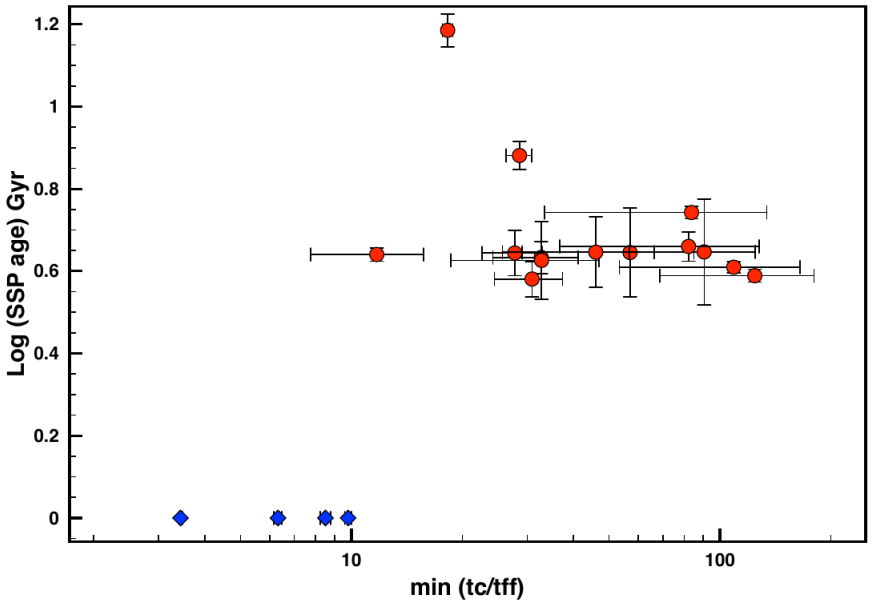


Figure 3.5: *Figure obtained from Loubser et al. (2016), their figure 10. The SSP ages of the inner apertures of 19 of the 32 BCGs that were analysed are plotted against the minimum cooling time (t_c) vs free-fall time (t_{ff}) ratio. The BCGs in blue have prominent young stellar components and are shown at Log (SSP age) = 0 for reference.*

For interest, we also show Figure 3.6 (taken from Loubser et al., 2018, their figure 2a) where the central velocity dispersion and K-band luminosity for the combined sample of 55 BGGs and BCGs are plotted. From this figure, it can be seen that the two populations, BGGs and BCGs, deviate in their Faber-Jackson relations[3]. Therefore, we do not expect BGGs to merely be the lower mass extensions of BCGs, but that they have different relations/properties[4].

[3]The Faber-Jackson relation, which was first introduced in Faber & Jackson (1976), is a power-law between the luminosity and velocity dispersion of elliptical galaxies.

[4]Some of this work is published in Havenga et al. (2019).

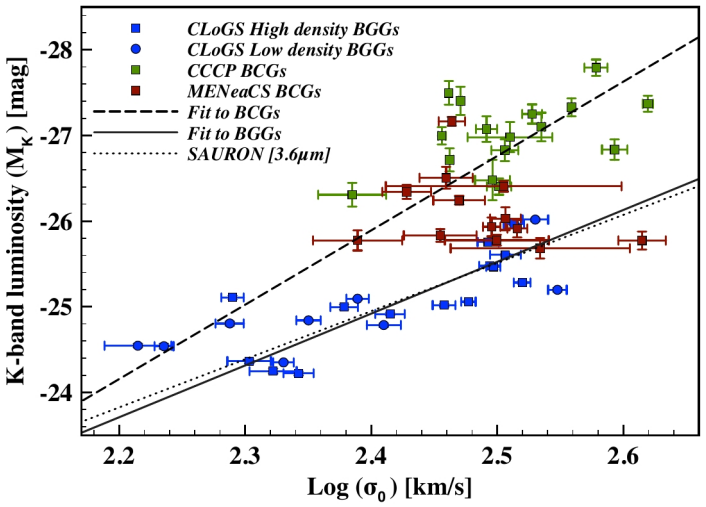


Figure 3.6: *The BGGs are plotted in blue, while the BCGs are plotted in green and red. Note the two different Faber-Jackson relations (FJRs) for the two classes. Figure from Loubser et al. (2018).*

The most important conclusion from this chapter is that the wavelength range is very important for stellar population study.

CHAPTER 4

Analysis of SSP models

During the stellar population analysis described in the previous chapter, it was found that for some galaxies there appears to be a very distinct mismatch in one part of the spectrum. Figure 4.1 shows NGC0410 as an example, and clearly shows a feature that is not well fitted by the model (around 5900 Å). The absorption line is that of NaD, which is strongly dependent on the IMF used in the models, according to Spiniello et al. (2012). Some articles have been written about the NaD over- or under-abundance in some galaxies (eg. La Barbera et al., 2017 and Nedelchev, 2016). According to Schwartz & Martin (2004), this phenomenon can also be seen in dwarf galaxies. This remarkable discrepancy occurs in 17 of the BGGs in this study sample and must be investigated further. This chapter is dedicated to finding out how galaxy spectra are affected by both α-enhancements and Na-enhancements, at different metallicities, ages and IMF slopes.

The aim of this chapter is therefore to investigate whether α-enhancements or different IMF types and -slopes will fit this feature better. We attempt to rather understand the different stellar population models and galaxy spectra than to just fit all 23 galaxies again to all the different models. This will help us to understand how the different parameters influence the spectra and NaD features at all ages and metallicities.

In order to understand why this is seen in 17 BGGs, we first investigate whether this mismatch is due to α-enhancements.

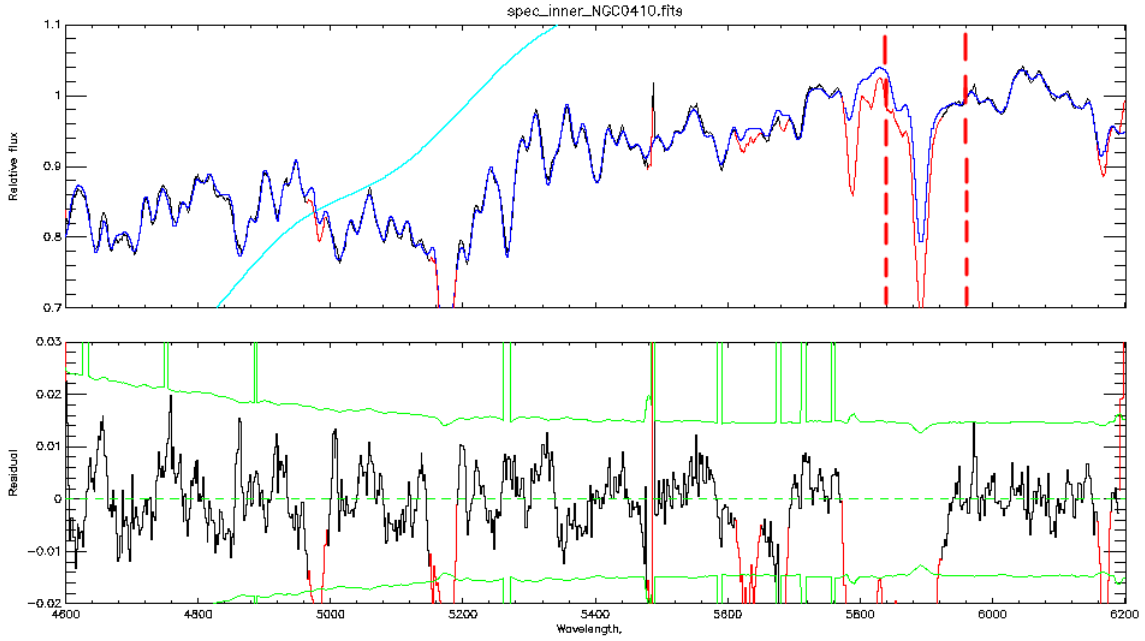


Figure 4.1: *This is the spectrum of NGC0410 (inner aperture). The NaD feature can be seen at 5900 Å (between the red dashed lines). The colours have the same meaning as in Figure 2.2. Just note that the observed spectrum and the model are almost indistinguishable, except for the NaD feature and other small variations.*

Some plots were made in this section, looking only at the wavelength range that is used in the SPS. These can be seen at https://drive.google.com/file/d/1fYM86LJDOVYFatcHAvurBHF7m1zaABgC/view?usp=sharing.

4.1 Analysis of model with the use of α-enhancements

4.1.1 What is α-enhancement?

Firstly, we need to define α-elements. These are elements that are built from the addition of He (α) particles, which include elements such as O, Ne, Mg and Si. α-elements are released by core collapse supernovae within massive galaxies. Type Ia supernova, on the other hand, releases particles, mostly consisting of Fe, but with a small temporal delay with regard to core collapse supernovae (Segers et al., 2016).

The [O/Fe] mass ratio in the ejected material of a simple stellar population, for example, decreases with time, according to Wiersma et al. (2009), with a ratio of 0.3 dex from 10 Myr to 10 Gyr. α-enhancement (the α-element-to-iron abundance ratio when compared to the solar abundance ratio) has therefore been used to characterise the timescales of star formation in massive elliptical galaxies. [α/Fe] can be determined using the following equation:

$$[\alpha/Fe] = \log(\alpha/Fe) - \log_{\odot}(\alpha/Fe) \tag{4.1}$$

In this equation, $\log_{\odot}(\alpha/Fe)$ indicates the logarithm of the α-element-to-iron ratio of the sun and $\log(\alpha/Fe)$ that of the galaxy under consideration.

It is found that the α-enhancement increases with stellar mass or velocity dispersion of galaxies. This is interpreted as galactic 'downsizing' (Segers et al., 2016). According to Segers et al. (2016), AGN feedback leads to an increasing [α/Fe] ratio as galaxy stellar mass and age increase.

4.1.2 Analysis of the model

The model that was used in ULySS is described by Vazdekis et al. (2010). This model is based on the MILES stellar library. To analyse the model, the online webtool to tune SSP models was used to obtain SSP models with different input parameters [1]. The basic input parameters were as follows:

```
SSP Models: MILES
Isochrone: BaSTI

Output parameters
Initial wavelength (angstroms): 3540.5
Final wavelength (angstroms):7409.6
Wavelength step (angstroms/pix): 0.1
Sampling: Linear
Redshift (z): 0.02
Resolution: 4.8
Format: ASCII
```

It is important to note that the MILES group has three different options regarding the α-enhancements. These are: **Base** [α/**Fe**] (which will be referred to as Base α), [α/**Fe**] = **+0.00** (Ep0.00) and [α/**Fe**] = **+0.40** (Ep0.40). The difference between the Base α and the Ep0.00 models is described in La Barbera et al. (2017) and is summarised as follows:

The Base α model is built from solar-scaled isochrones, which do not take into account the specific elemental abundance ratios of the spectra. These base models do, however, lack consistency when going to lower metallicities. For the Ep0.00 model, self-consistent models that are scaled-solar at all metallicities, with the use of spectra from Coelho et al. (2005, 2007), are used. However, as will be seen in the following sections, the differences between these two models are mostly minuscule. The only noticeable difference between these two models can be seen in Figure 4.9, which also shows the difference between these models as described by Vazdekis et al. (2015) and La Barbera et al. (2017).

The comparison that we want, however, is between the above-mentioned two models (Base α and Ep0.00) and the Ep0.40 model.

4.1.3 Varying α-enhancement

For the analysis of the model, we first kept the age and metallicity constant and then varied the α-enhancement. The age was chosen as 14.0 Gyr and the metallicity as $[Fe/H] = 0.15$ (this is typical for the galaxies that we analysed for this research).

[1] This can be found at www.iac.es/proyecto/miles/pages/webtools/tune-ssp-models.php

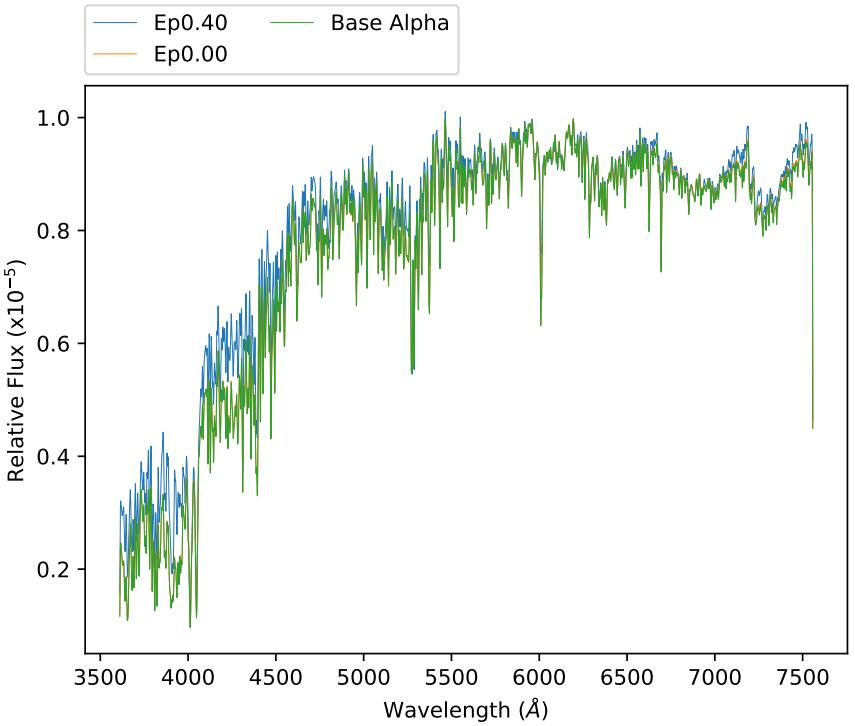


Figure 4.2: *The MILES-model for an SSP of 14.0 Gyr and [Fe/H]=0.15 with variable α-enhancement. The y-values are normalised with respect to the maximum value of the Base model spectrum.*

The Base α and the Ep0.00 are almost indistinguishable, as this is close to solar metallicity, but there are some small variations between the Base α and the Ep0.40, especially in the blue-end of the spectrum. The Mg absorption lines can be seen in the wavelength range between 5200 and 5400 Å (shown in Figure 4.3).

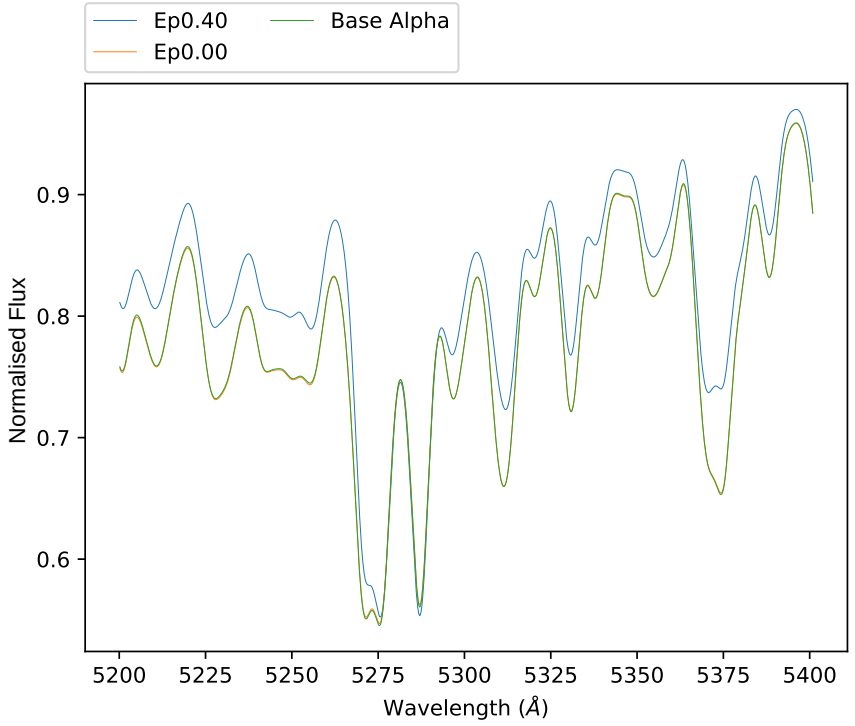


Figure 4.3: *The MILES-model for an SSP of 14.0 Gyr and [Fe/H]=0.15 with variable α-enhancement. The y-axis is normalised with respect to the maximum value of the Base α spectrum and the wavelength range is from 5200 Å to 5400 Å.*

In Figure 4.3, the Mg absorption lines were magnified to see the influence of the α-enhancement on specifically these absorption lines. It is interesting to see that the two models' Mg absorption lines are very similar, but the rest of the spectrum around these absorption lines has greater differences, especially in the relative flux. However, this feature is not important for the discussion yet. Figure 4.4 shows how the NaD feature is fitted by the different α-enhanced models.

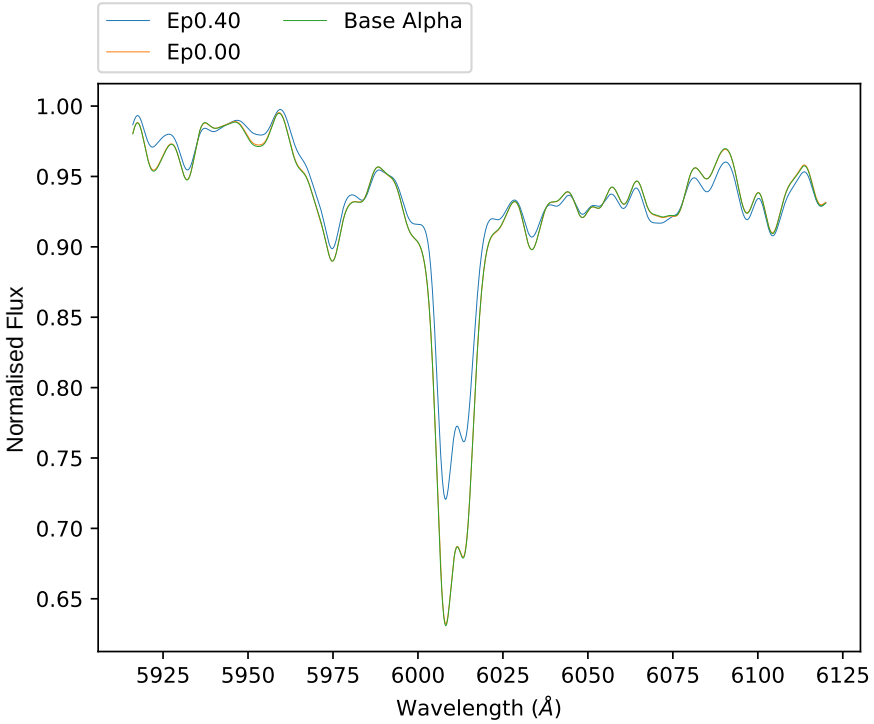


Figure 4.4: *The MILES-model for an SSP of 14.0 Gyr and [Fe/H]=0.15 with variable α-enhancement. The y-axis is normalised with respect to the maximum value of the Base α spectrum and the wavelength range is from 5916 Å to 6120 Å.*

As can be seen in this figure, the Ep0.40 α-enhanced model gives a spectrum with a shallower NaD feature. Because of the overabundance of sodium in the galaxies, this will be an even worse fit to the galaxy spectrum.

4.1.4 Varying α-enhancement and varying age

As can be seen from Section 1.6.1, the age of a galaxy has the dominant influence on its spectrum. Since α-enhancements do not seem to have a large influence on NaD at 15 Gyr, for completeness we do a similar comparison between Ep0.00 and Ep0.40 at other ages.

In Figure 4.5, the Ep0.40 α-enhanced model's flux is much higher than that of the base model, especially in the blue end of the young spectrum ($<$ 0.1 Gyr). From 0.2 Gyr, the enhanced model shows an overcompensation in the flux in the blue end, but then an under-compensation in the red end. This inconsistency can be seen until 0.7 Gyr. Then the enhanced model again has a higher flux than that of the base model, increasing the difference between the two, with the biggest disagreement in 1.0 Gyr spectra. The two models coincide at the 1.25 Gyr spectrum. Then the difference varies until about 4.5 Gyr. Between 4.5 Gyr up to about 14 Gyr, the difference between the models stays the same, with the flux of the α-enhanced model higher than that of the base model.

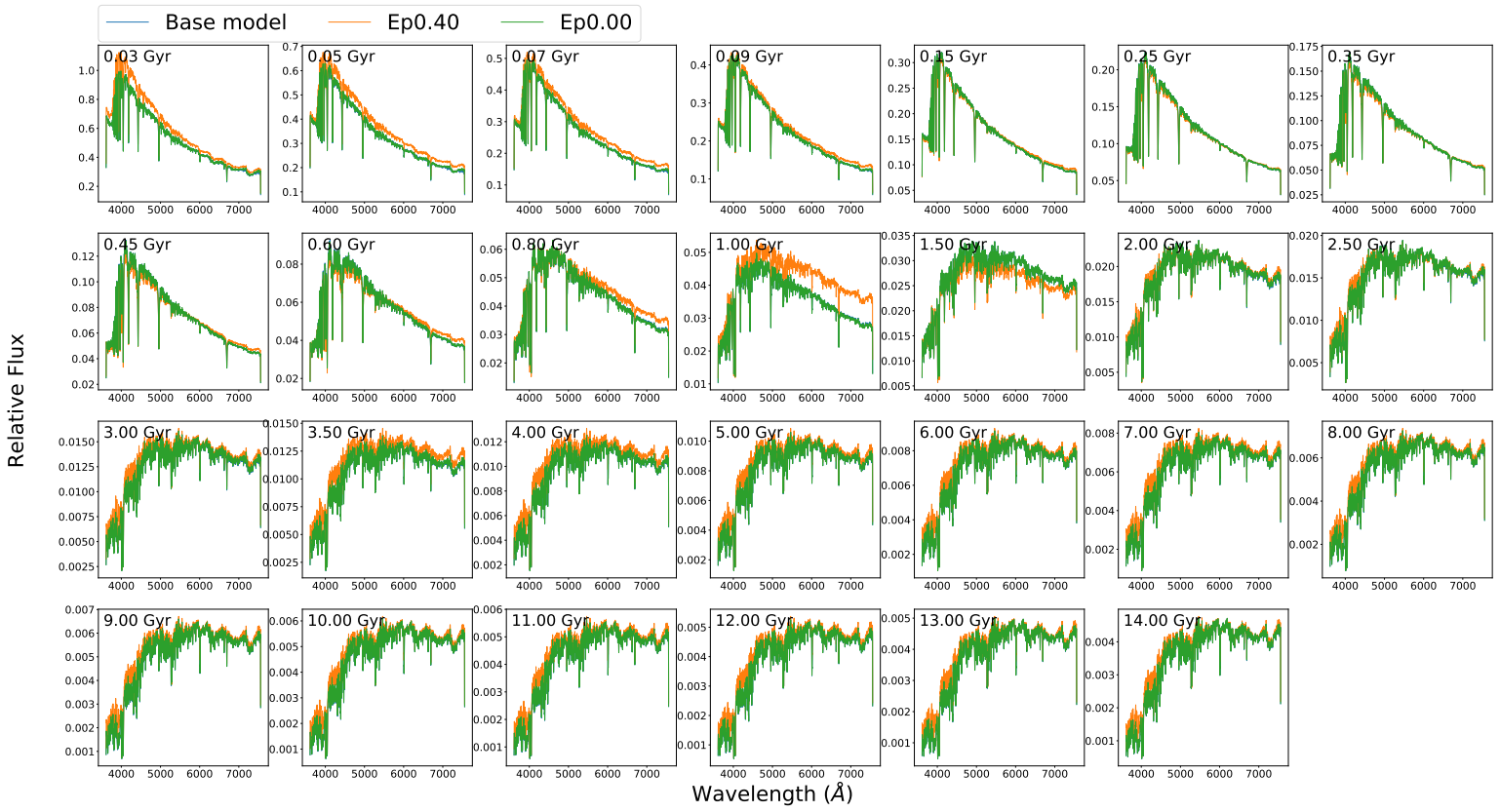


Figure 4.5: *The MILES-model for an SSP of [Fe/H]=0.15 with variable α-enhancement as well as variable age (increasing from 0.03 Gyr to 14.0 Gyr). The y-axis is normalised with respect to the maximum value of the Base α spectrum of the 0.03 Gyr model.*

In Figure 4.6, we zoomed into the NaD feature. As can be seen, the flux of the enhanced model is much higher than that of the base model. From 0.25 Gyr, however, the continuum of the enhanced model varies between lower and higher than the base model, whereas the NaD feature still stay the most shallow in the Ep0.40 enhanced model. It can therefore be seen that the NaD feature is not better fit by the α-enhanced model when looking at the NaD feature and the different ages specifically.

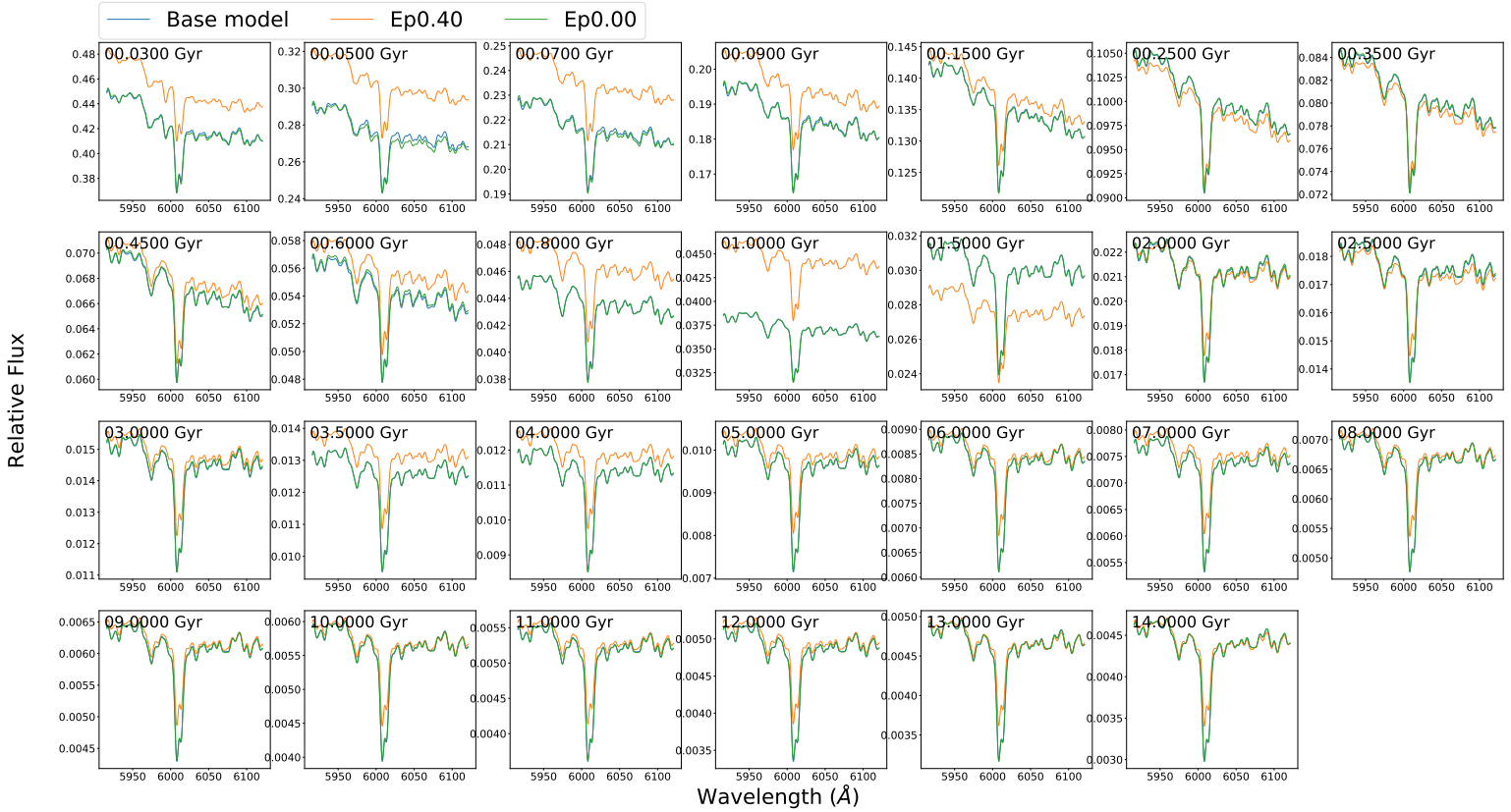


Figure 4.6: *The MILES-model for an SSP of [Fe/H]=0.15 with variable α-enhancement as well as variable age (increasing from 0.03 Gyr to 14.0 Gyr). The y-axis is normalised with respect to the maximum value of the Base α spectrum of the 0.03 Gyr model and the wavelength range is from 5916 Å to 6120 Å. The NaD absorption lines can be seen at the shifted wavelength of 6007.45 Å and 6013.84 Å (z = 0.02, rest wavelengths are 5889.95 Å and 5895.92 Å).*

4.1.5 Varying α-enhancement and varying metallicity

In this section, it is important to note that we already discussed the influence of metallicity on the individual galaxy spectrum in Section 1.6.2. We also already saw the influence of the α-elements on the NaD absorption doublet at a metallicity of [Fe/H]=0.15. For completeness, we will look at the influence of the α-enhancements on the spectra and specifically on the NaD feature at different metallicities.

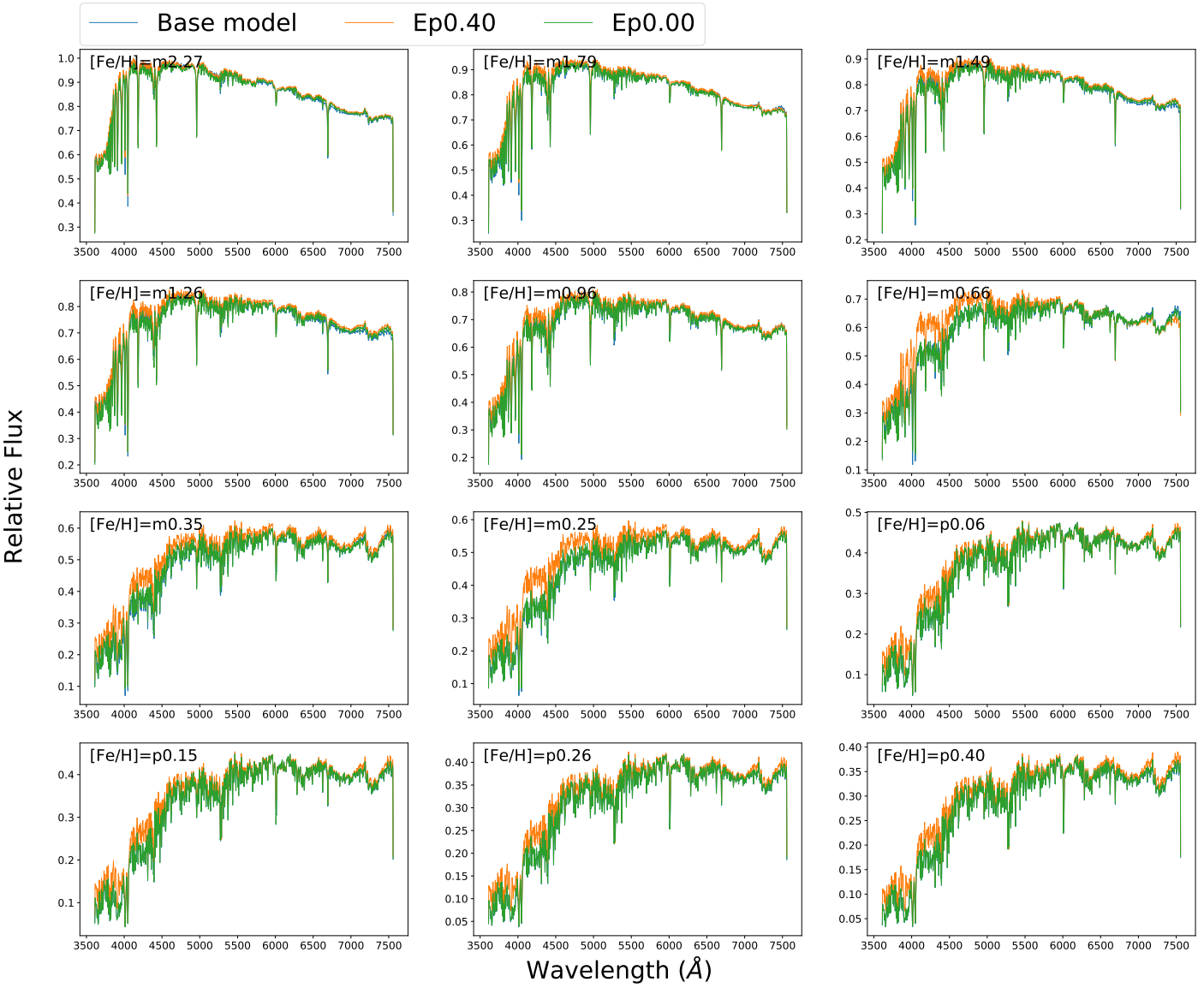


Figure 4.7: *The MILES-model for an SSP of 14.0 Gyr with variable α-enhancement as well as variable metallicity (increasing from $[Fe/H] = -2.27$ to $[Fe/H] = 0.40$). The y-axis is normalised with respect to the maximum value of the Base-α spectrum of the $[Fe/H] = -2.27$ model.*

In Figure 4.7, we look at the part of the spectrum that we analysed. In the top left subfigure, where the metallicity $[Fe/H] = -2.27$, we can see that the α-enhanced model has a higher relative flux than the base model. This continues to be the trend through the metallicity range of $[Fe/H] = -2.27 \rightarrow -0.96$, but with increasing difference between the relative flux of the enhanced model and the base model, specifically in the blue-end of the spectrum. However, at $[Fe/H] = -0.66$, the red-end of the spectrum has a higher base flux than the corresponding enhanced model, while the blue-end still remains with the enhanced model having a higher flux than the base model. In the metallicity range of $[Fe/H] = -0.35 \rightarrow +0.40$, the trend seems to be the same as with the lowest metallicity range, with the enhanced model at a higher relative flux than the base model, with a bigger difference in flux in the blue end of the spectrum.

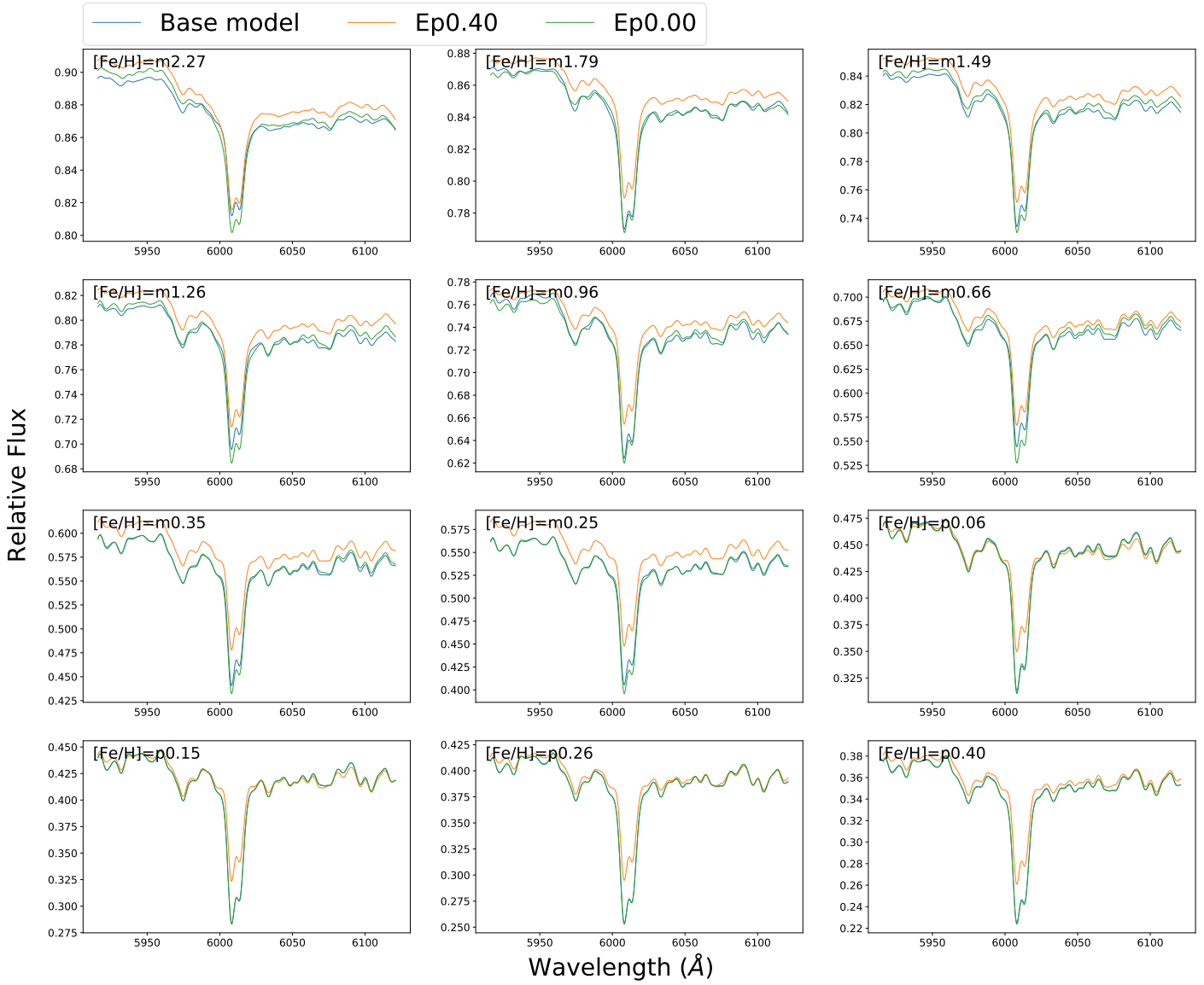


Figure 4.8: *The MILES-model for an SSP of 14.0 Gyr with variable α-enhancement as well as variable metallicity (increasing from $[Fe/H] = -2.27$ to $[Fe/H] = 0.40$). The y-axis is normalised with respect to the maximum value of the Base-α spectrum of the $[Fe/H] = -2.27$ model and the wavelength range is from 5916 Å to 6120 Å. The NaD absorption doublet can be seen at the shifted wavelength of 6007.45 Å and 6013.84 Å (rest wavelengths are 5889.95 Å and 5895.92 Å).*

In Figure 4.8, the α-enhanced model shows a shallow NaD absorption feature when compared to the base models. It is therefore clear that at all the metallicities, the α-enhanced model is worse at fitting the NaD feature than the base models.

Difference between Ep0.00 and the Base α model

We can also, at some metallicities, see a small difference between the Ep0.00 and the Base α model. The difference between the Base α model and the Ep0.00 model can be seen more clearly in Figure 4.9 when looking at the Mg absorption feature, but more specifically when looking at Figure 4.10.

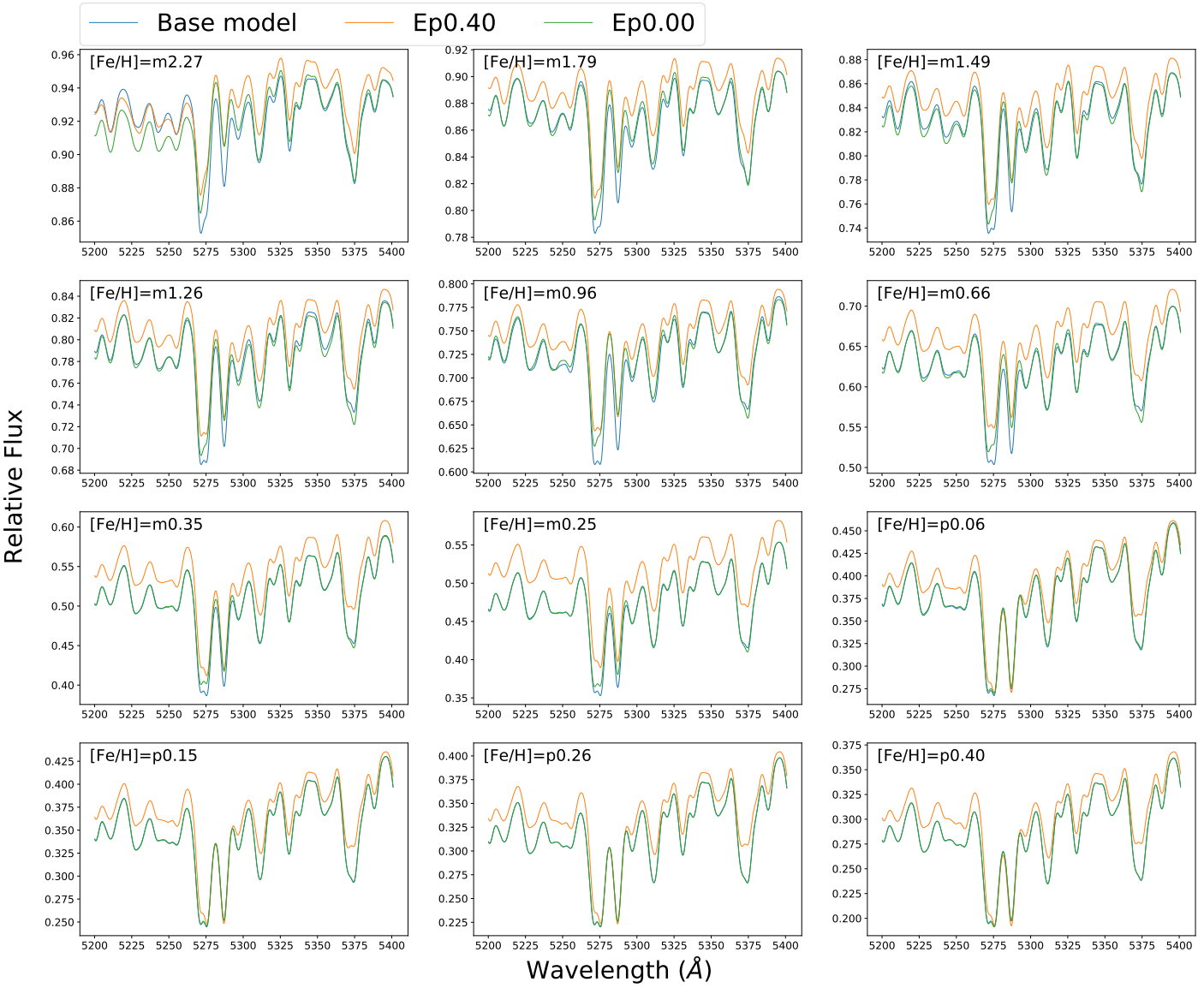


Figure 4.9: *The MILES-model for an SSP of 14.0 Gyr with variable α-enhancement as well as variable metallicity (increasing from $[Fe/H] = -2.27$ to $[Fe/H] = 0.40$). The y-axis is normalised with respect to the maximum value of the Base-α spectrum of the $[Fe/H] = -2.27$ model and the wavelength range is from 5200 Å to 5400 Å. The Mg absorption line can be seen at the shifted wavelength of 5280.2 Å (rest wavelength is 5176.7 Å).*

In Figure 4.9, the spectra are zoomed in to one of the most prominent α-element absorption lines in this wavelength range, namely Mg. Interesting to notice here, is that the difference between the Ep0.00 model and the base model actually surfaces, but only in the metallicities lower than solar metallicity. The differences between these two also increase as one goes from $[Fe/H] = -0.25$ to $[Fe/H] = -2.27$.

The big differences between the spectra at $[Fe/H] = -2.27$ and $[Fe/H] = 0.40$ are shown in Figure 4.10. Here, one can see that the Base α model has a higher relative flux than that of Ep0.00 at the blue-end, but from the Mg absorption feature, the Base α model drops to a lower relative flux than the Ep0.00 model.

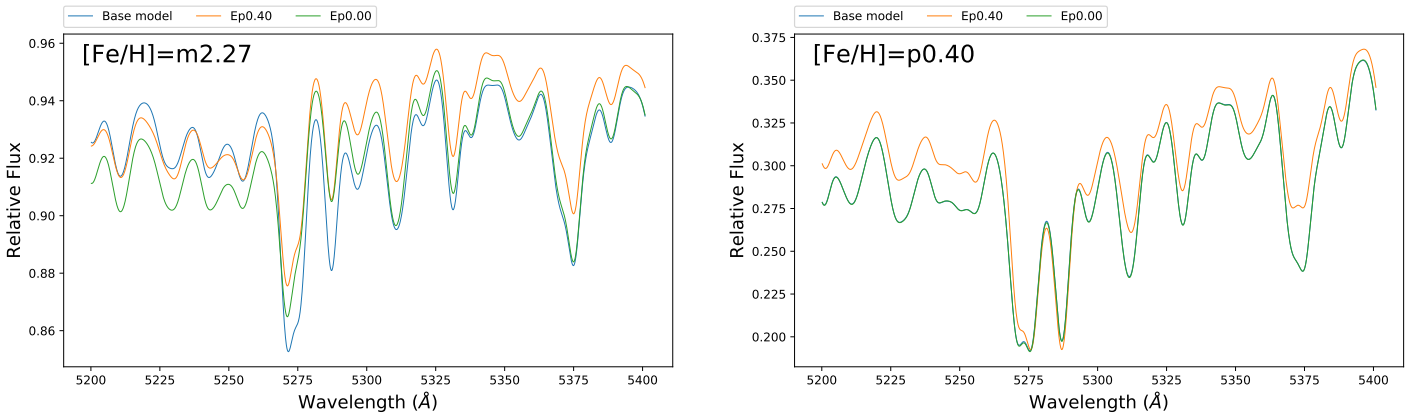


Figure 4.10: *The same plots as in Figure 4.9, but only at* $[Fe/H] = -2.27$ *(left) and* $[Fe/H] = 0.40$ *(right).*

The final conclusion is that α-enhancements underestimate the NaD feature even more, showing a shallower absorption feature. Therefore, using α-enhanced models is not the solution, but worsens the problem.

4.2 Analysis of model with the use of [Na/Fe]-enhancements

4.2.1 What is [Na/Fe]-enhancement?

The spectra used in this project have a wavelength range of 4600 Å to 6200 Å. The NaD doublet at 5889.950 Å and 5895.924 Å dominates the sodium emission spectrum. [Na/Fe]-enhanced models have recently been developed due to the underabundance of [Na/Fe] in some dwarf elliptical galaxies (Mentz, 2018) as well as overabundance in some early-type galaxies (La Barbera et al., 2017). La Barbera et al. (2017) also investigated the need for a non-universal IMF description, rather than the popular universal IMF, as the [Na/Fe] abundance depends on the IMF. According to La Barbera et al. (2017), sodium is more abundant when the IMF is bottom heavier (i.e. more low-mass stars).

To do this analysis of the model, the [Na/Fe]-enhanced models were downloaded from the MILES website. These enhanced models were derived from the new E-MILES library[2]. Note that these models are constructed for zero redshift galaxies, and the wavelength step of these models is 0.9 Å.

These models are used to investigate the new [Na/Fe] enhancements in the models and its influence on the NaD feature and whether this will solve the mismatch or not.

[2]This can be found at ftp://ftp.iac.es/Other_predictions/

4.2.2 Varying [Na/Fe]-enhancement

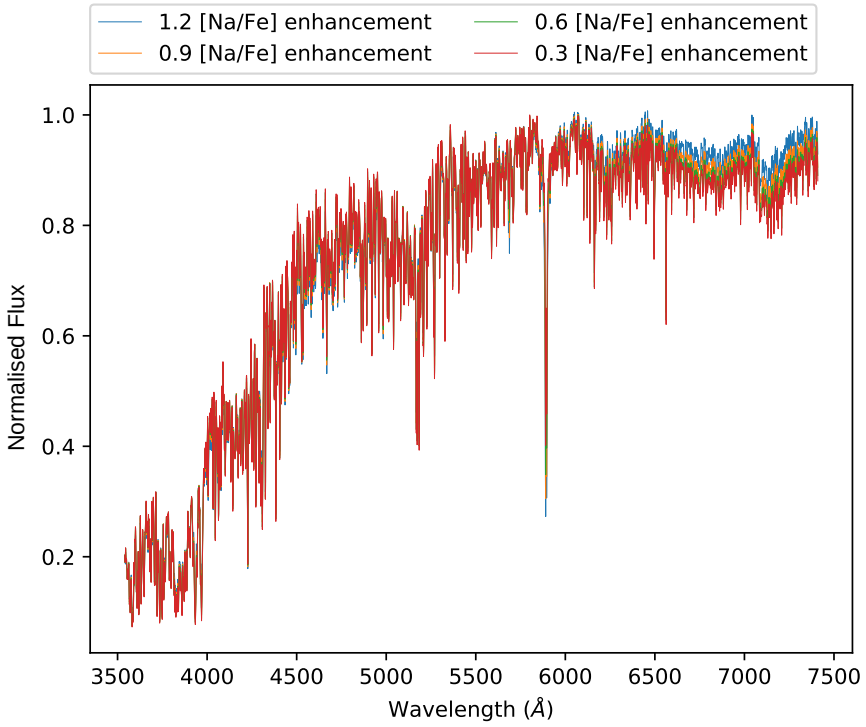


Figure 4.11: *The E-MILES-model for an SSP of 14.0 Gyr and [Fe/H]=0.15 with variable [Na/Fe]-enhancement ($[Na/Fe] = +0.3, 0.6, 0.9, 1.2$). The y-axis is normalised with respect to the maximum value of the $[Na/Fe] = +0.3$ enhanced spectrum.*

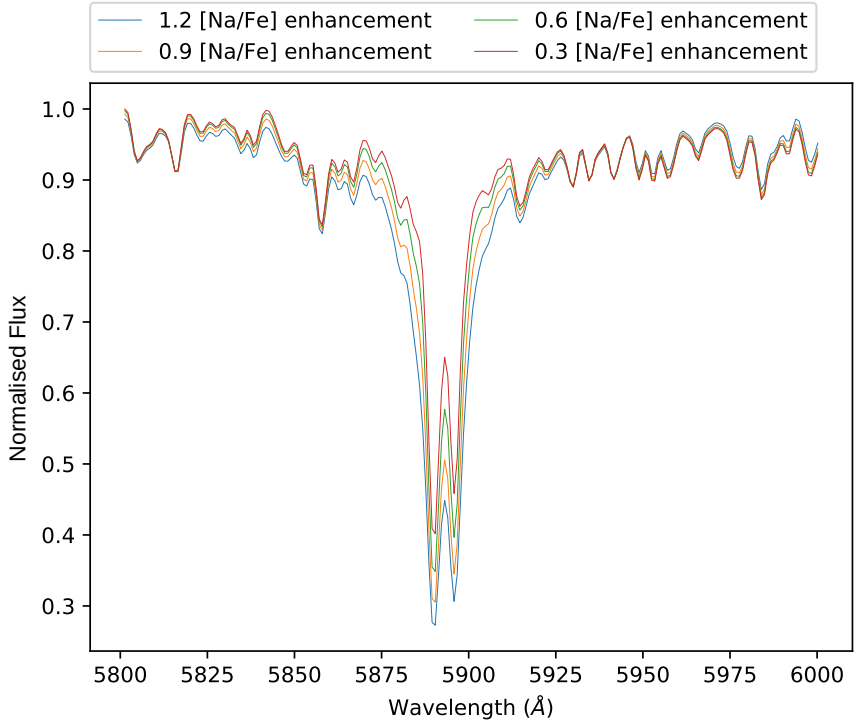


Figure 4.12: *The E-MILES-model for an SSP of 14.1 Gyr and [Fe/H]=0.22 with variable [Na/Fe]-enhancement. The y-axis is normalised with respect to the maximum value of the $[Na/Fe] = +0.3$ enhanced spectrum and the wavelength range is from 5800 Å to 6000 Å. The well-known NaD double absorption lines can be seen at 5889.95 Å and 5895.92 Å.*

Figures 4.11 and 4.12 show small differences between the models.

4.2.3 Varying [Na/Fe]-enhancement and varying age

For completeness, we repeat the analysis for all ages from 1 Gyr to 17.78 Gyr. In Figure 4.13, the changes still remain small, but there seems to be a difference between the enhanced models at the red-end of the wavelength range. This specific difference (at the red-end of the wavelength range) between the different enhanced models also increases as we go from the youngest galaxies to the oldest galaxies.

Figure 4.14 specifically shows the NaD doublet. The difference between the different models is only in the relative flux, and these differences, contrary to the red-end wavelength range, decrease as the age of the SSP increases. The most enhanced model also shows the deepest NaD absorption feature. The [Na/Fe] = 1.2 enhanced model has the deepest NaD absorption feature and will therefore be a better solution to the discrepancy between the data and the current stellar population models.

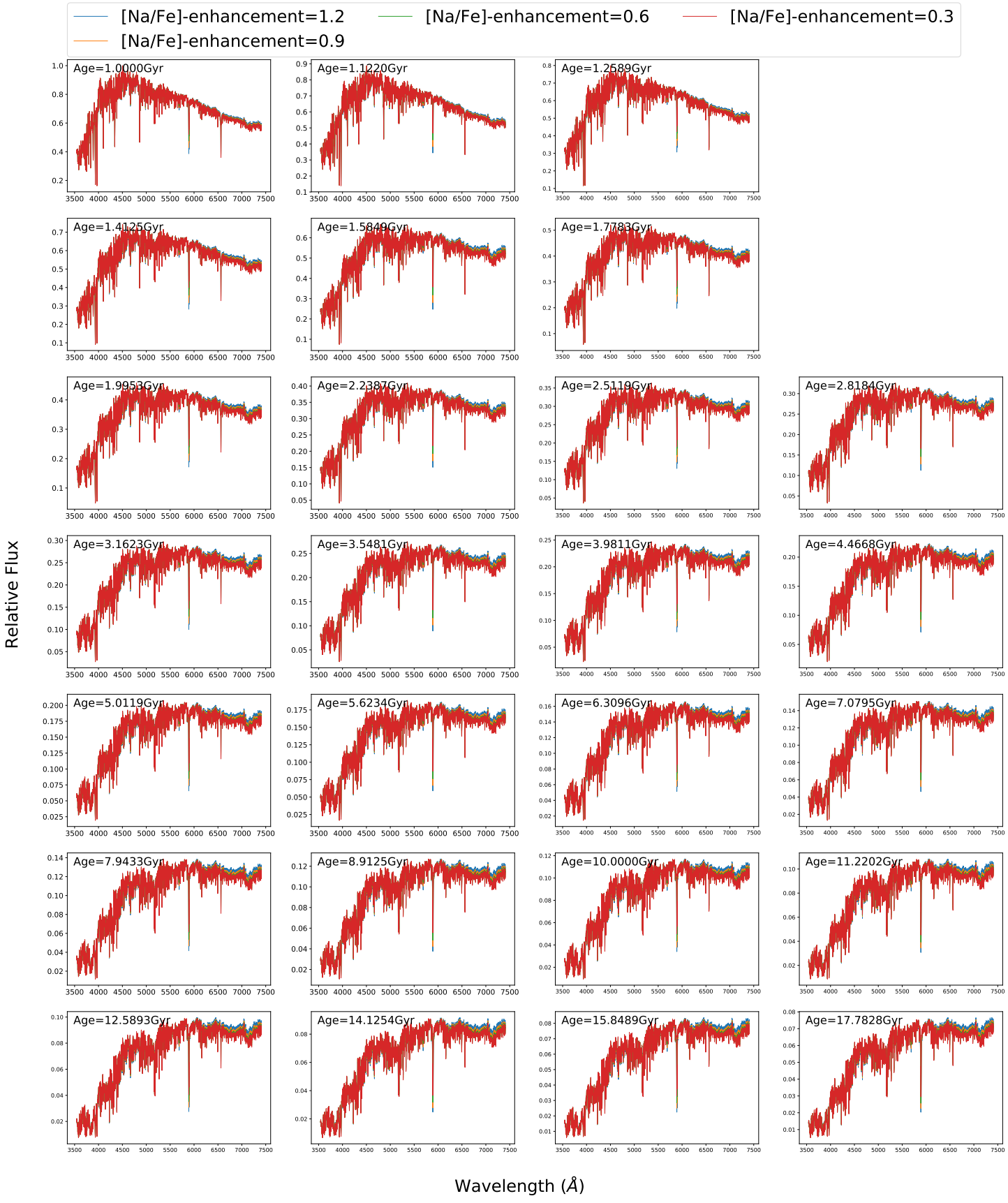


Figure 4.13: *The E-MILES-model for an SSP of [Fe/H]=0.22 with variable [Na/Fe]-enhancement as well as variable age (increasing from 1 Gyr to 17.78 Gyr). The y-axis is normalised with respect to the maximum value of the spectrum with [Na/Fe] = 0.3 and age of 1 Gyr.*

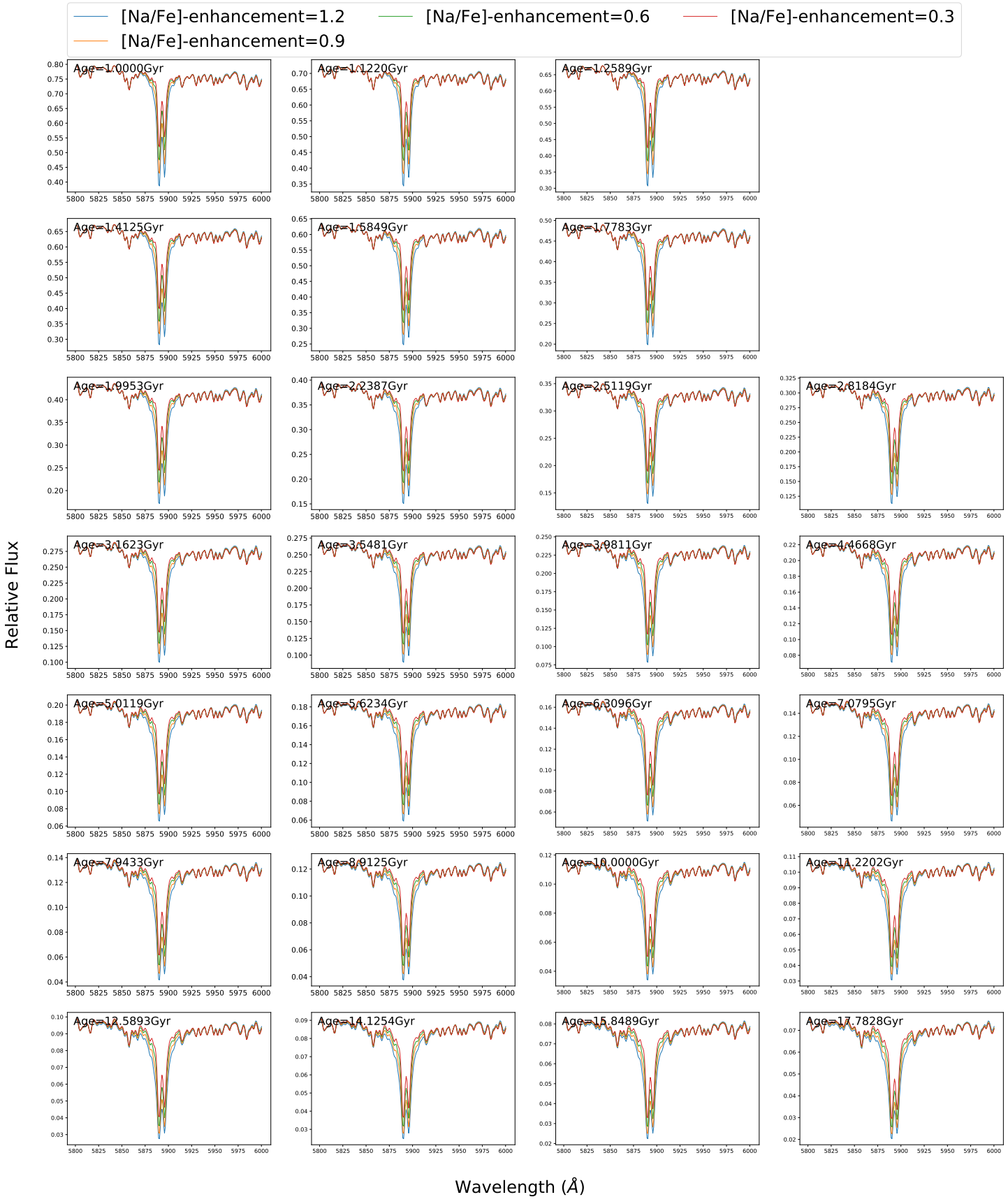


Figure 4.14: *The E-MILES-model for an SSP of [Fe/H]=0.22 with variable [Na/Fe]-enhancement as well as variable age (increasing from 1 Gyr to 17.78 Gyr). The y-axis is normalised with respect to the maximum value of the spectrum with [Na/Fe] = 0.3 and age of 1 Gyr and the wavelength range is from 5800 Å to 6000 Å. The well-known NaD double absorption lines can be seen at 5889.95 Å and 5895.92 Å.*

4.2.4 Varying [Na/Fe]-enhancement and varying metallicity

The E-MILES library only had three different metallicities for the [Na/Fe]-enhanced models. These three are studied here. In Figure 4.15, the biggest difference between the four models is only visible in the red-end of the spectra, with some differences at the blue-end. What is interesting though, is that the more enhanced models show higher relative flux in the red-end, while they show lower relative flux toward 4500 Å. In Figure 4.16, the difference between the [Na/Fe]-enhancements at the different metallicities, specifically around NaD, can be seen in their relative flux, with the [Na/Fe] = 1.2 enhanced model having the deepest NaD absorption feature. The difference between the enhanced models, however, decreases as the metallicity decreases. Therefore, the [Na/Fe]-enhancements are more important for metal-rich galaxies.

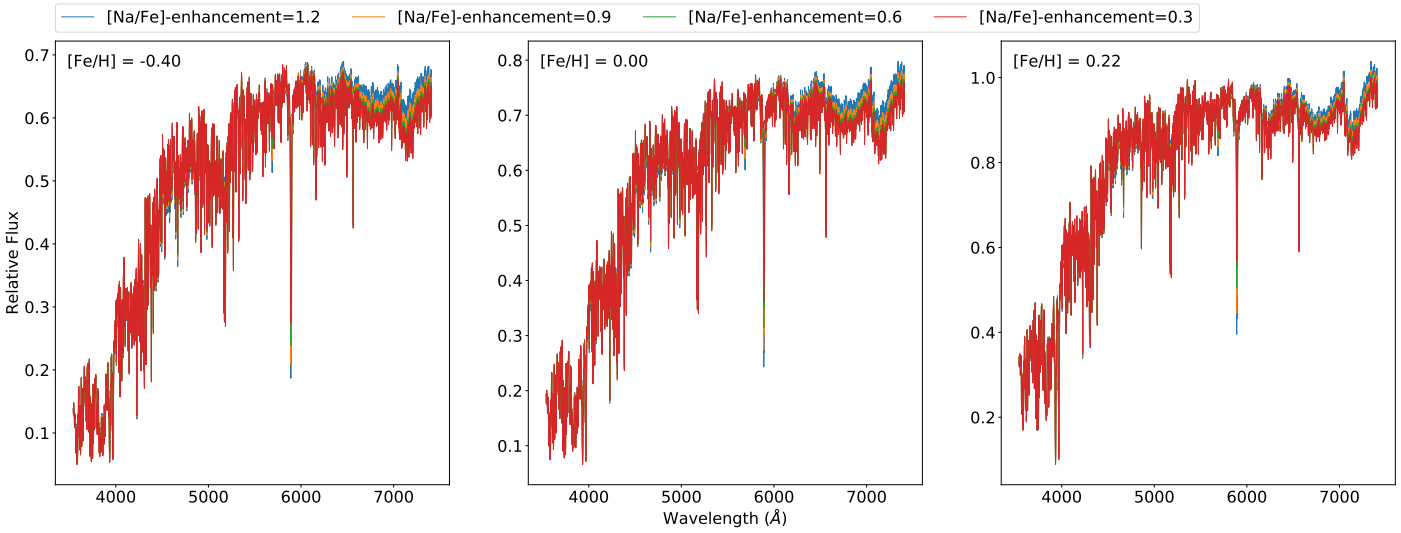


Figure 4.15: *The E-MILES-model for an SSP of age 14.1 Gyr with variable [Na/Fe]-enhancement as well as variable metallicities (from $[Fe/H] = -0.40$ increasing to $[Fe/H] = 0.22$). The y-axis is normalised with respect to the maximum value of the spectrum with [Na/Fe] = 0.3 and metallicity of $[Fe/H] = 0.22$*

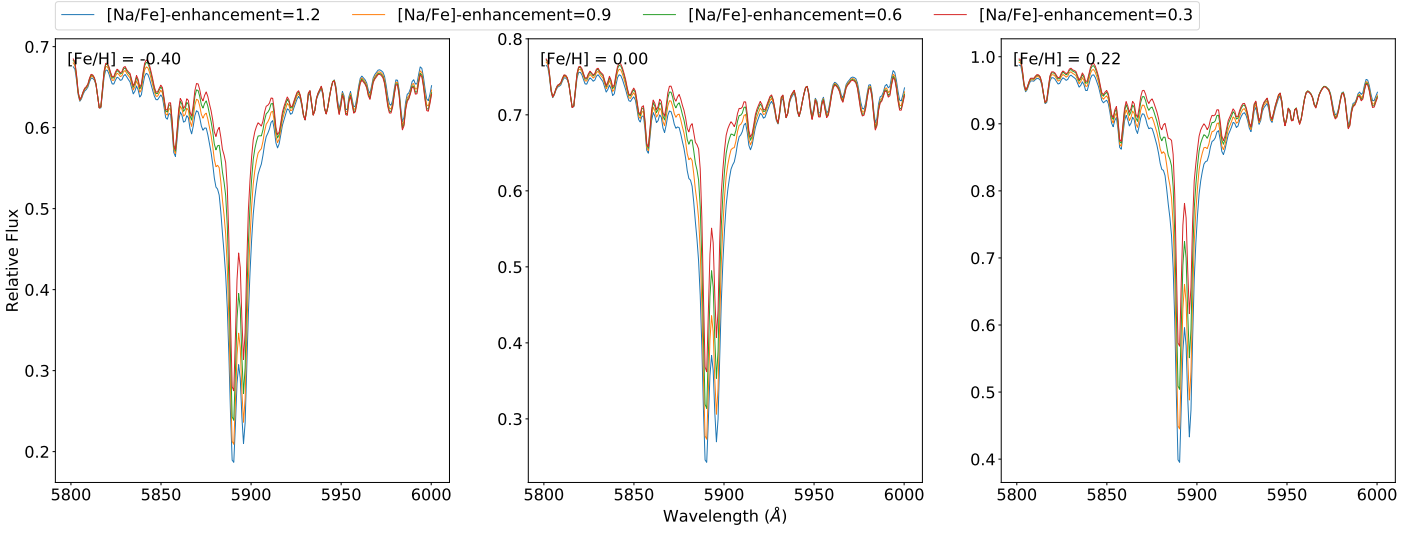


Figure 4.16: *The E-MILES-model for an SSP of age 14.1 Gyr with variable [Na/Fe]-enhancement as well as variable metallicities (from $[Fe/H] = -0.40$ increasing to $[Fe/H] = 0.22$). The y-axis is normalised with respect to the maximum value of the spectrum with [Na/Fe] = 0.3 and metallicity of $[Fe/H] = 0.22$ and the wavelength range is from 5800 Å to 6000 Å. The well-known NaD double absorption lines can be seen at 5889.95 Å and 5895.92 Å.*

Considering the metallicity and age, [Na/Fe]-enhancement seems to be important for young, metal-rich galaxies. BGGs, however, tend to be old and more metal-poor. But even the older and metal-poor SSPs seem to have a more realistic NaD absorption feature in the [Na/Fe]-enhanced models than without it.

4.3 Varying IMF

The IMF is already introduced in Chapter 1. We now want to determine the IMF's influence on the galaxy spectra. Note that when we refer to the IMF slope, we refer to alpha as described in chapter 1. Also refer to chapter 1 for more information on the different slopes of IMF and the slope of standard IMFs.

4.3.1 Varying unimodal IMF slope

A unimodal IMF is used for the first part of this study, varying only the IMF slope. Figure 4.17 shows that the biggest difference between the different IMF slopes' spectra is the relative flux. However, when we look at Figure 4.18, we can also see different shapes in the spectral continuum. This is because, as the IMF slope changes, the distribution of the stellar mass changes.

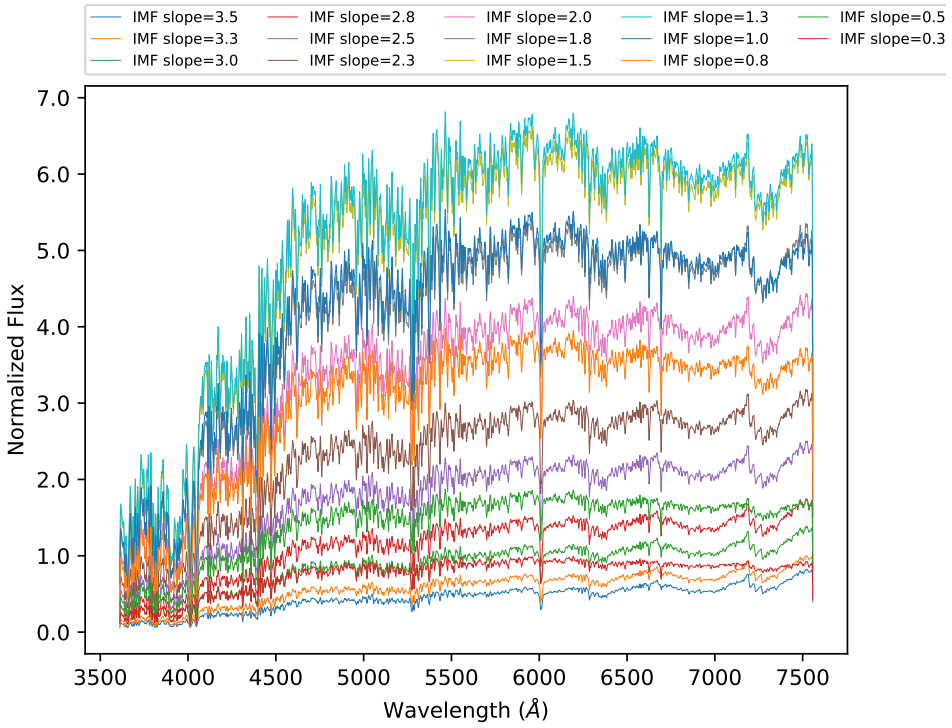


Figure 4.17: *The MILES-model for an SSP of varying unimodal IMF slopes (from a slope of 0.3 to 3.5), age at 14 Gyr, metallicity at* $[Fe/H] = 0.15$ *and no* α*-enhancements. The y-axis is normalised with respect to the maximum value of the galaxy with IMF slope* $= 0.03$*. This figure shows how the IMF slope influences the form of the whole observed spectrum. For a clearer view of the smaller changes in spectra, please refer to Figure 4.18.*

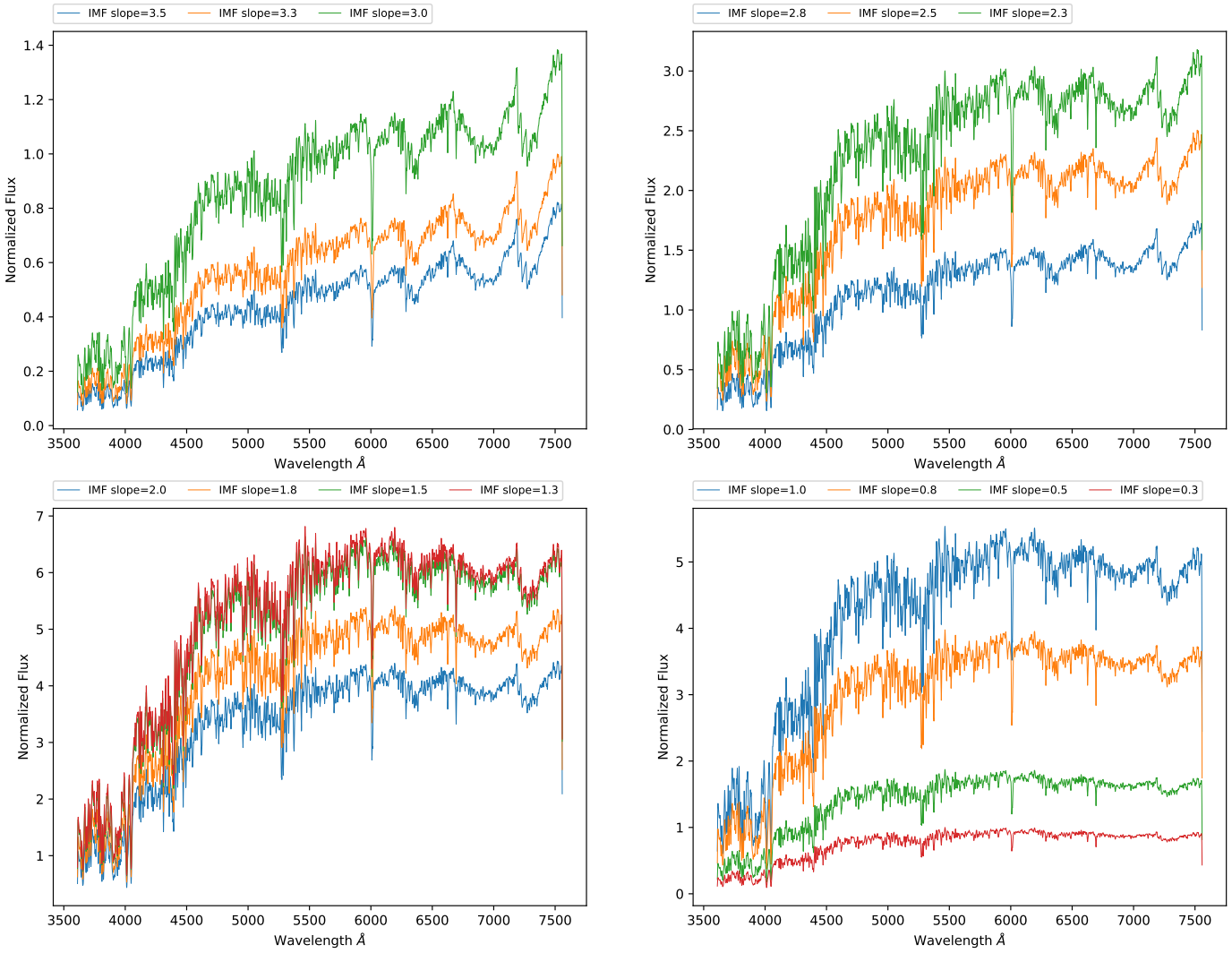


Figure 4.18: *The MILES-model for an SSP of varying IMF (from a slope of 0.3 to 3.5), a constant age at 14 Gyr and metallicity at* $[Fe/H] = 0.15$ *and no* α*-enhancements. The y-axis is normalised with respect to the maximum value of the galaxy with IMF slope* $= 0.3$

4.3.2 Varying IMF type

The different types of IMF are varied in this subsection. Figure 4.19 shows that the biggest difference between the different IMF types' spectra is the relative flux, with an increasing difference from 4500 Å upwards. When we look at Figure 4.20, we can see that the different IMF types influence the NaD feature on a small scale, with the Kroupa binary corrected IMF showing the best solution to the Na-excess problem, if all other parameters (α-enhancement, [Na/Fe]-enhancement) are kept constant.

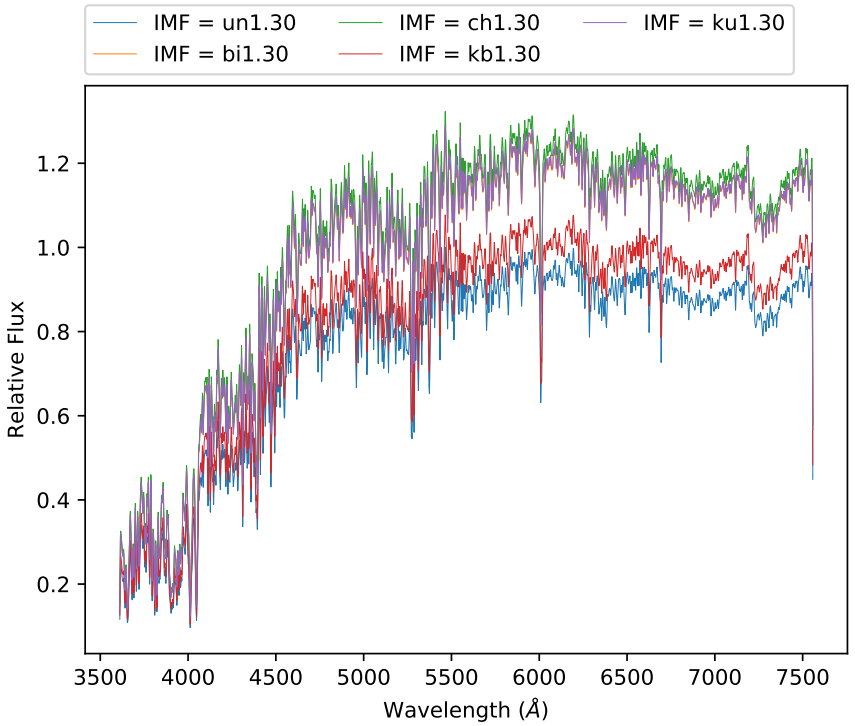


Figure 4.19: *The MILES-model for an SSP of varying IMF type with an IMF slope of 1.3, age at 14 Gyr, metallicity at* $[Fe/H] = 0.15$ *and no* α*-enhancements. The y-axis is normalised with respect to the maximum value of the galaxy with unimodal IMF type.*

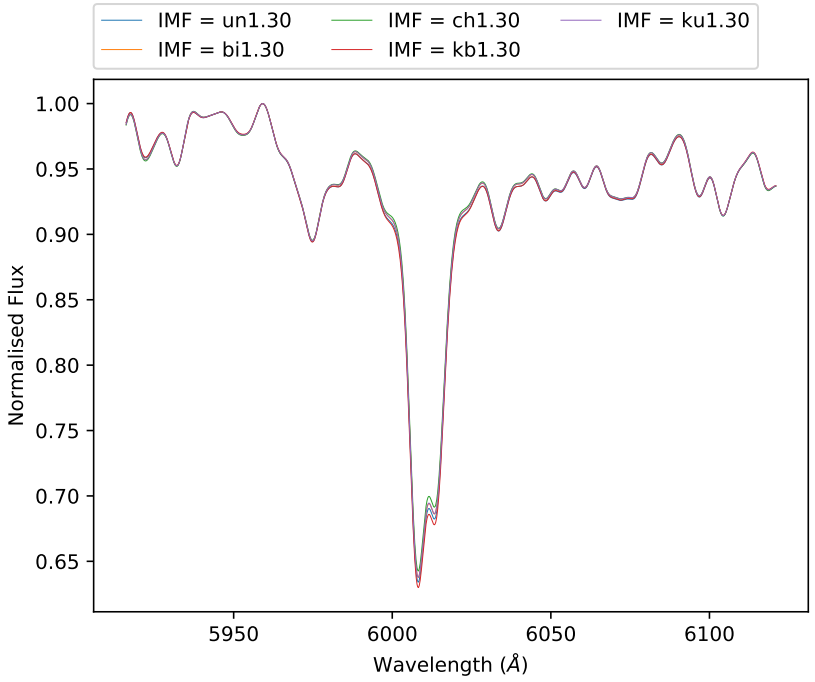


Figure 4.20: *The MILES-model for an SSP of varying IMF type with an IMF slope of 1.3, age at 14 Gyr, metallicity at* $[Fe/H] = 0.15$ *and no* α*-enhancements. This graph shows the NaD feature. All the plots are normalised so that the influence on the depth of the NaD feature can be investigated.*

4.3.3 Varying α-enhancement and varying IMF type

In this subsection, we compare the different α-enhanced models at different IMF slopes, to see if this could contribute to a solution for the NaD mismatch. Even though the α-enhancements seemed to not be the solution to the problem, it might be more important at other IMF slopes.

Varying unimodal and bimodal IMF types and IMF slope

In this part, the unimodal and bimodal IMF types, the IMF slope, and the α-enhancements were varied.

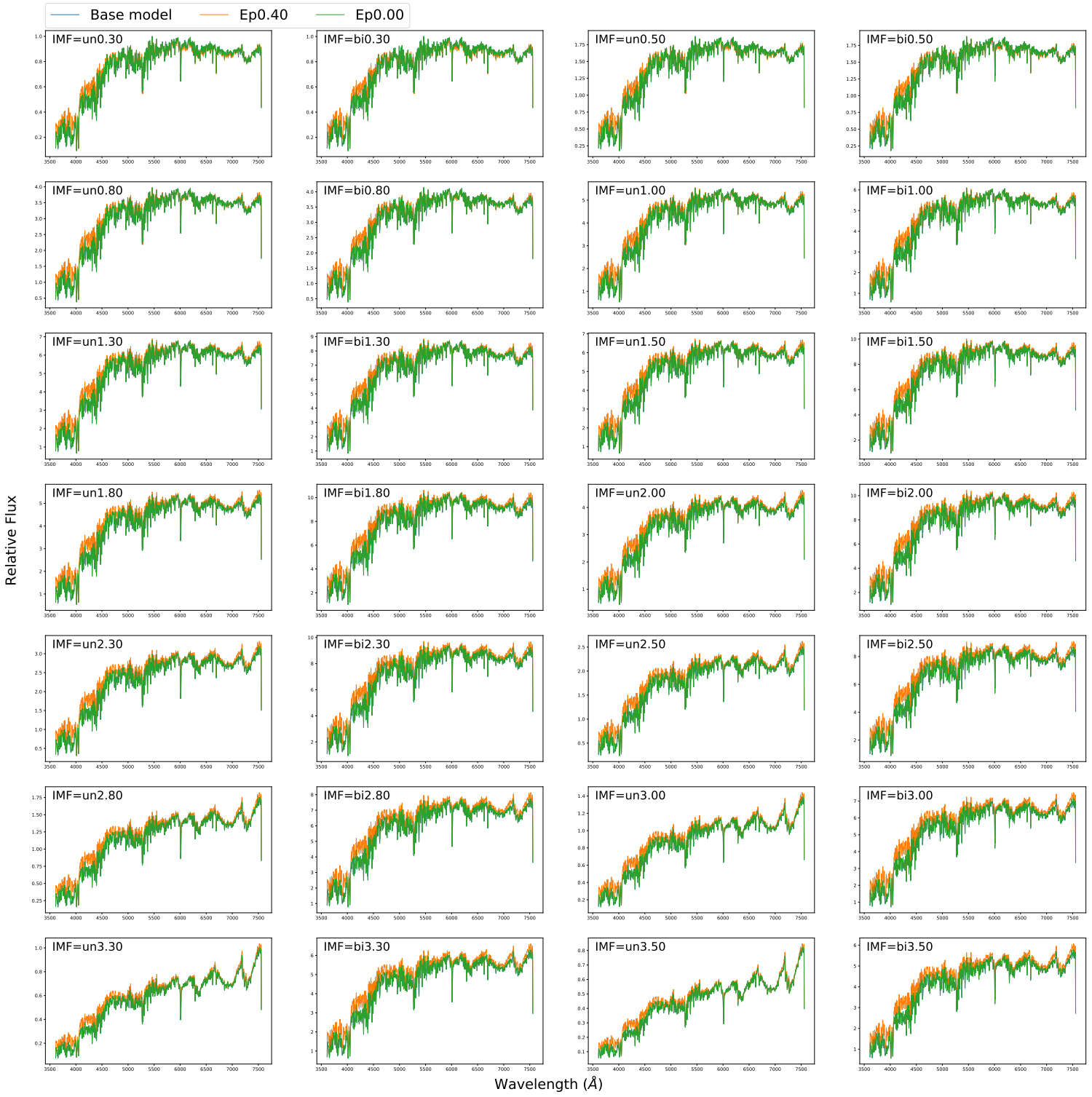


Figure 4.21: *The MILES-model for an SSP of 14.0 Gyr and* $[Fe/H] = 0.15$ *with variable* α*-enhancement as well as variable IMF slope (from a slope of 0.3 to 3.5). The bimodal and unimodal IMFs are plotted next to each other. The y-axis is normalised with respect to the maximum value of the Base* α *spectrum of the unimodal IMF with a slope of 0.30.*

In Figure 4.21, the α-enhanced model can be seen to have a higher relative flux at the blue-end of the spectrum than the base model, but at the red-end of the spectra these models coincide. What is interesting though, is the fact that the bimodal IMF shows a resulting continuum that seems much more constant throughout the different slopes than that of the unimodal IMF. Figure 4.22 focuses on the NaD absorption feature. Here it can be seen throughout all the

different IMF slopes that the α-enhanced model shows a more shallow NaD absorption feature than the base model. Thus, even when considering the different IMF slopes, the α-enhancements only aggravate the NaD problem and do not solve it.

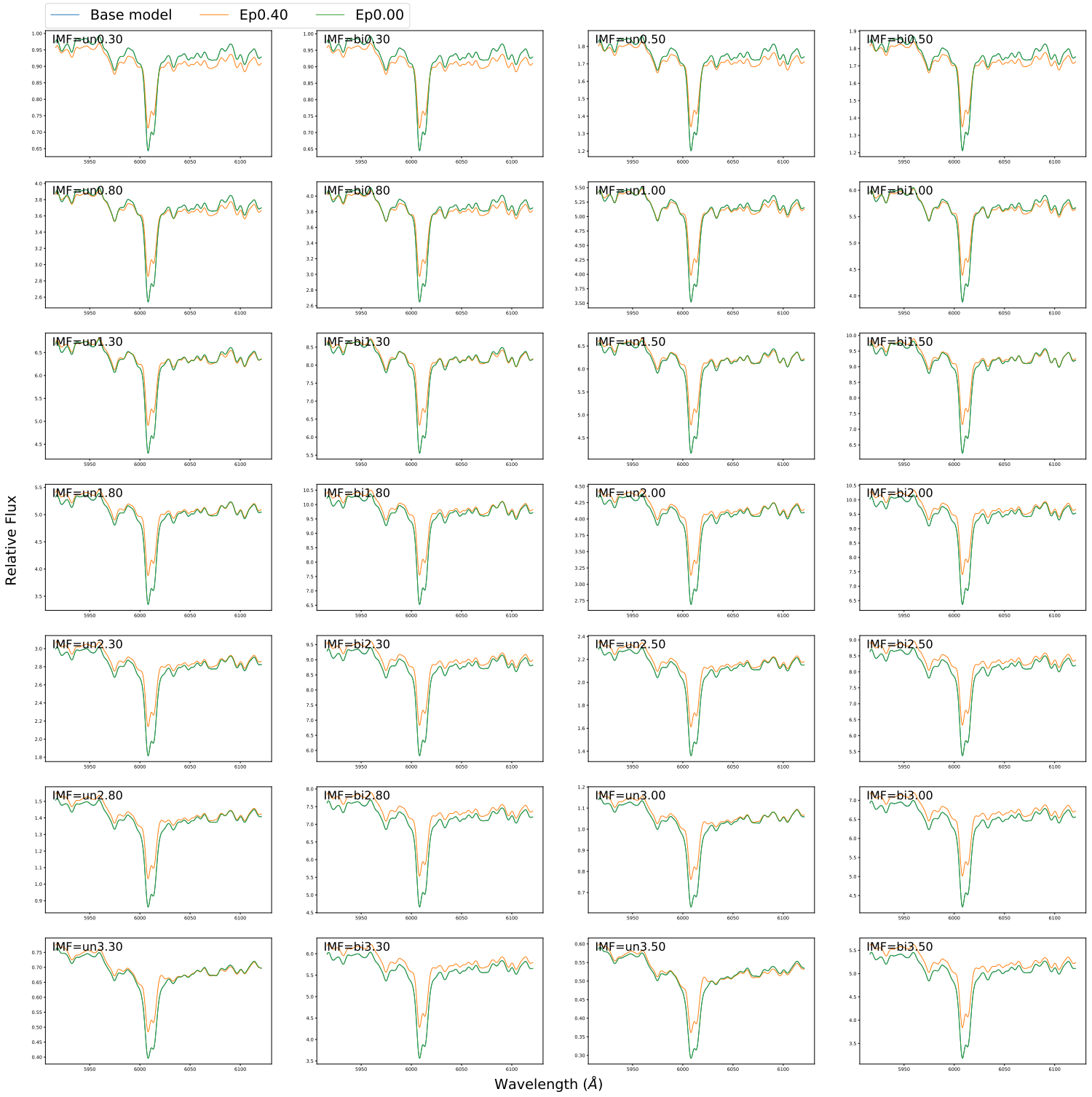


Figure 4.22: *The MILES-model for an SSP of 14.0 Gyr and* $[Fe/H] = 0.15$ *with variable* α*-enhancement as well as variable IMF slope (from a slope of 0.3 to 3.5). The bimodal and unimodal IMFs are plotted next to each other. The y-axis is normalised with respect to the maximum value of the Base* α *spectrum of the unimodal IMF with a slope of 0.30 and the wavelength range is from* 5200 *Å to* 5400 *Å. The Na absorption line can be seen at the shifted wavelength of 5280.2 Å (rest wavelength is 5176.7 Å).*

Varying IMF type

In the second part of testing the variable IMF, the type of IMF was also varied, but keeping the slope at a constant value of 1.3. The different IMF types are discussed in Appendix 1.4.2. In short: the unimodal IMF is based on Salpeter (1955), while the bimodal IMF flattens below one solar mass (Scalo, 1986), and therefore has two different slopes at different masses. The Kroupa and Chabrier IMFs have different broken power-laws than that of Miller-Scalo's bimodal IMF, but it is based on the same principle. Those that we look at here, include the unimodal, bimodal (Miller-Scalo's IMF) and Chabrier IMFs as well as the Kroupa Universal IMF and the Kroupa binary corrected IMF.

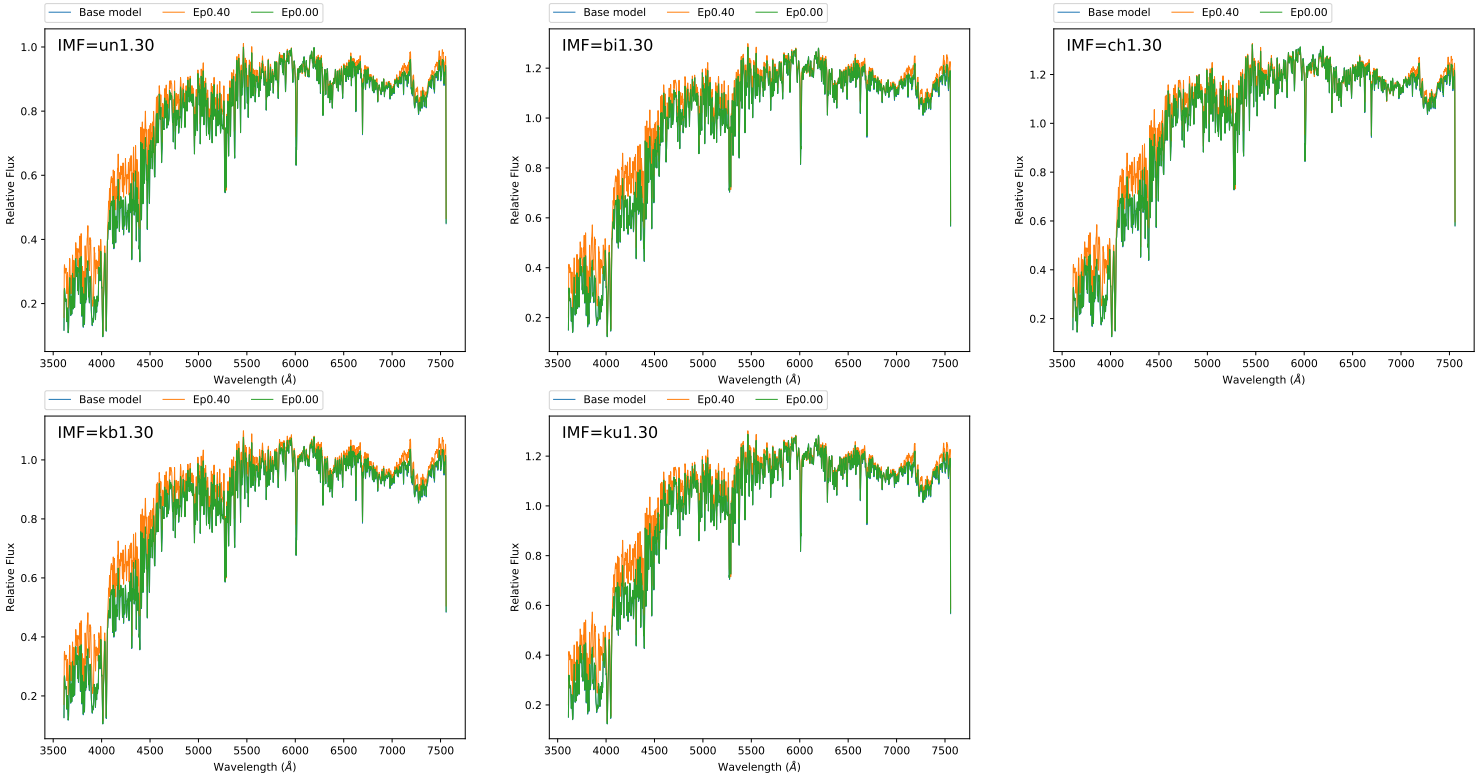


Figure 4.23: *The MILES-model for an SSP of 14.0 Gyr and* $[Fe/H] = 0.15$ *with variable* α*-enhancement as well as variable IMF type. The y-axis is normalised with respect to the maximum value of the Base* α *spectrum of the unimodal IMF. The different IMF types are unimodal (un1.30), bimodal (bi1.30), Chabrier IMF (ch1.30), Kroupa binary corrected (kb1.30) and the Kroupa Universal IMF (ku1.30).*

From Figure 4.21 and Figure 4.22, it is clear that the different IMFs only bring about small differences to the spectra. One of these differences is the difference in relative flux, with the bimodal, Chabrier and Kroupa Universal IMF resulting in a higher relative flux than the unimodal and Kroupa binary corrected IMFs. With regard to the NaD feature, it is clear that the α-enhancements still make the absorption feature more shallow, and thus contribute to the problem rather than resolving it. This is the case no matter which type of IMF is used.

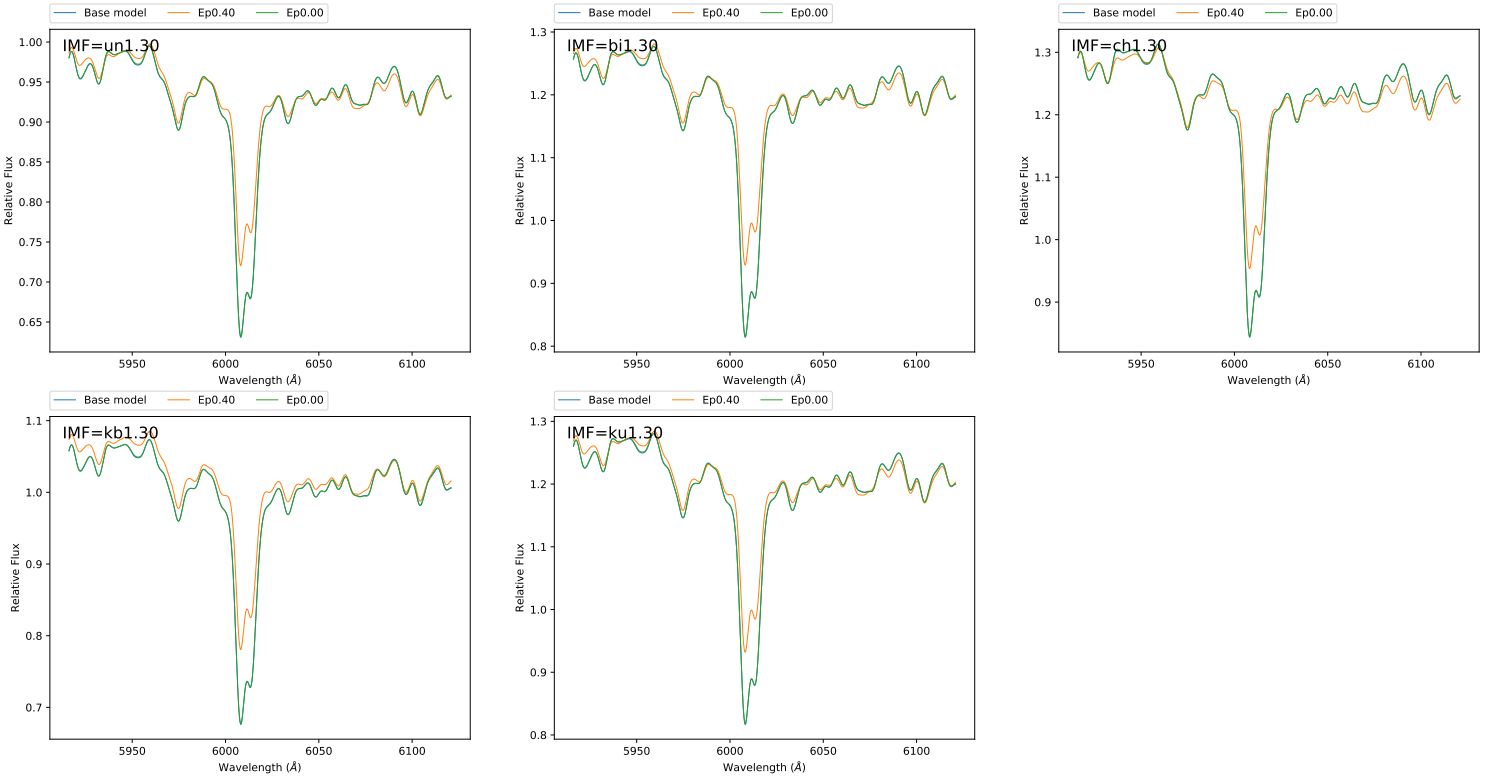


Figure 4.24: *The MILES-model for an SSP of 14.0 Gyr and* $[Fe/H] = 0.15$ *with variable* α*-enhancement as well as variable IMF type. The y-axis is normalised with respect to the maximum value of the Base Alpha spectrum of the unimodal IMF and the wavelength range is from* 5200 *Å to* 5400 *Å. The Na absorption line can be seen at the shifted wavelength of* 5280.2 *Å (rest wavelength is* 5176.7 *Å).*

4.3.4 Varying [Na/Fe]-enhancement and varying IMF

In this subsection, the IMF slope and IMF type will be varied, with the [Na/Fe]-enhancement to see whether or not the IMF slope and type have an influence on how this enhancement gives some resolution to the Na problem.

Varying unimodal IMF slope

Firstly, the unimodal IMF slope is varied. From Figure 4.25, the biggest influence of the IMF on the spectra still remains the relative flux and the overall continuum. The difference between the varying [Na/Fe]-enhancements still brings about a bigger difference towards the red end of the spectra. However, in our analysis, the multiplicative polynomial removes the continuum for the fitting process. Therefore, the overall continuum does not influence the NaD feature.

From Figure 4.26, a conclusion arises: The difference between the absorption feature from the different [Na/Fe]-enhancements seems to decrease as the IMF slope increases. This suggests that the the different [Na/Fe]-enhancement models have a lower impact on the spectra at higher IMF slopes than at lower IMF slopes. It can be seen at the IMF slope of 3.3 where the difference between the [Na/Fe]-enhancement of 1.2 and 0.3 is only about 0.0625 relative flux units whereas the difference between the [Na/Fe]-enhancement of 1.2 and 0.3 at the IMF slope of 0.3 is about 0.1357, showing about double the influence at the lowest IMF slope than at the highest IMF slope. This concurs with La Barbera et al. (2017), that NaD is an IMF sensitive index.

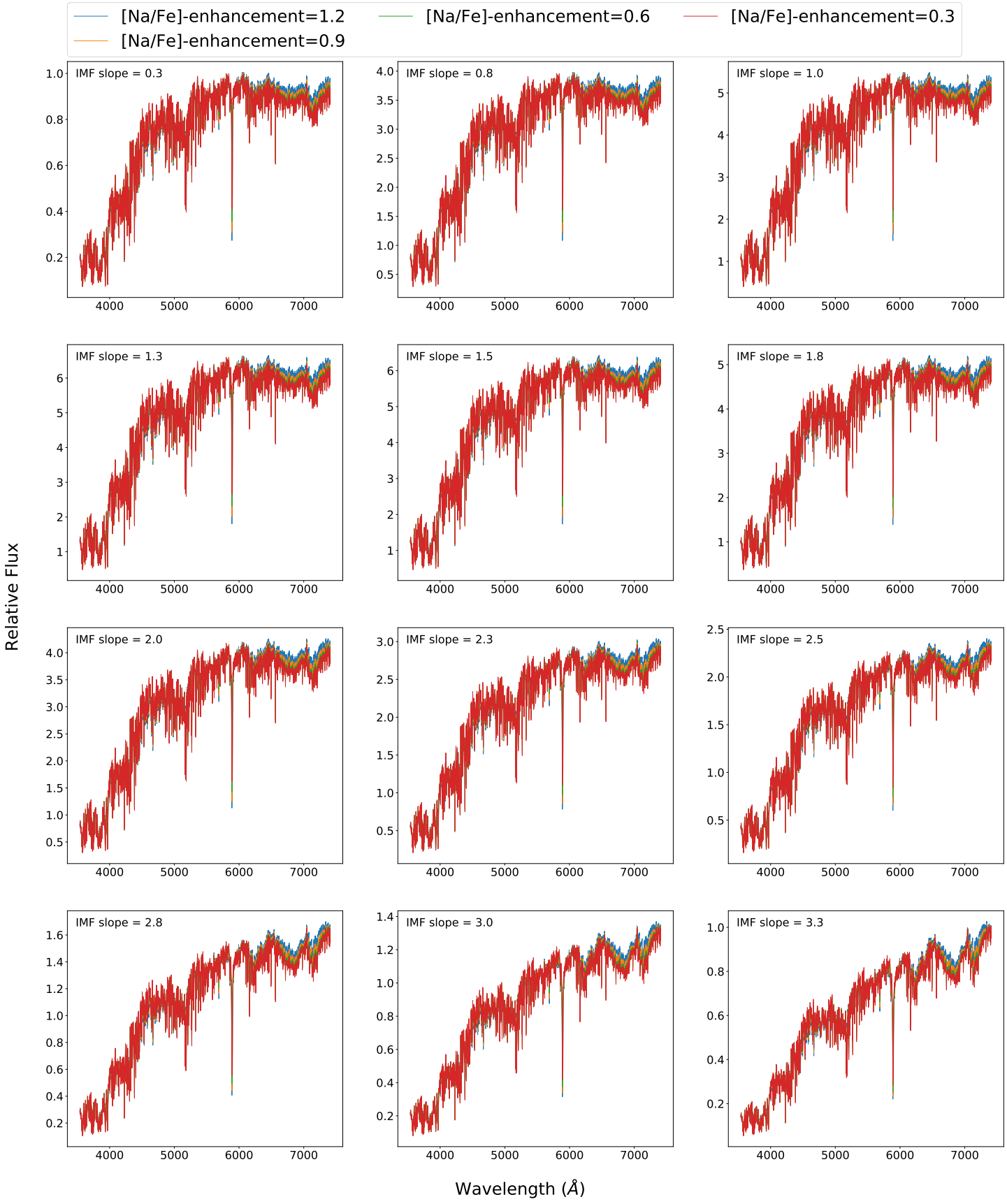


Figure 4.25: *The E-MILES-model for an SSP of age 14.1 Gyr and* $[Fe/H] = 0.22$ *with variable [Na/Fe]-enhancement as well as variable IMF (from a slope of 0.3 to 3.3). The y-axis is normalised with respect to the maximum value of the spectrum with [Na/Fe]* $= 0.3$ *and IMF slope of 0.3.*

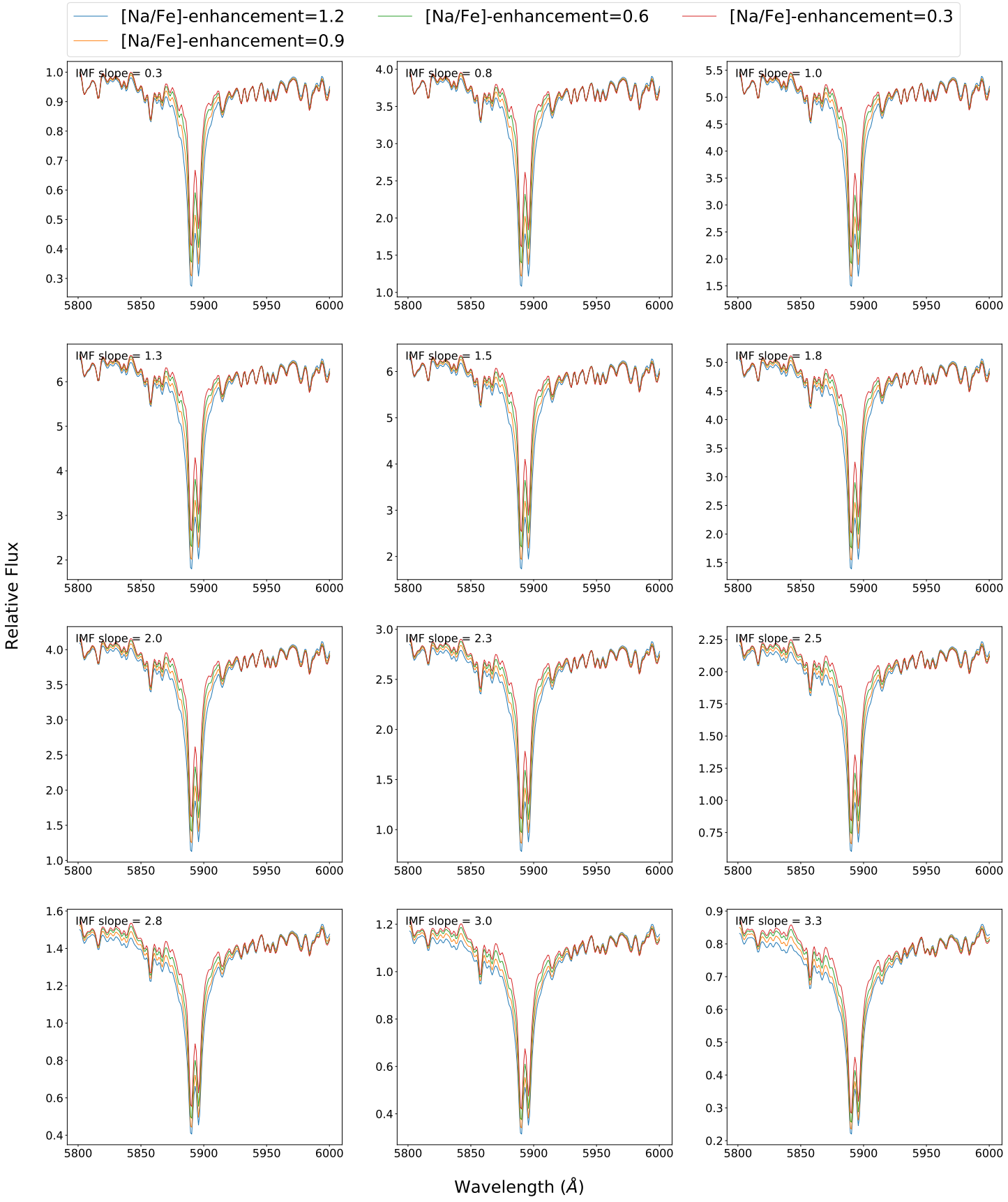


Figure 4.26: *The E-MILES-model for an SSP of age 14.1 Gyr and* $[Fe/H] = 0.22$ *with variable [Na/Fe]-enhancement as well as variable IMF (from a slope of 0.3 to 3.3). The y-axis is normalised with respect to the maximum value of the spectrum with [Na/Fe]* $= 0.3$ *and IMF slope of 0.3 and the wavelength range is from 5800 Å to 6000 Å. The well-known NaD double absorption lines can be seen at 5889.95 Å and 5895.92 Å.*

Varying unimodal and bimodal IMF slope

In this subsection, both the bimodal and unimodal IMF slopes are varied. From Figure 4.27, it is still evident that the bimodal IMF slope does not influence the overall spectral continuum as much as the unimodal IMF slope does. Some similarities, however, can be seen between the two different types of IMF, as the [Na/Fe]-enhanced models seem to influence the same parts of the spectrum in both cases.

Figure 4.28 gives another interesting conclusion: The bimodal IMF slope seems to have less of an effect on the amount of influence the [Na/Fe]-enhancement has on the spectra than the unimodal IMF slope does (see, for example IMF=bi0.30-IMF=bi3.30, where the depth of the absorption feature relative to the different [Na/Fe]-enhancements, stays the same, only the overall relative flux increases and decreases). A definite difference between the two plots of IMF=un3.30 and IMF=bi3.30 can be seen with regard to the relative depth of the absorption feature.

Unfortunately, the [Na/Fe]-enhanced models not yet include other types of IMF. But only from Figures 4.25, 4.26, 4.27 and 4.28 we can already see some evidence that coincides with the notion that the NaD feature is affected by the IMF (as studied in several papers, e.g. La Barbera et al., 2017).

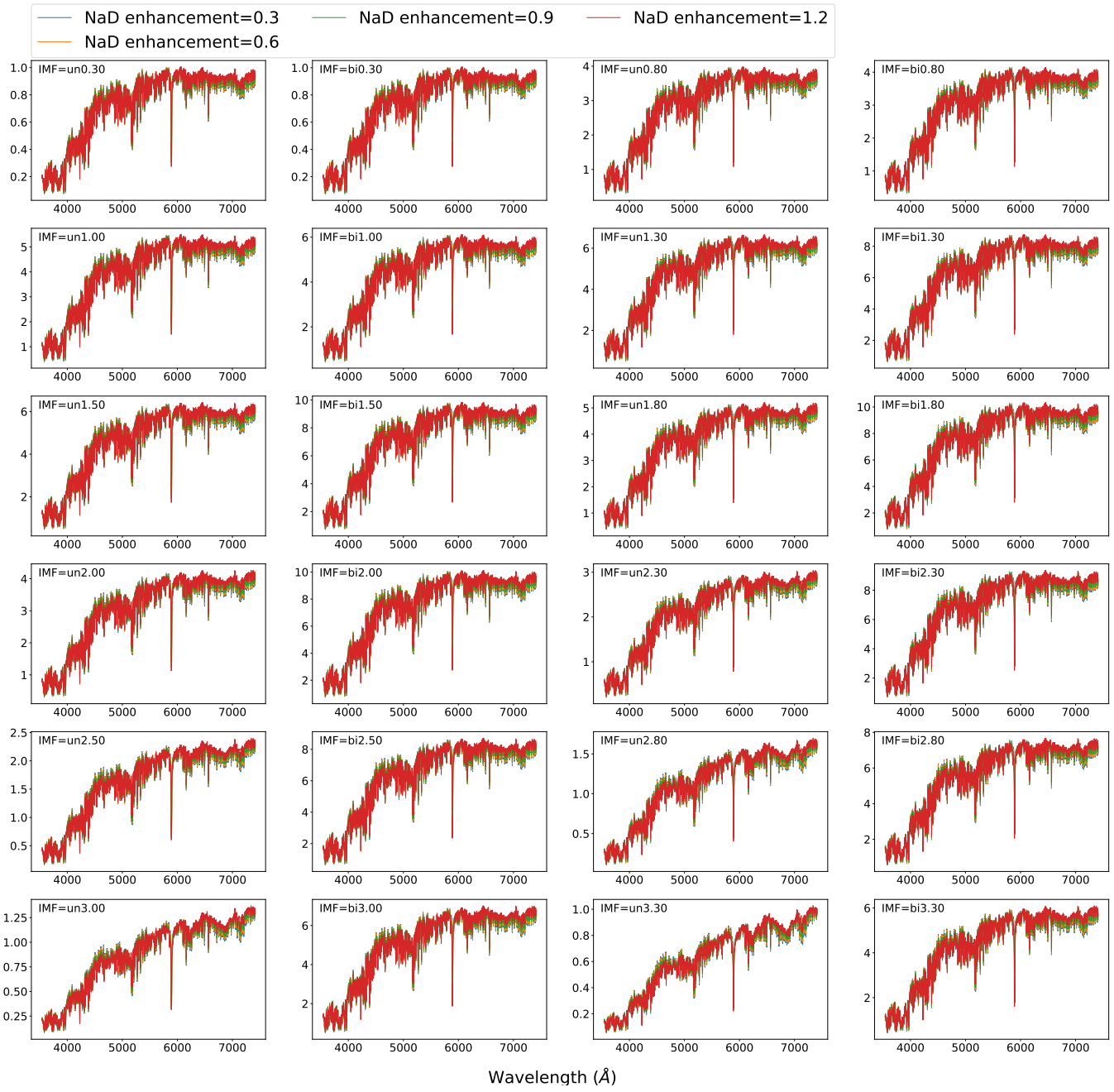


Figure 4.27: *The E-MILES-model for an SSP of age 14.1 Gyr and* $[Fe/H] = 0.22$ *with variable [Na/Fe]-enhancement as well as variable IMF type (unimodal and bimodal) and slope. The y-axis is normalised with respect to the maximum value of the spectrum with [Na/Fe]* $= 0.3$ *and unimodal IMF slope of 0.3.*

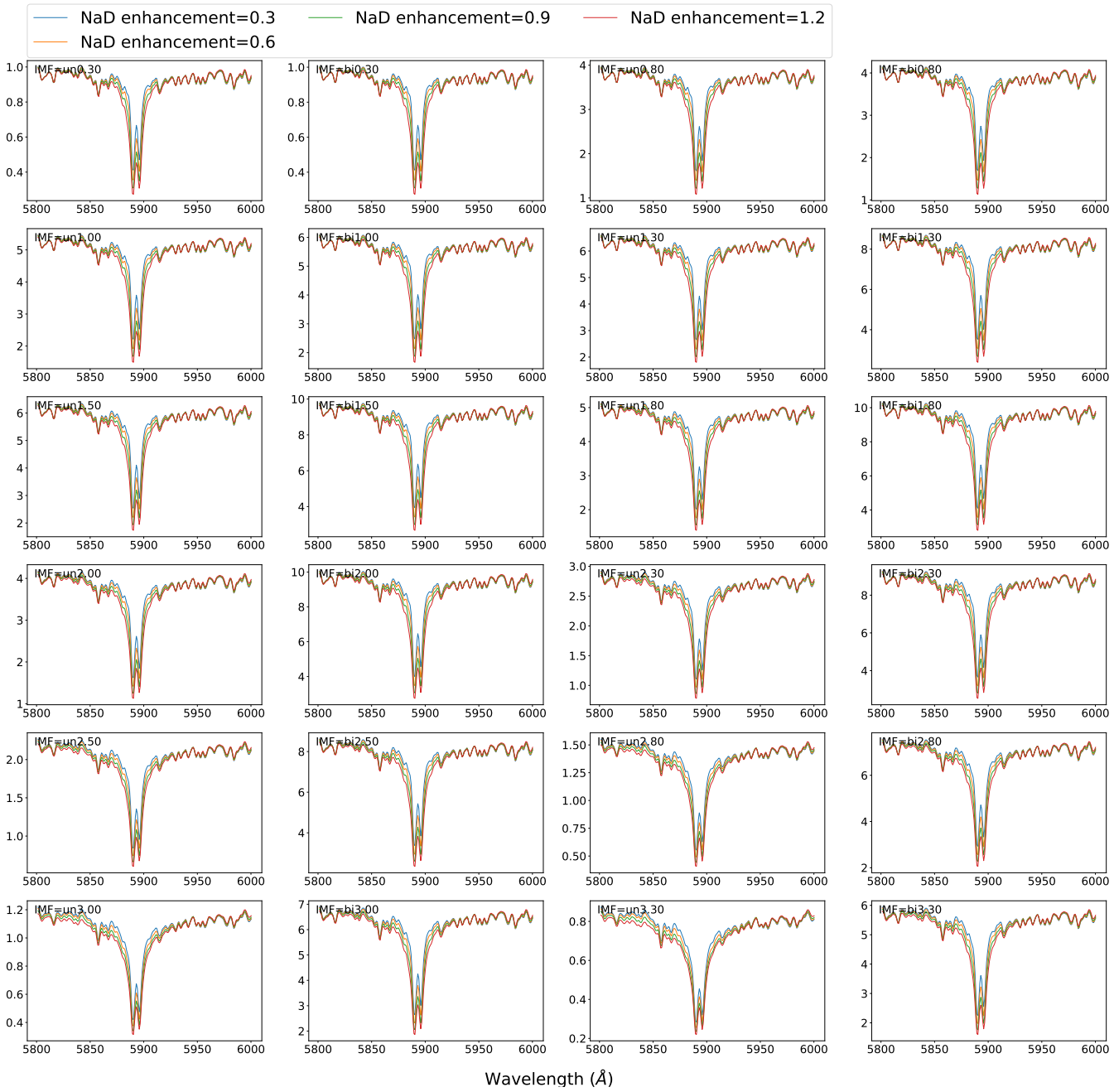


Figure 4.28: *The E-MILES-model for an SSP of age 14.1 Gyr and* $[Fe/H] = 0.22$ *with variable [Na/Fe]-enhancement as well as variable IMF type (unimodal and bimodal) and slope. The y-axis is normalised with respect to the maximum value of the spectrum with* $[Na/Fe] = 0.3$ *and unimodal IMF slope of 0.3 and the wavelength range is from 5800 Å to 6000 Å. The well-known NaD double absorption lines can be seen at 5889.95 Å and 5895.92 Å.*

4.4 Conclusion of SSP model analysis

Although α-enhancements do not solve the sodium overabundance and therefore the NaD mismatch, according to this analysis, the [Na/Fe]-enhanced models will be the best strategy. The Kroupa binary corrected IMF also shows some potential to obtain the best fit for the NaD feature (refer to section 4.3.2). To study the effect of the different parameters on the SP models more robustly, a measurement of the line flux can be done in future studies.

CHAPTER 5

NaD mismatches and analysis

5.1 Measuring the Na overabundances

As can be seen in Figure 5.1, the Na doublet is underestimated by the best-fit model for most BGGs, in particular in the inner bin. For this, an additional analysis was done to probe whether there is a correlation between this overabundance in the galaxies and some of the galaxy or group properties. A graphic measurement was done by measuring the length between point A and point B (called b) in Figure 5.1, the length between A and C (called $a+b$) and then subtracting AC from AB (thus obtaining a). The reason why this method was chosen, and not measuring a directly, is the fact that in some galaxy spectra a is so small that the subtraction would lead to a more accurate value of a than a direct measurement. This measurement was then divided by the length $a+b$ to obtain a dimensionless fraction of overabundance ($FO = \frac{a}{a+b}$). The reason why the overabundance is expressed as a fraction, is because all the SSP and CSP fits are normalised. Equation 5.1 was used to obtain the results presented in Tables 5.1 and 5.2.

$$\begin{aligned}(a \pm a_{err}) &= ((a+b)-b) \pm \sqrt{{(a+b)_{err}}^2 + {b_{err}}^2} \\ (FO \pm FO_{err}) &= \frac{(a \pm a_{err})}{((a+b) \pm (a+b)_{err})} \\ &= \frac{a}{a+b} \pm \frac{a}{a+b}\sqrt{(\frac{a_{err}}{a})^2 + (\frac{(a+b)_{err}}{(a+b)})^2}\end{aligned} \tag{5.1}$$

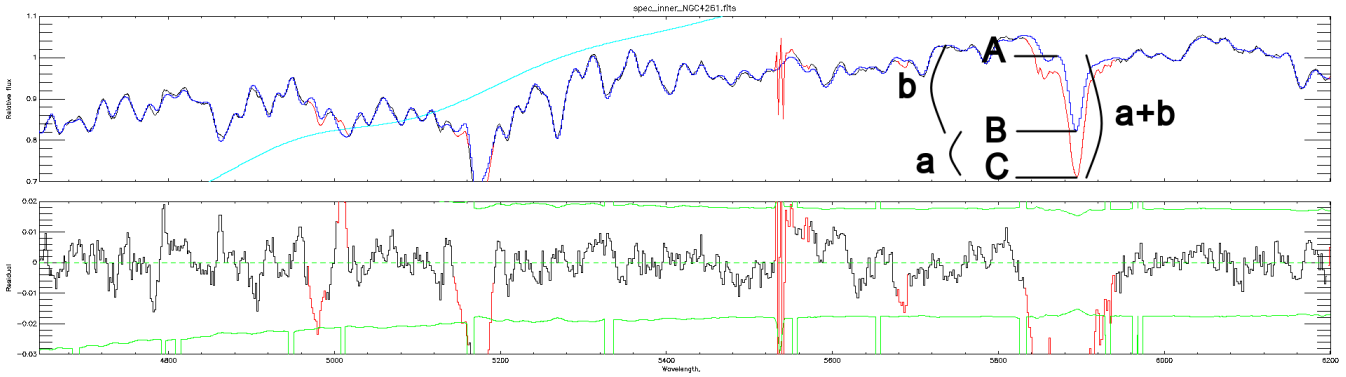


Figure 5.1: *The spectrum of NGC4261 inner SSP fit. The variables for the different measurements are:* $A \rightarrow B = b$ *and* $B \rightarrow C = a$.

5.2 NaD Overabundance measurements

The Na overabundances that were obtained by both the Vazdekis model and the Kroupa binary corrected model were measured (Tables 5.1 and 5.2, respectively). In the short discussion about the correlation between the overabundances and the other properties, mostly the Vazdekis model (with a unimodal Salpeter IMF) is considered. However, due to the probability that the Na overabundance can be linked to IMF (La Barbera et al., 2017), a different model, with a different IMF (namely Kroupa binary corrected model, with the Kroupa binary corrected IMF) was also used to see what the influence might be.

The S/N ratios in the outer bins of all the galaxies are lower than the inner bins. This is the reason why the FO in the outer bins is much less pronounced than in the inner bins, as the FO measurement and model fit are more difficult with small S/N ratios. Whether or not a Na overabundance is measured, therefore, relies on high enough S/N to measure it. There will thus be more focus on the inner bins.

To also see what model predicts the NaD feature better, the difference between each overabundance measurement was calculated, as can be seen in Table 5.3.

NaD Mismatches Vazdekis model																
High-richness																
Galaxy	SSP Inner				CSP Inner				SSP Outer				CSP Outer			
	$a+b$	b	a	**FO**	$a+b$	b	a	**FO**	$a+b$	b	a	**FO**	$a+b$	b	a	**FO**
NGC0410	14.0 ± 0.5	9.0 ± 0.5	5.0 ± 0.7	**0.357 ± 0.052**	14.5 ± 0.5	9.0 ± 0.5	5.5 ± 0.7	**0.379 ± 0.050**			0.0 ± 0.0	**0.000 ± 0.000**			0.0 ± 0.0	**0.000 ± 0.000**
NGC0584	12.0 ± 0.5	10.0 ± 0.5	2.0 ± 0.7	**0.167 ± 0.059**			0.0 ± 0.0	**0.000 ± 0.000**			0.0 ± 0.0	**0.000 ± 0.000**			0.0 ± 0.0	**0.000 ± 0.000**
NGC0777	12.0 ± 0.5	7.0 ± 0.5	5.0 ± 0.7	**0.417 ± 0.061**	17.0 ± 0.5	11.5 ± 0.5	5.5 ± 0.7	**0.324 ± 0.043**			0.0 ± 0.0	**0.000 ± 0.000**			0.0 ± 0.0	**0.000 ± 0.000**
NGC0924			0.0 ± 0.0	**0.000 ± 0.000**			0.0 ± 0.0	**0.000 ± 0.000**			0.0 ± 0.0	**0.000 ± 0.000**			0.0 ± 0.0	**0.000 ± 0.000**
NGC1060			0.0 ± 0.0	**0.000 ± 0.000**			0.0 ± 0.0	**0.000 ± 0.000**	12.0 ± 0.5	10.0 ± 0.5	2.0 ± 0.7	**0.167 ± 0.059**	12.0 ± 0.5	10.0 ± 0.5	2.0 ± 0.7	**0.167 ± 0.059**
NGC1453	13.0 ± 0.5	10.5 ± 0.5	2.5 ± 0.7	**0.192 ± 0.055**	10.0 ± 0.5	3.0 ± 0.7	13.0 ± 0.5	**0.231 ± 0.055**			0.0 ± 0.0	**0.000 ± 0.000**			0.0 ± 0.0	**0.000 ± 0.000**
NGC1587	13.0 ± 0.5	10.5 ± 0.5	2.5 ± 0.7	**0.192 ± 0.055**			0.0 ± 0.0	**0.000 ± 0.000**			0.0 ± 0.0	**0.000 ± 0.000**			0.0 ± 0.0	**0.000 ± 0.000**
NGC2563	14.0 ± 0.5	10.0 ± 0.5	4.0 ± 0.7	**0.286 ± 0.052**	13.5 ± 0.5	10.5 ± 0.5	3.0 ± 0.7	**0.222 ± 0.053**			0.0 ± 0.0	**0.000 ± 0.000**			0.0 ± 0.0	**0.000 ± 0.000**
NGC4261	18.0 ± 0.5	11.0 ± 0.5	7.0 ± 0.7	**0.389 ± 0.041**	18.5 ± 0.5	11.0 ± 0.5	7.5 ± 0.7	**0.405 ± 0.040**			0.0 ± 0.0	**0.000 ± 0.000**			0.0 ± 0.0	**0.000 ± 0.000**
NGC5353	14.5 ± 0.5	11.0 ± 0.5	3.5 ± 0.7	**0.241 ± 0.049**	12.5 ± 0.5	7.5 ± 0.5	5.0 ± 0.7	**0.400 ± 0.059**	10.0 ± 0.5	8.0 ± 0.5	2.0 ± 0.7	**0.200 ± 0.071**	10.0 ± 0.5	8.5 ± 0.5	1.5 ± 0.7	**0.150 ± 0.071**
NGC5846	11.5 ± 0.5	8.5 ± 0.5	3.0 ± 0.7	**0.261 ± 0.063**	11.5 ± 0.5	9.0 ± 0.5	2.5 ± 0.7	**0.217 ± 0.062**			N/A	**N/A**			N/A	**N/A**
NGC5982	12.0 ± 0.5	8.5 ± 0.5	3.5 ± 0.7	**0.292 ± 0.060**			0.0 ± 0.0	**0.000 ± 0.000**			0.0 ± 0.0	**0.000 ± 0.000**			0.0 ± 0.0	**0.000 ± 0.000**
NGC6658			0.0 ± 0.0	**0.000 ± 0.000**	13.0 ± 0.5	10.0 ± 0.5	3.0 ± 0.7	**0.231 ± 0.055**			0.0 ± 0.0	**0.000 ± 0.000**			0.0 ± 0.0	**0.000 ± 0.000**
NGC7619	13.0 ± 0.5	11.0 ± 0.5	2.0 ± 0.7	**0.154 ± 0.055**	13.0 ± 0.5	10.5 ± 0.5	2.5 ± 0.7	**0.192 ± 0.055**			0.0 ± 0.0	**0.000 ± 0.000**			0.0 ± 0.0	**0.000 ± 0.000**
Low-richness																
NGC0315			0.0 ± 0.0	**0.000 ± 0.000**			0.0 ± 0.0	**0.000 ± 0.000**			0.0 ± 0.0	**0.000 ± 0.000**			0.0 ± 0.0	**0.000 ± 0.000**
NGC0524	10.0 ± 0.5	9.0 ± 0.5	1.0 ± 0.7	**0.100 ± 0.071**	10.0 ± 0.5	9.0 ± 0.5	1.0 ± 0.7	**0.100 ± 0.071**			0.0 ± 0.0	**0.000 ± 0.000**			0.0 ± 0.0	**0.000 ± 0.000**
NGC1779	15.0 ± 0.5	12.5 ± 0.5	2.5 ± 0.7	**0.167 ± 0.047**	15.0 ± 0.5	13.5 ± 0.5	1.5 ± 0.7	**0.100 ± 0.047**			0.0 ± 0.0	**0.000 ± 0.000**			0.0 ± 0.0	**0.000 ± 0.000**
NGC2768	12.5 ± 0.5	10.5 ± 0.5	2.0 ± 0.7	**0.160 ± 0.057**			0.0 ± 0.0	**0.000 ± 0.000**			0.0 ± 0.0	**0.000 ± 0.000**			0.0 ± 0.0	**0.000 ± 0.000**
NGC3613			0.0 ± 0.0	**0.000 ± 0.000**			0.0 ± 0.0	**0.000 ± 0.000**			0.0 ± 0.0	**0.000 ± 0.000**			0.0 ± 0.0	**0.000 ± 0.000**
NGC3665			0.0 ± 0.0	**0.000 ± 0.000**			0.0 ± 0.0	**0.000 ± 0.000**			0.0 ± 0.0	**0.000 ± 0.000**			0.0 ± 0.0	**0.000 ± 0.000**
NGC5127			0.0 ± 0.0	**0.000 ± 0.000**			0.0 ± 0.0	**0.000 ± 0.000**			0.0 ± 0.0	**0.000 ± 0.000**			0.0 ± 0.0	**0.000 ± 0.000**
NGC5490	12.5 ± 0.5	10.5 ± 0.5	2.0 ± 0.7	**0.160 ± 0.057**	12.5 ± 0.5	10.5 ± 0.5	2.0 ± 0.7	**0.160 ± 0.057**			0.0 ± 0.0	**0.000 ± 0.000**			0.0 ± 0.0	**0.000 ± 0.000**
NGC5629	11.5 ± 0.5	10.0 ± 0.5	1.5 ± 0.7	**0.130 ± 0.062**			0.0 ± 0.0	**0.000 ± 0.000**			0.0 ± 0.0	**0.000 ± 0.000**			0.0 ± 0.0	**0.000 ± 0.000**

Table 5.1: *The readings of the NaD absorption line mismatches are recorded in this table. Refer to the discussion about how the measurements were done. The columns $a+b$ and b were measured in arbitrary flux units and then the columns a and FO (fraction overabundance) were calculated. Note that the errors were also calculated using the error propagation rule for subtraction and the error propagation rule for division. Where the FO was measured as zero, the model showed no significant mismatch. In the case of the outer bin for NGC5846, the signal-to-noise ratio was too little to make a measurement.*

NaD Mismatches Kroupa Binary Corrected model																
High-richness																
Galaxy	SSP Inner				CSP Inner				SSP Outer				CSP Outer			
	$a+b$	b	a	**FO**	$a+b$	b	a	**FO**	$a+b$	b	a	**FO**	$a+b$	b	a	**FO**
NGC0410	15.5 ± 0.5	9.5 ± 0.5	6.0 ± 0.7	**0.387 ± 0.047**	15.5 ± 0.5	10.0 ± 0.5	5.5 ± 0.7	**0.355 ± 0.047**			0.0 ± 0.0	**0.000 ± 0.000**			0.0 ± 0.0	**0.000 ± 0.000**
NGC0584	11.0 ± 0.5	9.0 ± 0.5	2.0 ± 0.7	**0.182 ± 0.065**			0.0 ± 0.0	**0.000 ± 0.000**			0.0 ± 0.0	**0.000 ± 0.000**			0.0 ± 0.0	**0.000 ± 0.000**
NGC0777	12.5 ± 0.5	7.5 ± 0.5	5.0 ± 0.7	**0.400 ± 0.059**	15.5 ± 0.5	9.5 ± 0.5	6.0 ± 0.7	**0.387 ± 0.047**			0.0 ± 0.0	**0.000 ± 0.000**			0.0 ± 0.0	**0.000 ± 0.000**
NGC0924			0.0 ± 0.0	**0.000 ± 0.000**			0.0 ± 0.0	**0.000 ± 0.000**			0.0 ± 0.0	**0.000 ± 0.000**			0.0 ± 0.0	**0.000 ± 0.000**
NGC1060			0.0 ± 0.0	**0.000 ± 0.000**			0.0 ± 0.0	**0.000 ± 0.000**	10.5 ± 0.5	9.0 ± 0.5	1.5 ± 0.7	**0.143 ± 0.068**			0.0 ± 0.0	**0.000 ± 0.000**
NGC1453	11.5 ± 0.5	9.0 ± 0.5	2.5 ± 0.7	**0.217 ± 0.062**	11.5 ± 0.5	8.5 ± 0.5	3.0 ± 0.7	**0.261 ± 0.063**			0.0 ± 0.0	**0.000 ± 0.000**			0.0 ± 0.0	**0.000 ± 0.000**
NGC1587	11.5 ± 0.5	9.5 ± 0.5	2.0 ± 0.7	**0.174 ± 0.062**	11.5 ± 0.5	9.5 ± 0.5	2.0 ± 0.7	**0.174 ± 0.062**			0.0 ± 0.0	**0.000 ± 0.000**			0.0 ± 0.0	**0.000 ± 0.000**
NGC2563	12.0 ± 0.5	8.5 ± 0.5	3.5 ± 0.7	**0.292 ± 0.060**	12.0 ± 0.5	9.0 ± 0.5	3.0 ± 0.7	**0.250 ± 0.060**			0.0 ± 0.0	**0.000 ± 0.000**			0.0 ± 0.0	**0.000 ± 0.000**
NGC4261	12.5 ± 0.5	10.5 ± 0.5	2.0 ± 0.7	**0.160 ± 0.057**	13.0 ± 0.5	10.5 ± 0.5	2.5 ± 0.7	**0.192 ± 0.055**			0.0 ± 0.0	**0.000 ± 0.000**			0.0 ± 0.0	**0.000 ± 0.000**
NGC5353	13.0 ± 0.5	10.0 ± 0.5	3.0 ± 0.7	**0.231 ± 0.055**	14.5 ± 0.5	9.0 ± 0.5	5.5 ± 0.7	**0.379 ± 0.05**	9.5 ± 0.5	7.5 ± 0.5	2.0 ± 0.7	**0.211 ± 0.075**	9.0 ± 0.5	7.5 ± 0.5	1.5 ± 0.7	**0.167 ± 0.079**
NGC5846	15.5 ± 0.5	12.0 ± 0.5	3.5 ± 0.7	**0.226 ± 0.046**	12.5 ± 0.5	10.5 ± 0.5	2.0 ± 0.7	**0.16 ± 0.057**			N/A	**N/A**			N/A	**N/A**
NGC5982	10.5 ± 0.5	8.0 ± 0.5	2.5 ± 0.7	**0.238 ± 0.068**			0.0 ± 0.0	**0.000 ± 0.000**			0.0 ± 0.0	**0.000 ± 0.000**			0.0 ± 0.0	**0.000 ± 0.000**
NGC6658			0.0 ± 0.0	**0.000 ± 0.000**			0.0 ± 0.0	**0.000 ± 0.000**			0.0 ± 0.0	**0.000 ± 0.000**			0.0 ± 0.0	**0.000 ± 0.000**
NGC7619	11.5 ± 0.5	10.0 ± 0.5	1.5 ± 0.7	**0.130 ± 0.062**	11.5 ± 0.5	10.0 ± 0.5	1.5 ± 0.7	**0.130 ± 0.062**			0.0 ± 0.0	**0.000 ± 0.000**			0.0 ± 0.0	**0.000 ± 0.000**
Low-richness																
NGC0315			0.0 ± 0.0	**0.000 ± 0.000**			0.0 ± 0.0	**0.000 ± 0.000**			0.0 ± 0.0	**0.000 ± 0.000**			0.0 ± 0.0	**0.000 ± 0.000**
NGC0524	9.5 ± 0.5	8.0 ± 0.5	1.5 ± 0.7	**0.158 ± 0.075**	9.0 ± 0.5	8.0 ± 0.5	1.0 ± 0.7	**0.111 ± 0.079**	10.5 ± 0.5	8.5 ± 0.5	2.0 ± 0.7	**0.190 ± 0.068**			0.0 ± 0.0	**0.000 ± 0.000**
NGC1779	13.5 ± 0.5	11.0 ± 0.5	2.5 ± 0.7	**0.185 ± 0.053**	13.5 ± 0.5	11.5 ± 0.5	2.0 ± 0.7	**0.148 ± 0.053**			0.0 ± 0.0	**0.000 ± 0.000**			0.0 ± 0.0	**0.000 ± 0.000**
NGC2768	11.5 ± 0.5	9.5 ± 0.5	2.0 ± 0.7	**0.174 ± 0.062**			0.0 ± 0.0	**0.000 ± 0.000**			0.0 ± 0.0	**0.000 ± 0.000**			0.0 ± 0.0	**0.000 ± 0.000**
NGC3613			0.0 ± 0.0	**0.000 ± 0.000**			0.0 ± 0.0	**0.000 ± 0.000**			0.0 ± 0.0	**0.000 ± 0.000**			0.0 ± 0.0	**0.000 ± 0.000**
NGC3665			0.0 ± 0.0	**0.000 ± 0.000**			0.0 ± 0.0	**0.000 ± 0.000**			0.0 ± 0.0	**0.000 ± 0.000**			0.0 ± 0.0	**0.000 ± 0.000**
NGC5127			0.0 ± 0.0	**0.000 ± 0.000**			0.0 ± 0.0	**0.000 ± 0.000**			0.0 ± 0.0	**0.000 ± 0.000**			0.0 ± 0.0	**0.000 ± 0.000**
NGC5490	11.0 ± 0.5	9.5 ± 0.5	1.5 ± 0.7	**0.136 ± 0.065**	11.0 ± 0.5	9.5 ± 0.5	1.5 ± 0.7	**0.136 ± 0.065**			0.0 ± 0.0	**0.000 ± 0.000**			0.0 ± 0.0	**0.000 ± 0.000**
NGC5629	10.5 ± 0.5	9.0 ± 0.5	1.5 ± 0.7	**0.143 ± 0.068**			0.0 ± 0.0	**0.000 ± 0.000**			0.0 ± 0.0	**0.000 ± 0.000**			0.0 ± 0.0	**0.000 ± 0.000**

Table 5.2: *The readings of the NaD absorption line mismatches (in arbitrary flux units) are recorded in this table. It is important to note that the model that was used here, is the Kroupa Binary Corrected stellar population model.*

Difference in NaD Mismatches between Kroupa Binary Corrected model and the Vazdekis Unimodal Salpeter IMF model								
Galaxy	**SSP Inner**		**CSP Inner**		**SSP Outer**		**CSP Outer**	
	Difference	**Better fit**	**Difference**	**Better fit**	**Difference**	**Better fit**	**Difference**	**Better fit**
High-richness								
NGC0410	0.030 ± 0.070	Salp	–0.024 ± 0.069	Krou	0.000 ± 0.000		0.000 ± 0.000	
NGC0584	0.015 ± 0.088	Salp	0.000 ± 0.000		0.000 ± 0.000		0.000 ± 0.000	
NGC0777	–0.017 ± 0.085	Krou	0.063 ± 0.064	Salp	0.000 ± 0.000		0.000 ± 0.000	
NGC0924	0.000 ± 0.000		0.000 ± 0.000		0.000 ± 0.000		0.000 ± 0.000	
NGC1060	0.000 ± 0.000		0.000 ± 0.000		–0.024 ± 0.090	Krou	–0.167 ± 0.059	Krou
NGC1453	0.025 ± 0.083	Salp	0.030 ± 0.084	Salp	0.000 ± 0.000		0.000 ± 0.000	
NGC1587	–0.018 ± 0.083	Krou	0.174 ± 0.062	Salp	0.000 ± 0.000		0.000 ± 0.000	
NGC2563	0.006 ± 0.079	Salp	0.028 ± 0.080	Salp	0.000 ± 0.000		0.000 ± 0.000	
NGC4261	–0.229 ± 0.070	Krou	–0.213 ± 0.068	Krou	0.000 ± 0.000		0.000 ± 0.000	
NGC5353	–0.010 ± 0.073	Krou	–0.021 ± 0.077	Krou	0.011 ± 0.103	Salp	0.017 ± 0.106	Salp
NGC5846	–0.035 ± 0.078	Krou	–0.057 ± 0.084	Krou	N/A	N/A	N/A	N/A
NGC5982	–0.054 ± 0.091	Krou	0.000 ± 0.000		0.000 ± 0.000		0.000 ± 0.000	
NGC6658	0.000 ± 0.000		–0.231 ± 0.055	Krou	0.000 ± 0.000		0.000 ± 0.000	
NGC7619	–0.024 ± 0.083	Krou	–0.062 ± 0.083	Krou	0.000 ± 0.000		0.000 ± 0.000	
Low-richness								
NGC0315	0.000 ± 0.000		0.000 ± 0.000		0.000 ± 0.000		0.000 ± 0.000	
NGC0524	0.058 ± 0.103	Salp	0.011 ± 0.106	Salp	0.190 ± 0.068	Salp	0.000 ± 0.000	
NGC1779	0.018 ± 0.071	Salp	0.048 ± 0.070	Salp	0.000 ± 0.000		0.000 ± 0.000	
NGC2768	0.014 ± 0.084	Salp	0.000 ± 0.000		0.000 ± 0.000		0.000 ± 0.000	
NGC3613	0.000 ± 0.000		0.000 ± 0.000		0.000 ± 0.000		0.000 ± 0.000	
NGC3665	0.000 ± 0.000		0.000 ± 0.000		0.000 ± 0.000		0.000 ± 0.000	
NGC5127	0.000 ± 0.000		0.000 ± 0.000		0.000 ± 0.000		0.000 ± 0.000	
NGC5490	–0.024 ± 0.086	Krou	–0.024 ± 0.086	Krou	0.000 ± 0.000		0.000 ± 0.000	
NGC5629	0.013 ± 0.092	Salp	0.000 ± 0.000		0.000 ± 0.000		0.000 ± 0.000	

Table 5.3: *The difference between the fraction overabundance between the unimodal IMF model and the Kroupa Binary corrected model. The difference is $FO_{Kroupa} - FO_{Unimodal}$. The* ***Better fit*** *column shows which model provides the best description of this specific feature in the galaxy spectrum (thus, the model that shows the smallest fraction overabundance).*

From Table 5.3, we can see that the Kroupa Binary corrected model fits the NaD feature better in 15 out of the 29 cases (considering only the inner bin, but taking into account both the SSP and CSP fits). The Vazdekis Model is better in 14 of the cases. However, in the Low-richness groups, the Vazdekis Model (with the unimodal IMF) seems to be a better fit. It is important to note that the SSP and CSP fits favour different IMFs in some of the galaxies (e.g. in NGC0410, where the Salpeter IMF best describes the SSP fit, but the Kroupa binary corrected IMF best describes the CSP fit).

5.3 Correlation with observed properties

As can be seen in Table 5.1 and Table 5.2, not all the galaxies show an overabundance. For this reason, and the fact that the NaD doublet is an important spectral feature, we want to look for any correlations with regard to other galaxy or group properties.

The galaxies that show sodium overabundance in the inner bin (with either SSP or CSP fit) are:
High-richness: NGC0410, NGC0584, NGC0777, NGC1060, NGC1453, NGC1587, NGC2563, NGC4261, NGC5353, NGC5846, NGC5982 and NGC7619.
Low-richness: NGC0524, NGC1779, NGC2768, NGC5490 and NGC5629.

The galaxies that show no sodium overabundance:
High-richness: NGC0924 and NGC6658.
Low-richness: NGC0315, NGC3613, NGC3665 and NGC5127.

5.3.1 Observations in other wavelengths (X-ray, radio, sub-mm)

The results of this analysis will be compared to several observations from other wavelengths.

O'Sullivan et al. (2017) presented the CLoGS sample and also compiled X-ray data of this sample. For the X-ray analysis, XMM-Newton (X-ray Multi-Mirror Mission) and Chandra observations were used.

Kolokythas et al. (2018) did radio observations of several CLoGS galaxy groups, using the Giant Metrewave Radio Telescope (GMRT) in dual-frequency, thus at 235 MHz and 610 MHz, with an average observational time of four hours per source. Fourteen of the 23 BGGs in our sample were also observed by Kolokythas et al. (2018) and nine of the 23 by Kolokythas et al. (2019).

O'Sullivan et al. (2018) presented IRAM 30 m telescope observations as well as APEX telescope observations on 36 group-dominant elliptical galaxies. They also used archival telescope data, completing the set of 53 CLoGS galaxies, which included all 23 of our sample. O'Sullivan et al. (2018) analysed the data to obtain molecular gas masses in these galaxies. In this analysis, they also used continuum fluxes, from the NRAO (National Radio Astronomy Observatory) VLA Sky Survey (NVSS (Condon et al., 1998, 2002)). Some of the information regarding other wavelengths is available in Appendix A.

5.3.2 Correlation between Na overabundance and other galaxy and group properties

The abovementioned Na overabundance was compared to different galaxy and group properties listed in Tables 2.1, 2.3, 2.4, 2.5, 2.6 and 2.7. Several plots were also made to see whether some correlation can be found between the overabundance ratios and the properties. These plots can be obtained from Appendix B.6[1].

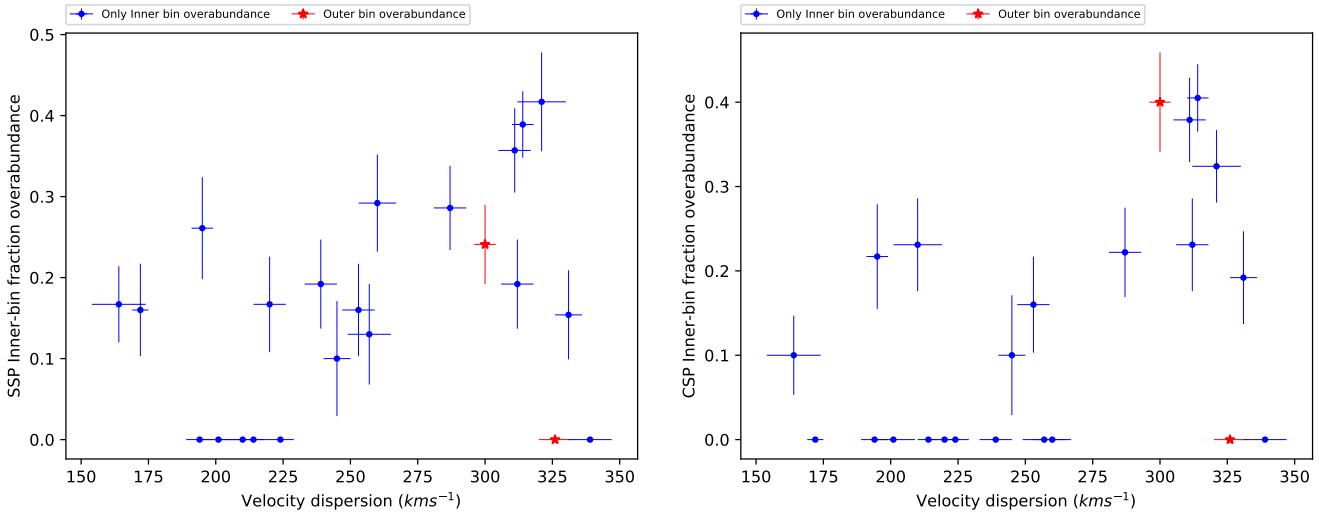
The first important conclusion from these plots is that there is no direct and clear correlation. This, however, does not discard the possibility that some correlation can be found after in-depth study.

When, for instance, looking at the fraction overabundance vs central velocity dispersion plots in Figure 5.2, it confirms that there are two populations of galaxies with regard to the sodium overabundance: those that have some sort of overabundance (all above 0 on the y-axis) and those that show no overabundance (at y=0). When looking at both

[1]Appendix C.6 can be obtained from https://drive.google.com/file/d/1_IUwfbguGI5-X2wEnNDcsZeeZ-eCtRPw/view?usp=sharing

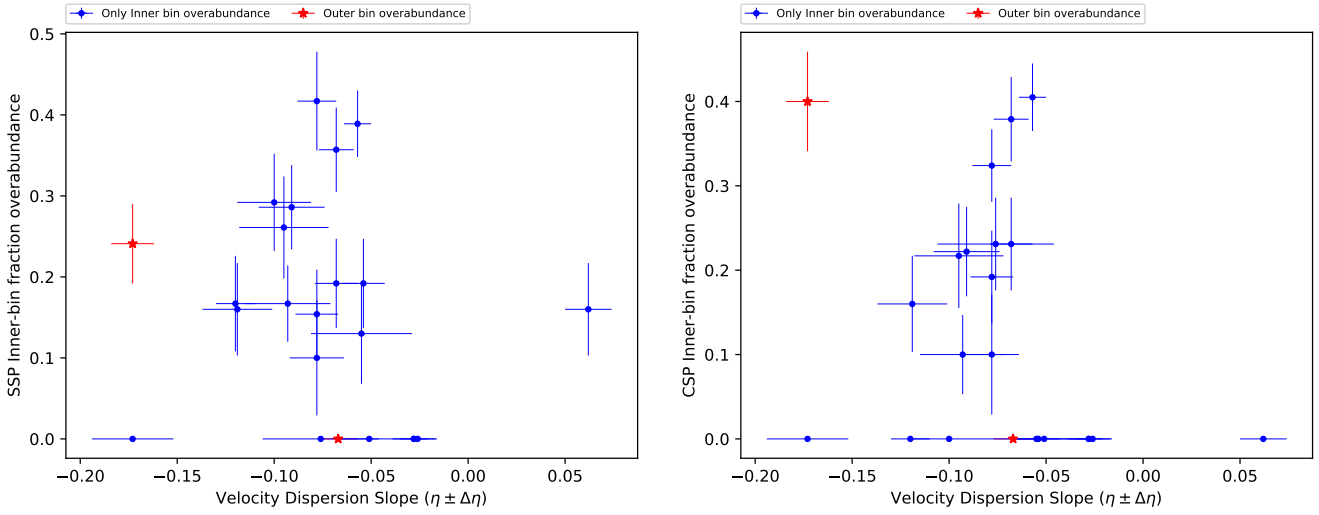
these plots, the more massive galaxies show a bigger scatter, which indicates more diverse properties, than the less massive galaxies. The fact that more massive galaxies show more diverse properties is also shown in papers such as Loubser et al. (2018), their figures 3 and 4.

This might also suggest that the sodium overabundance is a physical phenomenon, rather than an artifact caused by data reduction or modelling, as it was also discussed by researchers such as La Barbera et al. (2017).



(a) **(b)**

Figure 5.2: *The fraction of NaD overabundance in the SSP (left) and CSP (right) fits of the galaxies, vs the velocity dispersion from Table 2.4. Note that the red points indicate galaxies that have both inner and outer bin overabundances.*

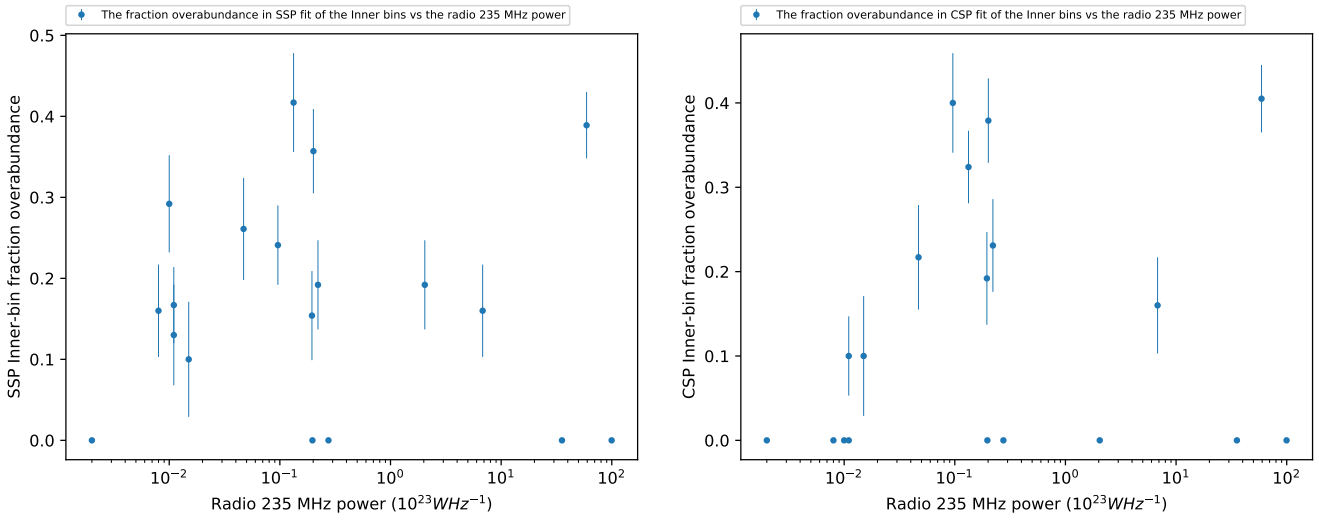


(a) **(b)**

Figure 5.3: *The fraction of NaD overabundance in the SSP (left) and CSP (right) fits of the galaxies, vs the velocity dispersion slope from Table 2.4. Note that the red points indicate galaxies that have both inner and outer bin overabundances.*

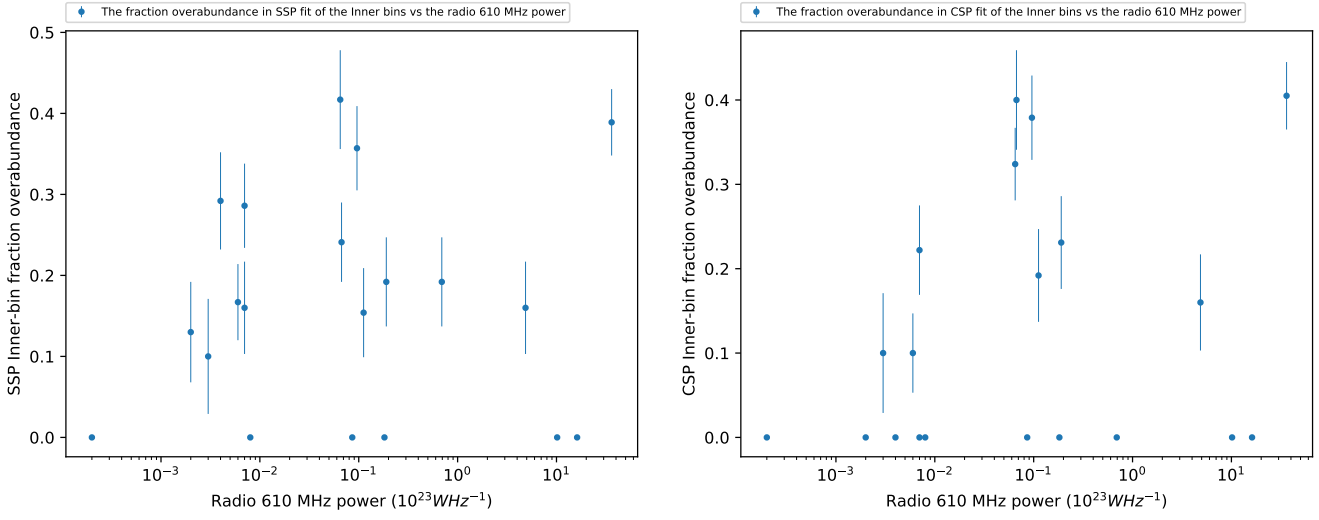
When looking at the radio power of the galaxies (in Table 2.6) and Figures 5.4, 5.5 and 5.6, there might be a weak correlation to this as well, as those with the lowest radio flux densities seem to have a mild upward trend of radio flux

with overabundance to a certain point, but then it flattens (thus creating a line for overabundance with an increase in flux density). However, a greater sample could be able to define a better correlation.



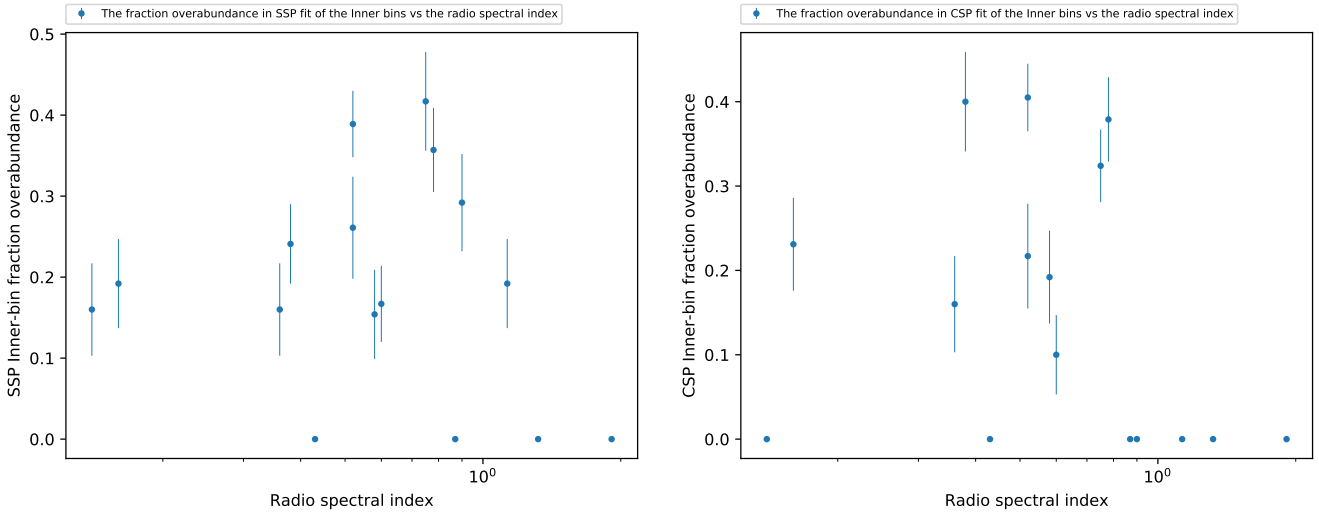
(a) **(b)**

Figure 5.4: *The fraction of NaD overabundance in the SSP (left) and CSP (right) fits of the galaxies, vs the radio output at 235 MHz from Table 2.6.*



(a) **(b)**

Figure 5.5: *The fraction of NaD overabundance in the SSP (left) and CSP (right) fits of the galaxies, vs the radio output at 610 MHz from Table 2.6.*



(a) **(b)**

Figure 5.6: *The fraction of NaD overabundance in the SSP (left) and CSP (right) fits of the galaxies, vs the radio spectral index from Table 2.6.*

It is important to note, however, because only six out of the 23 galaxies show no overabundance, a correlation cannot be made with confidence. The fact that the fraction overabundance is a function of S/N ratio and that the SSP or CSP fit shows different overabundances, could also lead to over-interpretation. The S/N ratio of the spectra needs to be more sufficient.

CHAPTER 6

Summary, conclusions and future work

During this study, the optical spectra of 23 BGGs (a sub-sample of CLoGS), observed by the HET, were analysed using ULySS. The spectra of the 23 galaxies were fitted to SSP and CSP synthetic spectra to estimate the age and metallicities of the galaxies (SSP) or of its components (CSP). Due to the NaD mismatch in many of the spectra, the SSP models that were used, were also analysed, together with [Na/Fe] and α-enhanced models. The wavelength range that was used was examined using a mock-spectra analysis.

The results can be summarised as follows:

- In Chapter 3, the classification results (whether the spectra can be better described with an SSP/CSP) with the Vazdekis (unimodal IMF) model, are given, with some problems arising: large error margins as well as discrepancies in the data itself with regard to hitting the upper limit of the model, as well as between the SSP and CSP fit results.
- To further investigate the contradictory results, four different stellar population models were used. The main results here were that there many discrepancies between the four models. Some of the models showed a better SSP fit whereas others showed a better CSP fit of the same galaxy and aperture.
- χ^2 plots showed no convergence in the ages of the stellar populations. This led to a mock spectra analysis from which the main conclusion was that the wavelength lacked important age sensitive indices in the blue-end of the optical wavelength range.
- In Chapter 4, the stellar population models were analysed using the MILES online webtool to generate spectra. This was done to investigate one specific feature, namely NaD, which was the most prominent feature that was underfit in the models. α-enhancements did not seem to solve the overabundance of sodium, but worsened the problem.
- The [Na/Fe]-enhanced models seem to hold the key to fit the NaD absorption doublet better. The [Na/Fe] abundances are correlated with the IMF of the stellar population, as is also shown in La Barbera et al. (2017).

- The IMF type also seems to have some influence on the NaD feature, but much smaller influence than the [Na/Fe]-models, with the Kroupa binary corrected IMF showing the best potential fit.
- In Chapter 5, the fraction overabundance of sodium in the SSP and CSP fits (using the Vazdekis unimodal IMF model) was measured, to give a fraction overabundance of each fit. Seventeen out of the 23 galaxies showed an overabundance in either the SSP or CSP fit of the inner bin.
- The fraction overabundance in the fits, using the Kroupa model (binary corrected IMF), was also measured. The fraction overabundance in the two models was compared and it was found that fourteen of the 29 mismatches in the inner bins (considering both the SSP and CSP fits) showed a better description of the NaD feature using the unimodal IMF and fifteen of the 29 using the Kroupa binary corrected IMF.
- The fractions of overabundance were also compared to galaxy and group properties as measured from observations in other wavelength regimes, e.g. X-ray and radio. No clear correlation was found, but more massive galaxies seem to have more diverse properties than the less massive galaxies, in agreement with a similar conclusion made in Loubser et al. (2018).

One of the main conclusions of this research is that a wavelength range of 4600 to 6200 Å is insufficient to accurately constrain the SFH of BGGs. This is because some of the indices to the blue-end of the spectrum, that are age sensitive, are not included in this wavelength. To make sure that the inability to confidently constrain any younger stellar populations were not due to the choice of the stellar population model, four different models were used to do SSP and CSP fits, with almost identical results to the first model used. A mock spectra study was also done to confirm this conclusion. When compared to a study done by Loubser et al. (2018) where a different wavelength range was used, the inability of a wavelength range not including indices bluewards of 4200 Å to detect small populations of younger stars, was confirmed.

Although the SSP/CSP classification results are now under scrutiny, the models still seemed to fit the galaxy spectra very well. One of the main features, however, that seemed to be underfit in the stellar population models, is the NaD feature (at 5889.950 Å and 5895.924 Å). Seventeen out of the 23 BGGs had a sodium overabundance in their inner bin with either the SSP or CSP fits. This led to a model analysis where theoretical spectra from the MILES library were plotted, changing different parameters to study the influence of these parameters on the spectra, and especially on the NaD feature. The main conclusion is that including non-solar α-enhancements seems to worsen the discrepancy, while [Na/Fe]-enhanced models seem to be an improvement. These models, however, are not yet detailed enough to be incorporated into stellar population software such as ULySS.

From the [Na/Fe] enhanced model analysis, it is evident that the NaD feature, and therefore sodium overabundance in galaxies is linked to the IMF, as is also studied by La Barbera et al. (2017). Most massive elliptical galaxies are best described by a bottom-heavy IMF (Conroy & van Dokkum, 2012; van Dokkum & Conroy, 2012; Smith et al., 2012; Spiniello et al., 2012; Ferreras et al., 2013). However, the model analysis showed that the effect of the [Na/Fe]-enhancement decreases as the IMF slope increases. The influence of the [Na/Fe]-enhancement is thus more important in galaxies with a top-heavy IMF, but the influence on ellipticals cannot be neglected.

The fraction of sodium overabundance was measured in all the galaxy spectra. Different galaxy and group properties from different wavelength observations (X-rays, radio, sub-millimetre, etc.) were compared to the fraction overabundance to see whether this overabundance could be explained by physical phenomena. One of the main conclusions here is that the more massive galaxies show more diverse properties, as was also found by Loubser et al. (2018). A scatter in the fraction overabundance vs velocity dispersion plots also corresponds to a bigger range in IMF slopes for massive galaxies. Smith et al. (2017) also showed that some massive elliptical galaxies are better described with an IMF less bottom-heavy than the Salpeter IMF (i.e. a non-universal IMF).

If it is possible to obtain wider wavelength spectra of these galaxies, or just more to the blue-end of the spectrum, the SFHs of the galaxies might be easier to constrain. To study the correlation between the NaD mismatch and the galaxy properties more effectively, a bigger selection of BGGs will also be needed. CLoGS will, in the future, be extended to 'eCLoGS' to include Southern Hemisphere groups as well as groups with a spiral galaxy as dominant group member.

The results, together with the model analysis, show us that the [Na/Fe]-enhanced models could be an answer to the NaD mismatch. These models, however, must still be developed for spectral analysis software and also for a wider variety of metallicities and ages as well as for different IMF types.

Appendices

APPENDIX A

Observations in other wavelengths

A.1 Observations in other wavelengths (X-ray, radio, sub-mm)

As can be seen in Appendix B.7, the 23 galaxies that are studied here have different names in different catalogues, with different types of sources as they are studied in different wavelengths. In this section, a summary of previous multiwavelength studies of all the galaxies is done. The groups in which the BGGs are, are labeled as LGG (Lyon Groups of Galaxies).

A.2 High-richness galaxy groups

A.2.1 NGC0410 in LGG18

According to O'Sullivan et al. (2017), LGG18 is an X-ray luminous group with a cool core. NGC0410 and a close group member, NGC0407, are both detected as point-sources in X-ray.

A.2.2 NGC0584 in LGG27

LGG27 is an X-ray faint system, with some extended emission around NGC0584 (O'Sullivan et al., 2017).

A.2.3 NGC0777 in LGG42

According to O'Sullivan et al. (2017), LGG42 is an X-ray luminous group as detected by RASS[1]. XMM and Chandra ACIS (Advanced CCD Imaging Spectrometer)-I trace the hot gas to a radius of about 275 kpc around NGC0777.

[1] ROSAT all-sky survey, where ROSAT is short for Röntgensatellit

A.2.4 NGC0924 in LGG61

LGG61 only has a point-like X-ray emission, NGC0924 (O'Sullivan et al., 2017). NGC0924 also lacks a significant hot gas halo. NGC0924 also has a radio point source detected at 610 MHz but not at 235 MHz.

A.2.5 NGC1060 in LGG72

XMM reveals a distributed intra-group medium (IGM) with X-ray peaks centered at NGC1060 as well as another bright elliptical (NGC1066). X-ray diffuse emissions fill an arc of length 250 kpc between the two peaks. According to observations, NGC1066 and several close members form a secondary group that is falling into the group centered around NGC1060. Due to the group now having two bright peaks, it was previously not included in the RASS survey, although it has comparable mass to the other galaxy groups. In the GMRT (Giant Metrewave Radio Telescope) observations, several radio sources were detected in this group. The 610 MHz data show small-scale bipolar jets associated with NGC1060 only extending about 4kpc. Temperatures between the two peaks of about 1.9 keV in magnitude are observed between the two peaks, which possibly indicates shock heating (O'Sullivan et al., 2017).

A.2.6 NGC1453 in LGG103

Although LGG103 has not been identified previously as an X-ray luminous object, the XMM observations indicate an IGM with temperature of about 0.75 keV in a radius of about 105 kpc surrounding NGC1453. This BGG also has a radio point source that has been detected by GMRT at 235 and 610 MHz as well as by the NVSS (NRAO VLA Sky Survey) at 1.4 GHz (O'Sullivan et al., 2017).

A.2.7 NGC1587 in LGG117

O'Sullivan et al. (2017) and Helsdon et al. (2005) found comparable evidence that LGG117 has X-ray emissions. Helsdon et al. (2005) confirmed an X-ray luminous IGM in LGG117 with the X-ray peak located at NGC1587. O'Sullivan et al. (2017) found a system temperature of about 0.37 keV, but also detected diffuse X-ray emission extending 135 kpc. Therefore, it confirms that this is an IGM rather than a galaxy halo.

Another interesting finding by O'Sullivan et al. (2017) is that NGC1587 contains H I and molecular gas and is also a radio source at 610 MHz. This radio emission is extended with a central point source surrounded by low surface brightness amorphous emission, with no clear jets or lobes.

According to Giacintucci et al. (2011), AGN (active galactic nuclei) activity may have heated the group core.

A.2.8 NGC2563 in LG158

According to Mulchaey et al. (2003), LGG 158 is X-ray luminous. This is supported by O'Sullivan et al. (2017) who traced the IGM to about 950 kpc. Both XMM and ACIS-I indicate that the IGM is regular and undisturbed with a cool core. A radio source is also detected in NGC2563 with the 610 MHz GMRT observations, but not with the 235 MHz observations (the data used by Morandi et al. (2017) in his analysis are also included in the work on NGC2563 by O'Sullivan et al. (2017)).

A.2.9 NGC4261 in LG278

According to O'Sullivan et al. (2017), ROSAT observations identified a hot IGM in the galaxy group LGG278, extending more than 370kpc from NGC4261. Croston et al. (2005, 2008) and O'Sullivan et al. (2011) have studied this IGM using Chandra and XMM data. According to O'Sullivan et al. (2017), NGC4261 is an FR-I radio galaxy (also called 3C 270), which is one of the most radio-luminous galaxies in the CLoGS sample. Chandra also revealed X-ray jets, which correspond to the inner few kpc of the radiojets (Gliozzi et al., 2003; Zezas et al., 2005). This confirms that the jets are aligned closely to the plane of the sky. According to Worrall et al. (2010), the jets swept clear conical regions in the core of the galaxy and the lobes inflated large cavaties in the IGM. These cavities are also surrounded by rims of compressed gas. Oddly enough, Chandra X-ray data also indicate the existence of a 10 kpc cool core, despite the large enthalpy of the cavities and the possibility of shock-heating (O'Sullivan et al., 2017).

A.2.10 NGC5353 in LGG363

NGC5353 is close to, and likely interacting with NGC5454 in LGG363 (O'Sullivan et al., 2017). The hot IGM of this group is centred on NGC5353, is approximately isothermal and extends to about 100kpc (Finoguenov et al., 2007). According to Mulchaey et al. (2003) and Osmond & Ponman (2004), the group is X-ray luminous. Borthakur et al. (2010) also show that the group is cold gas rich, containing more than $5 \times 10^9 M_\odot$ of H I. According to O'Sullivan et al. (2017), X-ray and radio point sources have also been detected in NGC5353 and subsidiary galaxies in LGG363.

A.2.11 NGC5846 in LGG393

LGG393 is an X-ray luminous group centred on NGC5846 (O'Sullivan et al., 2017). According to Giacintucci et al. (2011), NGC5846 also has an AGN with small-scale jets and lobes. These also have inflated cavities in the centre of the group's cool core (Machacek et al., 2011). An interesting finding by Machacek et al. (2011) and Gastaldello et al. (2013), using Chandra and XMM observations, is that the group is sloshing. This led to O'Sullivan et al. (2017) only using the north-east and south-west quadrants, avoiding the asymmetries.

A.2.12 NGC5982 in LGG402

NGC5982 has been detected by RASS (Beuing et al., 1999), but the XMM observations by O'Sullivan et al. (2017) were required to validate if the group is indeed X-ray luminous with an extended IGM. Accoring to O'Sullivan et al. (2017), the temperature profile is centrally peaked, with the scale of the innermost bin about 6 kpc, "making an unresolved small cool core unlikely". On the other hand, NGC5982 has a low entropy in its central temperature bin, of 14.4±2.9 keV cm^2, with a relatively short cooling time of about 250 Myr. NGC5982 also has an AGN, which is detected as a radio source (O'Sullivan et al., 2017). Cool gas has also been detected in NGC5982. According to Morganti et al. (2006), there is a $3.4 \times 10^7 M_\odot$ H I cloud about 6 kpc east and 200 km s^{-1} offset from the nucleus. Sarzi et al. (2006) studied the galaxy core kinematics and detected $2.3 \times 10^4 M_\odot$ of Hα-emitting ionised gas. According to O'Sullivan et al. (2017), NGC5982 is bracketed by two spiral galaxies. Both these spiral galaxies have been detected in radio observations. NGC5985, which is a face-on spiral galaxy east of NGC5982, has star formation in its disk, which is visible in the radio and in the XMM data.

A.2.13 NGC6658 in LGG421

According to O'Sullivan et al. (2017), no hot IGM is detected with XMM in this group, although NGC6658 and another group member, NGC6660, are detected as point-like sources. Spectral fitting also shows evidence of thermal and powerlaw in NGC6658. Neither of these two galaxies has any radio emissions.

A.2.14 NGC7619 in LGG473

A number of optical observations has identified this as a single group. However, X-ray data show that this is a merging system (O'Sullivan et al., 2017), with ROSAT observations showing the surface brightness distribution peaked at two galaxies: NGC7619 and NGC7626 (Mulchaey et al., 2003). Chandra mapping confirmed that each of these two galaxies sits at the centre of a cool core. A ridge of hotter gas (which is possibly shock-heated) forms a ridge between the two cool cores (Randall et al., 2009). Although NGC7619 is the brightest group elliptical (BGE) of LGG473 and is located in the brighter and more extended of the X-ray peaks, it only hosts a radio point source, while NGC7626 is an FR-I radio galaxy with approximately 100 kpc scale jets and lobes (Giacintucci et al., 2011).

A.3 Low-richness galaxy groups

A.3.1 NGC0315 in LGG14

According to Morganti et al. (2009), there are two HI absorbing systems within the central region of NGC0315. The gas that is detected here, might be also close to the galaxy's AGN, although faint optical absorption features suggest that it could be due to clouds falling into NGC0315.

A.3.2 NGC0524 in LGG23

LGG 23 contains an extended X-ray hot gas component, which is associated with NGC0524 (Mulchaey et al., 2003; Kharb et al., 2012). A radio point source is also detected in the 610 MHz, according to Kolokythas et al. (2019).

A.3.3 NGC1779 in LGG126

Condon et al. (1998) detected a weak 1.4 GHz point source in NGC1779 and Kolokythas et al. (2019) detected a weak radio point source in the galaxy in both 235 MHz and 610 MHz.

A.3.4 NGC2768 in LGG167

Fried & Illingworth (1994) observed a polar ionised O[II] gas disk in NGC2768, possibly as a product of a past merger. A radio source is detected at 1.4 GHz by Condon et al. (1998) and Brown et al. (2011). A radio point source is also detected within the galaxy in both 235 MHz and 610 MHz (Kolokythas et al., 2019).

A.3.5 NGC3613 in LGG232

In NGC3613, a faint radio source was detected at 1.4 GHz in the central part of the galaxy (Brown et al., 2011); however, no radio detection was made in 235 MHz nor in 610 MHz (Kolokythas et al., 2019).

A.3.6 NGC3665 in LGG236

LGG236 is a very luminous X-ray galaxy group, where the galaxies have an unusually low velocity dispersion (Helsdon et al., 2005). According to Xiao et al. (2018) NGC3665 has low-level star formation, though Young et al. (2011) and Alatalo et al. (2013) observed a cold gas reservoir that is significant. NGC3665 also has a weak double-jet radio source, according to Parma et al. (1986) and Nyland et al. (2016). The axes of the jets are almost perpendicular to the central molecular gas disk's major axis (Onishi et al., 2017). Condon et al. (1998) already detected a radio jet source in 1.4 GHz. The symmetric jet is also observed in the 235 MHz and 610 MHz frequencies (Kolokythas et al., 2019).

A.3.7 NGC5127 in LGG350

Liu & Xie (1992) found a radio jet in NGC5127.

A.3.8 NGC5490 in LGG376

According to Condon & Broderick (1988), NGC5490 has an FR I radio source, with Xu et al. (2000) and Kharb et al. (2012) observing a polarised core-jet structure. Brown et al. (2011) observed a source in the 1.4 GHz. Kolokythas et al. (2019) observed a core-jet morphology in 235 MHz and at 610 MHz a linear and thin radio jet.

A.3.9 NGC5629 in LGG383

Kolokythas et al. (2019) found no radio detection in either 235 MHz or 610 MHz of NGC5629.

APPENDIX B

Other documents

Several other plots and information can be obtained from
https://drive.google.com/drive/folders/1E9aLoi1L9b2PIRhwYxept0ARAhS861Bf?usp=sharing.
All the links shared throughout this thesis all lead to documents within this shared folder.

These include:
Appendix B.1: Model analysis plots for shorter wavelengths -
https://drive.google.com/file/d/1fYM86LJDOVYFatcHAvurBHF7m1zaABgC/view?usp=sharing
Appendix B.2: All of the codes used in the reduction of the data -
https://drive.google.com/file/d/1cd1r1P1B-h7Oq2zDdyKsHkEG5FMDpt7M/view?usp=sharing
Appendix B.3: The plots of the first SSP and CSP fits -
https://drive.google.com/file/d/1LP_WBPRHCn4BeTytbrl5-vJwvYEIzr0n/view?usp=sharing
Appendix B.4: The plots of four different models SSP and CSP fits -
https://drive.google.com/file/d/1-r7bAWSD--NwlFuo06oSSmW6XMIVMwWx/view?usp=sharing
Appendix B.5: The plots that were used to decide the MD -
https://drive.google.com/file/d/1ZfABuM7njp7K5ryDukucor5eHIIE96bt/view?usp=sharing
Appendix B.6: Plots of the amount of NaD overabundance vs galaxy and group properties -
https://drive.google.com/file/d/1_IUwfbguGI5-X2wEnNDcsZeeZ-eCtRPw/view?usp=sharing
Appendix B.7: A list of the different names of the galaxies in different catalogues -
https://drive.google.com/file/d/15OMzymX-lZw1-d-48tARi_3Av51rxOi1/view?usp=sharing
Appendix B.8: The SSP and CSP fits for the two models used in the NaD overabundance analysis -
https://drive.google.com/file/d/1MKsAQuwI0uadQmPayA9sfndmWoBza3eI/view?usp=sharing

APPENDIX C

SAIP Proceedings

Star formation histories of Brightest Group Galaxies in CLoGS

O C Havenga[1], S I Loubser[1], E O'Sullivan[2], A Babul[3] and A Ratsimbazafy[1]

[1] Centre for Space Research, North-West University, Potchefstroom, 2520, South Africa
[2] Harvard-Smithsonian Centre for Astrophysics, 60 Garden Street, Cambridge, MA 02138
[3] Department of Physics and Astronomy, University of Victoria, Victoria, BC V8P 1A1, Canada

E-mail: 24909629@nwu.ac.za

Abstract. An important component of galaxy formation and evolution studies, is to accurately constrain the star formation histories (SFHs) of galaxies. While the SFHs of most massive early-type galaxies can be described using a single passively-evolving stellar component (Single Stellar Population [SSP]), there is a fraction of massive early-type galaxies in the centres of galaxy groups and galaxy clusters where recent star formation is observed and are better described by two or more stellar components (Composite Stellar Population [CSP]). In this project we identify and constrain possible recent star formation episodes in a sample of 23 BGGs (Brightest Group Galaxies), which is a sub-sample of the Complete Local-Volume Groups Sample (CLoGS). Most of these BGGs are in the centres of X-ray rich groups and all are closer than 80Mpc. We use archival spatially-resolved long-slit spectroscopy from the Hobby-Eberly Telescope (HET) at the McDonald Observatory, and determine whether the BGGs are better described by an SSP or a CSP using ULySS. For this, stellar population models were fit to each of the 23 galaxies. The results showed that 11 of the BGGs were better described by a CSP while 12 of the BGGs were better described by an SSP. These results must be compared to the existing X-ray and radio observations of the groups.

1. Introduction

Galaxy groups are some of the best environments for studying the impact of galaxies on the surrounding Intergalactic Medium, as is done in [1].

The CLoGS sample is an optically selected sample of 53 galaxy groups within 80 Mpc. The sample selection is described in detail in [2]. X-ray, radio and sub-mm data have been collected for the entire sample [2]. In addition, [3] have analysed spatially-resolved long-slit spectroscopy from the 10m Hobby-Eberly Telescope (HET at the McDonald Observatory observed in September 2010 [4]) for a sub-sample of 23 BGGs. This project is a continuation, and uses the same sub-sample and data to derive star formation histories for the 23 BGGs. The aim is to study various properties of BGGs that serve as signatures of their evolutionary paths and also interpret the influence of the environment. The central galaxies (or BGGs) are in the centres of the groups' massive dark matter haloes and are thus ideal probes of galaxy evolution.

Table 1 gives information about the galaxies in this sub-sample. The sample was divided into two categories: a high-richness category and a low-richness category. [2] defined a richness parameter (R) as the number of galaxies within that group (within 1 Mpc from the centre and 3σ

in velocity of the BGG) with the luminosity constraint: $\log L_B \geq 10.2$. Groups with $4 \leq R \leq 8$ were classified as High-richness groups and groups with $R =$ 2-3 were classified as Low-richness groups.

Table 1. The basic information of the BGGs that are studied in this project.

Galaxy information				
High-richness				
Galaxy	**Redshift**	**RA**	**DEC**	**Velocity (km/s)**
NGC0410	0.0177	01h10m58.9s	+33d09m07s	5294
NGC0584	0.0060	01h31m20.7s	–06d52m05s	1802
NGC0777	0.0167	02h00m14.9s	+31d25m46s	5015
NGC0924	0.0149	02h26m46.8s	+20d29m51s	4461
NGC1060	0.0173	02h43m15.0s	+32d25m30s	5190
NGC1453	0.0130	03h46m27.2s	–03d58m08s	3886
NGC1587	0.0123	04h30m39.9s	+00d39m42s	3694
NGC2563	0.0149	08h20m35.7s	+21d04m04s	4480
NGC4261	0.0074	12h19m23.2s	+05d49m31s	2212
NGC5353	0.0078	13h53m26.7s	+40d16m59s	2325
NGC5846	0.0057	15h06m29.3s	+01d36m20s	1712
NGC5982	0.0101	15h38m39.8s	+59d21m21s	3017
NGC6658	0.0142	18h33m55.6s	+22d53m18s	4270
NGC7619	0.0125	23h20m14.5s	+08d12m22s	3762
Low-richness				
Galaxy	**Redshift**	**RA**	**DEC**	**Velocity (km/s)**
NGC0315	0.0165	00h57m48.9s	+30d21m09s	4942
NGC0524	0.0080	01h24m47.7s	+09d32m20s	2403
NGC1779	0.0111	05h05m18.1s	–09d08m50s	3313
NGC2768	0.0045	09h11m37.5s	+60d02m14s	1353
NGC3613	0.0068	11h18m36.1s	+58d00m00s	2051
NGC3665	0.0069	11h24m43.7s	+38d45m46s	2069
NGC5127	0.0162	13h23m45.0s	+31d33m57s	4862
NGC5490	0.0162	14h09m57.3s	+17d32m44s	4855
NGC5629	0.0150	14h28m16.4s	+25d50m56s	4498

[5] did a complimentary study on Brightest **Cluster** Galaxies (B**C**Gs), generally more massive and in denser environments than BGGs. It was found that there are two thresholds in the host clusters that determine whether star formation is allowed in the BCG. The two thresholds are the central entropy and the ratio of cooling-time (t_{cool}) to free-fall time (t_{ff}). We are interested in whether these or similar thresholds exist in X-ray rich groups.

The aim in this research is to constrain the SFH of BGGs. This can be done by classifying the galaxies as better described by a single stellar population (SSP) or a composite stellar population (CSP). According to [5] the convention is that most giant elliptical galaxies, such as the BGGs that is considered here, are passively evolving. Whether this holds true for BGGs, can be revealed by the SFH of the galaxies.

2. Method

2.1. Reduction

Since the data in the HET archive was not sky-subtracted, the first step was to do sky-subtraction. The data was then spatially binned into two bins - an inner bin (from 0 - 1 kpc) and an outer bin (from 1 - 2 kpc). This is done for each of the individual galaxies observed. This binning refers to binning along the spatial direction of the 2D spectra. This was done to ensure a high enough signal-to-noise ratio to have acceptable errors on the derived ages and metallicities.

2.2. ULySS

For the analysis, the stellar population code ULySS (University of Lyon Spectroscopic analysis Software) was used. The main routine in ULySS was used to compare the spectrum of a galaxy to the Vazdekis-MILES models [6] using all 985 stars.

The next step was to test the degree of the multiplicative polynomial. The multiplicative polynomial is used to subtract the continuum and dust as well as to account for any possible flux calibration differences between the galaxy and stellar template spectra. For this an SSP-fit was run for all 23 BGGs and for all MDs (Multiplicative Polynomial Degrees) between 1 and 30. After this, the resulting metallicity and age were plot against the different MDs. The optimal choice, where the solution converged, was a degree of 16.

Although the majority of stars inside the BGGs are believed to be old, we want to identify recent star formation episodes, by running both an SSP and a CSP fit for all 23 galaxies. This method is described in full in [5]. Thus, to accurately determine whether there is recent star formation in a galaxy, a CSP with two very different age components was chosen: a young component and an old component, even though no age or metallicity restrictions were placed on the two components.

The best way to do stellar population fitting is with a wide range of wavelengths, to break the age-metallicity degeneracy [7]. Due to some atmospheric features at the red-end of the spectrum (as can be seen in figure 1 and figure 2), the spectrum was truncated at 6200 Å, yielding a wavelength range of 4600-6200 Å, which is still wide enough for spectral fitting.

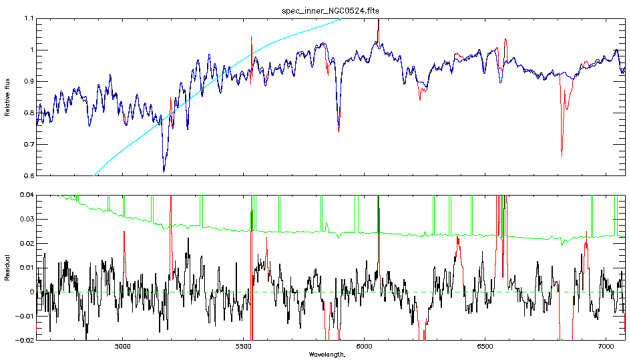


Figure 1. The spectrum of NGC0524 for the full observed wavelength-range. The black line indicates the observed spectrum, the blue line is the stellar population model of the best fit and the red is deviations that are masked during the fitting process. The light blue line shows the multiplicative polynomial that is used to normalize the continuum. The residuals are shown in the lower panel, where the green lines indicate the residuals as allowed by the error spectra (i.e. residuals larger than the green lines indicate deviations from the model as opposed to fluctuations caused by the noise in the spectrum).

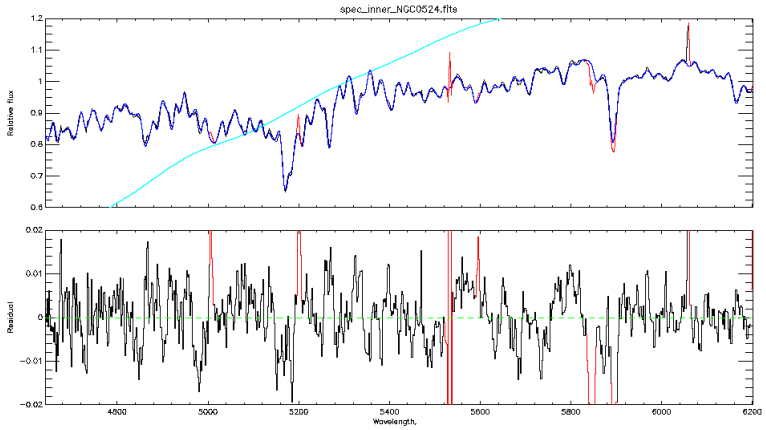


Figure 2. The same spectrum of NGC0524 as shown in figure 1, but now truncated at 4600-6200 Å. Thus, the atmospheric features are excluded.

3. Results and discussion

3.1. Classification

Table 2 gives a summary of the results obtained for both bins of all 23 galaxies.

Table 2. The results of the BGGs by using ULySS, indicating whether the bin was best fit by using a single or composite stellar population.

High-richness		
Galaxy	**Inner**	**Outer**
NGC0410	SSP	SSP
NGC0584	CSP	CSP
NGC0777	SSP	SSP
NGC0924	CSP	SSP
NGC1060	SSP	SSP
NGC1453	SSP	SSP
NGC1587	SSP	SSP
NGC2563	CSP	CSP
NGC4261	SSP	CSP
NGC5353	SSP	SSP
NGC5846	SSP	SSP
NGC5982	CSP	SSP
NGC6658	CSP	SSP
NGC7619	SSP	SSP

Low-richness		
Galaxy	**Inner**	**Outer**
NGC0315	SSP	SSP
NGC0524	CSP	SSP
NGC1779	CSP	CSP
NGC2768	SSP	SSP
NGC3613	SSP	CSP
NGC3665	SSP	SSP
NGC5127	SSP	CSP
NGC5490	SSP	SSP
NGC5629	CSP	SSP

In table 2 it is evident that some of the galaxies' inner bins are better described by a CSP while the outer bins are better described using an SSP. This is to be expected as the older stellar components mostly lie on the outskirts of the galaxy and the star formation mostly takes place in the central part of the galaxy (as is the case in NGC0924, NGC5982, NGC6658, NGC0524 and NGC5629). But, as is evident in NGC4261, NGC3613 and NGC5127, the inverse may also be possible (as described by [8] and [9]). For these three galaxies, it was found that the

inner bin was best fit by a single population, while the outer bin was best fit by a composite population. Naively, one might expect recent star formation to occur in the central parts of the BGGs. However, it is possible that processes such as galaxy mergers or infalling satellites can lead to younger stars in the outer parts. Whether this is indeed the case here, needs to be further investigated by also looking at the X-ray and radio observations.

3.2. NaD

Figure 3 clearly shows a feature that is not well fitted by the model (around 5900 Å). The absorption line is that of NaD, which may be sensitive for the initial mass function (IMF), according to [10]. According to [11] this phenomenon can also be seen in dwarf galaxies. This remarkable discrepancy occurs in 14 BGGs and must be investigated further.

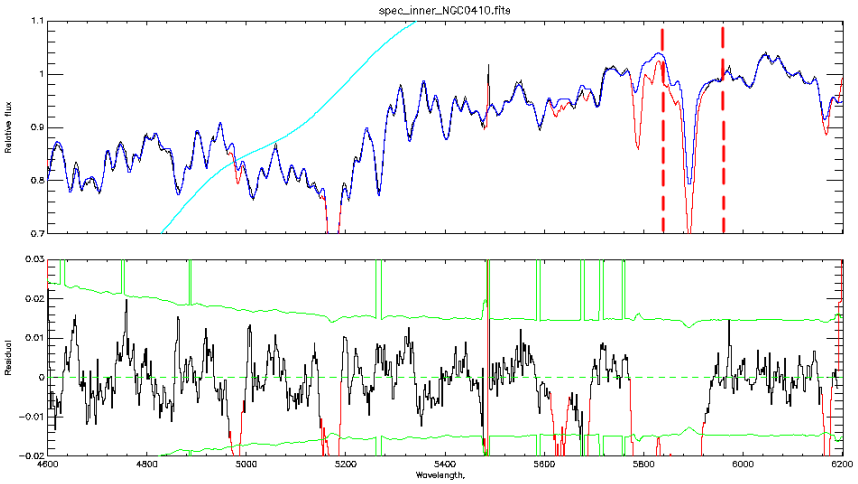


Figure 3. This is the spectrum of NGC0410. The NaD feature can be seen at 5900 Å (between the red dashed lines). The colours have the same meaning as in figure 1.

3.3. Brightest Cluster Galaxies

The same method was used in [5] for 32 BCGs to identify recent star formation episodes. Figure 4 (taken from [3], their figure 2a) shows the combined sample of 55 BGGs and BCGs. From this figure, it can be seen that the two populations, BGGs and BCGs, deviate in their Faber-Jackson relations. Now that we have star formation histories for all 55 central galaxies, these derived properties can be used to look for possible correlations between the galaxy and host group/cluster properties.

4. Conclusion and future work

The results obtained from the stellar population fitting now needs to be compared to data from other wavelengths (X-rays, radio, sub-millimetre, etc.). It is very important to verify why the galaxies which are better described by a CSP, had recent star formation episodes. The results can also be compared with the kinematic signatures of the galaxy groups [3]. After careful interpretation of the preliminary results presented here, we should be able to answer questions such as possible X-ray property thresholds for star formation in groups. Another important line of inquiry is to find out why there is a NaD overabundance as this may disclose some information of the IMF of the galaxies.

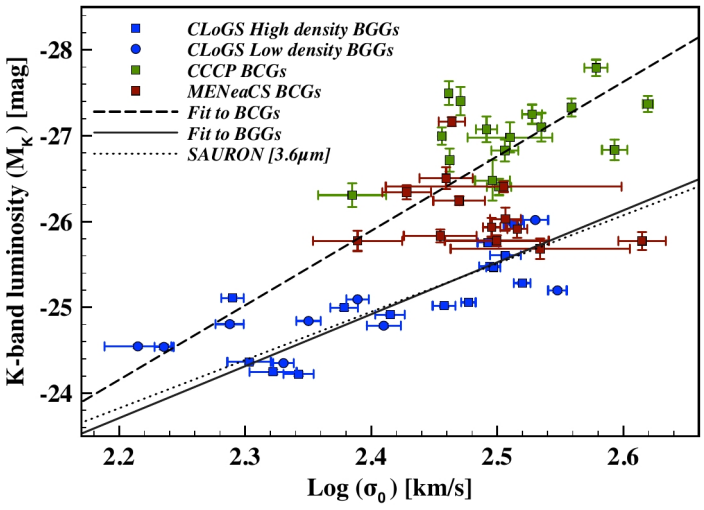


Figure 4. The BGGs are plotted in blue, while the BCGs are plotted in green and red. Note the two different Faber-Jackson relations (FJR) for the two classes. Figure from [3].

Acknowledgments

OCH is aided by the National Astrophysics and Space Science Programme (NASSP) and the National Research Foundation (NRF). SIL is aided by a Henri Chrétien International Research Grant administered by the American Astronomical Society and the NRF.

References

[1] Ponman T, Sanderson A J R and Finoguenov A 2003 The Birmingham-–CFA cluster scaling project – iii. Entropy and similarity in galaxy systems *MNRAS* **343** 331–42

[2] O'Sullivan E, et al. 2017 The Complete Local Volume Groups Sample - i. Sample selection and X-ray properties of the high-richness subsample *MNRAS* **472**(2) 1482–505

[3] Loubser S, Hoekstra H, Babul A, and O'Sullivan E 2018 Diversity in the stellar velocity dispersion profiles of a large sample of brightest cluster galaxies z $\leq$ 0.3 *MNRAS* **477** 335–58

[4] van den Bosch R C E, Gebhardt K, Gltekin K, Yıldırım A, and Walsh J L, 2015, Hunting for supermassive black holes in nearby galaxies with the Hobby-Eberly Telescope *ApJS* **218** 10

[5] Loubser S I, Babul A, Hoekstra H, Mahdavi A, Donahue M, Bildfell C, and Voit G M 2016 The regulation of star formation in cool-core clusters: Imprints on the stellar populations of Brightest Cluster Galaxies *MNRAS* **456** 1565–78

[6] Vazdekis A, Sánchez-Blázquez P, Falcón-Barroso J, Cenarro A J, Beasley M A, Cardiel N, Gorgas J, and Peletier R F 2010 Evolutionary stellar population synthesis with MILES i. The base models and a new line index system *MNRAS* **404** 1639–71

[7] Worthey G 1999 The age-metallicity degeneracy in spectrophotometric dating of stars and galaxies *ASPCS* **192** 283

[8] O'Sullivan E, Combes F, Hamer S, Salomé P, Babul A, and Raychaudhury S 2015 Cold gas in group dominant elliptical galaxies *A&A* **573** A111

[9] Davis D S, Mushotzky R F, Mulchaey J S, Worrall D M, Birkinshaw M, and Burstein D 1995 Diffuse hot gas in the NGC 4261 group of galaxies *ApJ*, **444**, 582–9

[10] Spiniello C, Trager S C, Koopmans L V E, and Chen Y P 2012 Evidence for a mild steepening and bottom-heavy initial mass function in massive galaxies from sodium and titanium-oxide indicators *ApJL* **753** L32

[11] Schwartz C M, and Martin C L 2004 A KECK/HIRES study of kinematics of the cold interstellar medium in dwarf starburst galaxies *ApJ* **610** 201–12

Bibliography

Alatalo K., et al., 2013, MNRAS, 432, 1796

Alonso S., Mesa V., Padilla N., Lambas D., 2012, AAP, 539, A46

Appenzeller I., 2013, Introduction to Astronomical Spectroscopy. UK: Cambridge University Press

Baade W., 1944, ApJ, 100, 137

Bastian N., Covey K. R., Meyer M. R., 2010, ARAA, 48, 339

Baugh C., 2006, Reports on Progress in Physics, 69, 3101

Bekki K., Shioya Y., Tanaka I., 1999, ApJL, 520, L99

Bell E. F., Phleps S., Somerville R. S., Wolf C., Borch A., Meisenheimer K., 2006, ApJ, 652, 270

Best P., von der Linden A., Kauffmann G., Heckman T., Kaiser C., 2007, MNRAS, 379, 894

Beuing J., Dobereiner S., Bohringer H., Bender R., 1999, MNRAS, 302, 209

Bildfell C., Hoekstra H., Babul A., Mahdavi A., 2008, MNRAS, 389, 1637

Borthakur S., Yun M. S., Verdes-Montenegro L., 2010, ApJ, 710, 385

Brown M. J., Jannuzi B. T., Floyd D. J., Mould J. R., 2011, ApJL, 731, L41

Burns J. O., 1990, AJ, 99, 14

Cardiel N., Gorgas J., Sánchez-Blázquez P., Cenarro A., Pedraz S., Bruzual G., Klement J., 2003, AAP, 409, 511

Cardiel N., et al., 2015, REDUCEME: Long-slit spectroscopic data reduction and analysis (ascl:1508.003)

Cassisi S., Pietrinferni A., Salaris M., Castelli F., Cordier D., Castellani M., 2006, MEMSAI, 77, 71

Cavagnolo K. W., Donahue M., Voit G. M., Sun M., 2008a, ApJ, 682, 821

Cavagnolo K. W., Donahue M., Voit G. M., Sun M., 2008b, ApJL, 683, L107

Chabrier G., 2003, PASP, 115, 763

Coelho P., Barbuy B., Meléndez J., Schiavon R. P., Castilho B. V., 2005, AAP, 443, 735

Coelho P., Bruzual G., Charlot S., Weiss A., Barbuy B., Ferguson J. W., 2007, MNRAS, 382, 498

Cole S., Lacey C. G., Baugh C. M., Frenk C. S., 2000, MNRAS, 319, 168

Condon J., Broderick J., 1988, AJ, 96, 30

Condon J., Cotton W., Greisen E., Yin Q., Perley R., Taylor G., Broderick J., 1998, AJ, 115, 1693

Condon J., Cotton W., Broderick J., 2002, AJ, 124, 675

Conroy C., 2013, ARAA, 51, 393

Conroy C., van Dokkum P. G., 2012, ApJ, 760, 71

Croston J., Hardcastle M., Harris D., Belsole E., Birkinshaw M., Worrall D., 2005, ApJ, 626, 733

Croston J. H., Hardcastle M. J., Birkinshaw M., Worrall D. M., Laing R. A., 2008, MNRAS, 386, 1709

Davis D. S., Mushotzky R. F., Mulchaey J. S., Worrall D., Birkinshaw M., Burstein D., 1995, ApJ, 444, 582

Dib S., 2014, MNRAS, 444, 1957

Donahue M., Cavagnolo K., O'Connell R., Voit G. M., 2008, Star Formation and AGN Feedback in Brightest Cluster Galaxies, Spitzer Proposal

Drinkwater M., 2017, Testing the universality of the stellar initial mass function, Keck Observatory Archive Z25

Eggen O., Lynden-Bell D., Sandage A., 1962, ApJ, 136, 748

Eke V., Baugh C., Cole S., Frenk C. S., King H., Peacock J. A., 2005, MNRAS, 362, 1233

Eke V., Baugh C. M., Cole S., Frenk C. S., Navarro J. F., 2006, MNRAS, 370, 1147

Ellis R., Abraham R., Menanteau F., 2000, Astronomy and Geophysics, 41, 2.10

Faber S., 1972, AAP, 20, 361

Faber S., Jackson R., 1976, ApJ, 204, 668

Ferreras I., La Barbera F., de La Rosa I., Vazdekis A., de Carvalho R., Falcon-Barroso J., Ricciardelli E., 2013, MNRAS, 429, L15

Ferreras I., La Barbera F., Vazdekis A., 2016, Astronomy and Geophysics, 57, 2.32

Finoguenov A., Ponman T. J., Osmond J. P. F., Zimer M., 2007, MNRAS, 374, 737

Forbes D. A., et al., 2006, PASA, 23, 38

Fried J. W., Illingworth G. D., 1994, AJ, 107, 992

Fukugita M., Hogan C., Peebles P., 1998, ApJ, 503, 518

Gaspari M., Ruszkowski M., Sharma P., 2012, ApJ, 746, 94

Gastaldello F., et al., 2013, ApJ, 770, 56

Geller M., Huchra J., 1983, ApJS, 52, 61

Giacintucci S., et al., 2011, ApJ, 732, 95

Gliozzi M., Sambruna R., Brandt W., 2003, AAP, 408, 949

Haines C., et al., 2018, MNRAS, 477, 4931

Havenga O. C., Loubser S. I., O'Sullivan E., Babul A., Ratsimbazafy A., 2019, in Engelbrecht J., ed., Proceedings of SAIP 2018, the 63rd Annual Conference of the South African Institute of Physics (University of the Free State, Bloemfontein, 2018). p. 178

Helsdon S. F., Ponman T. J., Mulchaey J., 2005, ApJ, 618, 679

Hoekstra H., Donahue M., Conselice C. J., McNamara B. R., Voit G. M., 2011, ApJ, 726, 48

Hu E., Cowie L., Wang Z., 1985, ApJS, 59, 447

Hudson D. S., Mittal R., Reiprich T. H., Nulsen P. E. J., Andernach H., Sarazin C. L., 2010, A&A, 513, A37

Kaler J. B., 1997, Stars and their Spectra, An Introduction to the Spectral Sequence. Cambridge University Press

Kartaltepe J., et al., 2007, ApJS, 172, 320

Kharb P., O'Dea C. P., Tilak A., Baum S., Haynes E., Noel-Storr J., Fallon C., Christiansen K., 2012, ApJ, 754, 1

Koleva M., Prugniel P., Ocvirk P., Le Borgne D., Soubiran C., 2008, MNRAS, 385, 1998

Koleva M., Prugniel P., Bouchard A., Wu Y., 2009, A&A, 501, 1269

Kolokythas K., O'Sullivan E., Raychaudhury S., Giacintucci S., Gitti M., Babul A., 2018, MNRAS, 481, 1550

Kolokythas K., O'Sullivan E., Intema H., Raychaudhury S., Babul A., Giacintucci S., Gitti M., 2019, MNRAS, 489, 2488

Kroupa P., 2000, MNRAS,

Kroupa P., 2001, MNRAS, 322, 231

Kroupa P., Tout C. A., Gilmore G., 1993, MNRAS, 262, 545

La Barbera F., Vazdekis A., Ferreras I., Pasquali A., Allende Prieto C., Röck B., Aguado D., Peletier R., 2017, MNRAS, 464, 3597

Larson R., 2006, in Revista Mexicana de Astronomia y Astrofisica Conference Series. pp 55–59 (arXiv:astro-ph/0602469)

Le Borgne D., Rocca-Volmerange B., Prugniel P., Lancon A., Fioc M., Soubiran C., 2004, A&A, 425, 881

Le Fèvere O., et al., 2000, MNRAS, 311, 565

Liu F., Xie G., 1992, AAPS, 95, 249

Lloyd-Davies E., Ponman T., Cannon D., 2000, MNRAS, 315, 689

Longair M. S., 1998, Galaxy Formation. Springer-Verlag Berlin Heidelberg

Loubser S., Sánchez-Blázquez P., 2012, MNRAS, 425, 841

Loubser S., Sánchez-Blázquez P., 2015, Highlights of Astronomy, 16, 127

Loubser S., Soechting I., 2013, MNRAS, 431, 2933

Loubser S., Sánchez-Blázquez P., Sansom A., Soechting I., 2009, MNRAS, 398, 133

Loubser S. I., Babul A., Hoekstra H., Mahdavi A., Donahue M., Bildfell C., Voit G. M., 2016, MNRAS, 456, 1565

Loubser S. I., Hoekstra H., Babul A., O'Sullivan E., 2018, MNRAS, 477, 335

Machacek M. E., Jerius D., Kraft R., Forman W. R., Jones C., Randall S., Giacintucci S., Sun M., 2011, ApJ, 743, 15

Maraston C., 1998, MNRAS, 300, 872

Matteucci F., 2012, The Chemical Evolution of the Galaxy. Astrophysics and Space Science Library, Springer Netherlands, doi:10.1007/978-3-642-22491-1, https://books.google.co.za/books?id=KuttCQAAQBAJ

McCarthy I. G., Balogh M. L., Babul A., Poole G. B., Horner D. J., 2004, ApJ, 613, 811

McCarthy I., Babul A., Bower R., Balogh M., 2008, MNRAS, 386, 1309

McIntosh D. H., Guo Y., Hertzberg J., Katz N., Mo H., van den Bosch F. C., Yang X., 2008, MNRAS, 388, 1537

Mentz J. J., 2018, Kinematics and stellar populations of dwarf elliptical galaxies, PhD thesis

Mo H., van den Bosch F., White S., 2010, Galaxy Formation and Evolution. Cambridge University Press

Morandi A., Sun M., Mulchaey J., Nagai D., Bonamente M., 2017, MNRAS, 469, 2423

Morganti R., et al., 2006, MNRAS, 371, 157

Morganti R., Peck A., Oosterloo T., van Moorsel G., Capetti A., Fanti R., Parma P., de Ruiter H., 2009, AAP, 505, 559

Moss C., Whittle M., 2000, MNRAS, 317, 667

Mulchaey J. S., Davis D. S., Mushotzky R. F., Burstein D., 2003, ApJS, 145, 39

Nedelchev B., 2016, On the Nature of Sodium Excess in Nearby Galaxies, MSc dissertation

Niederste-Ostholt M., Strauss M. A., Dong F., Koester B. P., McKay T. A., 2010, MNRAS, 405, 2023

Nyland K., et al., 2016, MNRAS, 458, 2221

O'Connell R. W., 1986, in Norman C. A., Renzini A., Tosi M., eds, Stellar Populations. p. 167

O'Sullivan E., Worrall D., Birkinshaw M., Trinchieri G., Wolter A., Zezas A., Giacintucci S., 2011, MNRAS, 416, 2916

O'Sullivan E., Combes F., Hamer S., Salomé P., Babul A., Raychaudhury S., 2015a, AAP, 573, A111

O'Sullivan E., Combes F., Hamer S., Salomé P., Babul A., Raychaudhury S., 2015b, A&A, 573, A111

O'Sullivan E., et al., 2017, MNRAS, 472, 1482

O'Sullivan E., et al., 2018, A&A, 618, A126

Onishi K., Iguchi S., Davis T. A., Bureau M., Cappellari M., Sarzi M., Blitz L., 2017, MNRAS, 468, 4663

Osmond J. P., Ponman T. J., 2004, MNRAS, 350, 1511

Parma P., de Ruiter H., Fanti C., Fanti R., 1986, AAPS, 64, 135

Patton D., Carlberg R., Marzke R., Pritchet C., da Costa L. N., Pellegrini P., 2000, ApJ, 536, 153

Patton D., et al., 2002, ApJ, 565, 208

Ponman T. J., Cannon D. B., Navarro J. F., 1999, NAT, 397, 135

Ponman T., Sanderson A., Finoguenov A., 2003, MNRAS, 343, 331

Prugniel P., Soubiran C., 2001, VizieR Online Data Catalog, p. III/218

Prugniel P., Soubiran C., 2004, arXiv e-prints, pp astro–ph/0409214

Prugniel P., Soubiran C., Koleva M., Le Borgne D., 2007, arXiv Astrophysics e-prints,

Rafferty D., McNamara B., Nulsen P., Wise M., 2006, ApJ, 652, 216

Randall S. W., Jones C., Kraft R., Forman W. R., O'Sullivan E., 2009, ApJ, 696, 1431

Salaris M., Cassisi S., 2005, Evolution of Stars and Stellar Populations. John Wiley & Sons Ltd

Salpeter E. E., 1955, ApJ, 121, 161

Sánchez-Blázquez P., et al., 2006, MNRAS, 371, 703

Sánchez-Blázquez P., et al., 2007, VizieR Online Data Catalog, p. J/MNRAS/371/703

Sarzi M., et al., 2006, MNRAS, 366, 1151

Scalo J., 1986, FCP, 11, 1

Schwartz C. M., Martin C. L., 2004, ApJ, 610, 201

Segers M. C., Schaye J., Bower R. G., Crain R. A., Schaller M., Theuns T., 2016, MNRAS, 461, L102

Serra P., Trager S., 2007, MNRAS, 374, 769

Smith R. J., Lucey J. R., Carter D., 2012, MNRAS, 426, 2994

Smith R. J., Lucey J. R., Edge A. C., 2017, MNRAS, 467, 836

Spiniello C., Trager S. C., Koopmans L. V. E., Chen Y. P., 2012, ApJL, 753, L32

Sun M., 2012, New Journal of Physics, 14, 045004

Tayler R. J., 1994, The Stars: their structure and evolution. Cambridge University Press

Toomre A., Toomre J., 1972, in BAAS. p. 214

Trager S., Faber S., Dressler A., 2008, MNRAS, 386, 715

Tully R. B., 1987, ApJ, 321, 280

Van den Bosch F. C., Jiang F., Hearin A., Campbell D., Watson D., Padmanabhan N., 2014, MNRAS, 445, 1713

Van den Bosch R. C. E., Gebhardt K., Gltekin K., Yıldırım A., Walsh J. L., 2015, ApJS, 218, 10

Vazdekis A., Casuso E., Peletier R., Beckman J., 1996, ApJS, 106, 307

Vazdekis A., et al., 2010, MNRAS, 404, 1639

Vazdekis A., et al., 2015, MNRAS, 449, 1177

White S., Rees M., 1978, MNRAS, 183, 341

Wiersma R., Schaye J., Theuns T., Dalla Vecchia C., Tornatore L., 2009, MNRAS, 399, 574

Worrall D. M., Birkinshaw M., O'Sullivan E., Zezas A., Wolter A., Trinchieri G., Fabbiano G., 2010, MNRAS, 408, 701

Worthey G., 1992, PhD thesis, California Univ., Santa Cruz.

Worthey G., 1994, ApJS, 95, 107

Worthey G., 1999, The Age-Metallicity Degeneracy. ASP Conference Proceedings, p. 283

Xiao M.-Y., Zhao Y., Gu Q.-S., Shi Y., 2018, ApJ, 854, 111

Xu C., Baum S. A., O'Dea C. P., Wrobel J., Condon J., 2000, AJ, 120, 2950

Young L. M., et al., 2011, MNRAS, 414, 940

Zakharova P., 1989, Astronomische Nachrichten, 310, 127

Zezas A., Birkinshaw M., Worrall D., Peters A., Fabbiano G., 2005, ApJ, 627, 711

van Dokkum P. G., Conroy C., 2012, ApJ, 760, 70